



The  
University  
Of  
Sheffield.

# **The Performance and Hydrodynamics in Unsteady Flow of a Horizontal Axis Tidal Turbine**

A dissertation submitted for the degree of Doctor of Philosophy

by

Binoe E. Abuan

The University of Sheffield

Department of Mechanical Engineering

August 2017

# Abstract

Tidal energy has clear potential in producing large amounts of energy as the world's capacity exceeds 120 GW. Despite being one of the oldest renewable energy sources exploited by man, the technology is still in its pre-commercialisation stage and so lags behind other renewable sources such as wind and geothermal energy in terms of development and energy produced. One of the emerging energy extraction technologies in the tidal energy field is the Horizontal Axis Tidal Turbine (HATT) which harness tidal stream energy the same way Horizontal Axis Wind Turbine (HAWT) extract energy from the wind. While HATT has been the topic of many researches over the past decade, there is still a gap in the current literature in terms of its performance in unsteady flow which is closer to the typical environment where HATTs are installed.

This thesis looks at the hydrodynamics and performance of the Sheffield HATT, a turbine designed in the University of Sheffield, both in steady and unsteady flow through numerical simulations. The initial design of the turbine has been done using QBlade which is a Blade-Element Momentum solver with a blade design feature. Structural simulation of the blade using BEM data was conducted before a Computational Fluid Dynamics (CFD) model of the turbine was created to be first tested in steady flow. The performance curve of the Sheffield HATT was determined and compared with the BEM results. A peak coefficient of performance (CP) of 41.88% was obtained for the  $k-\epsilon$  RNG case while it is 39.46% for the  $k-\omega$  SST model, both happening at  $TSR=6$  and both of them having values lower than that of the BEM simulation. The hydrodynamics of some tip speed ratio (TSR) on the turbine performance curve for the CFD cases were presented and were used to explain the complete response of the turbine.

An idealised unsteady flow boundary condition was used as the velocity inflow for the CFD simulation of the Sheffield HATT and the response of the turbine was presented in three TSR cases. The cyclic-average CP was shown to be less than the value with steady inflow at the same average TSR suggesting a negative effect of the unsteadiness to the turbine's performance. In all cases, a hysteresis curve was observed showing that the turbine's unsteady response does not follow the steady state curve at the amplitudes and frequencies investigated. The hydrodynamics of the turbine with unsteady flow was investigated to provide insight to the unsteady response of the turbine and explain the performance. The unsteady simulation at the turbine's optimum TSR ( $TSR=6$ ) was set to be the reference case for the other unsteady studies. The effect of varying the amplitude of the unsteady flow equation was conducted and it was found that as the amplitude increases, the cyclic-averaged CP of the turbine decreases. A frequency variation study was also shown where a drastic change in the turbine's hysteresis curve when the frequency of the turbine is greater than 1 which also results to a lower cyclic-averaged CP. All of the cyclic-averaged CP for all of the cases simulated in this thesis has value less than the steady state CP value, with the base case unsteady flow results showing a decrease of almost 2% while a maximum difference of 8.03% was seen for the low TSR case. All of this suggesting a detrimental effect of unsteady flow in the performance of HATTs

# Declaration

Described in this dissertation is work performed in the Department of Mechanical Engineering, the University of Sheffield between October 2014 to June 2017. I hereby declare that no part of this work has been submitted as an exercise for a degree at this or any other university. This dissertation is entirely the result of my own work and includes nothing which is the outcome of collaboration, except when stated otherwise. This dissertation contains 105 figures and approximately 49,000 words.

Signed:

Binoe E. Abuan

Dated: \_\_\_/\_\_\_/\_\_\_\_\_

*Dedicated to the cats Kitty, Mio, Indigo, Kuro, Paris, Mii and their owners.*

# Acknowledgement

Firstly, I want to thank my supervisor, Dr, Robert J. Howell, for all of his advices, comments, praises and constructive criticisms for the three years that I spent doing this research. I also want to acknowledge his patience and his encouragements for someone like myself who worry too much. His companionship and our bi-weekly talks about work and Lego really made my stay here enjoyable.

I also want to thank Dr. Louis Angelo M. Danao for acting like my second mentor throughout everything starting from the time when I was still in the Philippines and preparing to go here in Sheffield. I can't thank him enough for everything he has done to help me.

I would also like to acknowledge my colleagues in the research group: Radwan, for being my first friend here in Sheffield and for accompanying me through most of days in the office. Our daily chat about our researches and anything in general kept me sane especially during the time when we are the only people in the office. I also want to thank Jon, Danial, Dorit, Stuart and Cora for their advices and help regarding my numerical simulations during the early days of the study.

I am also grateful and indebted to my family for their support, help and love that did not diminish even when I am far from them. I am really thankful to my girlfriend, Krista, for everything she has done for me, from accompanying me during my first flight here in the UK to staying with me until the end of this study. I am so lucky to have you.

Lastly, I want to thank the One up above whom I know is beside me all along.

Special acknowledgement is given to the Engineering Research and Development for Technology (ERDT) through the University of the Philippines College of Engineering for the financial support that allowed me to pursue this study.

# Nomenclature

## Symbols

$A$	swept area of the extraction device, $m^2$
$A$	Amplitude of the unsteady flow velocity
$c$	blade chord length, m
$C_d$	coefficient of drag
$C_l$	coefficient of lift
$C_m$	moment coefficient
CP	coefficient of performance, power coefficient
$C_t$	coefficient of thrust
$D$	diameter of the turbine, m
$f$	frequency of the flow, Hz
$f$	frequency of the turbine
$F_{drag}$	drag force, N
$F_{lift}$	lift force, N
$k$	turbulent kinetic energy
$k$	reduced frequency (Leishman)
$\bar{k}$	frequency ratio
m	meter
N	Newton
n	number of blades
$P_a$	power available in the water, kW
$P_{atm}$	atmospheric pressure, Pa
Pa	Pascal (Pressure)
$P_e$	power extracted by the turbine, kW
$P_{trailing\ edge}$	trailing edge pressure, Pa
$P_x$	pressure at x position, Pa
Q	second invariant of the curl of the fluid flow
R	radius of the turbine, m
Re	Reynolds number
s	second
t	time, s
$V_{blade}$	blade velocity, m/s
$V_{rel}$	relative velocity, m/s
$V_{water}$	water fluid velocity, m/s
W	Watts
Wh	Watt-hours
°	degree
°C	degree Celsius

## Greek symbols

$\alpha$ , AoA	angle of attack, °
$\varepsilon$	dissipation rate
$\theta$	pitch angle. °
$\lambda_2$	lambda-2 criterion for vortex structures
$\mu$	dynamic viscosity, N-s/m <sup>2</sup>
$\mu_T$	Eddy viscosity
$\nu$	kinematic viscosity, m <sup>2</sup> /s
$\rho$	density of water, kg/m <sup>3</sup>
$\tau$	non-dimensionalised time
$\tau_{ij}$	Reynolds stress tensors
$\omega$	specific dissipation rate
$\omega$	rotational velocity of the turbine, rad/s

## Abbreviations

ACP	ANSYS Composite Prepost
BEM	Blade-Element Momentum
CFD	Computational Fluid Dynamics
DNS	Direct Numerical Simulation
EMEC	European Marine Energy Centre
EWT	Enhanced Wall Treatment
FEM	Finite Element Method
HATT	Horizontal Axis Tidal Turbine
HAWT	Horizontal Axis Wind Turbine
LES	Large Eddy Simulation
NACA	National Advisory Committee for Aeronautics
OTEC	Ocean Temperature Energy Conversion
RANS	Reynolds-Averaged Numerical Simulation
RNG	ReNormalised Group
SA	Spalart-Allmaras
SST	Shear Stress Transport
TSR	Tip-Speed Ratio
UDF	User-Defined Function
VATT	Vertical Axis Tidal Turbine
VAWT	Vertical Axis Wind Turbine
VLM	Vortex Lattice Method

# Table of Contents

<b>Chapter 1: Introduction</b> .....	<b>1</b>
1.1 Tidal Energy .....	5
1.2 Tidal Turbine in Steady Flow and Unsteady Flow .....	12
1.3 Project Aims .....	14
1.4 Thesis Contents .....	15
1.5 Publications .....	17
<b>Chapter 2: Literature Review</b> .....	<b>18</b>
2.1 Introduction .....	18
2.2 Horizontal Axis Tidal Turbine Fundamental hydrodynamics.....	18
2.3 Hydrofoil hydrodynamics .....	19
2.4 Tidal Turbine Design and Fundamentals .....	23
2.4.1 Solidity .....	24
2.4.2 Bio-fouling .....	25
2.4.3 Cavitation .....	26
2.4.4 Blade loading.....	28
2.5 Physical Modelling of Tidal Turbines.....	29
2.6 Numerical Modelling of Tidal Turbines .....	30
2.6.1 Blade-Element Momentum (BEM) Model.....	31
2.6.2 Computational Fluid Dynamics.....	33
2.7 Unsteady Flow in Tidal Turbines.....	40
2.8 Summary of Chapter .....	46
<b>Chapter 3: The Design of Sheffield Horizontal Axis Tidal Turbine</b> .....	<b>48</b>
3.1 Introduction .....	48
3.2 QBlade Validation.....	48
3.3 Sheffield Horizontal Axis Tidal Turbine .....	53
3.4 Sheffield HATT Structural Response Study .....	57
3.4.1 Numerical Verification and Validation of the FEA Model.....	58
3.4.2 Cantilevered Elliptical Tube: Mesh Density Study .....	60
3.4.3 Cantilevered elliptical shell with web: Von Mises and tip deflection....	63
3.4.4 Numerical Analysis of the Sheffield HATT blade (structural) .....	65
3.4.5 Isotropic analysis: maximum principal stress and tip deflection.....	69
3.4.6 Orthotropic analysis: maximum principal stress and tip deflection .....	71

3.4 Summary of Chapter .....	74
<b>Chapter 4: Numerical Modelling of the Sheffield HATT .....</b>	<b>76</b>
4.1 Introduction .....	76
4.2 Sheffield HATT CFD Model .....	76
4.3 CFD Solver.....	81
4.4 Mesh Independence Study .....	82
4.5 Boundary Size Study .....	84
4.6 Steady Flow Simulations.....	85
4.7 Summary of Chapter .....	100
<b>Chapter 5: Unsteady Flow Simulations of the Sheffield HATT .....</b>	<b>101</b>
5.1 Introduction .....	101
5.2 Unsteady Flow Simulations .....	101
5.3 Results and Visualisation for TSR = 6 Simulation .....	108
5.3.1 Process a to b.....	113
5.3.2 Process b, c, d to e .....	116
5.3.3 Process e to f.....	119
5.3.4 Process f, g to h .....	121
5.3.5 Process h to a.....	122
5.4 TSR = 4 Unsteady Flow Simulation .....	123
5.4.1 Three-Dimensional Visualisation of Vortices in the Flow using the $\lambda_2$ criterion..	127
5.4.2 Process a to b.....	130
5.4.3 Process b to c .....	132
5.4.4 Process c to d.....	134
5.4.5 Process d to a and the conclusion for the unsteady TSR= 4 simulation.....	136
5.5 TSR = 8 Unsteady Flow Simulation .....	138
5.5.1 Process a to b.....	142
5.5.2 Process b to c .....	144
5.3.3 Process c to d and d to a .....	145
5.6 Summary of Chapter .....	147
<b>Chapter 6: Influence of Amplitude and Frequency Variation in the Unsteady Flow to the Performance of Sheffield HATT .....</b>	<b>150</b>
6.1 Introduction .....	150
6.2 Amplitude Variation Comparative Study.....	150
6.3 High Amplitude Variation.....	151
6.3.1 Process a to b.....	159

6.3.2 Process b to c .....	161
6.3.3 Process c to d.....	163
6.3.4 Process d to a.....	167
6.3.5 Summary for the 43.5% amplitude unsteady simulation.....	170
6.4 Low Amplitude Variation .....	171
6.5 Effect of Amplitude Variation.....	175
6.6 Frequency Variation Comparative Study.....	177
6.7 Low Frequency Simulation .....	178
6.8 High Frequency Simulation .....	186
6.9 Additional Higher Frequency Simulations.....	190
6.10 Summary of Chapter .....	196
<b>Chapter 7: Conclusions and Recommendations .....</b>	<b>201</b>
7.1 Conclusions .....	201
7.2 Implications of the Results.....	204
7.2 Recommendations for future work.....	205
<b>References.....</b>	<b>207</b>

# List of Figures

Figure 1.1. Global temperature variation form 1880 to present.....	1
Figure 1.2. Greenhouse effect diagram, image from (CO <sub>2</sub> CRC, 2017).....	2
Figure 1.3. Concentration of carbon dioxide in the atmosphere from the 1700's to the present (Neftel, <i>et al.</i> , 1994), image from (PhysicalGeography, 2010).....	3
Figure 1.4. (a) Global annual emissions of anthropogenic greenhouse gasess from 1970 to 2004 (b) Share of different anthropogenic GHGs in total emissions in 2004 in terms of carbon dioxide equivalents (CO <sub>2</sub> -eq). (c) Share of different sectors in total anthropogenic GHG emissions in 2004 in terms of CO <sub>2</sub> -eq.....	4
Figure 1.5. La Rance 240 MW Tidal Power Plant located on the Rance River, Brittany, France (image source: <a href="http://theearthproject.com/know-tidal-power/">http://theearthproject.com/know-tidal-power/</a> ).....	7
Figure 1.6. Marine Current Turbines' 1.2 MW SeaGen twin rotor turbine (left) and Andrtiz Hydro Hammerfest 1.5MW single rotor turbine for Atlantis and MeyGen's project phase 1 (right).....	9
Figure 1.7. Open Hydro's Open Centre Turbine (left) and the TidGen by ORPC which is composed of multiple TGU devices (right).....	10
Figure 1.8. Minesto's Tidal Kite called Deep Gen (left) and an example of an oscillating hydrofoil (right).....	12
Figure 1.9 Turbine performance curve for the Southampton turbine at various combinations of pitch angle and fluid flow velocities.....	13
Figure 2.1. Velocity Triangle and Forces acting on a hydrofoil cross section in a tidal turbine.....	21
Figure 2.2 C <sub>l</sub> and C <sub>d</sub> vs AoA plots for NACA 4412 at Re = 1 x 10 <sup>6</sup> .....	22
Figure 2.3 The mechanism of boundary layer separation using velocity gradient visualization.....	23
Figure 2.4 Effect of increasing solidity in terms of the number of blades for HAWT (left) and HATT (right).....	25
Figure 2.5 An image taken from the experimental set-up by Wang <i>et al.</i> (Wang, Atlar, & Sampson, 2007) showing different kind of cavitation present in the tidal turbine. ....	28
Figure 2.6 BEM-CFD coupling integration as done by Malki <i>et al.</i> , 2012.....	37
Figure 2.7 λ <sub>2</sub> criterion vortex structures presented by Kang <i>et al.</i> with contours showing velocity magnitudes non-dimensionalised by the free stream velocity of 2 m/s.....	39
Figure 2.8 Comparison of tidal turbine performance with and without waves done by Luznik <i>et al.</i> (Luznik <i>et al.</i> , 2015).....	44
Figure 2.9 Tidal turbine performance in realistic unsteady flow compared with steady state data for the same mean TSR (Leroux <i>et al.</i> , 2016).....	46
Figure 3.1 XFOil predicted lift coefficient for NACA 4412 at Re=250,000 versus experimental data gathered from Pinkerton <i>et al.</i> (Pinkerton, 1938) for AoA between -15° to 18° ....	50
Figure 3.2 Results of the node density study for NACA 4412 (top) and NACA 4424 (bottom) at Re=250,000 with AoA from -25° to 25°.....	51

Figure 3.3 Comparison of performance curves from the QBlade BEM results and experimental data for the Batten <i>et al.</i> . (Batten, Bahaj, Molland, & Chaplin, 2007).....	53
Figure 3.4 CP vs TSR curve comparison for different NACA series showing the effect of camber and location of maximum thickness to the turbine performance at $Re=1,500,000$ .....	55
Figure 3.5 Sheffield HATT model from the turbine building function of QBlade.....	56
Figure 3.6 Performance curve comparison of the Sheffield HATT model.....	57
Figure 3.7. Illustration of beam with distributed load approximated by multiple point loads.....	59
Figure 3.8 Contours of (a) Von Mises stress and (b) directional–y deflection for ellipse tube.....	62
Figure 3.9. Contours of (a) Von Mises stress and (b) directional–y deflection for ellipse tube with web.....	64
Figure 3.10 Loads derived from the BEM simulation for the 2 m/s flow as applied on the blade.....	67
Figure 3.11 Mapped face mesh on the blade.....	68
Figure 3.12 Isotropic analysis of HATT blade: (a) Von Mises stress, (b) nodal deflection along y-direction.....	70
Figure 3.13 Orthotropic elastic modulus of EGlass reinforced Epoxy.....	71
Figure 3.14 Results of the composite analysis using orthotropic material properties: (a) maximum principal stress, (b) deflection in the y-direction.....	72
Figure 4.1 The rotational domain for the Sheffield HATT showing the geometry with (a) and without (b) mesh.....	78
Figure 4.2 Cut plane mesh for the Sheffield HATT at 25% span (a) and 75% span (b) of the blade.....	79
Figure 4.3 Outer mesh computational domain showing the boundary conditions applied in the CFD model (a) and mesh (b).....	82
Figure 4.4 CP values for each case mesh test case with the computational time in hours as data labels.....	84
Figure 4.5 The mesh used for the Boundary mesh study with domain at 10D by 10D by 20D.....	85
Figure 4.6 Percentage error for the turbulence models tested and compared with the experimental data from Ladson <i>et al.</i> at operating conditions of $Re = 6,000,000$ and $AoA = 4^\circ$ .....	86
Figure 4.7 Turbine performance curve comparison between BEM, k- $\epsilon$ and k- $\omega$ SST simulations for the Sheffield HATT.....	89
Figure 4.8 Sample streamline plot presenting the incident AoA and separation in a hydrofoil section of a tidal turbine.....	90
Figure 4.9 Flow visualisations for the k- $\epsilon$ RNG simulations at $R=0.8$ (a) and $R=1.6$ (b).....	92
Figure 4.10 Flow visualisations for the k- $\omega$ SST at $R=0.8$ (a) and $R=1.6$ (b).....	94
Figure 4.11 Pressure coefficient plots at 75% blade ( $R = 1.6$ ) span for $TSR = 2$ , $TSR = 4$ and $TSR = 6$ with k- $\epsilon$ RNG (left) and k- $\omega$ SST (right).....	96

Figure 4.12 Isolated flow visualisations for $R=0.8$ at $TSR=4$ with $k-\epsilon$ RNG (top) and $k-\omega$ SST (bottom).....	98
Figure 4.13 Pressure Coefficients at $R=1.6$ at various $TSR$ for $k-\epsilon$ RNG (left column) and $k-\omega$ SST (right column).....	99
Figure 5.1 Response of the Sheffield HATT to the unsteady flow scheme implemented.....	103
Figure 5.2 Unsteady flow response of the Sheffield HATT for one cycle with instantaneous Tip Speed Ratio ( $TSR$ ).....	105
Figure 5.3 Available water power and extracted power by the turbine with unsteady velocity (bottom).....	105
Figure 5.4 Unsteady Flow Hysteresis Curve for $TSR = 6$ over the steady flow performance curve for the Sheffield HATT.....	107
Figure 5.5.1 Streamlines for various positions in the hysteresis curve at 25% of the blade with points a to d (a) and points e to h (b) for the unsteady $TSR = 6$ simulation.....	110
Figure 5.5.2 Streamlines for various positions in the hysteresis curve at 75% of the blade with points a to d (a) and points e to h (b) for the unsteady $TSR = 6$ simulation.....	112
Figure 5.6 Streamlines at point a (a) and point b (b) for 25% of blade span (left) and 75% of the blade span (right) of the Sheffield HATT turbine blade.....	114
Figure 5.7 Normalised Pressure plots at 75% $R$ for points a and b.....	108
Figure 5.8 Streamlines at point d for 25% of blade span (left) and 75% of the blade span (right) of the Sheffield HATT turbine blade.....	118
Figure 5.9 Streamlines at point e for 25% of blade span (left) and 75% of the blade span (right) of the Sheffield HATT turbine blade.....	118
Figure 5.10 Normalised Pressure plots at 75% $R$ for points d and e.....	119
Figure 5.11 Normalised Pressure plots at 75% $R$ for points e and f.....	120
Figure 5.12 $C_l/C_d$ plot for NACA 4414 and NACA 4420 which is the aerofoil sections at 75% and 25% of the Sheffield HATT blade respectively.....	121
Figure 5.13 Normalised Pressure plots at 75% $R$ for points d and h.....	122
Figure 5.14 Unsteady Flow Hysteresis curve for $TSR=4$ over Steady flow performance curve.....	124
Figure 5.15 Velocity Streamlines for different position on the hysteresis curve at 25% (a) and 75% (b) span of the blade for unsteady $TSR = 4$ simulation.....	126
Figure 5.16 $\lambda_2$ criterion vortex tube representation at different points of the unsteady $TSR = 4$ simulation.....	129
Figure 5.17 Streamlines at point a for 25% of blade span (left) and 75% of the blade span (right) of the Sheffield HATT turbine blade.....	131
Figure 5.18 Streamlines at point b for 25% of blade span (left) and 75% of the blade span (right) of the Sheffield HATT turbine blade.....	131
Figure 5.19 Normalised Pressure comparison at 75% $R$ for the process a to b.....	132
Figure 5.20 Streamlines at point c for 25% of blade span (left) and 75% of the blade span (right) of the Sheffield HATT turbine blade.....	133
Figure 5.21 Normalised Pressure comparison at 75% $R$ for the process b to c.....	133
Figure 5.22 Streamlines at point c for 25% of blade span (left) and 75% of the blade span (right) of the Sheffield HATT turbine blade.....	135

Figure 5.23 Normalised Pressure comparison at 75%R for the process c to d.....	136
Figure 5.24 Normalised Pressure comparison at 75%R for the process d to a.....	137
Figure 5.25 Unsteady Flow Hysteresis curve for TSR=8 over Steady flow performance curve.....	139
Figure 5.26 Velocity Streamlines for different position on the hysteresis curve at 25% (a) and 75% (b) span of the blade for unsteady TSR = 8 simulation.....	141
Figure 5.27 Normalised Pressure plots at 75%R (a) and 25%R (b) for process points a and b.....	144
Figure 5.28 Normalised Pressure plots at 75%R for process points b and c.....	146
Figure 5.29 Normalised Pressure plots at 75%R for process points c and d.....	139
Figure 5.30 Complete unsteady simulation plot showing hysteresis curve for the three unsteady cases (TSR=4, 6, and 8).....	148
Figure 5.31 Cyclic-averaged CP for the unsteady flow at the three TSR with their steady state counterpart.....	149
Figure 6.1 Unsteady Flow Hysteresis Curve for 43.5% amplitude over the steady flow performance curve for the Sheffield HATT and the base case hysteresis curve.....	153
Figure 6.2 Sheffield HATT Response for the 43.5% Amplitude Simulation top: CP value plotted against normalised time superimposed with the base case CP plot and instantaneous TSR; bottom: Power extracted by the turbine plotted against normalised time superimposed with the water velocity profile and power available in the water.....	154
Figure 6.3 Velocity Streamlines for different position on the hysteresis curve at 25% (a) and 75% (b) span of the blade for unsteady 43.5% amplitude simulation at TSR = 6.....	158
Figure 6.4 Streamlines at point a (a) and point b (b) for 25% of blade span (left) and 75% of the blade span (right) of the Sheffield HATT turbine blade for the 43.5% amplitude simulation.....	160
Figure 6.5 Normalised Pressure plots at 75%R for points a and b for the 43.5% amplitude simulation.....	161
Figure 6.6 Streamlines at point c for 25% of blade span (left) and 75% of the blade span (right) of the Sheffield HATT turbine blade for the 43.5% amplitude simulation.....	162
Figure 6.7 Normalised Pressure plots at 75%R for points b and c for the 43.5% amplitude simulation.....	162
Figure 6.8 Streamlines at point d for 25% of blade span (left) and 75% of the blade span (right) of the Sheffield HATT turbine blade for the 43.5% amplitude simulation.....	163
Figure 6.9 Normalised Pressure plots at 75%R for points c and d for the 43.5% amplitude simulation.....	164
Figure 6.10.1 $C_l/C_d$ plot for NACA 4414 and NACA 4420 which is the aerofoil sections at 75% and 25% of the Sheffield HATT blade respectively.....	164
Figure 6.10.2 $C_d$ plot for NACA 4414 and NACA 4420 which is the aerofoil sections at 75% and 25% of the Sheffield HATT blade respectively.....	165
Figure 6.11 Unsteady Flow Hysteresis Curve for 43.5% amplitude over the steady flow performance curve for the Sheffield HATT and the base case hysteresis curve including points c1, c2, d1 and d2.....	166

Figure 6.12 Normalised Pressure plots at 75%R for points c and d for the 43.5% amplitude simulation including the in-between points c1 and c2.....	167
Figure 6.13 Normalised Pressure plots at 75%R for points c and d for the 43.5% amplitude simulation.....	168
Figure 6.14 Normalised Pressure plots at 75%R for points d and a for the 43.5% amplitude simulation including the in-between points d1 and d2.....	169
Figure 6.15 Normalised Pressure plots at 75%R for points d and a for the 43.5% amplitude simulation including the in-between points d1 and d2.....	170
Figure 6.16 Sheffield HATT Response for the 10% Amplitude Simulation top: CP value plotted against normalised time superimposed with the base case CP plot and instantaneous TSR; bottom: Power extracted by the turbine plotted against normalised time superimposed with the water velocity profile and power available in the water.....	172
Figure 6.17 Unsteady Flow Hysteresis Curve for 43.5% amplitude over the steady flow performance curve for the Sheffield HATT and the base case hysteresis curve.....	173
Figure 6.18 Normalised Pressure plots at 75%R for data points a, b, c and d for the 10% amplitude simulation.....	174
Figure 6.19 Unsteady Flow Hysteresis Curves for the amplitude variation study over the steady flow performance curve.....	176
Figure 6.20 Unsteady Flow Hysteresis Curve for $f=0.5$ unsteady simulation over the steady flow performance curve for the Sheffield HATT and the base case hysteresis curve.....	181
Figure 6.21 Sheffield HATT Response for the $f=0.5$ unsteady Simulation top: CP value plotted against normalised time superimposed with the base case CP plot and instantaneous TSR; bottom: Power extracted by the turbine plotted against normalised time superimposed with the water velocity profile and power available in the water.....	183
Figure 6.22 Streamlines at various part of the hysteresis curve for the $f=0.5$ simulation with correspondence.....	185
Figure 6.23 Unsteady Flow Hysteresis Curve for $f=2$ unsteady simulation over the steady flow performance curve for the Sheffield HATT and the base case hysteresis curve.....	187
Figure 6.24 Sheffield HATT Response for the $f=2$ unsteady Simulation top: CP value plotted against normalised time superimposed with the base case CP plot and instantaneous TSR; bottom: Power extracted by the turbine plotted against normalised time superimposed with the water velocity profile and power available in the water.....	188
Figure 6.25 Cyclic-averaged CP plotted against the frequencies used in the unsteady simulations with the steady-state CP plotted at $f=0$ .....	191
Figure 6.26 Unsteady Flow Hysteresis Curve for all unsteady simulation under the frequency variation study over the steady flow performance curve for the Sheffield HATT....	191
Figure 6.27 $\bar{k}$ values for all of the present cases discussed in detail in the thesis.....	194
Figure 6.28 Sheffield HATT Response for the $f=3.0$ unsteady Simulation top: CP value plotted against normalised time superimposed with the base case CP plot and instantaneous TSR; bottom: Power extracted by the turbine plotted against normalised time superimposed with the water velocity profile and power available in the water.....	199
Figure 6.29 Sheffield HATT Response for the $f=4.0$ unsteady Simulation top: CP value plotted against normalised time superimposed with the base case CP plot and instantaneous	

TSR; bottom: Power extracted by the turbine plotted against normalised time superimposed with the water velocity profile and power available in the water.....200

## List of Tables

Table 3.1 Sheffield HATT Geometry Specification.....	56
Table 3.2 Mesh Settings and FEA Results for the Numerical Verification of Ellipse Tube Model.....	60
Table 3.3 Comparison of Numerical and Analytical Model Results for Ellipse Tube.....	61
Table 3.4 Comparison of Numerical and Analytical Model Results for Ellipse Tube with Web.....	63
Table 3.5 Blade Force Data from BEM Simulation at 2 m/s Flow Velocity.....	66
Table 3.6 Blade Force Data from BEM Simulation at 5 m/s Flow Velocity.....	66
Table 3.7 Maximum principal stress and nodal deflection for ply angle variation.....	73
Table 4.1 Mesh Independence Study Results for the Sheffield HATT at water velocity=2m/s and TSR=6.....	83
Table 6.1 Cyclic-average CP value comparison for the unsteady simulation at TSR = 6.....	176
Table 6.2 Cyclic-average CP value comparison for the unsteady simulation at TSR = 6 (frequency variation).....	178
Table 6.3 Cyclic-average CP value comparison for all unsteady simulations under the amplitude variation studies.....	197
Table 6.4 Cyclic-average CP value comparison for all unsteady simulations under the frequency variation studies.....	198

# Chapter 1

## Introduction

Climate change is defined to be a long-term shift in the world's climate. Over the past few years, evidence suggesting climate change has been observed. This includes warming; sea level rising of about 17 cm over the last century; ice sheets in Greenland and Antarctica losing 150 cubic kilometers of ice between 2002 and 2005; glacial retreats on the mountain ranges of the world; and melting snow caps in the northern hemisphere (Met Office, 2017). Out of all the effects of climate change, global warming is the most well-known and discussed subject. Global warming is known to be the gradual increase of the world's average temperature; this includes the earth's biosphere and atmosphere and the earth's ocean systems (Livescience, 2017). The earth's global temperature in the year 2015 was higher by about 1°C than the 1880 readings, with 15 out of the 16 warmest years occurring since 2001 to 2015. Figure 1.1 shows the global temperature variation over the past 140 years. Scientists believe that the cause of this global warming phenomenon is the human expansion of the greenhouse effect – which is defined as the natural warming caused when the atmosphere traps the radiating heat from the earth (Santer, 1996).

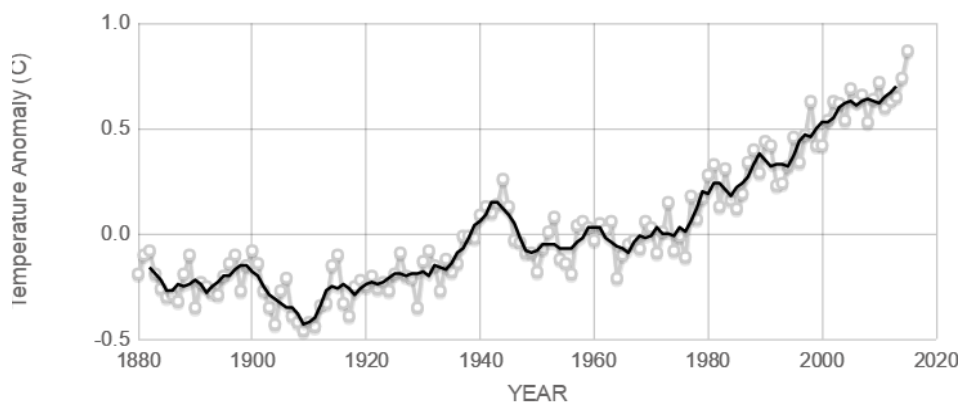


Figure 1.1. Global temperature variation from 1880 to present. (image captured from: <https://climate.nasa.gov/evidence/>)

The Greenhouse effect is actually a natural process that is essential to life on earth. A thin layer of the atmosphere is composed of greenhouse gases such as water vapor, carbon dioxide, methane and nitrous oxide. This layer serves as a greenhouse, trapping the heat radiating from earth and maintaining the temperature enough to sustain life. Without the greenhouse effect, the temperature of the earth would be below  $- 1^{\circ}\text{C}$ . Figure 1.2 shows a diagram of the greenhouse effect. This natural effect is enhanced by the increased concentration of carbon dioxide in the atmosphere. Carbon dioxide is naturally released into the atmosphere through respiration, and volcanic activities though it is increased through human processes such as burning fossil fuels and deforestation. Since the industrial revolution, the concentration of carbon dioxide in the atmosphere has increased by more than 36% (Neftel *et al.*, 1994). Figure 1.3 shows the increase of carbon dioxide concentration in the atmosphere since the early 1700's. The trend is increasing exponentially and extrapolation predicts higher emission in the near future.

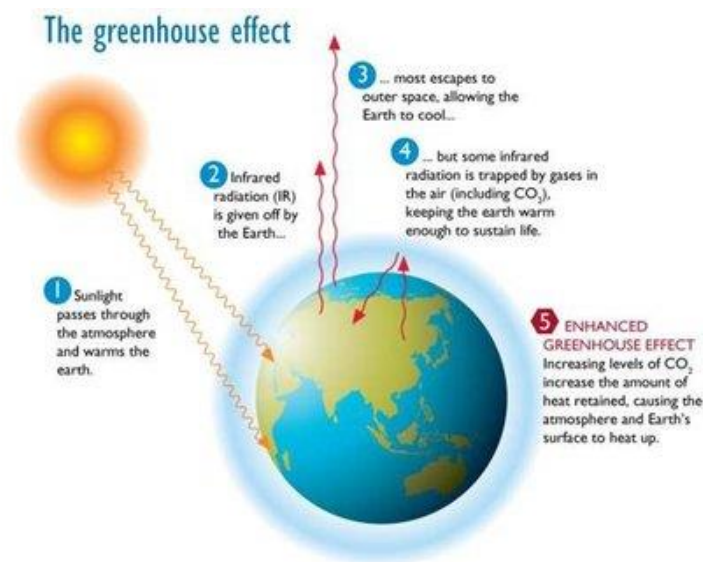


Figure 1.2. Greenhouse effect diagram, image from (CO2CRC, 2017)

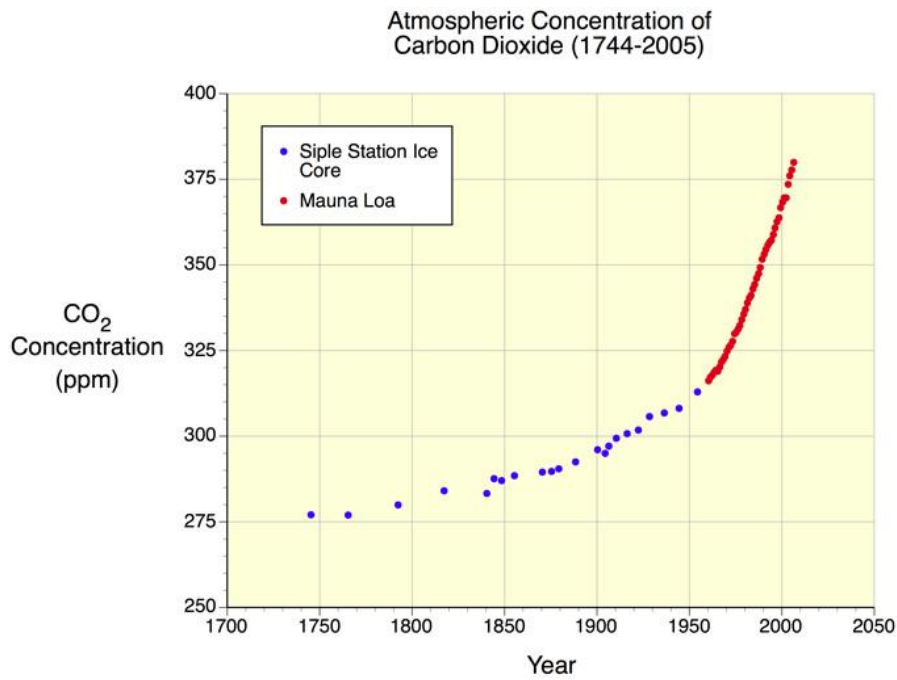


Figure 1.3. Concentration of carbon dioxide in the atmosphere from the 1700's to the present measured at Siple Station and Mauna Loa measurement locations (Neftel, *et al.*, 1994), image from (PhysicalGeography, 2010)

It can be seen in Figure 1.4(b) that the leading cause of greenhouse gases and carbon dioxide emissions was the burning of fossil fuel which shows a 56.6% share of the total greenhouse gas emissions in 2004. In Figure 1.4(c), it is shown that the energy sector has the biggest share of greenhouse gas emissions amounting to 25.9% of the total emissions with industry and transportation having shares of 19.4% and 13.1% respectively. This is the reason researchers and scientists are finding new ways to produce energy without the use of fossil fuels; to harness energy from the environment without the damaging effect.

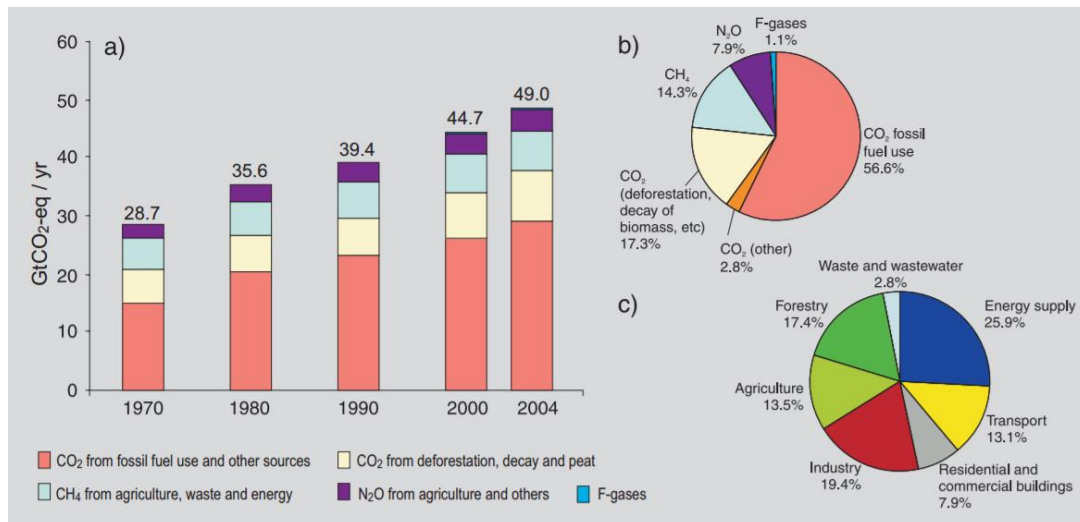


Figure 1.4. (a) Global annual emissions of anthropogenic greenhouse gases from 1970 to 2004 (b) Share of different anthropogenic GHGs in total emissions in 2004 in terms of carbon dioxide equivalents (CO<sub>2</sub>-eq). (c) Share of different sectors in total anthropogenic GHG emissions in 2004 in terms of CO<sub>2</sub>-eq. (image captured from Gov.uk, 2016)

Renewable energy technologies such as wind, solar, geothermal and tidal energy harness energy from the environment with minimal negative effects when compared to conventional energy sources. A lot of research and development is now pursuing renewable energy as the replacement for burning fossil fuels. In the year 2015, the share of renewable energy to the total electricity generation in the UK reached 24.7% which amounts to 83.3 TWh of power (Gov.uk, 2016). That energy share is composed of 18.6 TWh from plant biomass, 40.3 TWh from wind energy, 7.6 TWh from photovoltaic energy, 6.3 TWh from hydro energy (this includes shoreline wave and tidal) and the rest from other renewable energy sources such as geothermal, landfill gas, etc.

Wind energy, biomass and photovoltaic are the most researched and well-known renewable energy sources in the UK and this is reflected in the electricity generated in 2015. One of the less developed renewable energy source that is gaining attention nowadays is tidal energy. Tidal energy produced 0.01 TWh of energy in 2015 very far from the energy production of the other stated sources despite the fact that it has one of the biggest energy capacities in

terms of resources. Tidal energy has a projected global capacity of 120 GW and could produce up to 150 TWh per annum in excess of all energy consumption in the UK. The tidal energy capacity of the UK was projected to be more than 10GW which is about 50% of the Europe's tidal capacity (Marine Current Turbines, 2017). In order to promote this renewable energy source, further understanding of the technology itself is necessary, hence more research and development is needed.

## **1.1 Tidal Energy**

Tidal energy extraction is the system of harnessing energy from tidal flow – this includes the energy extracted from the ebb and flow of tides and energy from kinetic energy of marine tidal currents. The idea has been used since ancient times, from simple water mills and water wheels of the Middle Ages to the tidal wheels in London in the late 1500's (Hardisty, 2009). However, it is only in the twenty-first century that serious research and developments have been made to industrialise the process. Tidal energy is one of the best renewable energy sources available because of its big potential. Unlike other marine resources like wave energy and OTEC (Ocean Thermal Energy Conversion), which are dependent on the irregular cycles of the wind, tidal energy is predictable for a long period of time. The only problem is the way of collecting the resource because it is distributed over large areas of water and streams (Gorlov, 2001). The topic of much research nowadays that deals with the said technology is to harness the tidal energy efficiently. The target is to develop extraction devices that are efficient and cheap and at the same time, can be installed even in different places where water flow characteristics vary.

There are three existing technologies for extracting energy from tidal flows: tidal barrage, tidal lagoon and tidal stream. Tidal barrage uses the concept of collecting water from tidal flows in controlled basins called reservoirs and restricting the water to flow out. The water

will then be allowed to exit through an extraction device to harness the stored potential energy which is similar to the concept of a dam. This technique is optimised by installing two way turbines that can harness energy from either of the axial directions; hence energy can be collected from both incoming and exiting flows. One example of tidal barrage operating in the present is the La Rance plant. It is designed to produce 240 MW of power from its twenty-four 10MW low-head bulb-type turbines over a basin area of 22 km and a mean tide of 8.55 m. The plant generates a total of 540 GWh annually (Tidal Electric Inc., 2017). Another tidal power plant is located in Sihwa lake, South Korea. It is a 12.5 km barrage with ten 25.4MW bulb-type turbines adding up to a total of 254 MW designed power. It produces an annual energy generation of 552.2 GWh making it biggest tidal power plant in the world. It took seven years to build this power plant with an invested capital of about \$355.1 million. An even bigger tidal plant was proposed in the UK which is called the Severn Tidal Barrage (STB) in 1974. It is a design of 8640 MW barrage that will run on the Severn estuary between Wales and England. The project was not continued in 1987 due to economic and environmental problems similar to what is stated above. Although tidal barrages produce large amounts of energy from an inexhaustible resource, the cost will be usually very expensive as in the case of the Sihwa Lake turbine. It also comes with environmental issues because it has the potential to disrupt aquatic life such as the migration of fishes. It can block navigation in the waters though locks can be integrated in the design process as can be seen in the La Rance power plant.

Another tidal power plant that is currently being developed is the Swansea Bay Tidal Lagoon. Tidal Lagoon is a type of tidal energy extraction which is based on the extraction process of Tidal Barrages. The difference is that instead of a barrage that separates a smaller body of water, an enclosed body of water near a shore (lagoon) was created to serve as the basin for the tidal energy extraction. The Swansea Bay Tidal Lagoon is designed to have an output of 240 MW from its 9.5 km long sea wall with a reservoir area of 11.5 square kilometers.

It was expected to produce 400 GWh of annual energy and is expected to be finished by the year 2018.



Figure 1.5. La Rance 240 MW Tidal Power Plant located on the Rance River, Brittany, France (image source: <http://theearthproject.com/know-tidal-power/>)

Tidal stream systems harness the kinetic energy from marine currents resulting from tidal flows. Tidal stream devices are submerged underwater where the marine current is flowing. It is different to tidal barrages and lagoons due to the fact that not all of the incoming flow passes through the device, some of the flow will be around the equipment. Tidal stream devices are very similar to wind turbines but a big difference in size will be observed. Since the density of water is much higher than that of air, blades can be smaller and the turbines also turn slower while still producing the same amount of power when compared to wind turbines. Since the rotors are relatively smaller, tidal stream turbines are usually installed in an array so that power will be optimised over the area being used. Tidal turbines are usually designed with materials that can resist high axial thrust (especially for horizontal axis tidal turbine) again because of the high density of water. Blades are also treated against bio-fouling and cavitation in shallower water. This high standard of robustness is essential for limited maintenance to minimise operational cost and carbon dioxide emissions (Douglas, 2007). The European

Marine Energy Centre (EMEC) have identified the main types of tidal stream extraction devices which are briefly discussed as follows:

**Horizontal Axis Tidal Turbine (HATT)** has its axis of rotation parallel to the flow of the current, it is very similar its wind counterpart which is the Horizontal Axis Wind Turbine (HAWT) where the power produced by the turbine's rotation is converted to electricity. Current HATT in progress today includes the 500 kW Deepgen tidal stream turbine by Tidal Generation Limited (TGL) which is successfully installed in the EMEC's site at the fall of Warness at Eday in 2010. The turbine has reported to have produced 200 MWh to the national grid as of March 2012. Alstom acquired TGL in 2013 and they deployed a 1MW turbine in a project called ReDAPT (Reliable Data Acquisition Platform for Tidal) which aims to collect and publish data for tidal energy production for an 18 month duration. General Electric (GE) acquired Alstom in 2016 and they are planning to produce the next generation 1.4 MW Oceade Tidal Turbine (EMEC, 2017).

Aquamarine Power's Neptune, a 2.4 MW tidal stream turbine is currently in their final production designs and is currently interacting with the EMEC for site testing in the fall of Warness tidal site for three years. Aquamarine together with Ocean Flow Energy Limited has also design the Evopod which is a free floating tidal device with an advanced mooring system to allow optimum heading to the stream. They are planning to incorporate the Neptune into the Evopod's mooring system for next generation projects (Aqua Marine Power, 2017).

The Atlantis Resources Limited MeyGen project has deployed their first Andritz Hydro Hammerfest turbine operating in full power in December 2016. The turbine is part of MeyGen's phase 1a where they deployed four 1.5 MW turbines in the waters of Pentland Firth and the Orkney Islands installed in gravity support structures. The operation of the turbine will be monitored to provide information and to validate design turbine performance curves. The

project started in 2010 when the Crown Estate awarded MeyGen Limited a license to develop a tidal stream project near the island of Stroma in Northern Scotland with a design capacity up to 398 MW (Atlantis Resource Ltd, 2017).

Other projects include design using multiple open rotor HATT system which are designed to maximise the space occupied per support structure while optimising the power generation as two turbines are mounted in one support structure. The Marine Current Turbines' SeaGen twin turbines are twin horizontal axis rotor that drives a generator through a gearbox system similar to current designs in wind turbine. Each turbine was designed to produce 1.2 MW of power for tidal currents higher than 2.4 m/s. The rotors can also be lifted out of water through the support structure making it easier to maintain. It was successfully tested in December 2008 at the Strangford Lough, Northern Ireland (Marine Current Turbines, 2017).



Figure 1.6. Marine Current Turbines' 1.2 MW SeaGen twin rotor turbine (left) and Andritz Hydro Hammerfest 1.5MW single rotor turbine for Atlantis and MeyGen's project phase 1 (right)

**Enclosed tips (Venturi) Tidal Turbines** utilise the venturi effect whereby a funnel-like duct is concentrating the tidal flow passing to the turbine (usually a HATT). The enclosed system ensure that all of the concentrated flow will pass through the turbine. This will increase

the energy capture per unit area due to the accelerated flow and will make the blades insensitive to off-axis flow that will be experienced in a normal open rotor HATT. Lunar Energy has tested their 1MW LTT turbine, which uses the venturi concept, in Wando Hoenggan waterway in Korea. If the first deployed turbine performs successfully, the project will be scaled up to 300 MW project, and will be one of the biggest tidal power plant in the world (Lunar Energy, 2017).

Another type of ducted tidal turbine is the Open Centre Turbine by Open Hydro. The turbine concept uses permanent magnet rim generator which makes electricity from the turbine less complex as compared to ordinary gear drive trains. They have tested the Open Centre Turbine in the Fall of Warness site of EMEC in 2006 and successfully generated electricity for the Scottish Grid in May, 2008. The current design of the turbine is a 16m rotor with 2MW of power capacity (Openhydro, 2017).

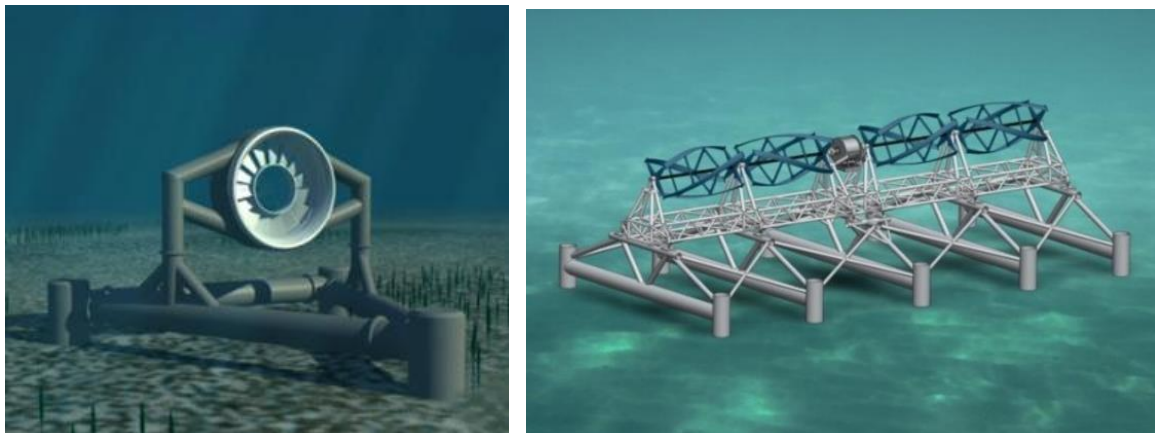


Figure 1.7. Open Hydro's Open Centre Turbine (left) and the TidGen by ORPC which is composed of multiple TGU devices (right)

**Vertical Axis Tidal Turbine (VATT)** or transverse axis tidal turbines have their axis of rotation perpendicular to the flow of the current and also very similar to the Vertical Axis Wind Turbine (VAWT) where the power produced by the turbine's rotation is converted to electricity. VATT has its advantages in terms of the structural efficiency and easier

maintenance technology though its biggest disadvantage lies on its lower efficiency as compared to HATT (King & Tryfonas, 2009). One of the notable VATT designs available is Blue Energy's Ducted Vertical Axis Hydro Turbine which utilise the effect of ducting in VATT. Preliminary prototype testing for this turbine has been done in the 1980's with the latest being in the University of British Columbia in 2006 and Oceanic towing tank in 2007 (Blue Energy, 2017). The Ocean Renewable Power Company has their cross-flow axis design Tidal Generator Unit (TGU). Current plans for this turbine include the Maine Tidal Energy Project in the Bay of Fundy which will house up to 5 MW configuration of ORPC's TGU's (ORPC, 2017).

#### **Other Tidal Stream Designs:**

The **Tidal Kite** is a new technology that utilises both ocean and tidal current. The kite itself houses a wing and a turbine below it. When the kite is submerged within a tidal current, the current will produce a hydrodynamic lift on the wing pushing the kite forward. The kite which is tethered will then be controlled to move in a figure of 8. The combination of the movement of the kite and the tidal current increases the relative velocity as seen by the turbine itself making it up to 10 times the current speed thus increasing the power produced by the turbine. The Deep Green technology by Minesto is currently doing long term sea trials in Strangford Lough, Northern Ireland. Their aim is to deploy a 1.5MW deep green turbine array in 2017 then increase it to 10MW array afterwards (Minesto, 2017).

An **Oscillating hydrofoils** is a submerged hydrofoil wing attached to an oscillating arm. As the current pass by the hydrofoil, the wing will gain lift based on the angle of attack of the velocity relative to the hydrofoil resulting in an oscillating movement. This movement will then drive the fluid in the hydraulic system converting the tidal energy to electrical energy.

**Archimedes Screw** is actually a water transfer device in the old times but is gaining popularity nowadays as a tidal stream converter of energy. It is a helical corkscrew that is rotating in a cylindrical shaft. As the tidal stream passes the screw, water will move through the helix thus making the screw rotate. The rotation produced will then be converted into electrical energy.



Figure 1.8. Minesto's Tidal Kite called Deep Gen (left) and an example of an oscillating hydrofoil (right)

## 1.2 Tidal Turbine in Steady Flow and Unsteady Flow

Steady flow can be defined when general parameters such as velocity, pressure and density, which describes the behaviour of the fluid, at any point is not changing with respect to time. Having the flow unsteady makes the analysis of the fluid flow and hence the tidal turbine response simpler which is also the reason why most of the equations of fluid motion assumes steady flow regime. In practice and in real life, steady flow is not the rule but is rather an exception but a lot of problems can be effectively studied using steady flow analysis, this includes systems with minor fluctuations of velocity and other parameters with respect to time whereas the average remains unchanged over a certain amount of time (Massey, 1979).

In terms of tidal turbines, most of the current designs are based on steady flow analysis where the velocity of the fluid flow is assumed to be constant over a period of time. This can

be assumed for small fluctuations in velocity but this is not always the case since tidal stream flow can be very complex as it can non-uniform (fluid flow parameters changes from one point to another) and unsteady (fluid flow parameters changes with respect to time) at the same time. One of the most popular and most cited tidal turbine performance analysis is from the University of Southampton (Bahaj *et al.*, 2007, Batten *et al.* 2007, Batten *et al.*, 2006) which includes a series of experiments in a cavitation tank with validation studies done for Blade-Element Momentum (BEM) simulations. The performance of a tidal turbine is usually presented in a  $C_p$  vs tip speed ratio (TSR) curve (also called turbine performance curve) where TSR is the ratio of the turbine's rotational velocity to the free-stream fluid velocity, shown in Figure 1.9 is one turbine performance curve for the tidal turbine used for their series of experiments.

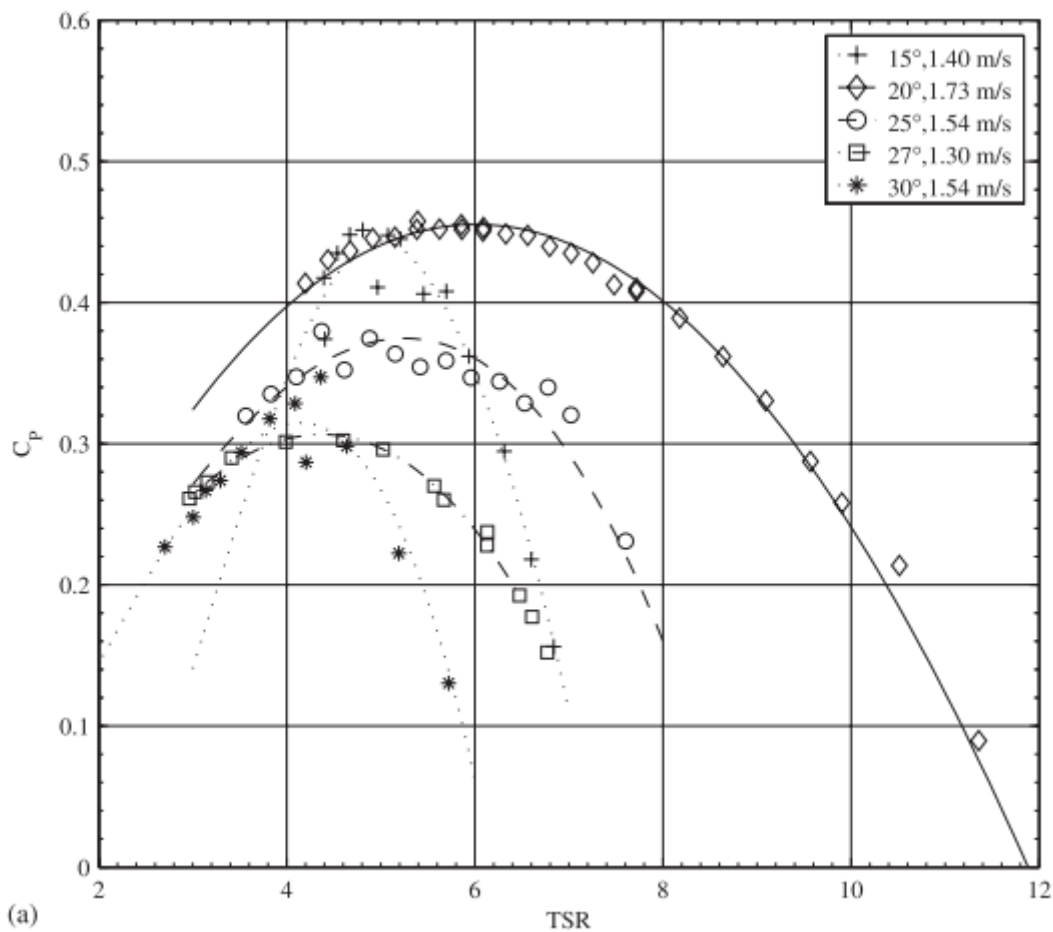


Figure 1.9 Turbine performance curve for the Southampton turbine at various combinations of pitch angle and fluid flow velocities

Again, it can be assumed that flow for tidal turbines can be steady but it is not always the case as unsteadiness in tidal stream turbines exists and is mainly caused by the following; the turbulence of the incident flow, surface waves and current interaction, and also depth-wise variation in the mean flow. It will be presented in the literature review how unsteadiness is affecting tidal turbine not only in terms of the performance but the design and the reliability of rotors as well. Notable references include the unsteady flow experiments done by the group of Milne et al which looks at blade loading in unsteady flow (Milne *et al.*, 2012) (Milne *et al.*, 2016). Another one will be the real flow performance assessment of a HATT in Nova Scotia by LeRoux et al which will be reviewed in the next section (LeRoux *et al.*, 2016). As with this thesis, the aim is to look at the effects of unsteadiness in the flow to the performance of a newly designed Horizontal Axis Tidal Turbine by using an idealised sine wave to induce velocity variation in the flow. The main objectives of the study will be elaborated in the next section.

### **1.3 Project Aims**

The goal of this project is to present the performance response of the Sheffield Horizontal Axis Tidal Turbine, a turbine designed at the University of Sheffield, to the unsteadiness in the incoming flow velocity induced by using an idealized sine wave. Listed below are the objectives that will be addressed in the entirety of the thesis:

- The first objective is to design a tidal turbine that has a flat turbine performance curve which means that it has a high CP for a large range of TSR which is good for unsteady flow as the velocity and hence TSR is changing instantaneously.
- The second objective is to compare the performance of the Sheffield HATT in steady and unsteady flow for various mean TSR's. Three unsteady cases will be investigated which is at optimum TSR (TSR=6) and two other cases at TSR=4 and TSR=8. Flow

physics in the turbine will be explained using parameters such as streamlines and pressure plots for both steady and unsteady cases.

- The last objective is to show the effects of amplitude and frequency variation of the idealised sine wave to the performance of the Sheffield HATT in unsteady flow.

Understanding the effects of unsteadiness to performance will add to the knowledge pool for the next generation of tidal turbine designs and will give an idea to future designers on which aspects of tidal turbines can be improved and developed.

## **1.4 Thesis Contents**

This thesis is composed of seven chapters and listed below are the contents of each chapter in condensed form:

An introduction to tidal energy and tidal turbines will be presented in Chapter 1. The available types of tidal turbine have also been shown together with the details of current tidal turbines that have been deployed in the waters. An introduction to steady flow and unsteady flow is also included as well as the main objectives of the thesis.

Chapter 2 provides a grasp of the current literature pertaining to tidal turbines mainly in numerical simulation and unsteady flow. The basic hydrodynamics of tidal turbines is presented first to provide an understanding of the basic theories in tidal turbine analysis as well as the common design parameters present in tidal turbine design like cavitation, blade loading and solidity. Current literature in physical and numerical modelling is also presented with emphasis on CFD modelling of tidal turbines and unsteady flow.

The design of the Sheffield HATT is presented in Chapter 3. The whole design process is shown starting from the validation of QBlade which is used for the initial design of the turbine together with an idea of its performance using a BEM solver. A structural response study which is a collaboration with Dr. Louis Angelo M. Danao is also been presented.

The numerical model that will be used for the remainder of the thesis is presented in Chapter 4. Mesh analysis, independence and boundary studies as well as the description of the model are provided in this chapter. The steady state performance analysis of the Sheffield HATT is also included together with a comparative study between two turbulence models used.

After the selection of the numerical model in Chapter 4, unsteady flow simulation for the Sheffield HATT model is conducted and is presented in Chapter 5. The base case unsteady simulation has been defined as the simulation at the peak TSR with a velocity variation with 24.5% amplitude and a frequency of 1Hz. Two off-peak unsteady simulations are also presented which are for a mean TSR of 4 and 8. Comparison of the results with the base case is also presented in this chapter and flow physics is explained using flow streamlines, pressure plots and vortex structure plots.

Chapter 6 looks at the effects of the variations in amplitude and frequency of the unsteady flow velocity on the performance of the tidal turbine. Comparison of the turbine's performance with the base case simulation is also included.

Chapter 7 provides the summary and conclusion for the whole thesis together with its limitations and possible recommendations for future works regarding the topics presented.

## 1.5 Publications

Throughout the duration of the study, several parts of the thesis has been presented and published in a conference while a paper is submitted for a journal publication in Renewable Energy. Listed below are the papers co-written by the author:

Abuan, B.E. and Howell, R. J. (2016). Effect of Idealised Unsteady Flow to the Performance of Horizontal Axis Tidal Turbine. *2nd Asian Wave and Tidal Conference (AWTEC)*, Marina Bay Sands, Singapore.

Danao, L.A.M., Abuan, B.E. and Howell, R.J. (2016). Design Analysis of a Horizontal Axis Tidal Turbine. *2nd Asian Wave and Tidal Conference (AWTEC)*, Marina Bay Sands, Singapore.

## Chapter 2

# Literature Review

### 2.1 Introduction

The main purpose of this chapter is to present the current available literature in the field of tidal turbines. Topics included in this chapter vary from HATT and hydrofoil fundamental hydrodynamics, tidal turbine design analysis, physical modelling and numerical modelling with emphasis on Computational Fluid Dynamics in tidal turbine operations. The current literature regarding unsteady flow in tidal turbines is also presented.

### 2.2 Horizontal Axis Tidal Turbine Fundamental Hydrodynamics

Before going to the main sections of this thesis, a good understanding of basic theories and information concerning HATT's must be established. This includes flow properties, fundamental hydrofoil and turbine hydrodynamics, and power generation. One of the most important parameter to describe a flow is the Reynolds number,  $Re$ . It was first derived by Osborne Reynolds in 1833 and is defined as the ratio of the inertia force in the flow to the corresponding viscous force (Reynolds, 1883). For a hydrofoil,  $Re$  can be defined as shown in equation 1, where  $\rho$  is the density of the fluid,  $V_{rel}$  is the fluid's relative velocity,  $\mu$  is the dynamic viscosity and  $\vartheta$  is the ratio of  $\mu$  over  $\rho$  and is defined as the kinematic viscosity.

$$Re = \frac{\rho V_{rel} l}{\mu} = \frac{V_{rel} l}{\vartheta} \text{ (eq. 1)}$$

$Re$  is important in the classification of the boundary layer in an aerofoil/hydrofoil. For lower  $Re$ , the boundary layer is laminar where the viscous forces is still dominating. The flow is in layers and is characterised by a uniform streamwise velocity change in the flow away from

the wall. As Re increases, there will come a time when the viscous force can no longer hold the streamwise velocity flow in layers; the fluid will start to rotate and inertial forces will dominate making the boundary layer turbulent.

For a Newtonian fluid, where the viscosity of the fluid remains constant with shear rate *e.g.* water, Re is used for the identification of the flow state from laminar to transition to turbulent. For  $Re < 2300$ , the flow is classified as laminar while for  $Re > 4000$ , it is considered to be turbulent. If Re is between 2300 and 4000, the flow is said to be in transition from laminar to turbulent flow. Re is also an important parameter when discussing operating conditions in tidal turbines. The performance of a hydrofoil is dependent on Re, therefore a tidal turbine's performance will also be dependent on Re.

### 2.3 Hydrofoil hydrodynamics

The forces acting in a hydrofoil when it is subjected to an incoming flow together with the corresponding velocity triangle is presented in Figure 2.1. The relative velocity as seen by the blade ( $V_{rel}$ ) can be expressed by the vector sum of the water velocity ( $V_{water}$ ) and the blade rotational velocity ( $V_{blade}$ ).  $V_{blade}$  is expressed as  $-\omega R$  where  $\omega$  is the rotational speed of the turbine and R is the radius where the velocity is taken. The angle formed by  $V_{rel}$  with  $V_{blade}$  is denoted as  $\phi$ , this is also the sum of the blade pitch angle ( $\theta$ ) and the angle of attack ( $\alpha$ ) of the relative velocity.

$$\mathbf{V}_{rel} = \mathbf{V}_{water} + \mathbf{V}_{blade} \text{ (eq. 2)}$$

As a hydrofoil is subjected into a stream flow,  $V_{rel}$  will act on the hydrofoil geometry causing a pressure difference between the suction side (top side) and the pressure side (bottom side). Hydrofoils, or aerofoils in general, are designed to have a higher pressure on the pressure side which will result into a force perpendicular to the relative velocity called the lift force,  $F_{lift}$ . There will also be a force that will act parallel on the direction of the relative velocity

which will be the result of the resistance of the hydrofoil to the fluid motion called the drag force,  $F_{drag}$ . These forces are usually converted into dimensionless numbers called the coefficient of lift ( $C_l$ ) and coefficient of drag ( $C_d$ ) which are usually defined per unit span and is stated in Equations 3 and 4 (Anderson, Jr., 2001).

$$C_l = \frac{F_{lift}}{\frac{1}{2}\rho V_{water}^2 c} \text{ (eq. 3)}$$

$$C_d = \frac{F_{drag}}{\frac{1}{2}\rho V_{water}^2 c} \text{ (eq. 4)}$$

$C_l$  and  $C_d$  are the fundamental parameters describing the performance of a hydrofoil in a certain flow and are usually plotted against angle of attack (AoA) as shown in a performance plot for NACA 4412 in Figure 2.2. Looking at the positive side of the figure, it is seen that from  $0^\circ$  to  $15^\circ$  there is a linear increase in lift and a relatively smaller increase in drag. After  $15^\circ$ , a decrease in lift is observed together with a sudden steep increase in drag. At this instance, the foil is said to be experiencing stall, where the flow is no longer following the contour of the hydrofoil and will be more likely separated (Dick, 2015).

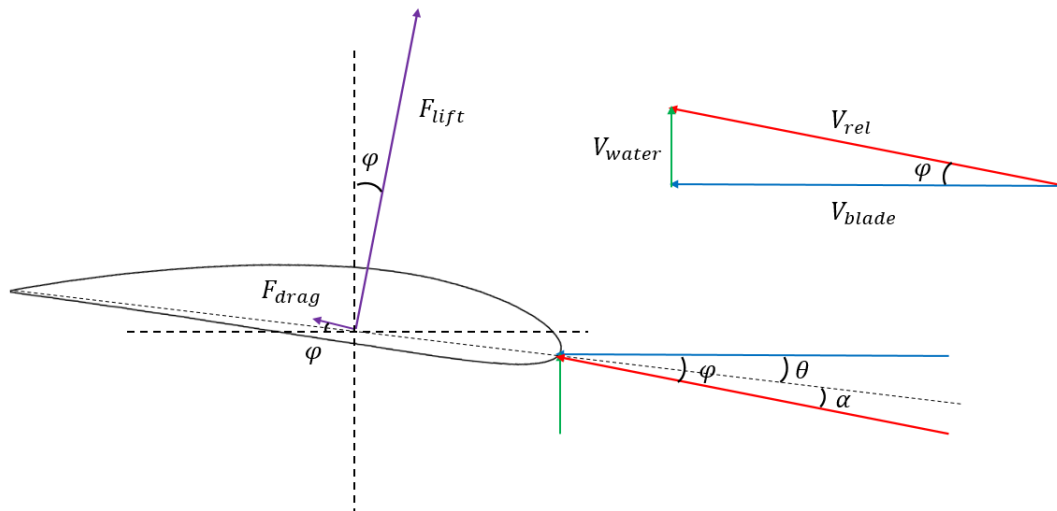


Figure 2.1. Velocity Triangle and Forces acting on a hydrofoil cross section in a tidal turbine

The concept of boundary layer is an important concept to discuss to understand certain flow physics in a hydrofoil. The boundary layer is defined to be the region away from the hydrofoil's wall where viscous force is still affecting the flow. It extends to some distance defined to be the boundary layer thickness. When a hydrofoil is subjected to a flow and AoA is still low, the boundary layer will be most likely attached which means that the wall shear stress is positive and the flow is still following the contour of the aerofoil. As AoA increases, there will come a time when an adverse pressure gradient will be present in the flow causing the velocity near the hydrofoil's wall to be zero and the boundary layer to thicken and separates. The wall shear stress will be negative and it will induce some parts of the flow to move in reverse thus creating circulation. This mechanism is shown in Figure 2.3. Boundary layer separation has some effects on the hydrofoil's performance. This includes a sudden increase in drag. Since boundary layer becomes thicker as it separates, changes in the outside pressure fields leads to a pressure imbalance hence increasing pressure drag. Boundary layer separation also changes the effective shape of a hydrofoil. At high AoA, the effective area of the hydrofoil increases and thus increasing form drag. Since the hydrofoil does not have its streamlined shape

when separation occurs, this also results in a loss in lift, also known as aerodynamic stall.

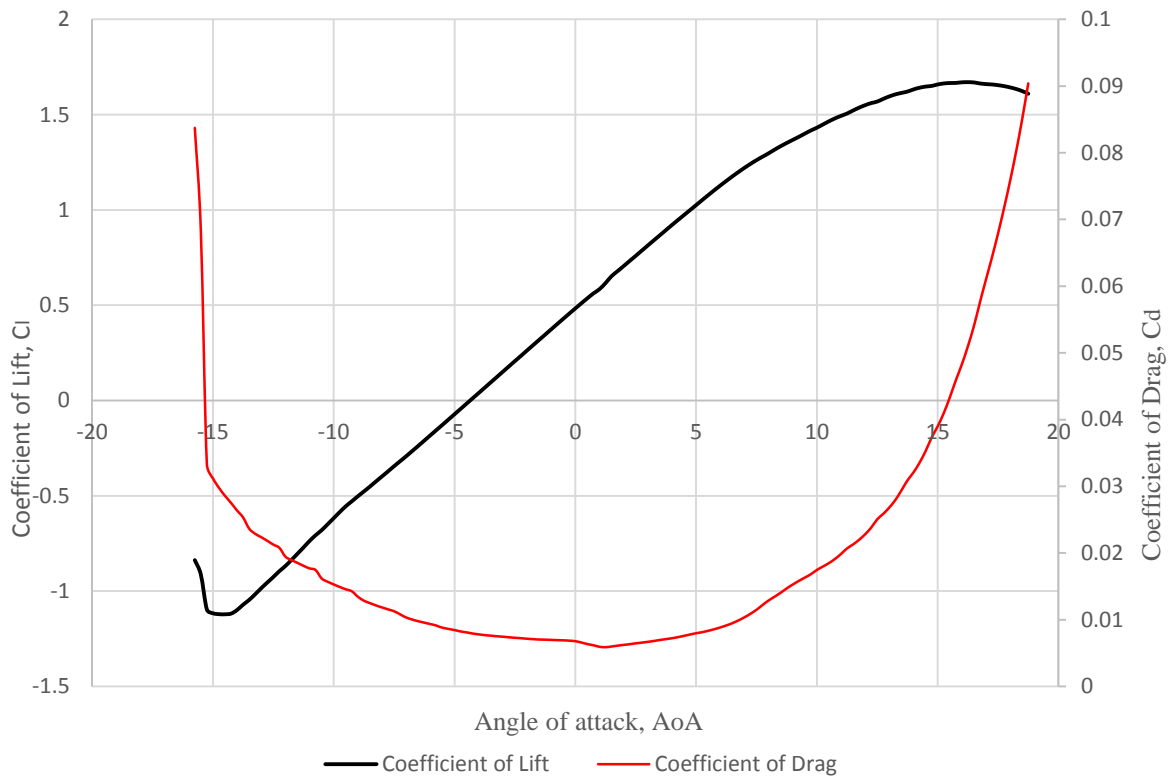


Figure 2.2  $C_l$  and  $C_d$  vs AoA plots for NACA 4412 at  $Re = 1 \times 10^6$

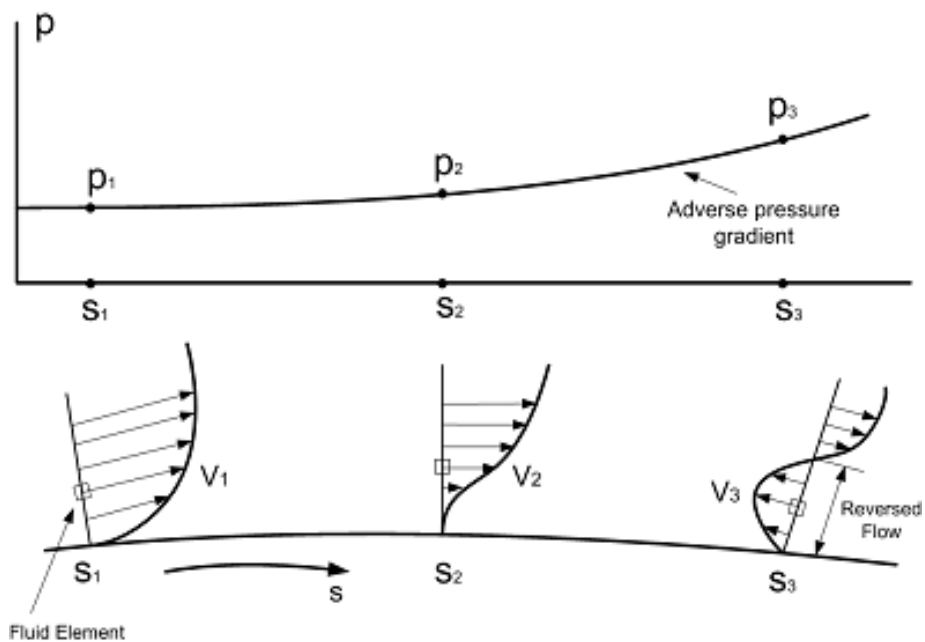


Figure 2.3 The mechanism of boundary layer separation using velocity gradient visualisation (Image taken from Anderson, Jr., 2001)

## 2.4 Tidal Turbine Design and Fundamentals

The power generation in HATT is very similar to that of a HAWT where the turbine extract energy from a moving stream of fluid. The total theoretical water power ( $P_a$ ) that can be harnessed from a tidal stream is dependent on the velocity of the stream ( $V_{water}$ ), the density of the fluid ( $\rho$ ), and the area of the extraction device ( $A$ ) (Hardisty, 2009). It can be expressed as:

$$P_a = \frac{1}{2} \rho A V_{water}^3 \text{ (eq. 5)}$$

The torque that will be produced by the interaction of hydrodynamic forces acting on one blade ( $T_{blade}$ ) multiplied by the number of blades ( $n$ ) and the rotational velocity of the turbine ( $\omega$ ) is equal to the power generated by the turbine ( $P_e$ ) as expressed in eq. 6.

$$P_e = T_{turbine} \omega = n T_{blade} \omega \text{ (eq. 6)}$$

The ratio of  $P_e$  to  $P_a$  is defined as the Coefficient of Performance (CP) which is used as the basis of a turbine's efficiency. It is usually plotted against the tip speed ratio (TSR,  $\lambda$ ) to complete the CP-TSR curve also known as the turbine performance curve. TSR is defined as the ratio of tangential speed at the tip of the blade to the actual velocity of the flow as shown in eq. 6. The turbine performance curve of a turbine is used to characterise the turbine and is also a critical part of the turbine design. The maximum theoretical CP was established to be  $16/27$  and is called the Betz limit named after Albert Betz which derived it in the 1920's. (Betz, 1928) In 2014, Vogel discussed the possibility that the Betz limit can be exceeded theoretically for tidal turbines since the limit is derived only for kinetic energy extraction while arguably tidal turbines can also derive energy from potential energy due to the process of free surface drop (Vogel, Wilden, & Houlby, 2014).

$$CP = \frac{P_e}{P_a} \text{ (eq. 7)}$$

$$TSR, \lambda = \frac{\omega R_{blade}}{V_{water}} \text{ (eq. 8)}$$

### 2.4.1 Solidity

Solidity can be defined as the area swept by the turbine and is mostly affected by the number of blades and the blade span and section chords. It was stated that in HAWT, increasing the number of blades will also increase the power coefficient by the turbine but will have diminishing effect for each additional blade (Hau, 2006). Similar observations for HATT was observed by Morris (Morris, 2015). Morris used Computational Fluid Dynamics (CFD) to look at the effects of solidity mainly to performance and wake recovery as well as blade deflection. Figure 2.4 shows the effect of increasing the solidity by the addition of rotor blades for HAWT and HATT from Hau and Morris researches respectively.

It can be seen that as the number of blades increases, the maximum CP also increases although the turbine performance curve became narrower. For Morris HATT, the CP increase presented from 3 to 4 blades is just around 4.5% to 4.8% which is lower than the observed of about 10.8% to 11.5% when the number of blades is increased from 2 to 3. It was also stated that for the HATT used in Morris' research, higher solidity rotors will have to withstand lower loads in the event of failure and the thrust (and hence, blade deflection) increases as the number of blades decreases. A three-bladed tidal turbine that will be presented in chapter 3 will be used for the rest of the thesis. A three-bladed design was chosen by the author as it shows the largest increase in CP when one blade is added to the two-bladed design. The three-bladed design also allows a good range of TSR values that will be important for the analysis in unsteady flow simulation.

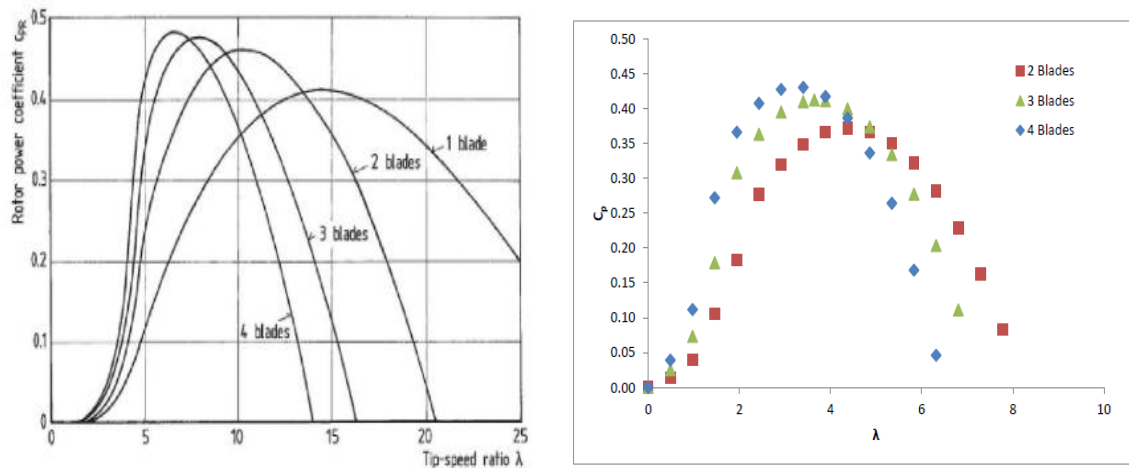


Figure 2.4 Effect of increasing solidity in terms of the number of blades for HAWT (left) and HATT (right)

### 2.4.2 Bio-fouling

One of the main factors affecting tidal turbine design is the material selection for the blade itself. The main problems that submerged devices encounter are the harsh corrosive sea water, fouling growth and abrasive suspended particles. Of the three, bio-fouling is the most common cause of degradation on performance of marine devices due to surface roughness. At worst cases, it may even destroy the blade due to erosion (Wood *et al.*, 2010). Marine fouling is caused by the deposition of microorganisms in the surface of the device that will eventually colonise parts of the blade. It depends on water depth, temperature and salinity and thus may vary from one site to another. Despite its dependence in location, Hellio *et al.* stated that at 5m below water, tidal systems will be covered in fouling especially the low velocity parts like the blade root and the rotor hub wherever the location is (Hellio *et al.*, 2009).

Fouling can be prevented by using fouling control coatings. These coatings are typically used for ship hulls and are categorized into two major groups, the biocide-based paints and the fouling-release coatings. The first one was based on controlled-release of active ingredients to control fouling while the latter was based on the physical properties of the coating itself. Yebra *et al.* presented the characteristics of these two coatings in terms of turbine efficiency over

time-immersion with the coating. Biocide paint will not have significant drop for the first few years of installation though a big drop will be experienced after 2-3 years. Foul-release coatings may have a sudden decrease in efficiency for the first few years but will eventually self-clean and recover efficiency. Yebra *et al.* also presented a study on the effects of three different fouling mechanisms (three situations from three different coatings) in the performance of tidal turbines. The results showed a decrease of about 7.5%, 22.5% and 40% in the daily power produced after 5 years exposure for the three coatings respectively (Yebra *et al.*, 2010). Chen even stated that at high level of fouling on the blade of a tidal turbine may have 70% loss on efficiency (Chen L. , 2015).

### **2.4.3 Cavitation**

Cavitation is another difference between wind and tidal turbine design in general, aside from bio-fouling. If bio-fouling usually occurs on blade surfaces with low velocity, cavitation mostly occurs near fast moving areas of the blades. Static pressure will suddenly drop because of the increase in the dynamic head at high velocity location and will cause the formation of vapour bubbles. These bubbles will eventually breakdown and will produce high frequency and extremely high over pressure pulses that will erode the surface of an even metal blade making the blade surface rougher. Again, a rough blade will decrease the efficiency of the blade as it changes the shape of the aerofoil especially if the roughness is happening near the tip of the blade where the peak of energy production is generated. If the vapour bubble is still present during operation, it can also cause separation and hence will do negative effects in the turbine's efficiency.

Wang *et al.* explore the possibility of using cavitation tunnels and marine propellers testing method to be applicable in the study of small-size tidal turbine performance when cavitation is most likely to be present. It was proven to work and applicable and different forms of cavitation that will be in effect to the turbine's performance was observed as shown in Figure

2.5. It was also presented that cavitation will cause increase noise especially in severe cases and may disrupt marine life. It was also suggested that tidal turbines should be placed at least one diameter size above the seabed to avoid erosion and sediment transport in the seabed. (Wang *et al.*, 2007) Bahaj *et al.* agreed with the idea of negative effects of cavitation to tidal turbine's power extraction but stated it still depends on the design of the blade. It was also suggested that for the tidal turbine tested for their research, blade tip speed should be less than 7 m/s to prevent cavitation (Bahaj & Myers, 2001). Barber *et al.* did a number of numerical analysis using a BEM-FEM solver to look at blade response to cavitation. It was stated that the blade response is independent of the material orientation. It was also found out that cavitation for the tidal turbine tested was observed at the turbine's normal operating condition therefore it should be included in the design process (Barber & Motley, 2016). In terms of modern design, it was found by Nicholls *et al.* that adaptive blades, turbine blades that can change or adapt according to the flow conditions, decreases the likelihood of cavitation in their BEM analysis of a model tidal turbine (Nicholls-lee & Turnock, 2007).

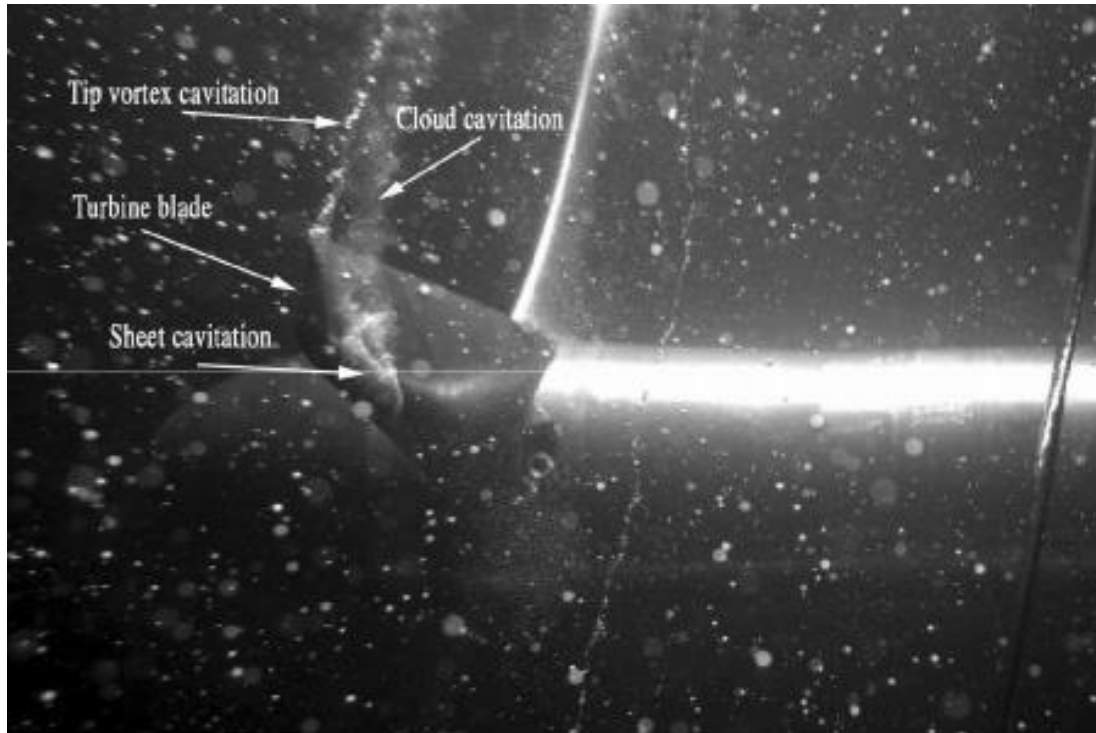


Figure 2.5 An image taken from the experimental set-up by Wang *et al.* (Wang *et al.*, 2007) showing different kind of cavitation present in the tidal turbine

#### 2.4.4 Blade Loading

Since the goal of tidal turbines is to be another mean of renewable energy generation, it must be designed to last for long number of years without failure. Tidal turbines are designed to withstand certain degree of loads before being subjected into the waters but still, a lot of prototypes and test turbines failed because of the underestimation of loads which results to under-designed turbines (Liu & Veitch, 2012). These underestimation of blade loads is due to the inaccurate site loading data and bathymetry which also includes effects of turbulence and wave effects. It was stated by Faudot *et al.* that loading analysis and dynamic effect analysis is site dependent (Faudot & Dahlhaug, 2012).

Bahaj *et al.* did a number of steady state experiments measuring the power and thrust of a model tidal turbine in a cavitation tunnel and towing tank which provides a lot of information in steady flow blade loading (Bahaj *et al.*, 2007; Batten *et al.*, 2006). Liu *et al.*

states that the tensile stress due to the out-of-plane bending moment is the critical parameter to be looked at when dealing with blade strength and integrity. It was also identified that small changes in blade thickness has very little effect on power coefficient. This is important as small modifications in thickness to increase blade strength is negligible to the hydrodynamic performance (Liu & Veitch, 2012). Blade loading due to unsteady flow effects will be presented in the section of the literature review about unsteady flow in Section 2.7.

## **2.5 Physical Modelling of Tidal Turbines**

Full-scale tidal turbine testing and even prototype testing costs a lot of money to conduct and will require very long amount of time to be finished. That is why scale modelling of tidal turbine in laboratories is carried out to observe tidal turbine behaviour in a way that is less expensive with greater control of parameters tested and that can be done over relatively small amount of time. Small scale tidal turbine testing can also be used as iterative measures for designs before doing prototype testing in real tidal streams. Bahaj *et al.* did a number of tidal turbine experiments using a model tidal turbine in a test tank and cavitation tunnel. One of the notable literatures produced from those experiments include power and thrust measurements of a tidal turbine. Results showed that the test tank and cavitation tunnel experiments were sufficient for looking at the performance of tidal turbines in yawed flow, effects of tip immersion and cavitation. Results also provides a number of experimental data to be used for future design and for the validation of theoretical and numerical methods (Bahaj *et al.*, 2007). Wang *et al.* did some experiments in a cavitation tunnel used for marine propellers to look at the onset of cavitation in tidal turbines as already been mentioned in section 2.4.3 (Wang *et al.*, 2007).

Chamorro *et al.* did a number of experiments using model tidal turbines, this includes a 3D Particle Image Velocimetry (PIV) of the wake formed by a model tidal turbine without

any attached instrumentation and an open channel tidal turbine experiment to look at turbulence of the flow to the tidal turbine wake where the first observation of wake meandering was included (Chamorro *et al.*, 2013). Walker looks at the effects of support structure and wake downstream a tidal turbine using scale models in a circulating water flume (Walker, 2014) while Morris examined solidity, wake recovery and blade deflection on HATT using a water flume as well (Morris, 2015). These literatures presented above proved small scale modelling in different laboratory environments such as cavitation tunnels, tow tank, open water channels and water flumes can present good data for different tidal turbine parameters being studied.

Experimental analysis is also applied for the study of tidal stream turbine interaction, Mycek *et al.* conducted a study which looked at two scaled turbines at different separation distances and it was found out that even at a distance of 10D from each other, only up to 80% of unrestricted turbine performance can be achieved (Mycek *et al.*, 1990). In terms of the unsteady analysis that will be the focus of the thesis, experimental modelling in unsteady flow has been done by Milne *et al.* using a moving carriage holding the tidal turbine in a steady flow towing tank. The movement of the carriage will induce an unsteady surging motion in the flow as seen by the turbine. Milne *et al.* stated that this set-up is a simplification of the very complex tidal stream flow and the simplicity of the set-up allows analysis to be easier and deeper (Milne *et al.*, 2013, 2016). The result of the researches done by Milne *et al.* in unsteady flow will be explained in detail in Section 2.7.

## **2.6 Numerical Modelling of Tidal Turbines**

Although a lot of time and money can be saved by the use of experimental modelling of tidal turbine instead of testing prototypes in the waters right away, further savings can be achieved by using numerical modelling. Although numerical simulations further minimise design iterations and parameter studies for tidal turbines, the search for the correct and suitable

model became the largest obstacle for researchers, this is the reason for the increased number of tests and checks before using numerical methods. Presented in this section are the two most used numerical models for tidal turbines; the Blade-Element Momentum (BEM) model and Computational Fluid Dynamics (CFD).

### **2.6.1 Blade-Element Momentum (BEM) Model**

The BEM method was first introduced by Froude in 1878 (Froude, 1878) and was further developed and applied by Glauert for the analysis of airplane propellers (Glauert, 1935). This method primarily uses the same blade-element theory where a rotor blade was divided into smaller sections where individual forces will be calculated, the sum of all of the forces acting on each section will be the force acting on the blade. The combination of the momentum theory solved the problem of the blade element method regarding the induced velocity in the rotor.

BEM modelling was then integrated into the design of wind and tidal turbines firstly by Sorensen which uses 360° extrapolated aerofoil lift and drag data as input for the numerical analysis. Such technique is still used in the wind turbine industry until present times. Masters *et al.* integrated BEM with tidal rotor designs and proved that it can be used to calculate tidal turbine performance, correction factors for hub and tip losses using BEM was also presented as these parameters are not included in the main BEM algorithm (Masters *et al.*, 2010). Bahaj and Batten *et al.* also validated BEM with the use of experimental modelling in cavitation tunnel and towing tank (Bahaj *et al.*, 2007). BEM has been integrated into many wind and tidal turbine software. Gerard Hassan's Bladed and Tidal Bladed uses BEM as the main solver for turbine performance and design which was validated by the Energy Technologies Institute (ETI) as well as Bahaj *et al.* QBlade, a wind turbine open source software which integrates BEM with XFOIL and polar extrapolation into a complete rotor performance solver. QBlade's

BEM solver is explored in this paper as a tool for tidal turbine design and performance analysis and will be presented in Section 3.2.

Performance analysis of HATT using BEM has been done by a number of researchers already. Chen *et al.* did a combination of BEM with CFD for a performance simulation for a 6.2 m commercial HATT showing that it has a flat peak with a maximum CP of 47% at TSR=7 (Chen, Choi, & Yoon, 2013). Nicholls Lee et al. did BEM analysis to look at the effect on performance of adaptive blades and it was found out that the turbine captures 2.5% more energy from the water and the most important part is the reduction of the thrust coefficient that was decreased by 14.5% (Nicholls-lee & Turnock, 2007).

BEM shows a promising potential in the design and performance analysis of tidal turbines with the advantage of being faster and less computationally intensive to other numerical methods but it can have a few limitations that may be critical to certain analyses. First of all, the forces are calculated based on lift and drag ratios of hydrofoil used for the rotor blade and does not include other forces that can occur as a result of the interaction of the blade to the incoming flow. Malki *et al.* stated that in BEM, the forces that are averaged across the blade does not account to any flow perpendicular to the blade profile which is addressed by using the next numerical method that will be presented which is Computational Fluid Dynamics (CFD) (Malki *et al.*, 2013).

In terms of unsteady flow effects in wind and tidal turbines, a number of improvements on the BEM method to capture unsteady effects has been developed over the years. The effects of stall dealy and dynamic stall, which will be discussed in detail in Section 2.6.3, has been incorporated into BEM by Leishman although it was not proven yet if the wind turbine codes will be applicable fully to tidal stream turbines (Leishman, 2006). Another improvement has been done by Whelan who used the dynamic model done by Pitt and Peters model to determine

the effect of dynamic inflow and was able to demonstrate lift and blade loads over shoots (Whelan, 2010).

### **2.6.2 Computational Fluid Dynamics (CFD)**

Although BEM has been proven to be widely used in tidal turbine design and analysis with validations through experimental and numerical comparisons (Batten *et al.*, 2007), it needs additional help especially when used to investigate specific problems in tidal turbine hydrodynamics like forces acting on the blade, flow over the blade itself and the flow physics in the blade sections. Computational Fluid Dynamics (CFD) has been used and developed to serve as an additional and/or alternative tool for further investigation of specific problems in tidal turbine performance. CFD uses numerical analysis and algorithms to solve fluid flow problems, it can present more data and information about fluid flow in tidal turbines at the expense of larger and longer simulation times.

There are different methods of CFD that is being used in the study of wind and tidal turbines, each varies on how the fluid flow was modelled and solved, accuracy and computational time also differs. The most computationally intensive method is the Direct Numerical Simulation (DNS), this method solves the full Navier-stokes equation for the all elements in the computational domain from the smallest to the largest eddies which requires very large computing power and time. Reynolds-Averaged Numerical Simulation (RANS) on the hand uses the time-averaged Navier-Stokes equation to reduce the number of equations to be solved per time step to allow faster simulation. However, time-averaging the equations of fluid motion results to the emergence of additional terms, which are called Reynolds stress tensors which are there to characterise the turbulence of the flow  $\tau_{ij} = -\rho u_i u_j$ . The emergence of these additional terms result to an unbalance in the number of equations and unknowns requiring another equation to solve for it. In 1880, Joseph Boussinesq introduced

the eddy-viscosity model where an analogy between the viscous shear of the mean velocity and a corresponding shear of the turbulent velocity fluctuations was made using the eddy viscosity,  $\mu_T$ . Now, the Reynolds stress tensors can now be written as  $\tau_{ij} = \mu_T \left( \frac{\partial u_i}{\partial x_j} + \frac{\partial u_j}{\partial x_i} \right)$  and the only unknown to be solved using the turbulence closure model is the eddy viscosity term. This is known as the Boussinesq hypothesis.

Turbulence models are developed to provide additional equations for the incompressible RANS equation with the Boussinesq hypothesis. The Spalart-Allmaras (SA) uses a one equation model directly solving for the eddy viscosity which makes it the most economical and fastest model available. It was designed to be used for aerospace application but it is known to be inferior to other turbulence models when predicting lift and drag on aerofoils especially at stall region (Fluent 16, Theory guide) which was shown by Geize *et al.* when they investigate the flow around a NACA 0015 aerofoil proving that SA is inferior to two-equation turbulence models k- $\epsilon$  and k- $\omega$  (Geize *et al.*, 2004). The k- $\epsilon$  model is a two-equation model that uses two different transport equations for the turbulent kinetic energy (k) and the dissipation rate ( $\epsilon$ ) to solve the eddy viscosity using the relation  $\mu_T \propto \rho \frac{k^2}{\epsilon}$ . The standard model was known to be good for high-Re flow which is of much use for tidal turbine applications (Fluent 16, Theory guide) but has problems predicting adverse pressure gradients and flow separations. These problems has been addressed in two other k- $\epsilon$  variants which are the ReNormalised Group (RNG) method and the realisable case. k- $\epsilon$  RNG uses analytical equations in its k and  $\epsilon$  solution which results for its capability to allow low-Re and more accurate near-wall treatment. The realisable case uses an exact equation for the dissipation and the formulation of the eddy viscosity relation has become more complex. This results in a more accurate k- $\epsilon$  model than the other variants with a slight increase in computational time. The other two-equation turbulence model is the k- $\omega$  model which solves the specific dissipation

rate ( $\omega$ ) and using the relation  $\mu_T \propto \rho \frac{k}{\omega}$  to solve for the eddy viscosity term. The model was made to overcome the limitations and shortcomings of the k- $\epsilon$  model and is known to be accurate for near-wall applications and capturing flow separations. Its most used variant, the shear stress transport (SST) model, developed by Menter, reduces the free stream dependence by using the near-wall accuracy of the k- $\omega$  model while utilising the k- $\epsilon$  model at far-field because of its free-stream independence which makes it more accurate and reliable than the standard k- $\omega$  model (Menter, 1994). In this thesis, the k- $\epsilon$  RNG and the k- $\omega$  SST model will be used and will be tested in Chapter 4 for the steady-state simulation while the better model will be used for the rest of the simulations that will be presented in Chapters 5 and 6.

RANS has been the most commonly used method since it does not require very large computing resources and can be used in the University level. Another discrete CFD method is the Large Eddy Simulation (LES) which is a combination of DNS applied in the large eddy scales in the computational domain and RANS at the smaller scales. This is said to be more accurate when compared to RANS (Kang *et al.*, 2012) but is also more intensive and will require larger computational resources though it requires less than that of full DNS. Afgan *et al.* compared blade loading and turbulence in tidal turbine using RANS and LES. A validation of the flume testing experiment from Bahaj *et al.* was done using the two models, results showed that for TSR between 6 to 10, the mean thrust and power coefficients ( $C_t$  and  $C_p$ ) are predicted to be 3% within the experimental values for both RANS and LES. For lower TSR range from 2 to 6, similar accuracy was found for LES but an under prediction within 10% of the experimental value was determined using RANS. It was found out that RANS under predict suction pressure near the leading edge. It was stated in the paper that although the computational cost for LES is much greater than RANS, the blade-resolved simulations presented in the paper shows that the LES approach provides greater insight into flow physics particularly at low TSR. The LES simulations done in the paper was conducted using IBM

Gene P supercomputer using 2048 processors and requires 4.4 million CPU hours compared to the 0.14 million CPU hours for RANS (Afgan, et al., 2013).

Presented in the following sections are some parts of the current literature that have used CFD to explore problems and topics about tidal turbines. Malki *et al.* used a coupled BEM-CFD model to investigate the influence the upstream hydrodynamics on rotor performance. It was stated that the coupling of CFD to BEM address the limitation of BEM in analysing effects of rotor to the surrounding flow, analysis of wake dynamics and flow physics around the blade. Navier-Stokes equations are solved by the CFD model using RANS producing results for velocity and pressure parameters throughout the flow domain dependent on the initial and boundary conditions. Momentum source terms are then introduced using the BEM model which is defined by the blade characteristics and the current TSR. The process of integration the BEM to CFD is illustrated in the figure 2.6 below. Validation results showed that the BEM-CFD model shows good correlation with the published flume data used in the study. CP variations were found when compared to classical BEM results but it was stated that the BEM-CFD model gives a more realistic estimation of the turbine performance where the incoming flow is non-uniform due to the effect by upstream devices and due to natural bathymetric (Malki *et al.*, 2013).

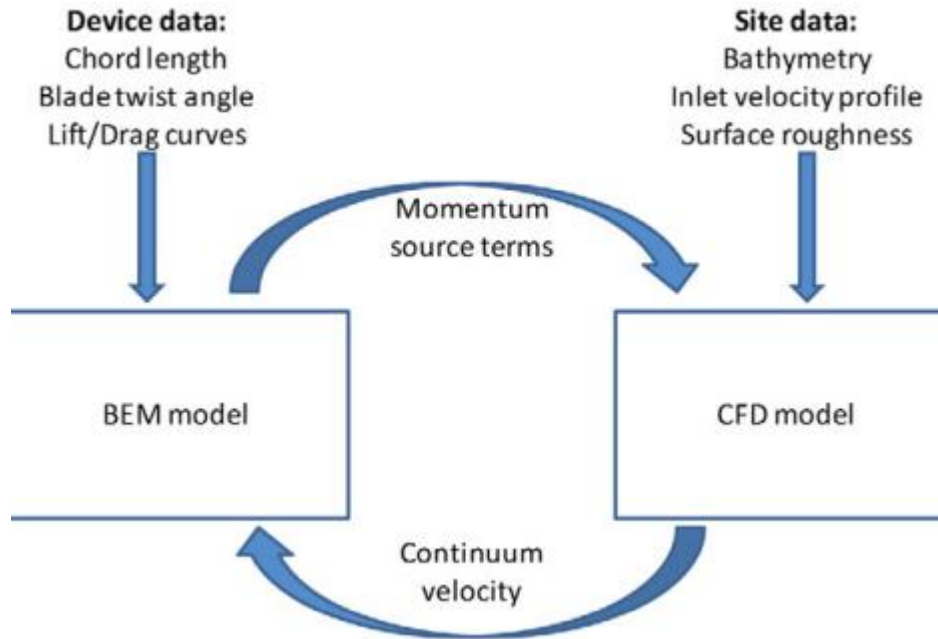


Figure 2.6 BEM-CFD coupling integration as done by Malki *et al.*, 2013

Wake modelling in tidal turbines was also done using CFD simulations, Batten *et al.* presented findings from a two dimensional CFD model to show how the wake from an upstream device changes the turbulence intensity incident to a downstream device in an array. It was stated that a turbine located 10D downstream has the same turbulence intensity when compared to that of the first turbine (Batten *et al.*, 2006). MacLeod *et al.* also developed an in-house code named “3D-NS” which is a RANS solver with  $\kappa$ - $\epsilon$  closure to simulate clusters of turbine in any configuration. Results showed that flow recovery is faster in areas of greater ambient turbulence intensity and turbines with higher thrust coefficients has wake recovery that is slower. It was also found that 5D separation between turbines is enough for turbine arrays as the velocity is recovered at that distance (MacLeod *et al.*, 2002). Gant and Stallard used porous disc modelling for tidal turbines with a RANS  $k$ - $\epsilon$  to determine the effect of large-scale flow oscillations on the wake of the turbine (Gant & Stallard, 2008). CFD using LES was also used in tidal turbine wake investigation, Churchfield *et al.* uses an LES model using the sub-filter scale (SFS) turbulence model for the RANS simulation for smaller scales. A complete

time-dependent solution was obtained which contains all of the large eddies within the flow which can be used to improve turbulence models for full RANS modelling (Churchfield *et al.*, 2013).

Morris *et al.* uses Finite Element Analysis and CFD RANS model in tidal turbine to observe solidity effects in various parameters in tidal turbine using an unstructured mesh. CFD results shows that increasing the number of blades also increase the peak CP and decrease the TSR by which it occurs, although the value increased diminishes as the number of blade increase as shown in Figure 2.4. Blade deflection was also shown to increase with a reduction in solidity due to the increased thrust per blade. It was determined that for 2 and 4 bladed rotors in the study, power output was seen to first increase with deflection but then decrease with further deflection. For 3 bladed turbine, power output decreased as the blade starts to deflect (Morris, 2015).

Mason-Jones *et al.* used RANS with Reynolds stress model (RSM) to simulate plug flow or profiled high shear flow to a tidal stream turbine. The results process asymmetric loading in the turbine for a complete rotation cycle. The effects of having a stanchion was also investigated and it was shown that it leads to a higher amplitude and more complicated loading in the turbine (Mason-Jones *et al.*, 2013). A very similar model was used by O'Doherty *et al.* when they looked at the feasibility of tidal turbine sites in the Welsh coast. The CFD study compared the torque, power and axial thrust of a 10 m diameter turbine operating in a scaled velocity profile to the same turbine operating at uniform flow with the mean velocity of the sheared flow. Results showed that the turbine subjected to real flow has lower performance than that of the turbine in uniform flow (O'Doherty *et al.*, 2010). The results shows a very important effect of sheared flow to the turbine's performance but Bryden *et al.* argued that it is better to use the root of the mean cube of the the velocity over the swept area instead of using

the mean velocity of the sheared flow as it will tend to over estimate the energy flux from the water (Bryden *et al.*, 2007)

Kang *et al.* used LES to model complete 3D simulation flow for marine hydro-kinetic turbine. The LES method was used with the CURVIB method developed by the authors of the paper. Two sets of simulations were conducted. The first one is using an isolated rotor and the second one is a complete turbine simulation. In terms of power coefficients, the results from the two simulations were similar, this suggests that the pressure fields near the blades which generates torque form extracting power from available water power, is not significantly affected by the other parts of the turbine. This also proposes that the simulation of an isolated rotor is enough for predicting power in the turbine geometry being used. Results from the LES simulation also produced complete high resolution 3D structures presented using  $\lambda_2$  criterion which agrees with the results seen by Afgan *et al.* An image of the high resolution image for both the isolated rotor and the complete turbine is presented in Figure 2.7 (Kang *et al.*, 2012). Another CFD simulation done using LES is by Churchfield *et al.* which looks at the effects of fatigue loading and has demonstrated that the positioning of a turbine in a channel can significantly affect its efficiency (Churchfield *et al.* , 2013).

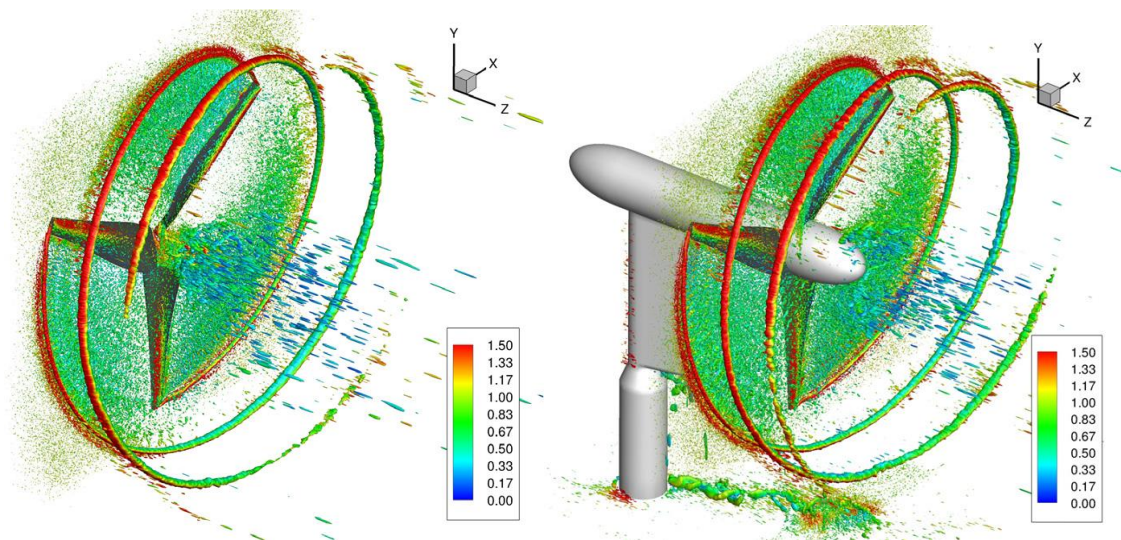


Figure 2.7  $\lambda_2$  criterion vortex structures presented by Kang *et al.* with contours showing velocity magnitudes non-dimensionalised by the free stream velocity of 2 m/s

## 2.7 Unsteady Flow in Tidal Turbine

Steady flow simulations and experiments have been the main topic of research in tidal turbine operations but researchers are also looking at the more realistic but more complicated unsteady flow simulations and its effects in tidal turbine operations. Unsteadiness in the incident flow can be caused mainly by three factors; the turbulence of the incident flow, surface waves and current interaction, and also the depth-wise variation in the mean flow. For this thesis, the effect of a time-varying incident velocity defined by an idealised sine-wave function. A sinusoid has been chosen for this study for the mere reason that it is easy to model and it is also easier to see the effects of the unsteadiness in the underlying physics in the flow when compared to real life unsteady tidal stream flows. This section will provide a review of the current literatures available in the field of tidal turbine and the gap by which the topic of the study presented in the later chapters will fit into.

Gant and Stallard observed the effect of large-scale flow oscillations on the wake of a tidal turbine modelled using the porous disc approach. The unsteadiness of the flow used in the study was defined by the presence of a turbulent flow field generated using assumed velocity profiles and/or turbulence spectra. Results proved that RANS simulation is sufficient enough to model this kind of unsteadiness also it was found out that a shorter wake was observed for the unsteady flow simulation compared to steady state using the same method (Gant & Stallard, 2008). Milne *et al.* also investigate the effects of unsteadiness due to turbulence which was defined to be a combination between non-circulatory and circulatory effects (dynamic inflow) (Milne *et al.*, 2016). The dynamic inflow effect is described to be the dynamic response of the inflow velocities in the rotor plane to the changes in the load conditions in the rotor. For

example, an instantaneous change in the inflow velocity will cause the AoA to change but not instantaneously. There is time needed for the change to happen and instead of an equilibrium change of AoA, an overshoot will be observed thus presenting an increase in lift and changing the physics of the flow as well (Snel & Schepers, 1993).

One of the underestimated effect on blade loading which might cause failures in tidal turbines is the effect of unsteady blade loading (primarily bending with additional fatigue loading) due to unsteady flows. Unsteady flow effects on tidal turbine hydrodynamics includes added mass, dynamic inflow and dynamic stall.

Added mass can be defined as the additional force acting on a body due to its acceleration as it moves some volume of the surrounding fluid when the body moves through fluid. It is called “added mass” because it seems like an additional weight to the body as fluid particles which have to move around the body when it is in unsteady motion (acceleration or deceleration) through the fluid. The effect of added mass to tidal turbine was explored by Miniaci *et al.* using unsteady aerodynamics analysis program (FAST and AeroDyn). The added mass model only includes the added mass due to acceleration perpendicular to the rotor disc and not the effect of blade deflection. It was found out that added mass has significant effect on blade loading (Miniaci, 2012) A similar observation was found by Young *et al.* using a coupled BEM-FEM solver and stated that at highly-loaded off-design the maximum von Mises stress exceeds the design material’s yield strength by 65% suggesting the same effect to the blade through fatigue loading (Young *et al.*, 2010). The contrary was observed by Whelan *et al.* when it was stated that axial added mass of rotor operating in a mean current and subject to passing waves was shown to be small (Whelan *et al.*, 2009). Whelan’s conclusion was supported by Faudot and Dalhaug when they compare theoretical blade loading in tidal turbine using BEM with the assumptions of stiff blade, constant rotational speed, and no pitching involved (Faudot & Dahlhaug, 2012).

Dynamic inflow is defined to be the response of the flow field to turbulence and other changes in the rotor operation such as rotor speed variation including blade pitch angles. When the velocity of the incident flow changes, the power extracted by the turbine will respond accordingly, this is known for steady state flow based on BEM theory. For quick changes in velocity, it was found that the greater flow field cannot respond quickly enough to establish steady state conditions and an overshoots in the blade loading was observed (Whelan, 2010) (Burton, 2001). Results from planar oscillatory experiments in tidal turbines by Milne *et al.* shows there is an increase in blade loads with frequency and exceeded the steady blade loads by up to 15%. A phase lead of the blade loads was also observed over velocity which is also an expected effect of dynamic inflow. It was also shown that the amplitudes of multi-frequency loading can be modelled using superposition which will be important in the design stage of tidal turbines to investigate fatigue loads through superposition. For lower TSR, delayed separation, phase lag, and dynamic stall were observed. These results to exceeding the steady loading by up to 25% while exhibiting a large degree of hysteresis. (Milne *et al.*, 2012) Dynamic stall is defined as the result of unsteady and/or fluctuating time histories which leads to a variation in velocity over the turbine rotor. This results to changes in lift and drag coefficients due to flow separation around the foil which is dependent on the time-dependent changes in AoA. Dynamic stall also results to overshoots in load magnitudes over steady flow values and will induced hysteresis. Detailed explanation about dynamic stall in an oscillating aerofoil can be find in the study done by Lee *et al.* (Lee & Gerontakos, 2004) and dynamic stall explained in helicopter and wind turbine settings is found works done by Leishman (Leishman, 2006). Dynamic stall phenomenon at low TSR in tidal turbine under unsteady flow is also presented in Milne *et al.* study when they explains hysteresis curve variation when frequency of the forcing velocity was changed (Milne *et al.*, 2015).

A recent research by McNae includes an investigation of the feasibility of vortex lattice method (VLM) to study unsteady flow in tidal turbines. It was shown that VLM can be used in investigating the presence of dynamic inflow by looking at the shape and strength of the turbine's turbulent wake. It was also validated using an experiment using a tidal turbine model attached in a movable carriage to implement unsteady flow phenomenon, out-of-plane bending moment at the root was measured and results shows good agreement with the VLM results. An impulsive step change experiment was conducted and it was determined that thrust loads overshoots were observed, which in turns confirms the significance of dynamic inflow in highly unsteady conditions. Planar oscillatory experiments were also conducted and a consistent small phase lead in the load was observed over the velocity except for high frequency cases (McNae, 2014). Galloway did a study on the effects of waves and misaligned flow to tidal turbines. The aim of the study is to provide more information for device reliability through the experiments and numerical modelling performed in the study. Results from experiments for the steady state experiment was compared to a detailed BEM with the addition of static stall and tip-losses corrections, modifications for yaw and blade azimuth, linear waves, dynamic inflow and dynamic stall models. The results of the study in general proved that the presence of waves and motor misalignment has negative effects on tidal turbines. Wave effects are found to be not significant in terms of power output but is significantly affecting blade loading because of the resulting cycling loading which will result into increased fatigue on the blades. It was also shown that BEM rapidly loses its applicability for off-set TSR. It was stated by the author that it is less important in low TSR since the turbine cannot usually operate at those conditions, I think that is should also be covered, because large separations and variation in the flow happens at lower TSR (Galloway, 2013).

Luznik *et al.* conducted an experiment on a three-bladed HATT with and without the absence of waves to look at effects in performance, they did present measurements comparing

the two cases but the measurements for the unsteady cases was illustrated only as cycle average for certain TSR's to compare it with the case with no wave as shown in Figure 2.8. Results suggests that the effect of the wave is insignificant as the values of CP with waves shows very similar results with that of the steady case one (Luznik *et al.*, 2013).

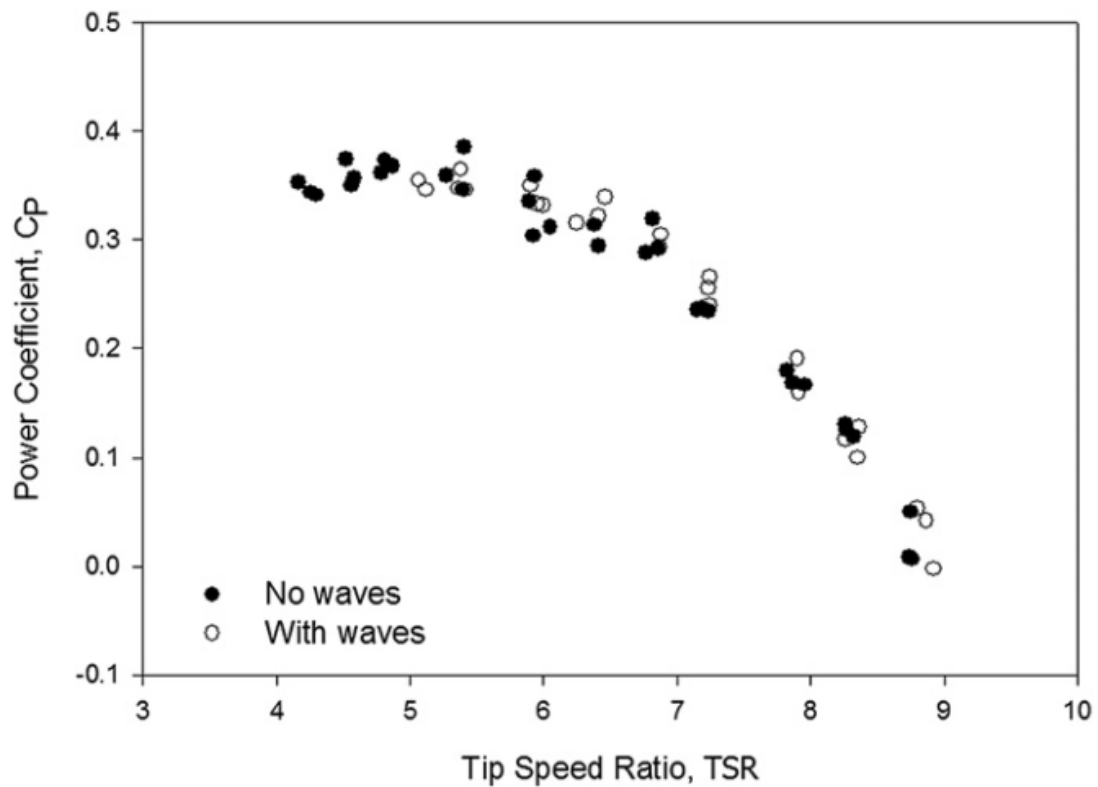


Figure 2.8 Comparison of tidal turbine performance with and without waves done by Luznik *et al.* (Luznik *et al.*, 2013)

An unsteady flow investigation of a model tidal turbine subjected to realistic flow from measurements obtained from the Grand Passage, Nova Scotia was conducted by Leroux *et al* (Leroux *et al.*, 2016). CFD modelling was used to present the effect of the realistic inflow to the coefficient of thrust and performance of the tidal turbine and the comparison between steady and transient simulation for the same mean TSR was also presented as shown in Figure 2.9. Their result shows very small difference between the steady and unsteady flow

performance which only accounts to a difference of 0.83%. The unsteady velocity profile presented in the study has a mean velocity of 2.05% and a maximum amplitude of 10%. Whilst this is one of the few unsteady performance investigation in tidal turbine that has been published, the hydrodynamics of the unsteady effects is not presented because of the complexity of the inflow boundary condition used in the study. The summary of the effect whereas a very small variation in the CP of the turbine was observed was presented but there is no explanation on what is happening in the flow because of the complexity of the inflow boundary condition. This is the reason for the author of this thesis to choose a simpler inflow boundary condition (sine wave) - to present the hydrodynamics that is happening in the simple unsteady case by showing step by step changes in the flow physics in response to the changes in the unsteady sine wave velocity inflow.

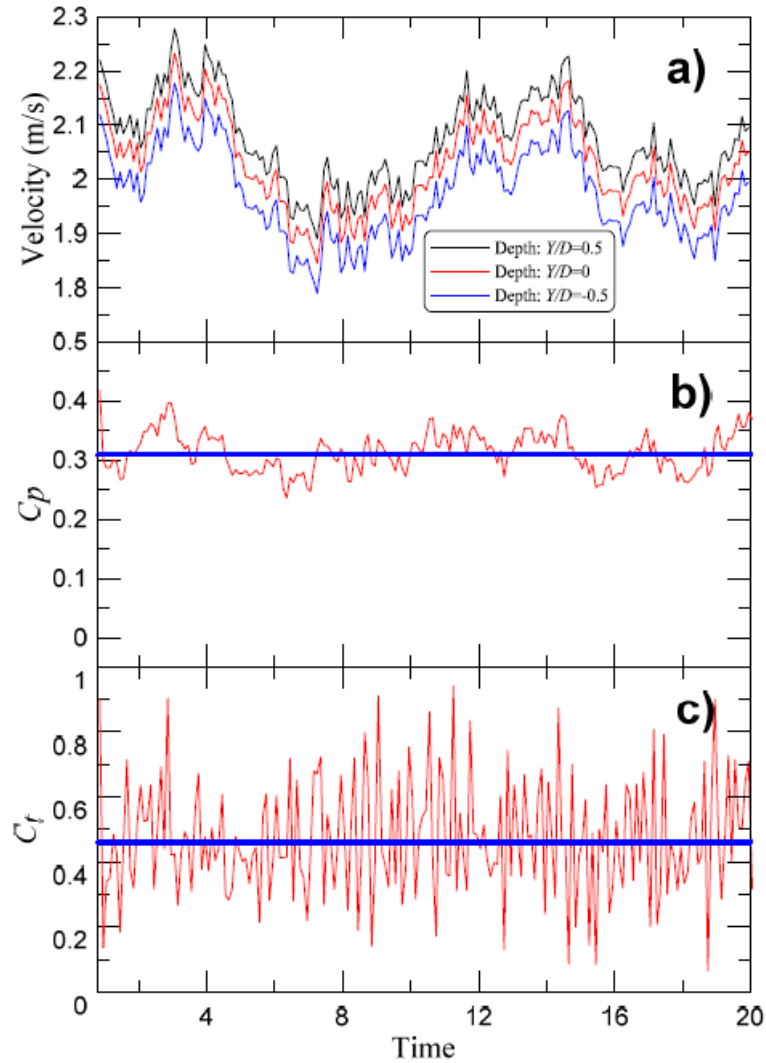


Figure 2.9 Tidal turbine performance in realistic unsteady flow compared with steady state data for the same mean TSR (Leroux *et al.*, 2016)

## 2.8 Summary

This Chapter presents the current literature in the field of tidal stream turbines with emphasis on CFD modelling and the effect of unsteady flow in tidal turbine. It was proven that RANS-CFD has been widely used in tidal stream modelling and even unsteady flow analysis especially in blade loadings as can be seen in the lists of CFD modelling journal and conference proceedings presented in the previous sections of this chapter. It was also shown in this review of current literature that most of unsteady case study in tidal turbines focus on the topic of

device reliability and dynamic loading on tidal turbine blades. In the knowledge of the author of this paper, there are very few literatures that show investigation in the effects of unsteady loadings in the performance of tidal turbines. One of which looks at the effect of surface waves to the turbine's performance (Luznik *et al.*, 2013) and one looking at a model tidal turbine response to a complex real unsteady flow (Leroux *et al.*, 2016). Both presenting only the collective effect of unsteadiness, which was shown to have a negative effect on performance, and not the detailed hydrodynamics of the unsteady flow due to the complexity of the presented inflow boundary condition.

It is true that device reliability and engineering design is the most important part when it comes to devices like tidal turbines but improving the performance of one turbine based on the environment where it is installed is also a crucial step in the development of the said technology. This is the reason why the author of this study has chosen to look at the effect of unsteady flow in a tidal turbine designed in the University of Sheffield using a time-varying idealised velocity profile in RANS CFD. Having an idealised sine wave for the inflow boundary condition was chosen because of its simplicity making it easier to understand the effects of unsteadiness to the performance in unsteady flow and visualise the flow physics in detail. Chapter 5 and 6 of this thesis will present a detailed explanation of the unsteady flow effects on performance through different operating conditions but before that the design phase of the Sheffield HATT will be discussed in Chapter 3 with the numerical model and steady state simulation presented in Chapter 4.

## Chapter 3

# The Design of Sheffield Horizontal Axis Tidal

## Turbine

### 3.1 Introduction

This chapter will explain the design process used to create the tidal turbine used for the succeeding chapters in this research study. The goal for the design is to have a turbine that will maintain a high CP over a variation of TSR – which can be seen as a flatter performance curve when plotted. The reason for this is to accommodate the instantaneous velocity changes that are likely to occur when a turbine is subjected in unsteady flow. The turbine was designed using the turbine blade building function of QBlade, an open source software that also includes XFOIL and BEM capabilities. QBlade validation is shown in this chapter and was later used for the BEM simulation of the turbine's performance curve. The resulting performance curve will then be compared to CFD results in Chapter 4. This chapter also includes the structural design of the turbine which was carried out using ANSYS Composite Prepost (ACP) Module which is an add-on in ANSYS Mechanical. The structural part of the Sheffield HATT design is a collaboration of the author with Dr. Louis Angelo M. Danao, a researcher from the University of the Philippines.

### 3.2 QBlade Validation

The tidal turbine geometry that was generated to form the design of the turbine used in this research was designed with the aid of QBlade (Wendler *et al.*, 2013). QBlade is an open-source (wind/tidal) turbine design software that includes a blade geometry building function as well as Blade-Element Momentum (BEM) solver for calculating the performance of turbines.

QBlade includes the XFOIL code which has the capability to simulate the hydrodynamic properties of a hydrofoil performance at defined flow conditions. It can estimate full 360° polar from XFOIL results using either Montgomerie (Montogomerie & Forkningsinstitut, 2004) or Viterna (Viterna & Corrigan, 1982) extrapolation techniques. The polar data generated is then used within the rotor BEM solver to produce performance data for the designed blade.

The first step in using QBlade was to validate the hydrodynamic polars generated by XFOIL, hence a case study using the NACA 4412 profile was conducted. XFOIL formulation is a linear vorticity stream function panel method that includes a viscous boundary layer solution which interacts via a surface transpiration model. The lift coefficient curve for the NACA 4412 was generated using XFOIL for a range of  $-15^{\circ}$  to  $18^{\circ}$  at Reynolds number of 250,000 to match an experiment by Pinkerton (Pinkerton, 1938). Figure 3.1 shows the plot of the XFOIL generated data against Pinkerton's experimental results. The correlation between the two plots is generally acceptable although an over prediction of QBlade's results can be observed for angles of attack greater than  $10^{\circ}$ . The flow after this point will be harder to predict because of flow separation and turbulence.

Another parameter in QBlade simulation that has been investigated is the number of nodes used in the models. The effect of node density was inspected using two different hydrofoils: NACA 4412, NACA 4424. The first one was intended to be located at tip of the turbine blade design since it has higher lift to drag ratio while the other was to be placed in the root because it is thicker and will be suitable for the blade's structural design. The simulated results for both hydrofoils are presented in Figure 3.2. It can be seen that a surface node of 200 is sufficient enough for node independent numerical simulations as it displayed minimal difference on  $C_l$  values compared to the curves with 300 nodes. The resulting  $C_l$  curves for the 100 surfaces node also showed good correlation with the 200 and 300 nodes curves although discrepancies can be observed in regions with high angles of attack. This means that the

solution with this number of nodes is not node independent as it cannot capture the effects of adverse pressure gradients resulting to flow separation.

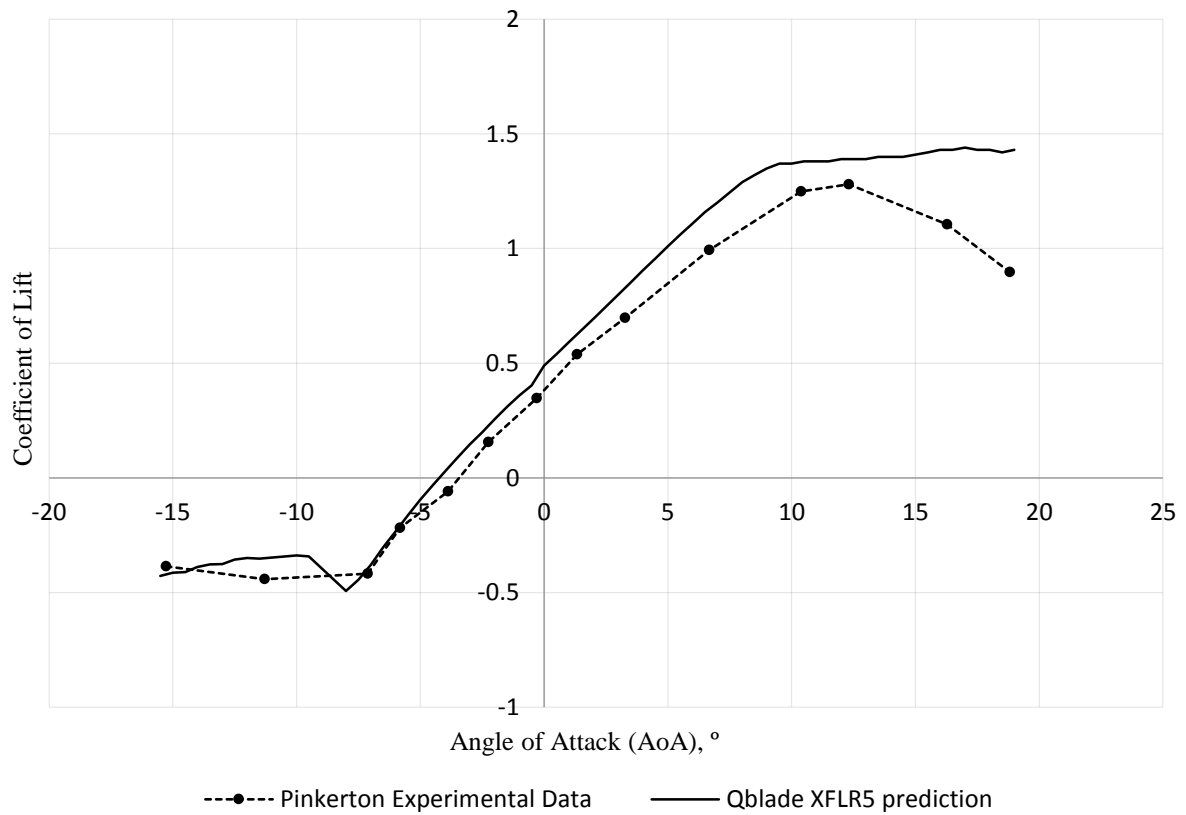
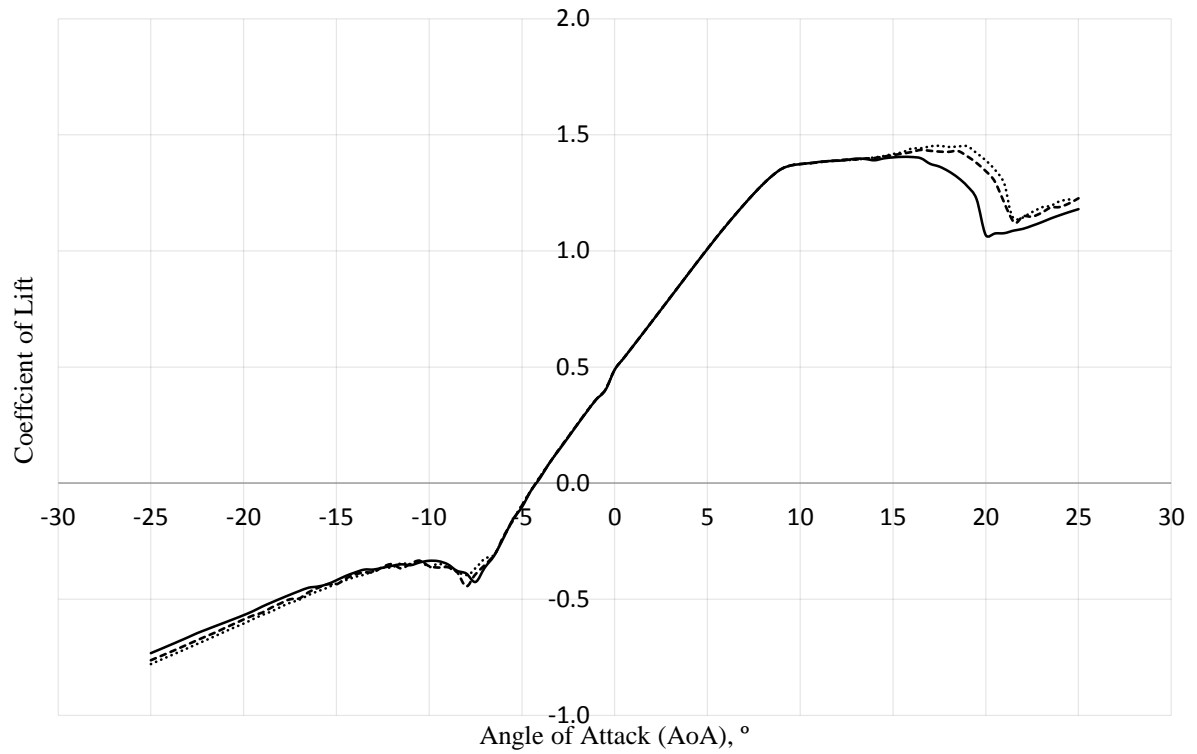
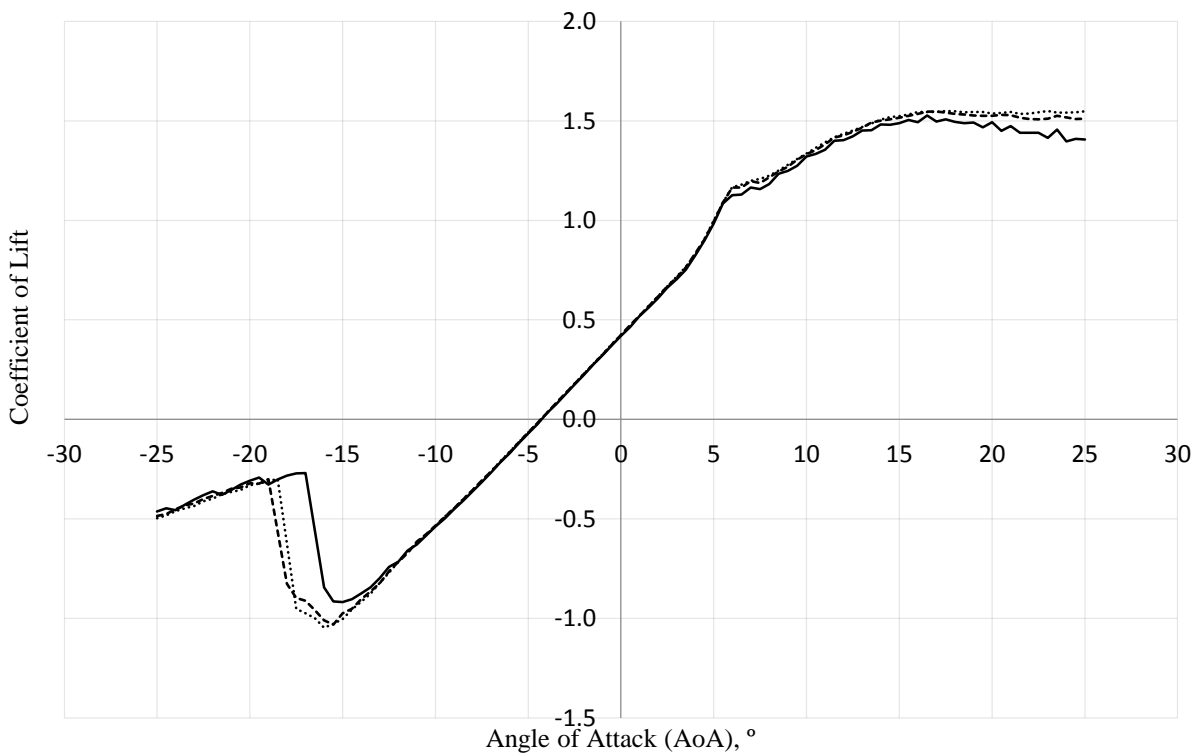


Figure 3.1. XFOIL predicted lift coefficient for NACA 4412 at  $Re=250,000$  versus experimental data gathered from Pinkerton *et al.* (Pinkerton, 1938) for AoA between  $-15^\circ$  to  $18^\circ$



..... 4412 300    - - - - - 4412 200    ——— 4412 100



..... 4424 300    - - - - - 4424 200    ——— 4424 100

Figure 3.2. Results of the node density study for NACA 4412 (top) and NACA 4424 (bottom) at  $Re=250,000$  with AoA from  $-25^\circ$  to  $25^\circ$

The next step was to test the blade element momentum (BEM) solver of QBlade. This was carried out by validating the results with the experimental data of Bahaj *et al.* (Bahaj *et al.*, 2007). The blade used in the experiment has a geometry composed of NACA 63-8xx foils with NACA 63-824 at the root and NACA 63-812 at the tip. The rotor performance curves (CP vs TSR) in the reference were compared with the results of the QBlade simulations as shown in Figure 3.3. The rotor was simulated for two pitch angles at 20° and 25° over a TSR range of 2 to 10. These pitch angles were chosen by the Bahaj group with the 20° pitch as the optimum pitch angle. As can be seen in the plot, there is satisfactory agreement between the two sets of data. The general trend of the experimental plot was captured by the QBlade simulation. There is some under prediction especially for low TSRs where higher AoA on the blade is expected, making the performance harder to predict because of possible flow separation. Overall, QBlade shows a good prediction of the rotor performance and is deemed acceptable to be used as a design tool.

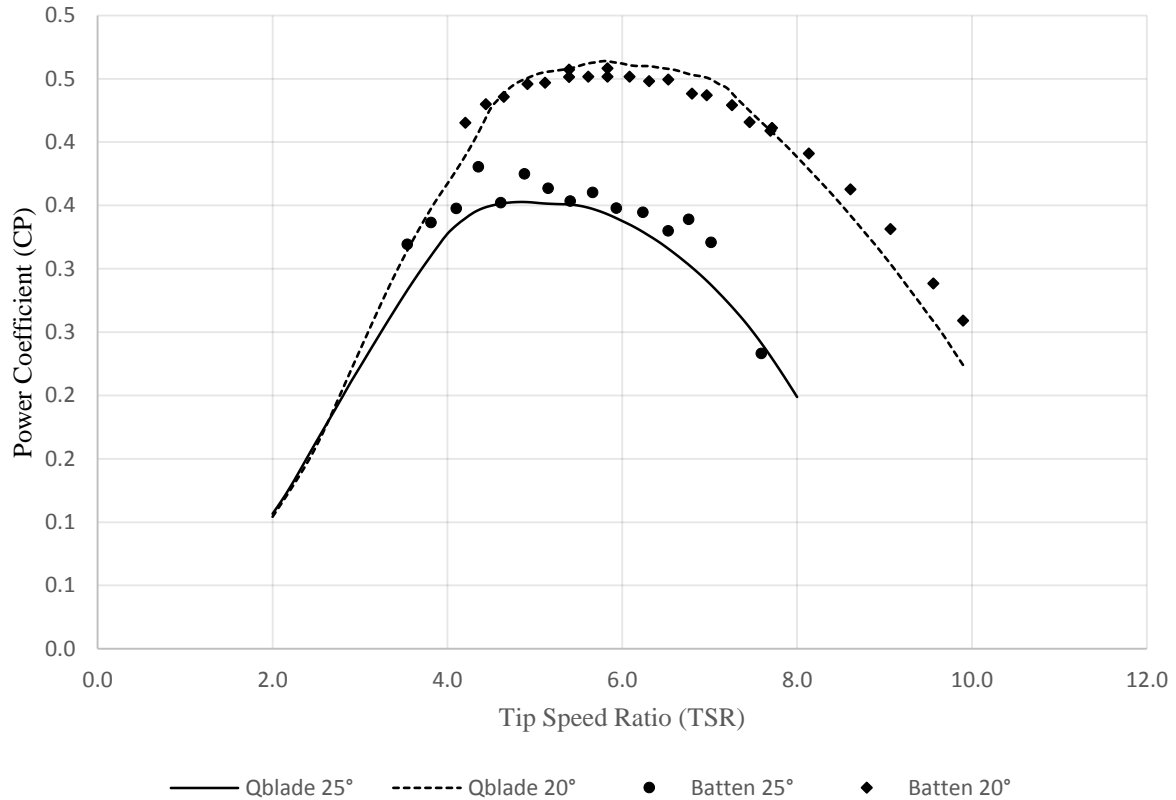


Figure 3.3. Comparison of performance curves from the QBlade BEM results and experimental data for the Bahaj *et al.* (Bahaj *et al.*, 2007)

### 3.3 Sheffield Horizontal-Axis Tidal Turbine

The author of this thesis is currently funded by the government of the Philippines through the University of the Philippines Engineering Research and Development for Technology's (ERDT) Faculty Development Grant. In line with this, a current project in development phase is looking at the deployment and testing of tidal turbine prototype in the waters of the Philippines. The Sheffield HATT designed in this thesis can be used as one of the prototype that will be tested in the Philippines after the completion of the research.

The design aim for the Sheffield HATT was to achieve a flatter turbine performance curve (power coefficient versus tip speed ratio) as compared to the tidal turbine used by Bahaj (Bahaj *et al.*, 2007) and an iterative process was used to determine the most suitable profiles to achieve this. The reason for this target was to have an advantage in unsteady flow where turbine

rotates at a constant RPM but the water velocity changes (and so TSR) – and so to maintain higher performance over a wider range of TSR. Since there is changes in the inflow velocity if the flow is unsteady with respect to time, it is better for the new turbine to have a turbine performance curve that will maintain a higher CP even if there is changes in the TSR. This is based on the type of location the turbine was intended to be deployed. Tidal power resources in the Philippines are located in shallower waters and channels where there are abrupt changes in water flow velocity. Having an advantage and understanding of the turbine's response in this kind of water flow will then be an important parameter to succeeding designs in the future. This of course depends on the rotational frequency of the turbine and the frequency of the flow's unsteadiness, *i.e.* the reduced frequency, as well as unsteady flow amplitude.

The resulting design is a 2 meter three bladed HATT that uses NACA 44xx series aerofoil across the span of the blade. The length of the turbine was chosen referring again to the prototype testing that will be used for the development of tidal turbines in the Philippines. This study can be used as a reference to any changes that will be adjusted for the future iterations of the tidal turbines that will be employed in the Philippines. The NACA 44xx series was chosen for its high lift to drag ratio and its consistency at various Reynolds number. The aerofoil was recommended for tidal turbine operations by Meyers (Myers, 2005) and was also used in previous designs of Marine Current Turbine's Seaflow project. NACA 44xx series also shows good performance even at post-stall AoA which can be useful for extreme operating conditions for unsteady flow (Ostawari & Naik, 1985). The effect of camber and location of maximum thickness was also investigated shortly. Foil profiles such as NACA 43xx, 42xx, 34xx, and 54xx was used in the blade design together with the NACA 44xx blade. Performance curves resulting from initial BEM simulation at  $Re=1,500,000$  is presented in Figure 3.4. These performance curves were simulated using the BEM function of QBlade and altering the foils used for the Sheffield HATT. The NACA 54xx series blade has the highest CP but has a slightly

pointed performance curve. The NACA 44xx blade was still preferred because it has a relatively higher max CP (second to the NACA 54xx blade) and wider curve for TSR range from 3 to 9. The final geometry specifications are presented in Table 3.1 and the design image of the rotor blade is presented in Figure 3.5.

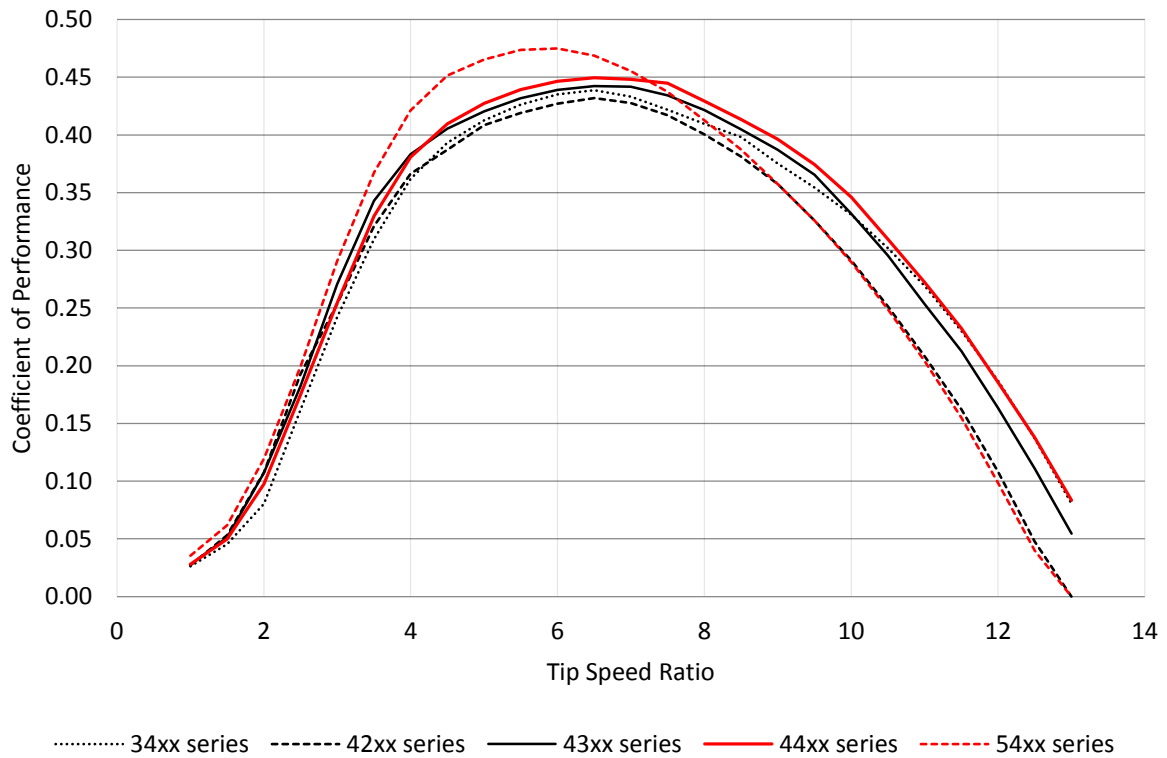


Figure 3.4 CP vs TSR curve comparison for different NACA series showing the effect of camber and location of maximum thickness to the turbine performance at  $Re=1,500,000$

Table 3.1  
Sheffield HATT Geometry Specification

Radial Position (m)	Chord Length (m)	Twist (°)	Foil Profile
0.4	0.25	20	NACA 4424
0.6	0.2312	14.5	NACA 4420
0.8	0.2126	11.1	NACA 4418
1.0	0.1938	8.9	NACA 4417
1.2	0.175	7.4	NACA 4416
1.4	0.1562	6.5	NACA 4415
1.6	0.1376	5.9	NACA 4414
1.8	0.1188	5.4	NACA 4413
2.0	0.1	5	NACA 4412

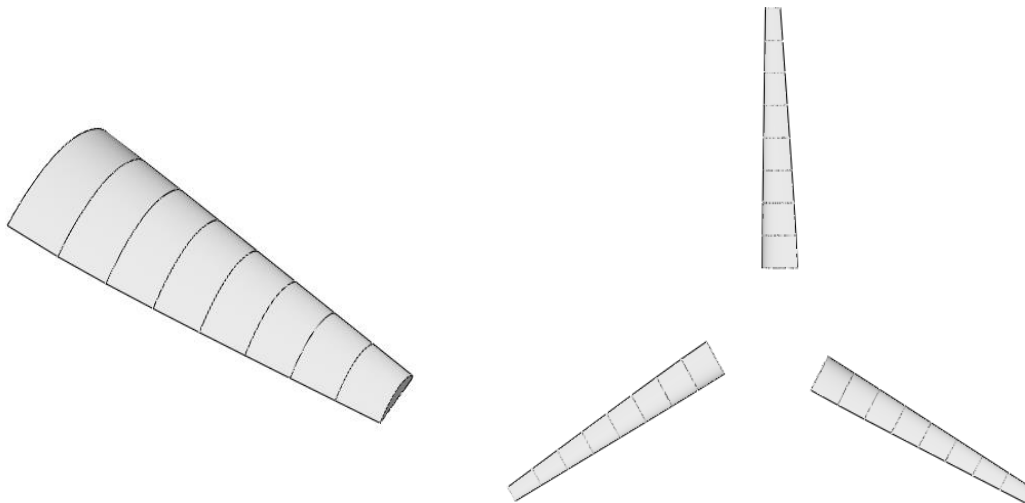


Figure 3.5 Sheffield HATT model from the turbine building function of QBlade

QBlade's BEM function was used to simulate the turbine performance curve of the Sheffield HATT and compare it with that of the Batten model under the same operating condition with incoming water speed of 2 m/s over a TSR range from 2 to 10. The Xfoil function of QBlade was used to gather the lift and drag data for each hydrofoil sections and the 360° polar Montogomerie extrapolated method is used. Data from Xfoil was loaded in the BEM

function of Qblade using the resulting design of the Sheffield HATT. The resulting performance curves are plotted in Figure 3.6. The Sheffield HATT performance curve maintained a CP value of over 40% from TSR range of 4 to 9 with maximum CP of 47% at TSR=6. This shows a slightly higher performance curve over a wider range of TSR value as compared to the Bahaj and Batten (Bahaj *et al.*, 2007)(Batten *et al.*, 2007) The Sheffield HATT configuration defined in this section will be used for all succeeding simulations that will be included in this thesis.

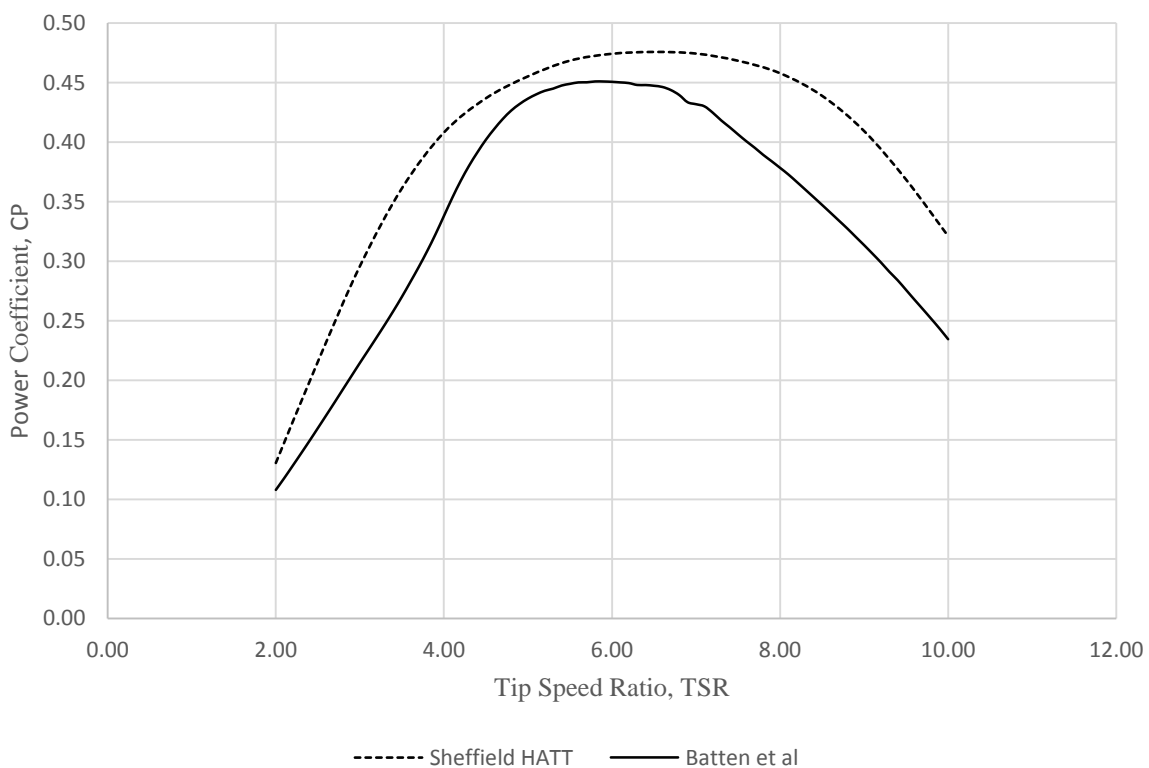


Figure 3.6 Performance curve comparison of the Sheffield HATT model.

### 3.4 Sheffield HATT Structural Response Study

The rotor blade designed in the previous section provides the outer geometry for the turbine, but to create a full turbine rotor blade capable of being manufactured, a good structural design is required for the rotor. This is particularly important since the expected loads on the

blades are significantly high due to the density of seawater and a well-designed blade has to be both efficient for energy conversion and structurally sound for extended operation under extreme condition. This is again in line with possibility that the new design will be used as a prototype in future projects in the Philippines therefore a good initial structural design should be established. This part of the thesis is a collaboration with Dr. Louis Angelo M. Danao, a colleague of the author from the University of the Philippines.

### **3.4.1 Numerical verification and validation of FEA model**

There is an absence of structural performance data in current literature a twofold validation approach was used in this study. The first step will be the FEA analysis conducted on a simple cantilevered ellipse that has similar length and thickness as the Sheffield HATT rotor blade using ANSYS Mechanical. This is to serve as validation to the method being used as the results of the FEA analysis can be compared to analytical solution structural mechanics. Once the numerical method is validated, it will be applied to the Sheffield HATT blade design whereas the analysis and critical parameters are investigated. The structural methodology was first done by Dr. Danao and has been replicated by the author for the tidal turbine being used in this project. All of the analysis presented in this chapter is also done by the author.

A numerical verification study was conducted on the elliptical tube model. The ratio of the minor diameter to the major diameter of the ellipse is matched to the ratio of the thickness to chord of NACA 4424, the thickest profile section on the blade. The chosen major diameter for the ellipse is 0.25 while the minor diameter is 0.0625 which has a ratio of 0.25. The shell thickness was set to be 0.005m which is 2% of the ellipse's major diameter similar to the 2% of the blade root chord. The length of the cantilevered beam was chosen to be 1.8m which is chosen to imitate the length of the Sheffield HATT blade, which is 1.6 m., plus the length of the connector to the hub where it is fixed which is assumed to be the additional 0.2 m. One end

of the elliptical tube was assigned a fixed support to make it similar to the fixed rotor blade in the hub of the turbine. The material chosen is isotropic in nature with properties close to fiberglass composite, with Young's Modulus  $E = 20\text{GPa}$  and density  $\rho = 1,850\text{ kg/m}^3$ . (MatWeb, 2015)

Since the blade loading data exported from the BEM simulation in QBlade are point loads and not line load, the loading used in for the elliptical tube study was chosen to be a 500 N/m distributed load but approximated as point loads along the span of the blade as shown in Figure 3.7. The exported blade loading from QBlade will be used for the FEA study of the blade itself and will be presented later in this chapter. Verification of the results is carried out by comparing the maximum Von Mises stress and the beam tip deflection against analytical solutions offered by Budynas et. al. (Budynas, Nisbett, & Shigley, 2015). A further study using an elliptical tube with a web along the minor diameter is presented in a later section. This simulates an actual blade with a stiffener along the span.

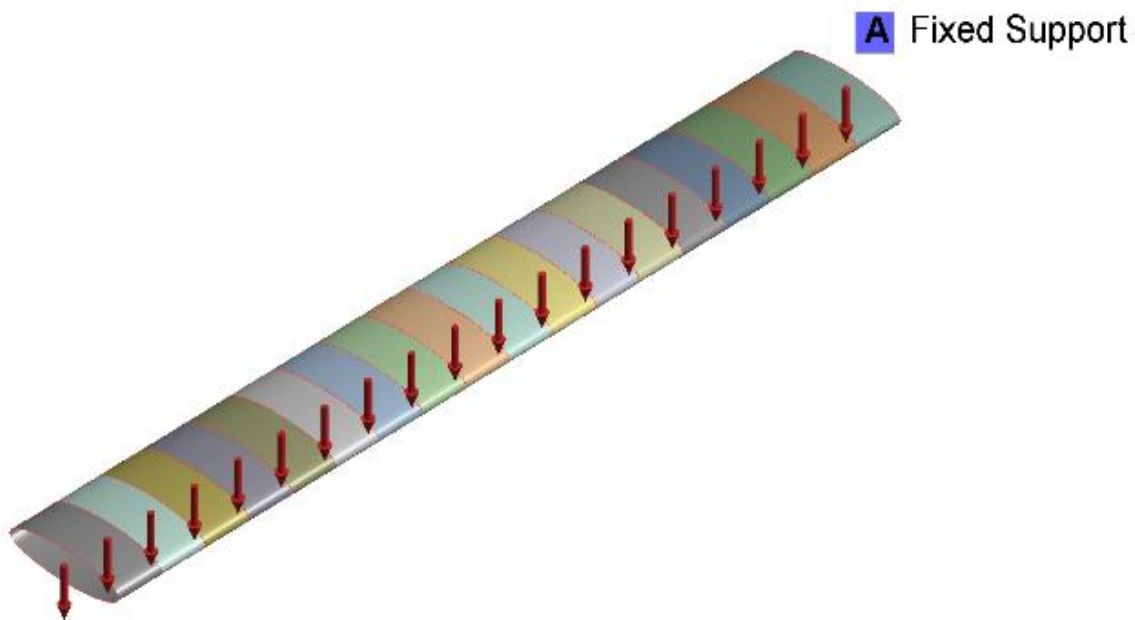


Figure 3.7. Illustration of beam with distributed load approximated by multiple point loads

### 3.4.2 Cantilevered Elliptical Tube: Mesh Density Study

Mesh density sensitivity analysis was performed to determine the appropriate node density on the model. The model surface mesh was restricted to quad elements using the mapped face mesh control. The element properties that were varied for the study were maximum element face size and minimum element mesh size as these two properties define the coarseness of the mesh. From Table 3.2, it can be seen that at the coarsest mesh level, the predicted maximum Von Mises stress is 22.052 MPa with a beam tip deflection of 25.029 mm. As the mesh is refined by reducing the element face size twice over, the values of Von Mises stress and tip deflection only slightly change with increased number of elements. At the finest mesh level, the maximum Von Mises stress is computed as 22.603 MPa and the tip deflection is 24.997 mm. As such, model 2 has been chosen as the appropriate mesh level to be used for succeeding investigations.

Table 3.2  
Mesh Settings and FEA Results for the Numerical Verification of Ellipse Tube Model

	<b>max face size (mm)</b>	<b>min mesh size (mm)</b>	<b>number of elements</b>	<b>Max Von Mises stress (MPa)</b>	<b>tip deflection (mm)</b>
model 1	100	2	23,995	22.052	25.029
model 2	50	1	56,463	22.487	25.021
model 3	25	0.5	87,148	22.603	24.997

Model 2 results are compared to analytical solutions of the same problem using expressions from Budynas et. al. (Budynas, Nisbett, & Shigley, 2015) From classical mechanics, the beam problem can be analysed using linear elastic, small displacement assumptions. This approach is particularly accurate for structural problems involving steel and similarly stiff materials. Additionally, shear effects can be assumed negligible when the aspect

ratios of beams are high and the dominant load is bending. As such, the critical point in a cantilevered beam is at the support where maximum bending loads are experienced. The state of stress of the critical point reduces to a single normal stress component directed along the span. This stress component is effectively the maximum principal stress and the Von Mises stress.

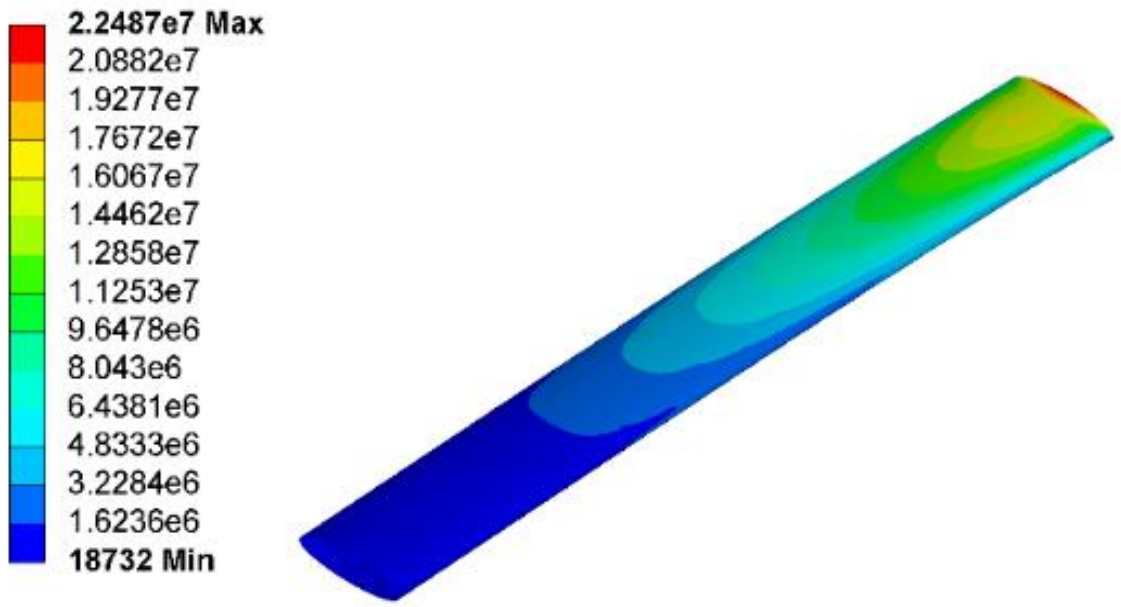
Table 3.3  
Comparison of Numerical and Analytical Model Results for Ellipse Tube

	<b>Von Mises stress (MPa)</b>	<b>tip deflection (mm)</b>
model 2	22.487	25.021
analytical	19.601	25.404

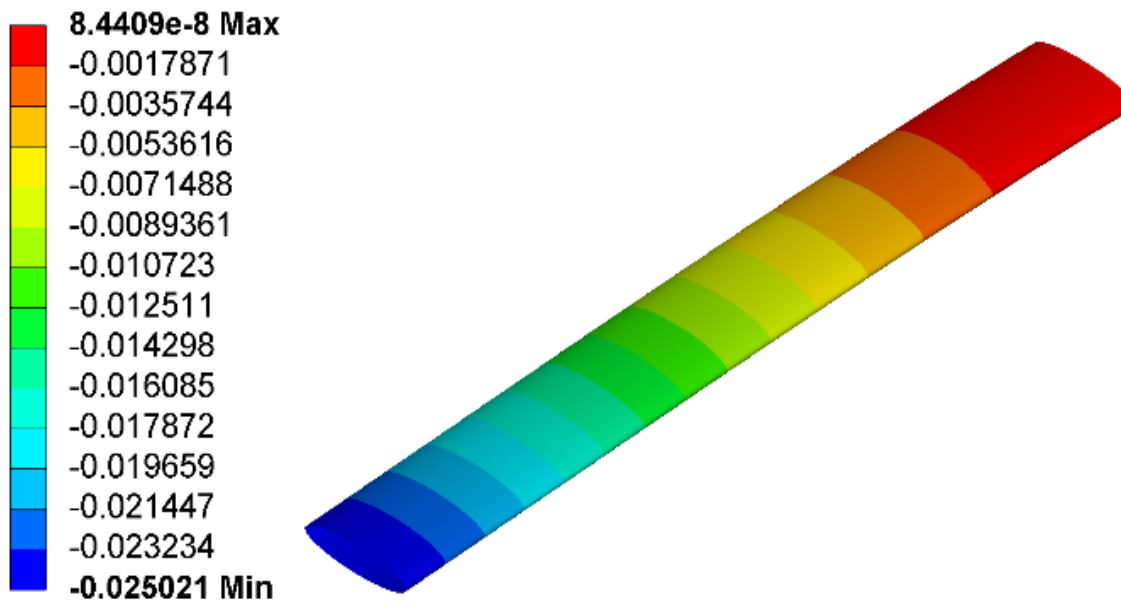
Table 3.3 shows the results of the verification study. There is an observed difference in the computed Von Mises stress between numerical and analytical models. This may be due to several factors. One factor could be the approximated distributed load in the numerical model versus the ideal distributed load in the analytical model. Another factor could be the computation of the second moment of inertia for the analytical model which was assumed to be the second moment of the elliptical area minus the second moment of the smaller elliptical area (the hole is approximated as with major and minor outer radii less the shell thickness). Lastly, the analytical model assumes linear, small displacement theory while the numerical model includes shear and other non-linear effects in the analysis. Given all the possible factors for the difference, the results still show comparable values of stress and deflection within acceptable limits of variation.

Figure 3.8a shows the location of the maximum Von Mises stress on the tube which occurs on the fixed support within the minor diameter location as expected. Not shown is the bottom portion of the same section where the magnitude of the Von Mises stress is close to the maximum value of 22.487 MPa. The minimum value of Von Mises stress is 18.732 kPa near

the free end of the beam where there should be no stress to be computed when speaking in analytical perspective. This value is induced but the shear effects of the distributed load making it non-zero but it is relatively small as compared to the other stresses measured at the other sections of the blade.



a.



b.

Figure 3.8 Contours of (a) Von Mises stress and (b) directional-y deflection for ellipse tube.

Figure 3.8b shows the nodal deflection along the y–direction. The computed maximum value is 25.021 mm and is located at the free end. The minimum is practically negligible at 8.44E–9 mm located at the fixed end where no deflection should occur and might be only due to numerical computational errors.

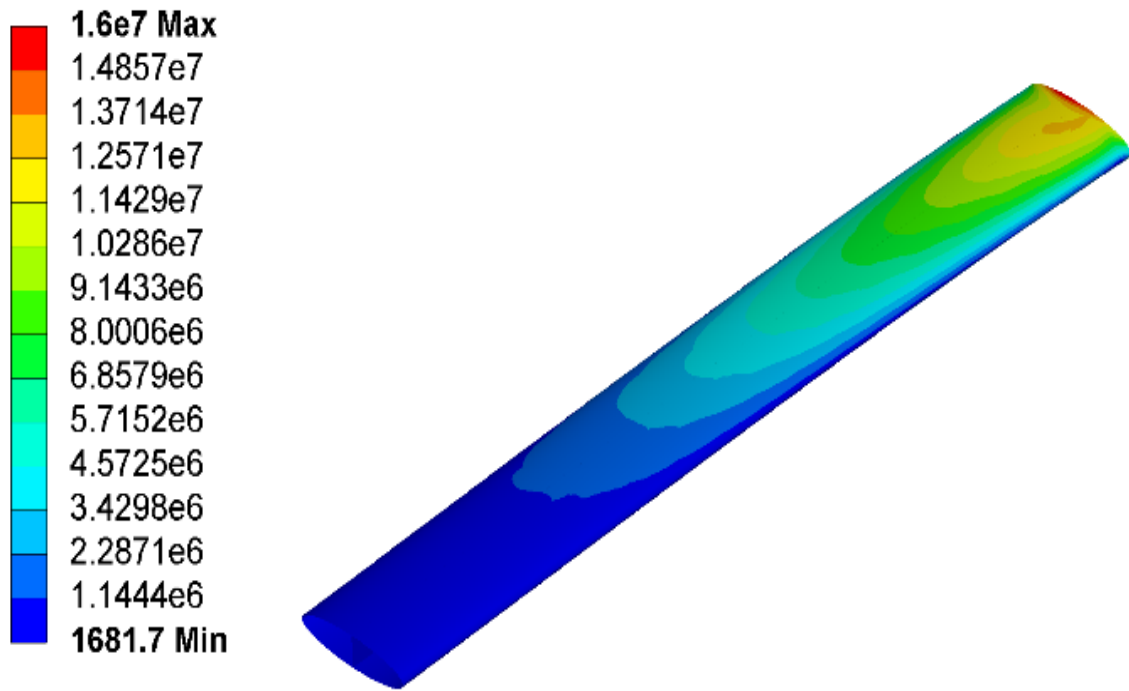
### 3.4.3 Cantilevered elliptical shell with web: Von Mises and tip deflection validation

Another study was carried out to further validate the numerical method. In this, a span-wise web was added to the elliptical tube model described in the first FEA study. This web will add stiffness to the blade and hence a difference in the structural response should change. The purpose of this study is to see if the numerical model is sensitive enough to see the small change applied to the elliptical tube. The web has a thickness of 0.02m which is 8% of the major diameter, all other parameters of the elliptical tube was maintained.

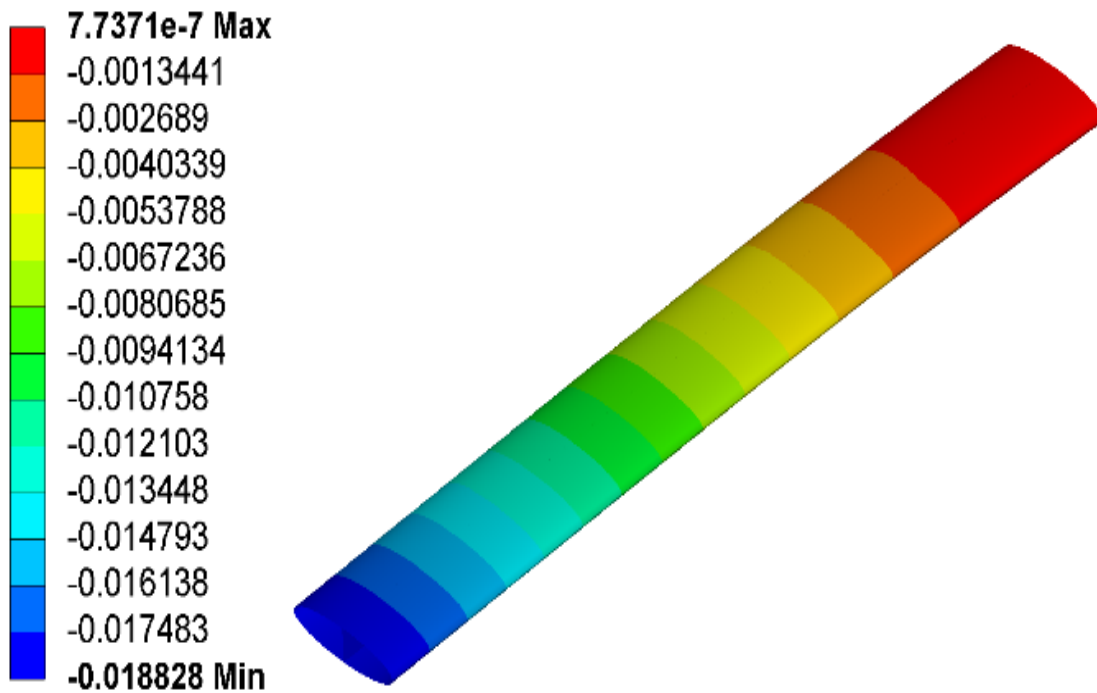
Table 3.4 shows the numerical results against the analytical results. Similar observations are made regarding the difference of the two methods. The FEA results over predict the Von Mises stress versus the analytical computation, the same trend as the previous case. The maximum Von Mises stress is still located at the fixed support end with a value of 16 MPa. The nodal deflection of the free end is computed at 18.828 mm, an under prediction when compared to the analytical value of 19.317 mm. The results are consistent to the previous case where the model 2 maximum deflection is also lower than the analytical prediction.

Table 3.4  
Comparison of Numerical and Analytical Model Results for Ellipse Tube with Web

	<b>Von Mises stress (MPa)</b>	<b>tip deflection (mm)</b>
FEA	16	18.828
analytical	14.905	19.317



a.



b.

Figure 3.9. Contours of (a) Von Mises stress and (b) directional-y deflection for ellipse tube with web.

The contours of Von Mises and directional deflection for the ellipse tube with web case are shown in Figure 3.9a and Figure 3.9b, respectively. The location of highest stresses are at the fixed support end with a gradual tapering of values towards the free end. The computed minimum Von Mises stress is 1.682 kPa and is not at the free end but near it. The actual stress value at the free end, minor radius location is 19.674 kPa. The non-zero stress again was argued to be caused by the shear effects that is present in the FEA and is not considered analytically. The maximum nodal deflection computed along the y direction is 18.828 mm for the free end of the beam while the minimum is near zero for the fixed support end with a computed value of  $7.74E-7$  mm.

Considering the results of the FEA study presented above, it can be concluded that the numerical method can be considered acceptable and accurate enough to be used in the succeeding structural analysis of the Sheffield HATT blade in the following sections.

#### **3.4.4 Numerical Analysis of Sheffield HATT blade (Structural)**

The Sheffield HATT blade was modelled as a shell structure with a constant thickness of 2% of the maximum chord of the blade all throughout. A web running through the quarter chord of each station was included as a stiffener with a thickness of 8% of the maximum chord. To analyse the structural response of the rotor under hydrodynamic loads, only one blade was necessary. The blade force data was extracted from the BEM simulations for both 2 m/s and 5 m/s flow conditions at optimum tip speed ratio of about 6 and are presented in Table 3.5 and Table 3.6, respectively. The 2 m/s flow represents the average flow condition while the 5 m/s flow was assumed for extreme flow conditions.

Table 3.5  
Blade Force Data from BEM Simulation at 2 m/s Flow Velocity

<b>radial position (m)</b>	<b>tangential force (N)</b>	<b>normal force (N)</b>	<b>resultant force (N)</b>
2.0	36.072	418.441	419.993
1.8	121.475	1,036.200	1,043.296
1.6	142.404	1,041.260	1,050.953
1.4	151.030	969.055	980.754
1.2	154.613	860.287	874.070
1.0	155.630	724.558	741.084
0.8	151.657	568.066	587.962
0.6	134.533	393.101	415.485
0.4	40.060	103.387	110.877

Table 3.6  
Blade Force Data from BEM Simulation at 5 m/s Flow Velocity

<b>radial position (m)</b>	<b>tangential force (N)</b>	<b>normal force (N)</b>	<b>resultant force (N)</b>
2.0	317.34	1,138.84	1,182.227
1.8	776.01	2,315.25	2,441.838
1.6	826.44	2,215.30	2,364.436
1.4	848.60	2,046.94	2,215.871
1.2	849.72	1,834.24	2,021.499
1.0	767.82	1,640.95	1,811.702
0.8	765.97	1,419.51	1,612.984
0.6	738.39	1,160.21	1,375.248
0.4	302.46	434.04	529.030

Both the tangential and normal loading forces imported from the BEM simulation was applied to the Sheffield HATT surface at each defined section location as “Remote Forces”. This means that the forces were not applied directly on the blade to avoid local stress concentrations but rather they are assumed to be forces caused by a source that is away from the blade. These forces were applied to the quarter chord location at each defined sections assuming this point to be the aerodynamic centre. The resultant loads for each station are automatically computed by the software and are presented in Figure 3.10. To introduce centrifugal effects in the simulation, a rotational velocity was imposed on the blade. This is added for completeness but is likely to have little effect on the overall results.

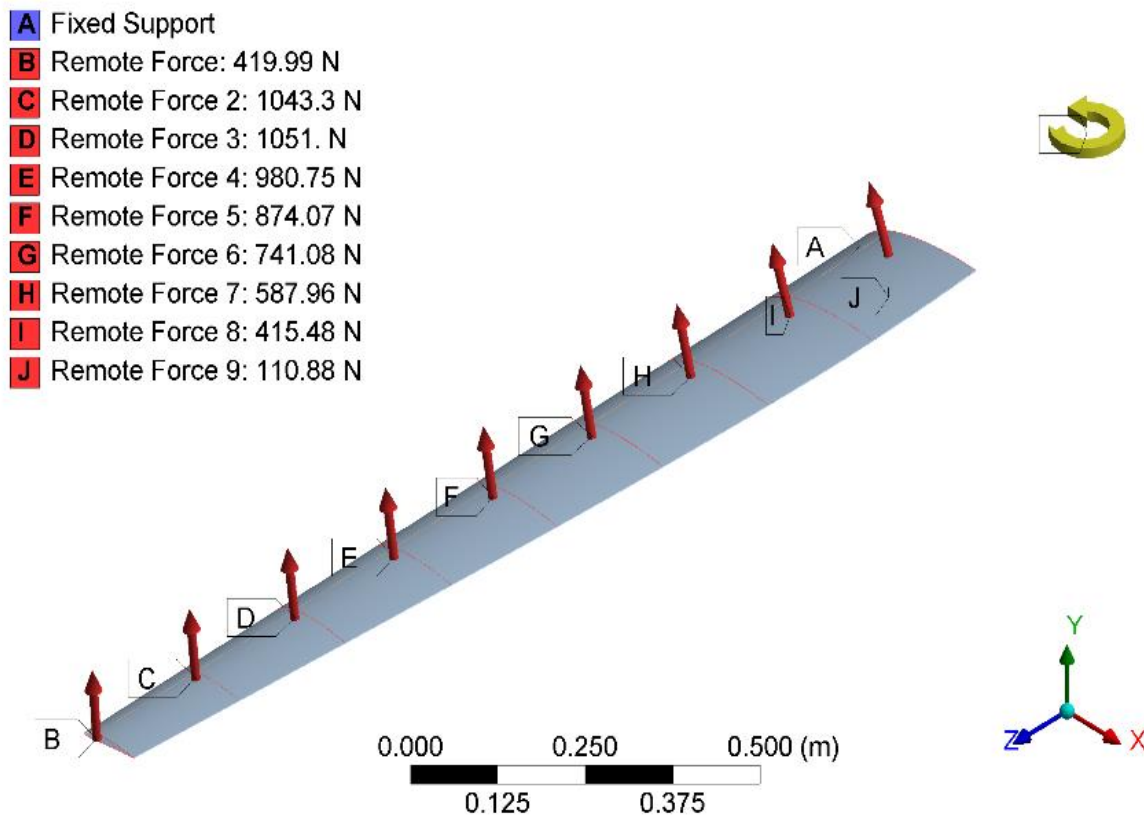


Figure 3.10 Loads derived from the BEM simulation for the 2 m/s flow as applied on the blade.

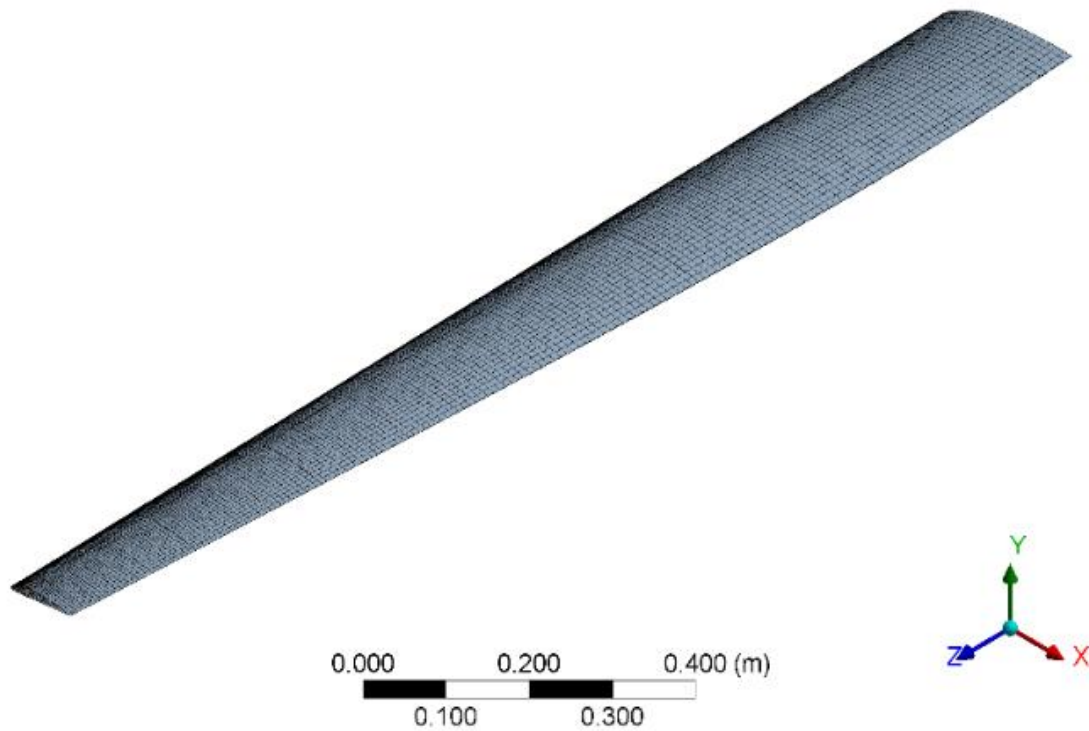


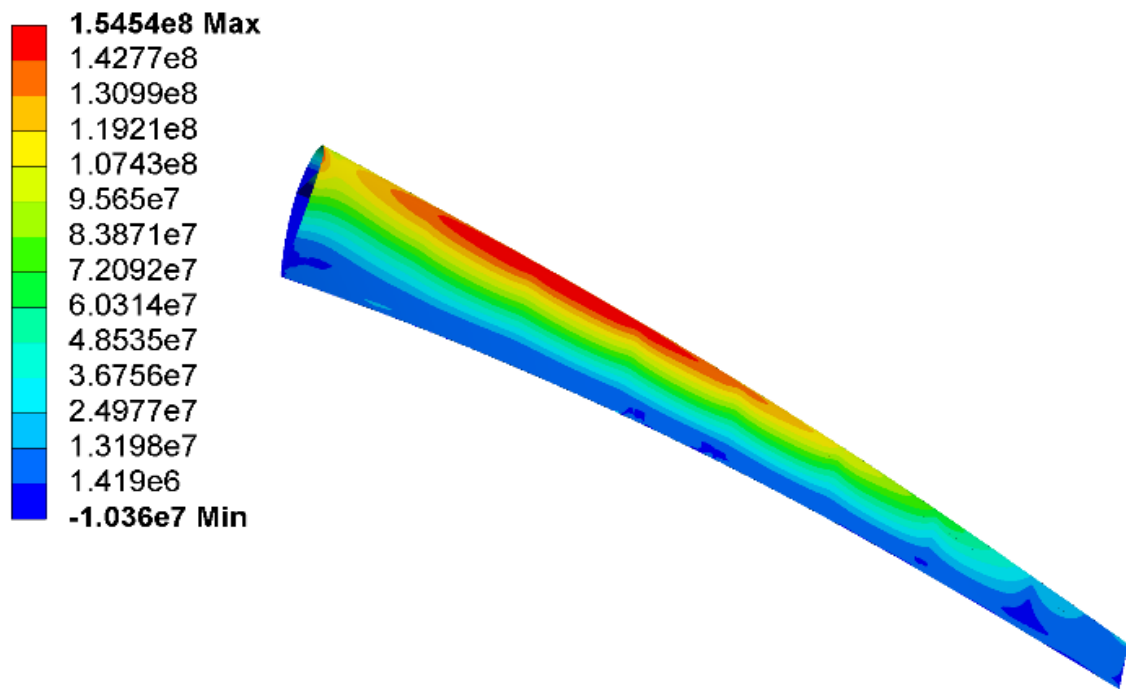
Figure 3.11 Mapped face mesh on the blade.

The same meshing techniques applied for the elliptical tube was used to mesh the Sheffield HATT Blade. The meshing parameters was based on model 2 of the elliptical tube FEA study. Figure 3.11 shows the mapped mesh face of the Sheffield HATT blade where the quad elements formed were presented as well.

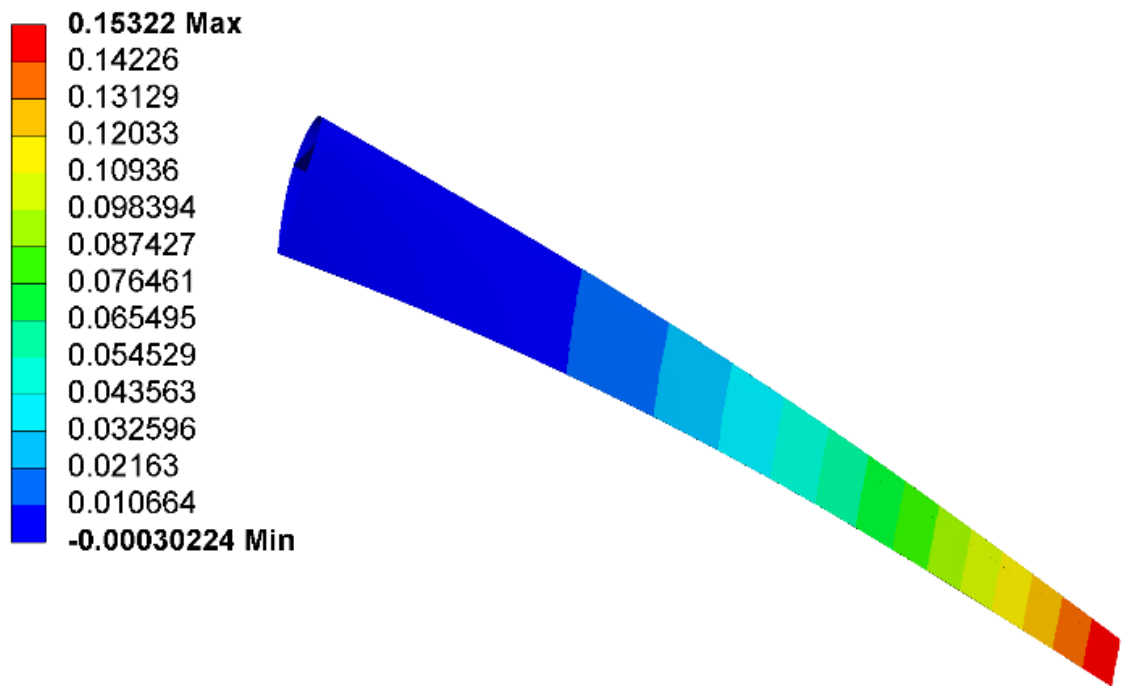
### **3.4.5 Isotropic analysis: maximum principal stress and tip deflection**

The first step for the analysis of the structural response of the turbine is to determine a material to be used where the stress levels will be compared to. The initial material chosen was an isotropic material from ANSYS Composite PrepPost (ACP) module with elastic modulus  $E = 45 \text{ GPa}$  and tensile strength at  $1,100 \text{ MPa}$  (ANSYS) to match the material that will be used later in the orthotropic analysis presented in the next section. The material was chosen to be isotropic so that the FEA results can be a quick comparison to the material strength.

The results of the FEA study for the Sheffield HATT using the material presented above was shown in Figure 3.12. The maximum Von Mises stress is computed to be  $154.54 \text{ MPa}$  which is located at about 25% to 35% location of the blade span from the root near the leading edge of the turbine. The location of the maximum Von Mises stress might be due to the abrupt change in aerofoil thickness near the root of the blade. The hydrofoil thickness was 24% at the root then 20% and 18% for the next two sections over a 0.2m interval, the succeeding sections has gradual decrease in thickness of 1% change per 0.2m interval. The value of the maximum Von Mises stress is within the ultimate tensile strength of the material and has a factor of safety of 7.11. Figure 3.12b shows the deflection of the blade where the maximum value is located at the tip with a deflection of  $153.22 \text{ mm}$ . This deflection is 8.5% of the total blade length. For the extreme case with water speed of  $5 \text{ m/s}$ , the maximum principal stress was recorded to be  $350.1 \text{ MPa}$  with a maximum deflection of  $355.76 \text{ mm}$ . While the loading is still within the tensile limit for the material being used, the F.S. for the extreme case is only 3.14.



a.



b.

Figure 3.12 Isotropic analysis of HATT blade: (a) Von Mises stress, (b) nodal deflection along y-direction

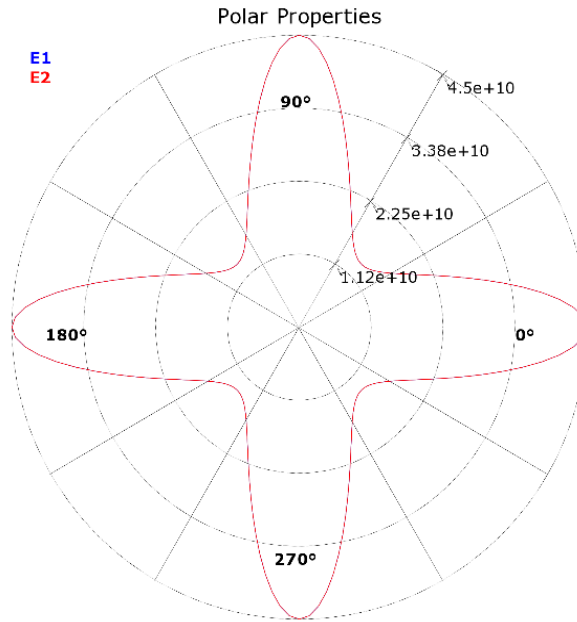
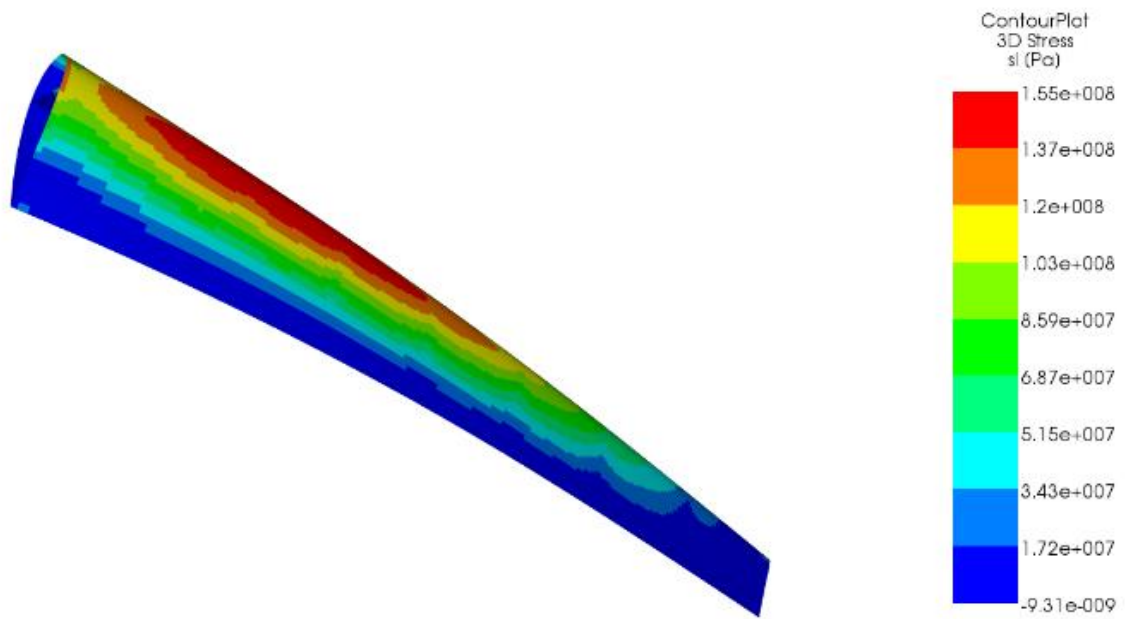


Figure 3.13 Orthotropic elastic modulus of E-Glass reinforced Epoxy

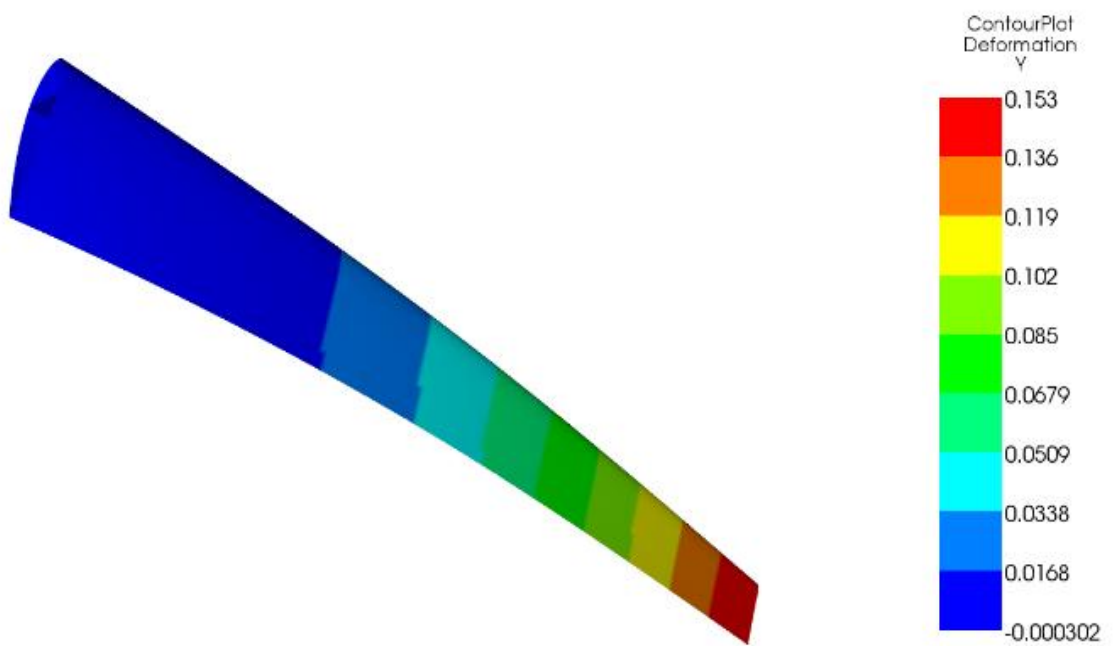
### 3.4.6 Orthotropic analysis: maximum principal stress and tip deflection

The next step is to look at how the numerical model of the Sheffield HATT Blade will respond to the same loading but this time using a composite material which will represent a more realistic model of the blade. The ANSYS Composite PrepPost (ACP) module was used where the pre-processor allowed the design of a composite fabric layup on the model with specifications on ply thickness, ply angle, fabric stack up and the material itself. The chosen material for the blade is E-glass reinforced epoxy that has a unidirectional properties. The material applied to the blade was an edited version with the orthotropic strength properties and elastic modulus with polar plot shown in Figure 3.13.

The maximum elastic modulus of the material has a value of 45 GPa along the perpendicular directions following the fibre direction. The ply angle was set to lie along the fibre direction (0 to 180° line). This will result to a composite material with fibres perpendicular to each other which will result to the configuration with the lowest maximum stress and minimum deflection.



a.



b.

Figure 3.14 Results of the composite analysis using orthotropic material properties: (a) maximum principal stress, (b) deflection in the y-direction

Figure 3.14 shows the simulation results using the Ansys Composite PrepPost Module. For this study, the maximum principal stress (S1) was monitored instead of the Von Mises stress that was used for the isotropic analysis. It can be seen from Figure 3.13a that the maximum S1 value is 154.2 MPa which is close to the isotropic Von Mises stress. The location of maximum S1 also occurred at the location of maximum Von Mises stress for the isotropic FEA study. The maximum deflection for this orthotropic simulation has a value of 153.14 mm located at the blade tip. Comparing Figure 3.12 and 3.14, it can be concluded that both simulations have comparable stress distribution and maximum deflections across the blade span.

Other ply angles available are at 30°, 45° and 60° and for each of these angles, the same structural analysis to determine the effect of the ply angle and results are presented in Table 3.7. It can be seen that the 0° ply angle shows the lowest maximum principal stress and tip deflection and the 45° ply angle has the worst values. This proves that 0° ply angle is best choice for the turbine.

Table 3.7  
Maximum principal stress and nodal deflection for ply angle variation

Ply angle (°)	Maximum principal stress (MPa)	Tip deflection (mm)
0	154.2	153.14
30	204.1	263.75
45	230.7	309.26
60	210.1	282.63

### 3.5 Summary of Chapter

This chapter has illustrated the methods used for the design of a new tidal turbine, the Sheffield HATT. Validation studies were carried out to show that QBlade, the software used for the BEM simulation, was fit to be used for the numerical approximation of the performance curve of the turbine. The results of the BEM simulation for the Sheffield HATT shows that the new design has succeeded in achieving the objective of a flatter CP vs TSR curve with CP higher than 40% over the TSR range from 4 to 9 with maximum CP of 47% occurring at TSR=6. This has a slightly higher and flatter performance curve than the reference model by Batten *et al.* (Batten *et al.*, 2007).

The numerical study of the Sheffield HATT's structural response was conducted using ANSYS Mechanical. The numerical method was first validated using an elliptical tube with distributed loading. The resulting Von Mises stress and deflection has good agreement with analytical solution confirming that the method is fit for succeeding analysis. The next study was done on the Sheffield HATT blade with spar using both isotropic and orthotropic material properties. The resulting Von Mises stress for the isotropic study has a maximum value of 154.54 MPa located at the leading edge from 25% to 35% span of the blade from the root. This value is well within the yield strength with a factor of safety of 7.11. The maximum deflection was 153.22 mm at the blade tip. A more realistic case using orthotropic Sheffield HATT blade was studied using the same numerical method. The material was chosen to be E-glass reinforced epoxy with fibres span-wise and cross-wise (0° ply angle). The resulting first principal stress was 154.2 MPa at the same location as the isotropic case with a maximum blade deflection of 153.14 mm. The results of both the isotropic and orthotropic structural analysis of the Sheffield HATT proves that the new design has low stress and deformation levels at the normal flow velocity of 2 m/s. For the extreme case of 5 m/s, the maximum stress was recorded to be 350.1 MPa with a max deflection of 355.76 mm.

The next chapter will discuss the formulation of the Sheffield HATT CFD model together with the steady state simulations and methodologies together with the comparison with to the BEM simulation results that are presented in this Chapter.

## Chapter 4

# Numerical Modelling of the Sheffield HATT

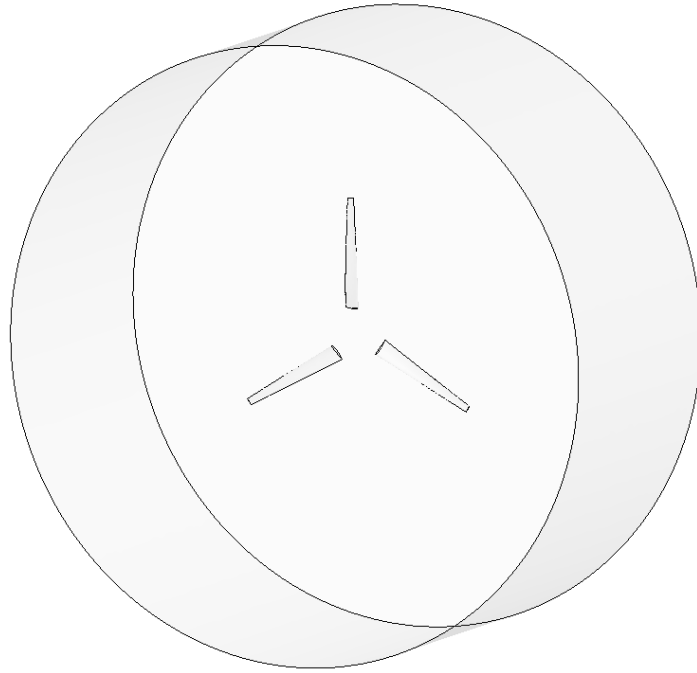
### 4.1 Introduction

This chapter will discuss how the numerical model that will be used for the rest of the thesis was created. Information about the mesh generation will be detailed including parametric studies such as mesh independence and boundary size studies. Steady flow simulations of the mesh were conducted using two turbulence models ( $k-\epsilon$  RNG and  $k-\omega$  SST); resulting performance curves were compared to the BEM results presented in Chapter 3. Analysis and discussions for the steady state results using streamlines and pressure coefficients over hydrofoil sections are also included. This steady state simulation results will serve as the basis for all simulations in the succeeding chapters.

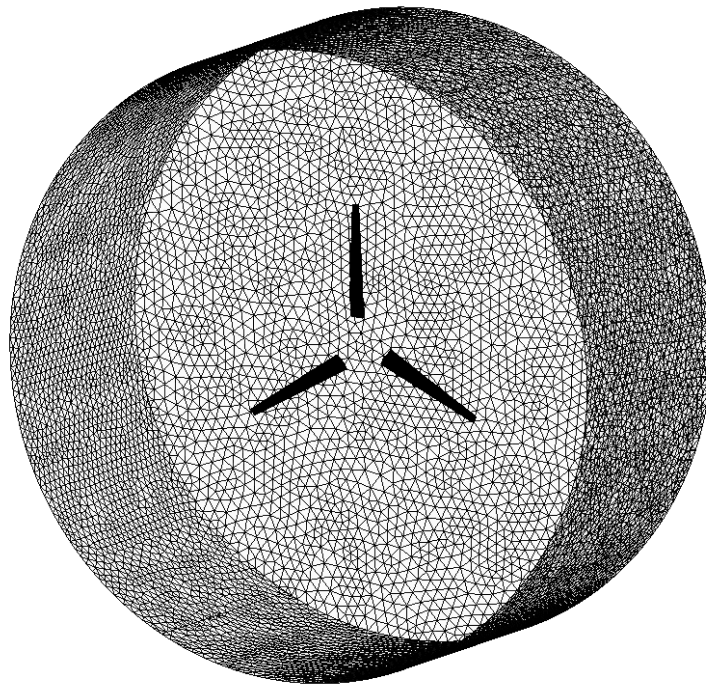
### 4.2 Sheffield HATT CFD Model

A three-dimensional CFD model for the Sheffield HATT was created using the meshing software ANSYS-ICEM. The blade geometry specifications was imported based on the final design that was used for the BEM simulations in Chapter 3, blade surfaces were generated and the three bladed rotor was built afterwards. The turbine was then enclosed in a cylindrical domain, 2.5 times the rotor diameter, which will serve as the rotational part of the mesh as shown in Figure 4.1a. Unstructured tetrahedral mesh is then produced from the surface of the blade to the cylinder using the unstructured mesh generator included in ANYSYS-ICEM. Unstructured mesh is favoured to make the mesh generation process simpler in the expense of being more memory demanding. Prism layers are grown from the blade's surface to capture the boundary layers near the aerofoil sections of the blade. Since the flow conditions that will be simulated using this mesh will be fully turbulent,  $y^+$  values greater than 30 was the basis of

computing the first cell height of the prism layer – this is to have the first cell in the log-layer or the fully turbulent region that is necessary for Standard Wall Functions (SWF). In terms of the mesh quality, the minimum mesh angle for all of the meshes was maintained to be greater than  $18^\circ$  as it is the threshold for ICEM. The target value for the equiangle skewness for ICEM was 0.5 which will result to a 0.5 skewness in FLUENT (skewness in FLUENT =  $1 - \text{skewness in ICEM}$ ) which requires a value less than 0.8 for accuracy and convergence. The minimum quality of the mesh was at 0.34 which is higher than the suggested value in ICEM and FLUENT at 0.3. The resulting mesh for the rotational domain is shown in Figure 4.1b while cut-plane mesh for the 25% and 75% span of the blade is presented in Figure 4.2. The boundary condition for the blade surface was set to be non-slip wall while the extent of the surface of the rotational domain was set to be interface as they will be appended to the outer boundary of the mesh that will be described next.

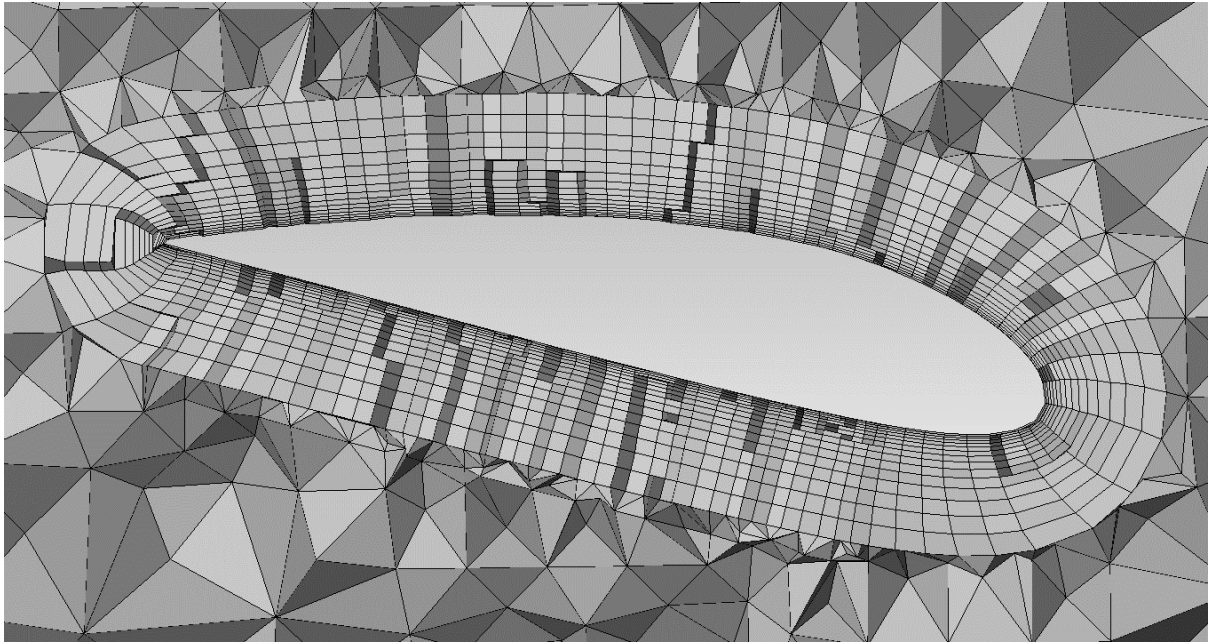


(a)

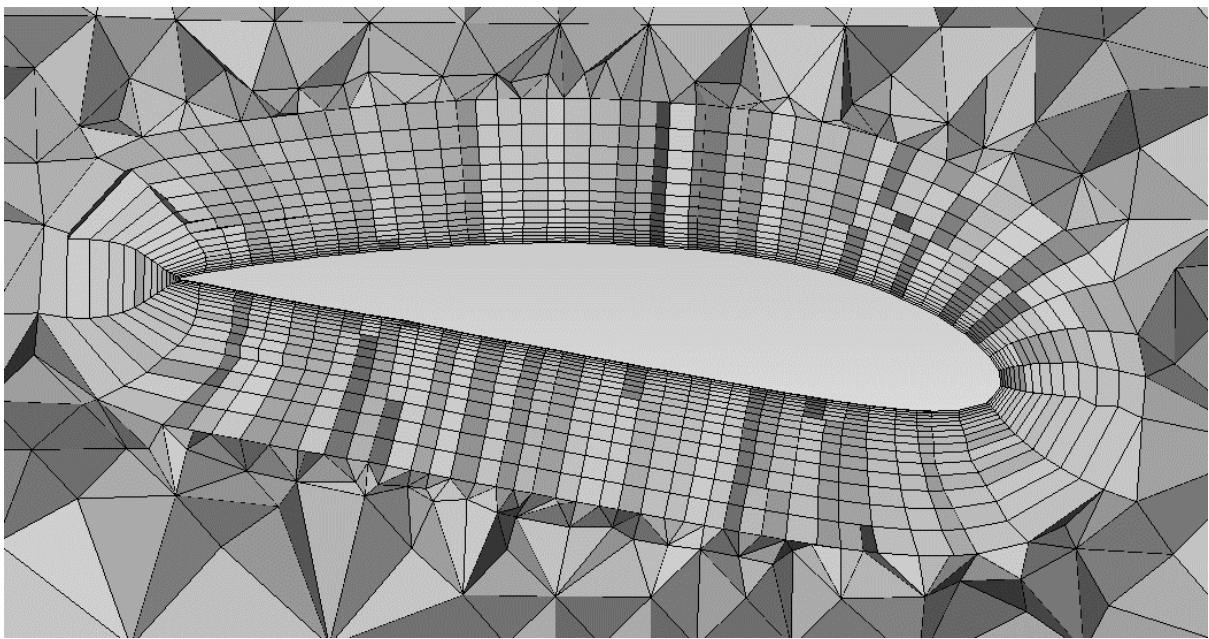


(b)

Figure 4.1 The rotational domain for the Sheffield HATT showing the geometry with (a) and without (b) mesh



(a)



(b)

Figure 4.2 Cut plane mesh for the Sheffield HATT at 25% span (a) and 75% span (b) of the blade

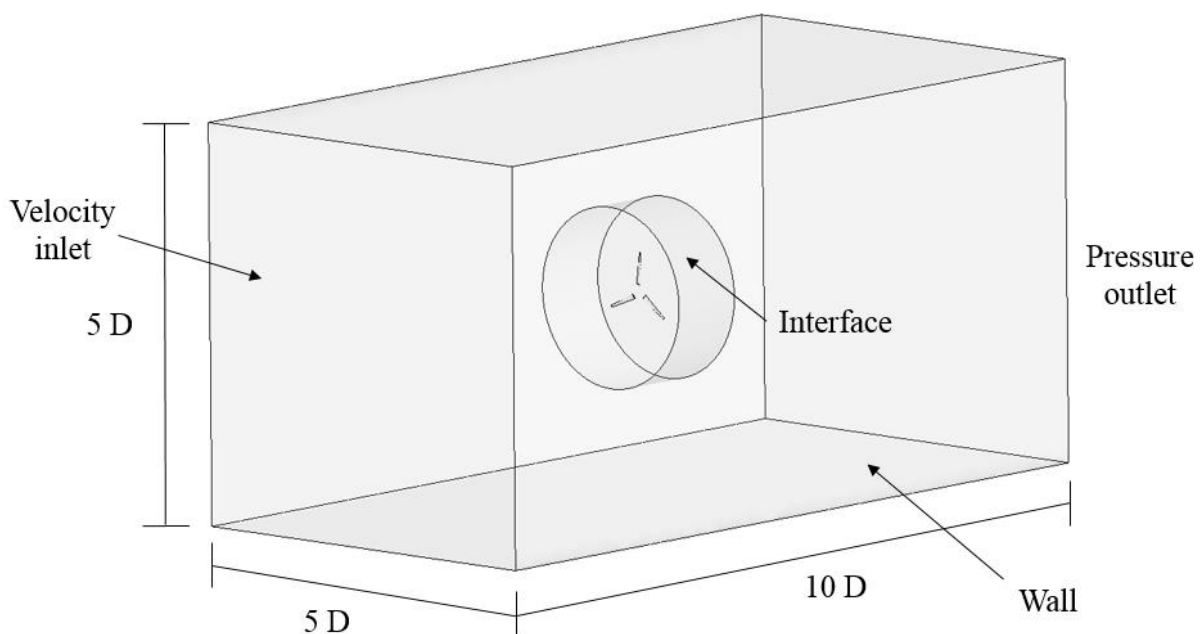
The stationary domain with a geometry of  $5D$  by  $5D$  by  $10D$  (where  $D$  is the diameter of the Sheffield HATT) was created using the same meshing technique without the prism layer. The domain extent consideration by the author was based on the University of Sheffield's wind

tunnel which has a 1.2m x 1.2m x 3m test section since a validation study for the Sheffield HATT was planned beforehand using the same boundary configuration but different size to match the Re limit of the wind tunnel. Another basis is a study done by Osborne which looked at the effect of domain length and blockage effects to a model tidal turbine. The initial numerical boundary study was based in the cavitation tank with a test section of 1.2m x 2.4m x 5.6m, the boundary extent was 1.5D x 3D x 7D. It was found out that the domain length has a very small effect in turbine performance accounting only to 0.5% difference or less for all domain length cases tested which varied from 5D to 30D. Osborne's results also showed that 5D downstream is enough for near wake and turbine performance analysis which will be enough for the extent of this study. The domain size was doubled and then tripled in his study to see the effect of blockage in the turbine performance and no significant effect was seen when compared to the initial cross section of 1.5D by 3D (Osborne, 2015). Similar blockage study was done by the author and will be presented later in this chapter.

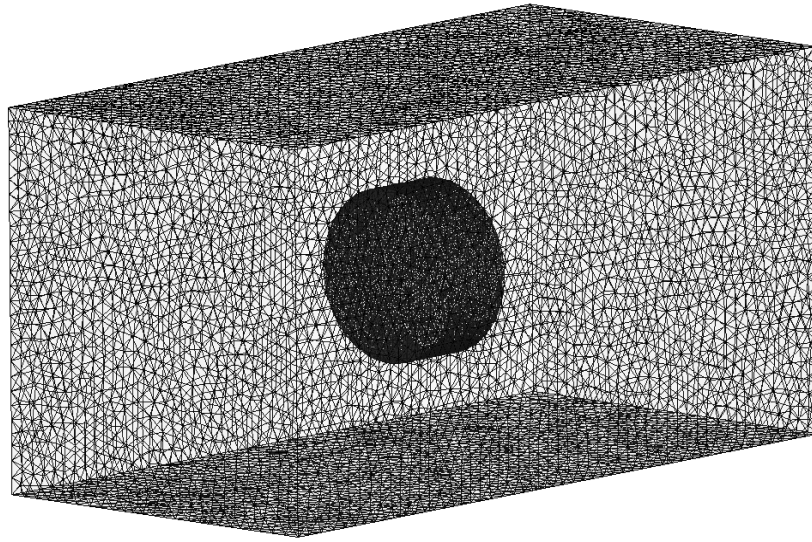
Figure 4.3a shows the outer domain for the numerical model and the mesh is shown in Figure 4.3b. This mesh was made to be coarser than the inner rotational mesh but still enough to capture flow physics and hydrodynamics. The rotational mesh discussed beforehand will be appended to the corresponding cylinder in the outer stationary mesh. Mesh configuration at this section was set to be similar, if not the same, to avoid numerical dissipation. Other boundary conditions for the outer stationary mesh were also shown in Figure 4.3a, velocity-inlet and pressure-outlet were used for the inlet and the outlet portion of the domain, the sides, bottom were set as walls. The top part of the domain was also set as wall because the simulation was first intended to serve as a comparison for a wind tunnel experiment for the validation of the study. Since the mesh was intended to be validated by a wind tunnel experiment with similar Re, the top part of the mesh was not set to be a free-surface but was set as a wall instead.

### 4.3 CFD Solver

The solver used for all of the simulations conducted in the study is the CFD package ANSYS FLUENT v. 16.1 which uses finite volume technique to resolve governing fluid equations. This solver was chosen because it is the most validated CFD software by date and was proven to have worked for a lots of earlier simulations in tidal turbines as shown in the literature review. The Reynolds-Averaged Navier Stokes (RANS) equations were used for this study with closure turbulence models  $k-\epsilon$  RNG and  $k-\omega$  SST. Second-order transient implicit formulation is chosen to assure convergence for most time steps. Finally, since the mesh were made using unstructured tetrahedral meshes and the mesh grid is mostly not aligned to the flow, the second-order upwind discretisation scheme were used throughout all simulations for improved accuracy at the expense of slightly longer convergence time.



(a)



(b)

Figure 4.3 Outer mesh computational domain showing the boundary conditions applied in the CFD model (a) and mesh (b)

#### 4.4 Mesh Independence Study

It is important in a CFD simulation that the numerical solution is independent of the mesh resolution being used. As the number of elements in a mesh increases, the accuracy of the solution also increases but a limit exists when the solution does not change significantly even if the mesh density is increased furthermore. This is the optimum mesh being sought in a mesh independence study – to find a mesh that is fairly accurate but will not be too computationally expensive.

A mesh independence study in terms of the number of cells around the surface of the aerofoil at  $0.75R$  of the blade and the total number of cells was performed. Six different meshes with varying number of cells with brief description presented in Table 4.1 were simulated for this study. Water flow velocity was chosen to be set at 2 m/s, this is based on the ideal speed range for tidal turbine presented by Carbon Trust which is from 2 to 3 m/s (Carbon Trust,

2005). Based on the BEM simulation presented in Chapter 3, the best operational condition for the Sheffield HATT will be at TSR=6 therefore the rotational velocity of the turbine was set at  $\omega = 6$  rad/s to have the optimum tip speed ratio. The described operating condition corresponds to a Reynolds number of 1,350,000 at the 75% span of the blade. Simulation was carried out using the solver configuration mentioned beforehand in the computing network of the University of Sheffield called Iceberg, 48 cores were being accessed during each simulation. Results are set to be converged if the continuity residuals gone down to values less than  $5e-5$ . The coefficient of performance (CP) for the turbine for each case was computed and was presented in Table 4.1 together with the time it took for the solution to converge.

It can be deduced from Figure 4.4 that mesh 4 is the optimum point by which the value of CP is not varying significantly with further increase of the mesh density. In terms of computational time, mesh 4 has converged 9 hours faster than mesh 5 having the same CP value. It is therefore concluded that mesh 4 will be used for the succeeding test where the effect of boundary size was tested.

Table 4.1  
Mesh Independence Study Results for the Sheffield HATT at water velocity=2m/s and TSR=6

<b>Mesh no.</b>	<b>Target no. of Cells at 0.75 span</b>	<b>Total no. of cells</b>	<b>Coefficient of Performance</b>	<b>Computational time (at 48 cores, hours)</b>
1	50	836,654	0.373	6
2	100	1,661,936	0.403	8
3	200	3,217,579	0.411	12
4	300	4,259,402	0.418	20
5	350	6,500,103	0.418	29
6	400	8,308,612	0.417	38

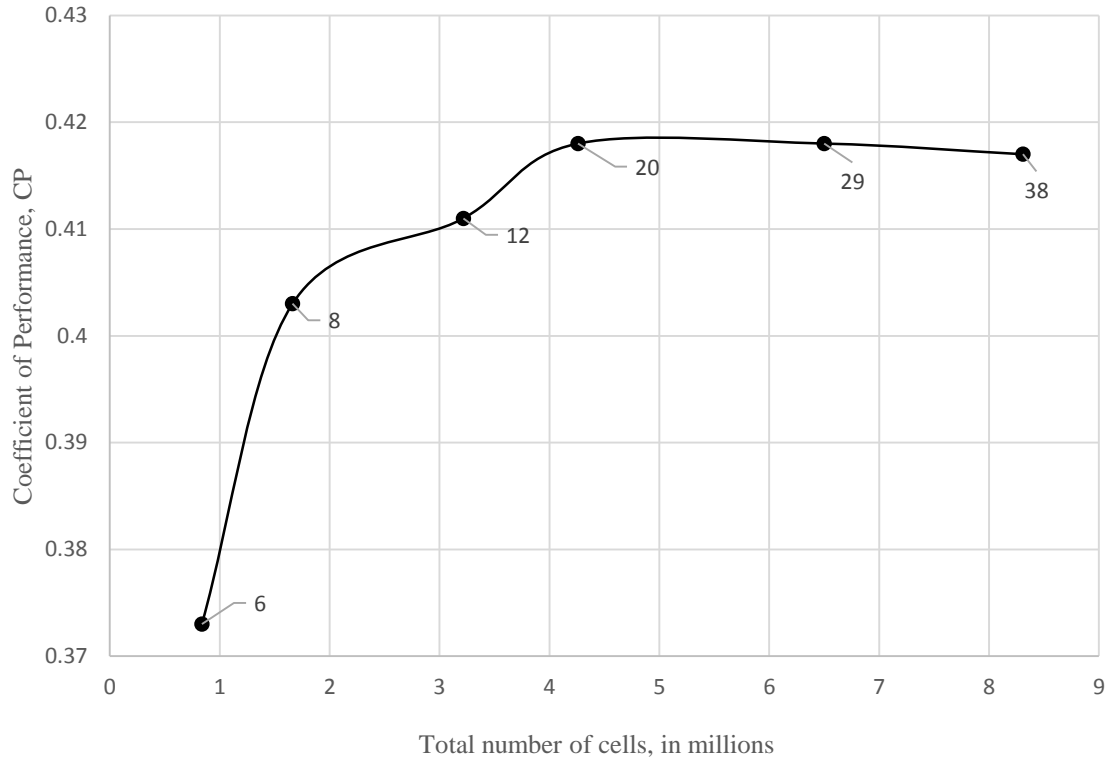


Figure 4.4 CP values for each case mesh test case with the computational time in hours as data labels

#### 4.5 Boundary Size Study

In the previous study, mesh 4 was chosen and was said to be mesh independent in terms of the mesh density but as mentioned before, it is also important that the mesh is also independent in terms of the numerical domain. The domain extent used was chosen and was compared to other studies but it will still be worth doing a boundary study just to see if there is a boundary effect in performance. Mesh 4 was used in this study with its stationary outer mesh boundary increased by 100% in three directions resulting to a new domain extent of 10D by 10D by 20D while maintaining the size of the rotational domain as shown in Figure 4.5. The operating condition was maintained with a water velocity at 2 m/s at TSR=6. Same convergence criterion as that of the mesh independent study was implemented. The CP for the bigger boundary mesh was computed to be 0.4174 which has a negligible difference of 0.4% when compared to the CP computed for Mesh 4 at the same operating condition.

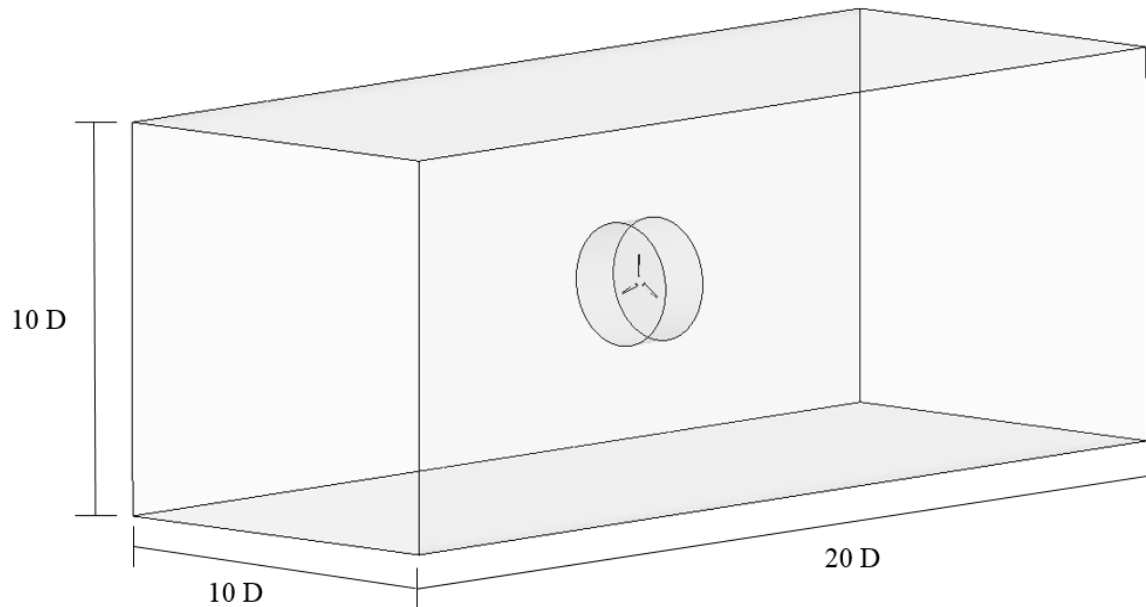


Figure 4.5 The mesh used for the Boundary mesh study with domain at 10D by 10D by 20D

#### 4.6 Steady Flow Simulations

This section will present the steady state formulation and simulation results for the Sheffield HATT CFD model for two chosen turbulence model for fully turbulent flow together with the comparison with the BEM simulation results shown in Chapter 3. Detailed discussion trying to explain the flow physics for different operating condition is also included.

Steady flow simulations were conducted for the chosen mesh under two turbulence models ( $k-\epsilon$  RNG and  $k-\omega$  SST). The two turbulence models are selected firstly out of a turbulence model study done by the author using  $k-\epsilon$  and  $k-\omega$  families of turbulence models though it was limited to the standard wall function (SWF) family of  $k-\epsilon$  (since the flow is highly turbulent and the mesh was made to have the first cell in the log layer) and the  $k-\omega$  family. It was a 2D NACA 0012 validation study which was compared to the experimental data from Ladson *et al.* (Ladson, 1988) Experimental aerodynamics data at  $\text{AoA} = 4^\circ$  with  $\text{Re} = 6,000,000$

gathered were  $C_l = 0.4316$  and  $C_d = 0.00823$ ; errors from the different turbulence model used was presented in figure 4.6. It can be seen that the turbulence model with the smallest error in terms of  $C_l$  is that of the k- $\epsilon$  standard and RNG models though the k- $\epsilon$  RNG shows a relatively smaller error in terms of  $C_d$ . The k- $\omega$  SST model has the least error in terms of drag coefficient and is therefore also considered to be used in the steady state simulation. The two models (k- $\epsilon$  RNG and k- $\omega$  SST) were both used in the steady state simulation of the Sheffield HATT and results were used for the final selection of the turbulence model to be discussed later in this section.

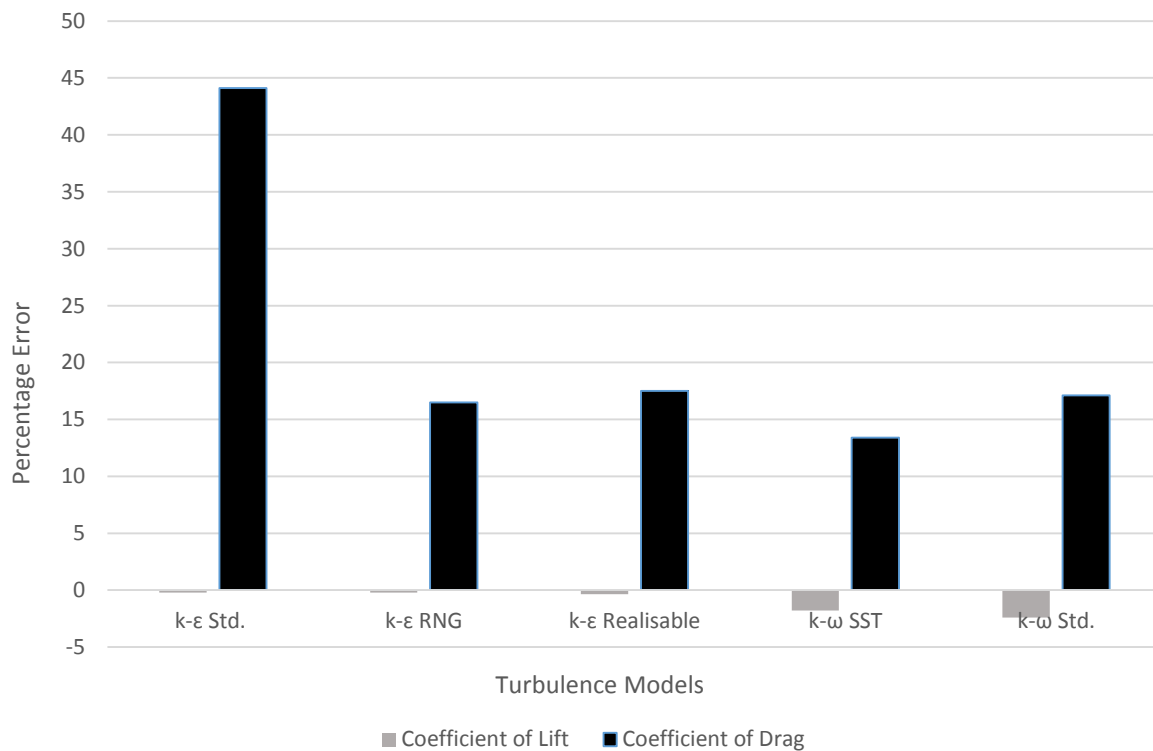


Figure 4.6 Percentage error for the turbulence models tested and compared with the experimental data from Ladson *et al.* at operating conditions of  $Re = 6,000,000$  and  $AoA = 4^\circ$

A similar turbulence model study done by Sobotta where CFD model of NACA 65-421 is simulated for different turbulence models to serve as validation to experimental data by Devinant *et al.*. Spalart-Allmaras (S-A), k- $\epsilon$  and k- $\omega$  families of turbulence models were used and compared to the experimental results at  $Re = 400,000$ . Results are narrowed down to the

k- $\epsilon$  RNG model with enhanced wall treatment (EWT) and k- $\omega$  SST without Low-Re corrections. The k- $\omega$  SST model presented closer values to the experimental data referenced while the k- $\epsilon$  RNG model predicted high aerodynamic coefficients and is proven by the author to be the most mesh insensitive model based on growth rate. Further examination using the two models were done and this includes comparing the flow field to experimental results done by Fujisawa *et al.* Finally, the k- $\omega$  SST without Low-Re corrections were chosen for the final model for the rest of the study (Sobotta, 2014).

Steady state simulations using k- $\epsilon$  RNG and k- $\omega$  SST without low-Re corrections were conducted for flow conditions with water velocity at 2 m/s and  $Re = 1,350,000$  for TSR's between 2 and 10 which are achieved by changing the rotational velocity of the turbine. The solver used in these simulations is as described in Section 4.3. Simulations were submitted to the University of Sheffield's high computing system (HPS) called Iceberg with computing cores composed of Intel Xeon E5-2650 v2 and 48 cores were accessed for each simulation. Time step was set to be equal to one degree of rotation. Residuals per simulation were monitored and convergence was set at  $5 \times 10^{-5}$  for continuity residuals which was usually achieved after 8 turbine revolutions.

CP values were calculated for both turbulence models per operating condition and were plotted against TSR to complete the turbine performance curve for the turbine which is presented in Figure 4.7. The BEM simulation results from Chapter 3 was also superimposed in the plot to serve as comparison between both numerical methods CFD and BEM. The shape of the three turbine performance curves shows a good agreement with each other with both the CFD results having the same wide curve with optimum operating condition near  $TSR=6$ . The maximum CP value obtained for the BEM simulation is at 47.42% which is higher than that of the CP values for the CFD simulations which is at 41.88% for the k- $\epsilon$  RNG case and 39.46% for the k- $\omega$  SST model. This is reflected as both of the CFD results predicted a lower turbine

performance curve as compared to that of the BEM simulation as shown in Figure 4.7. It can be attributed to the fact that BEM is a pure mathematical model that is based on the polar plots of aerodynamic data on the aerofoil sections and does not account for additional three-dimensional effects such as the increase in form drag and pressure drag which then lowers the lift-drag ratio and hence CP. Nevertheless, it can be concluded that the two numerical methods has good correlation with each other. Another notable observation is the difference between the results from the two CFD models where the k- $\omega$  SST predicted a lower turbine performance curve as compared to the k- $\epsilon$  RNG model. It can be seen in Figure 4.6 that there is a less negative error for the k- $\epsilon$  RNG model in terms of the  $C_l$  for that specific case meaning that the model predicted a higher lift value. Results of Sobotta's turbulence model study supports this observation although the highest lift coefficient predicted in the study was that for the k- $\epsilon$  RNG with EWT though k- $\epsilon$  RNG (SWF) still has higher lift predicted as compared to that of the k- $\omega$  SST model (Sobotta, 2014). This can be the reason for the slight difference between the two models which has a largest difference of 0.0337 in terms of CP at TSR=8.

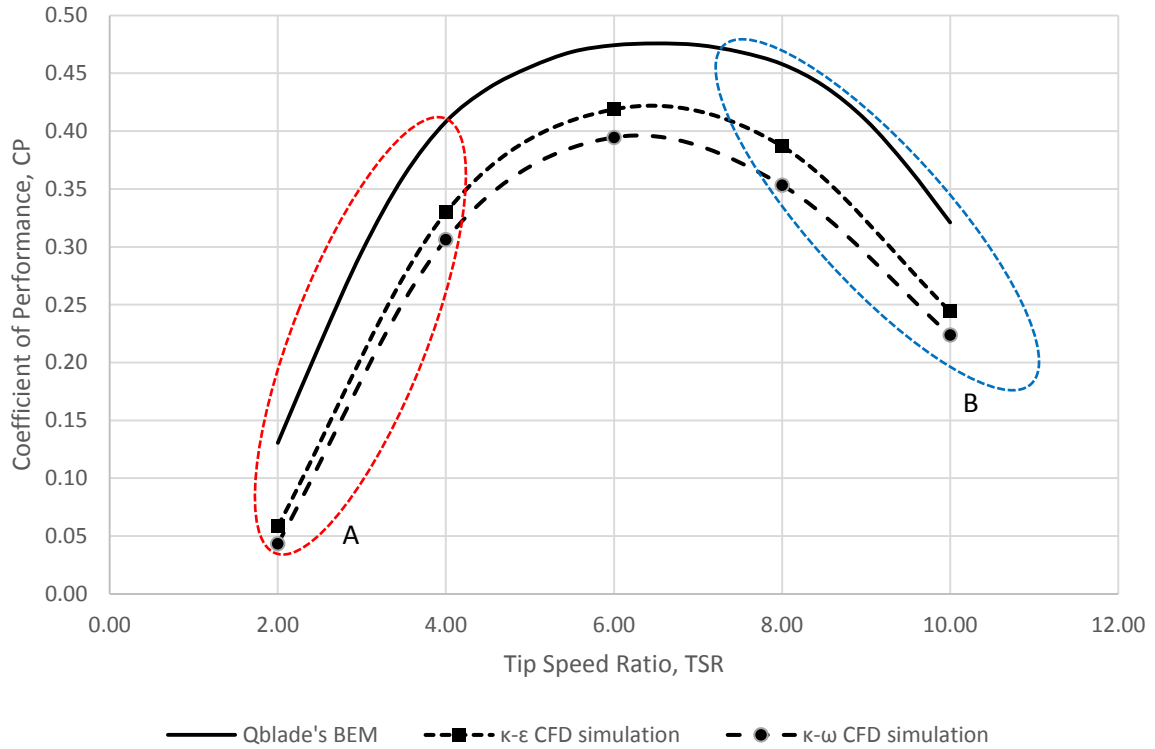


Figure 4.7 Turbine performance curve comparison between BEM, k- $\epsilon$  and k- $\omega$  SST simulations for the Sheffield HATT

The shape of the turbine performance curve shows a steep drop in CP values going to the left side where TSR is decreasing. This can be attributed to flow separation and even stall that can happen because of high incident AoA prediction in this area (highlighted by area A in Figure 4.7). From hydrofoil fundamentals, having a higher AoA means an increase in lift until a point where separation of flow occurs and eventually stall. On the incidence of flow separation, lift can still increase but drag will also increase due to the additional effects of form drag making the lift to drag ratio decrease and hence CP. When stall occurs, drag will continue to increase but lift will suddenly drop in value which results to a lower lift to drag ratio and hence CP. Same observation was presented by Milne *et al.* whereas steep decay in CP results from steady flow experiments and was associated to the effect of stall domination in the flow (Milne *et al.* 2012).

CFD results are post-processed to produce flow streamlines for every operating conditions (TSR's) presented in the turbine performance curve. Streamline plots are usually used for fluid flow visualisation in CFD as it shows curves that are tangent everywhere to an instantaneous vector field. Streamlines can be used to show separation in fluid flow as well as a visualisation of the incident AoA as shown in Figure 4.8. The same visualisation is presented in Figure 4.9 and 4.10 for various operating conditions for both of the turbulence models used in the steady state simulation.

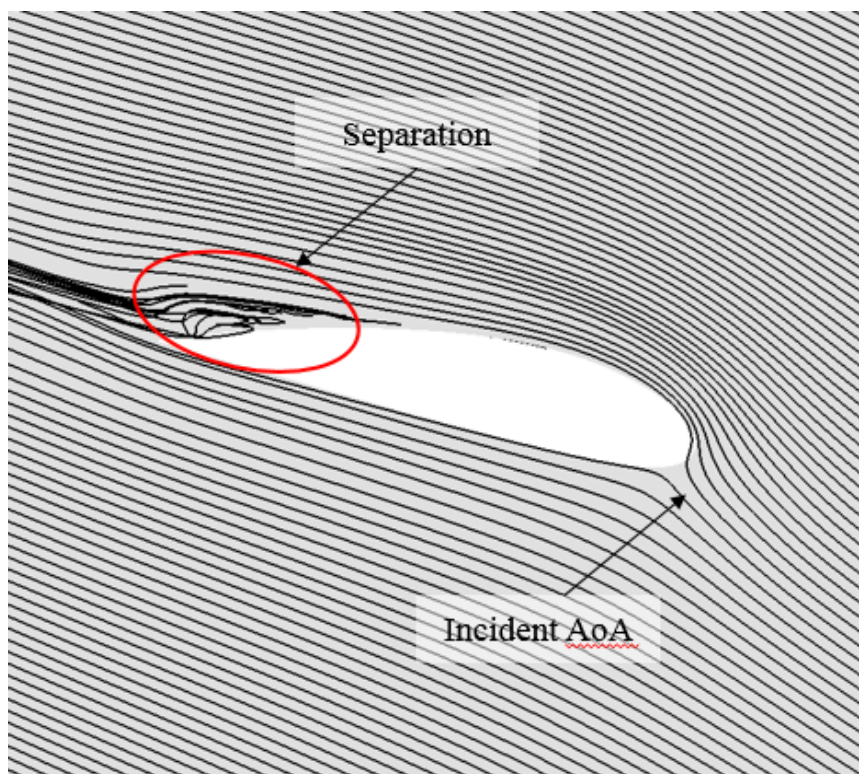
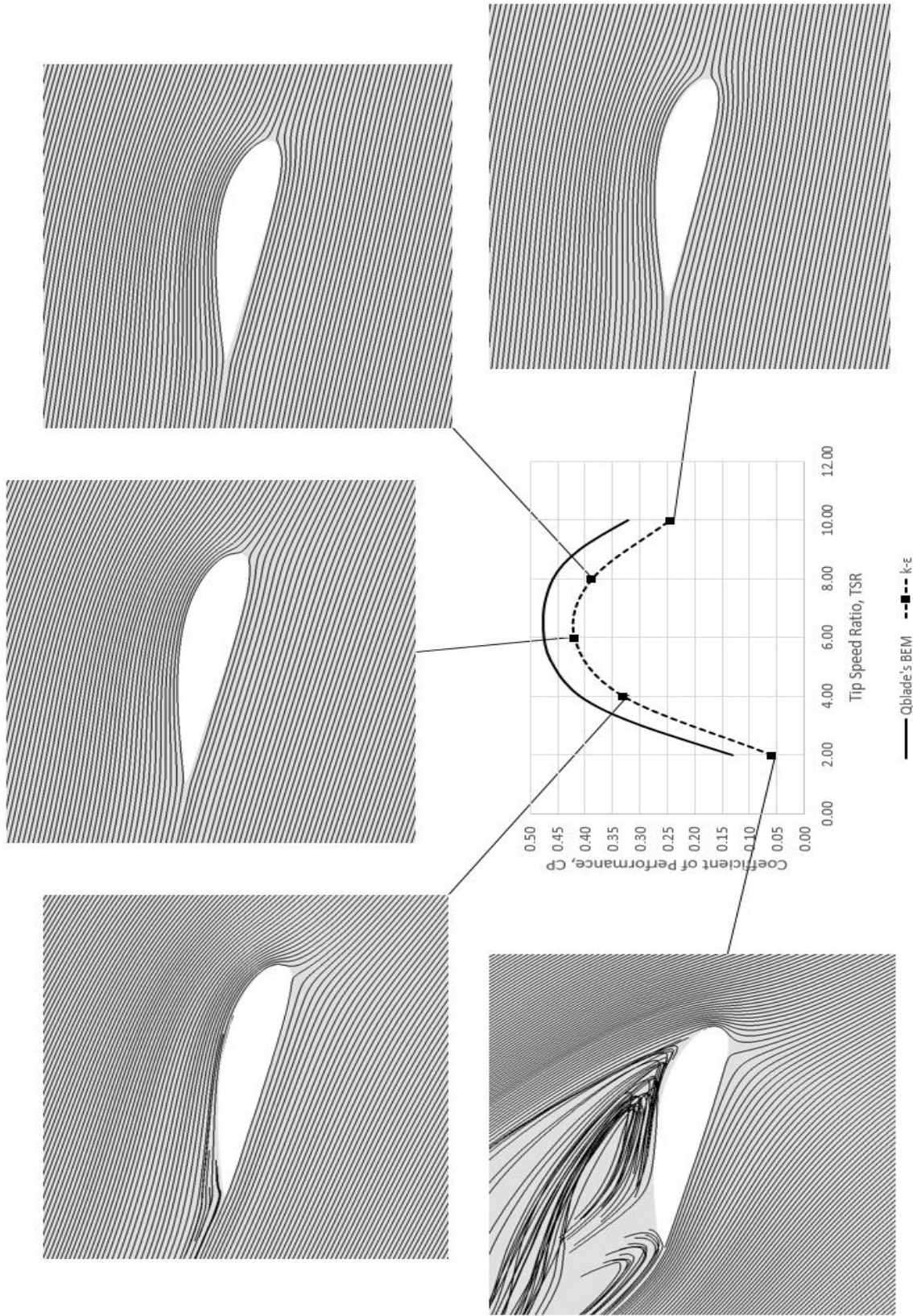
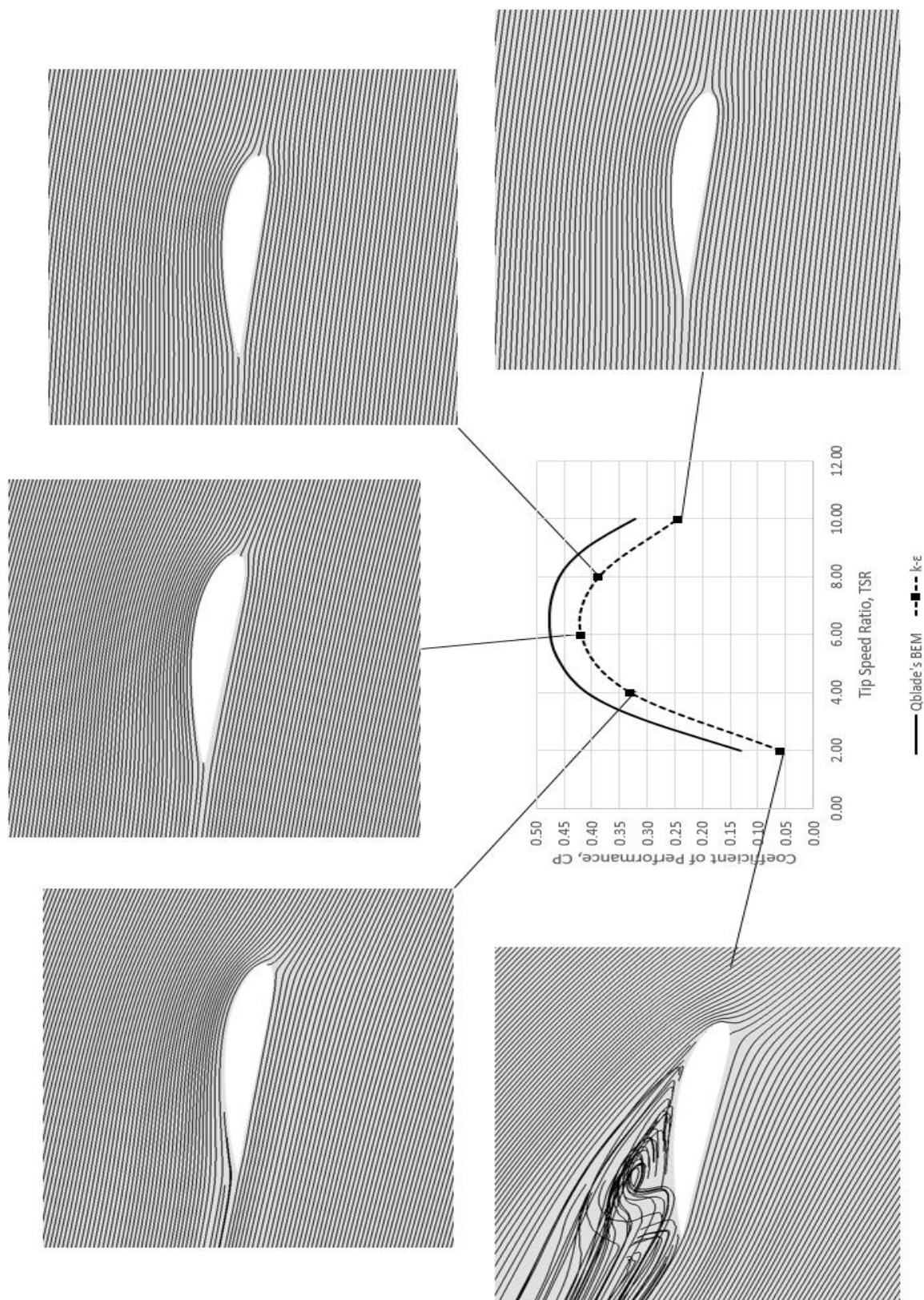


Figure 4.8 Sample streamline plot presenting the incident AoA and separation in a hydrofoil section of a tidal turbine

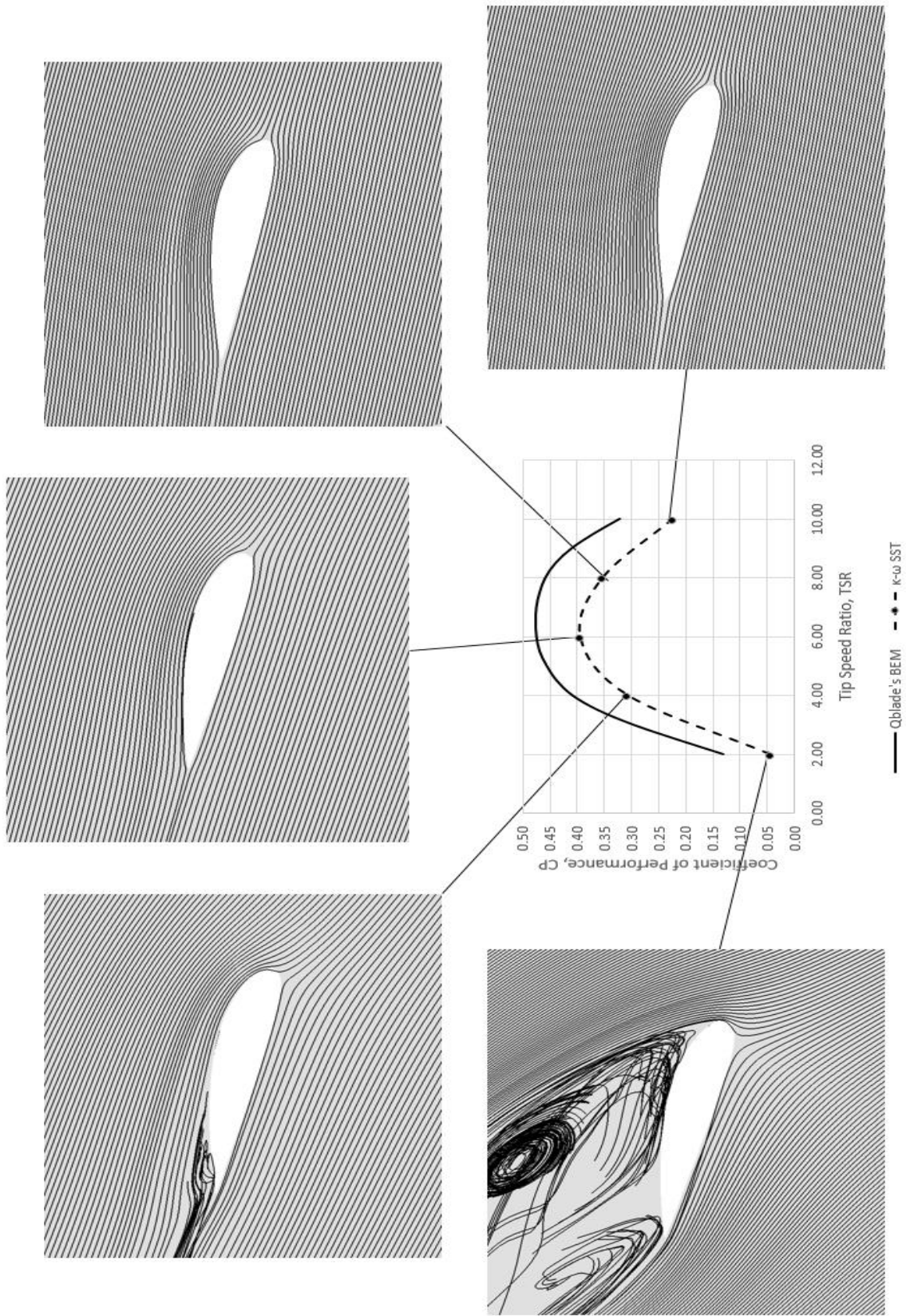


(a)

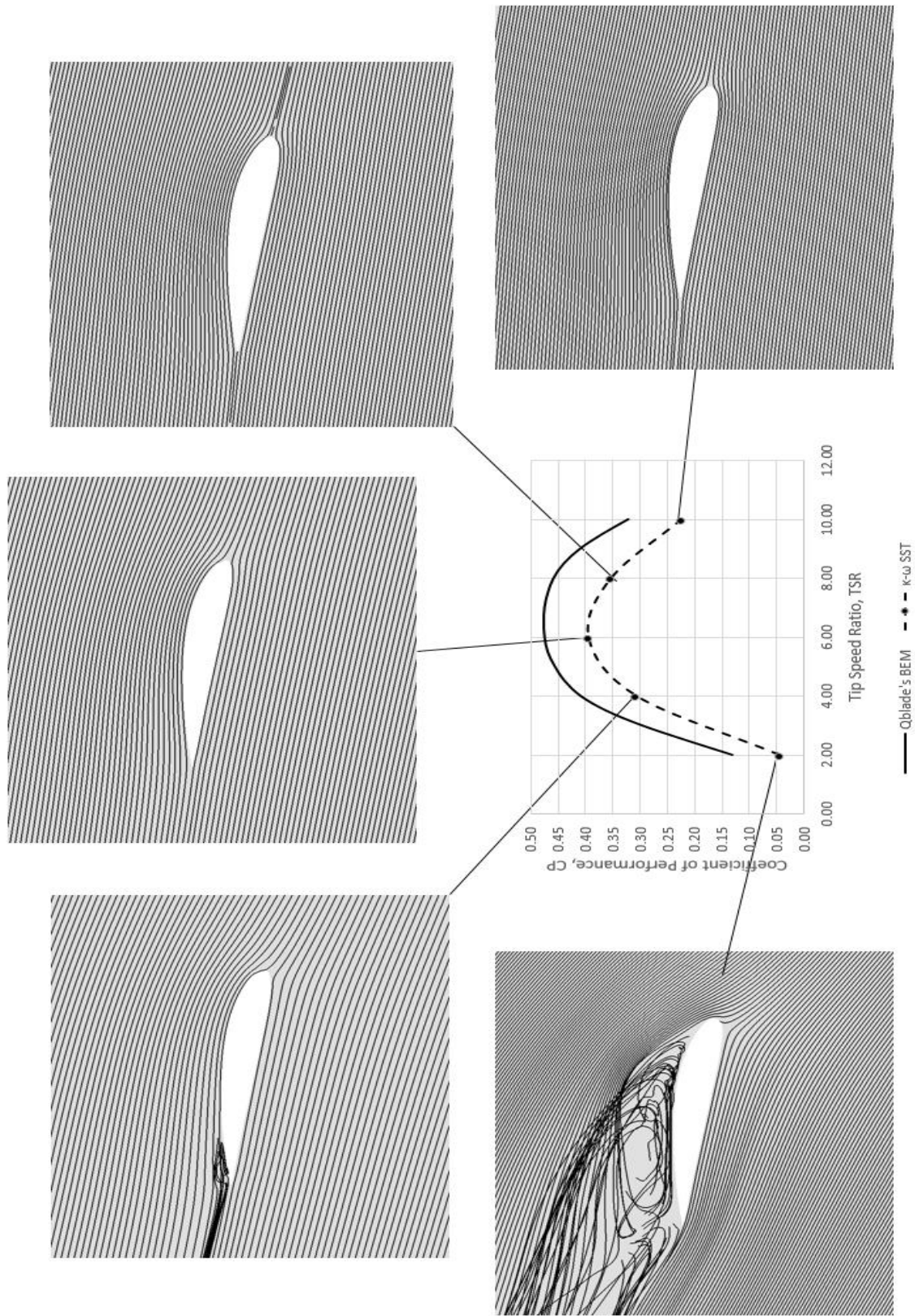


(b)

Figure 4.9 Flow visualisations for the k-ε RNG simulations at R=0.8 (a) and R=1.6 (b)



(a)

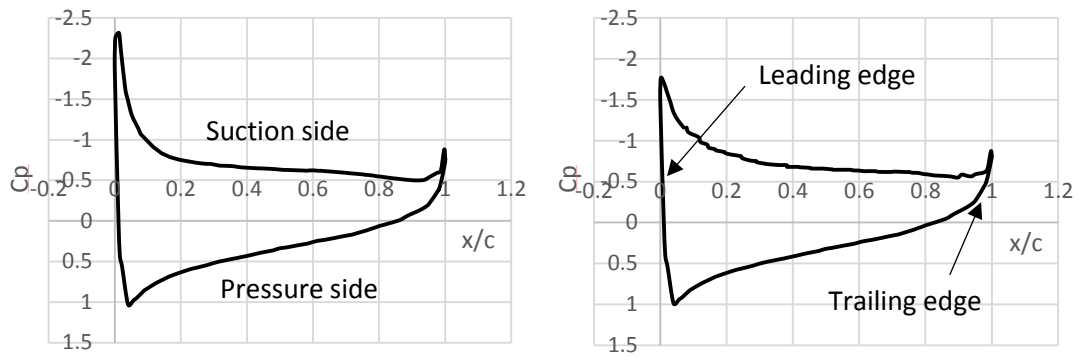


(b)

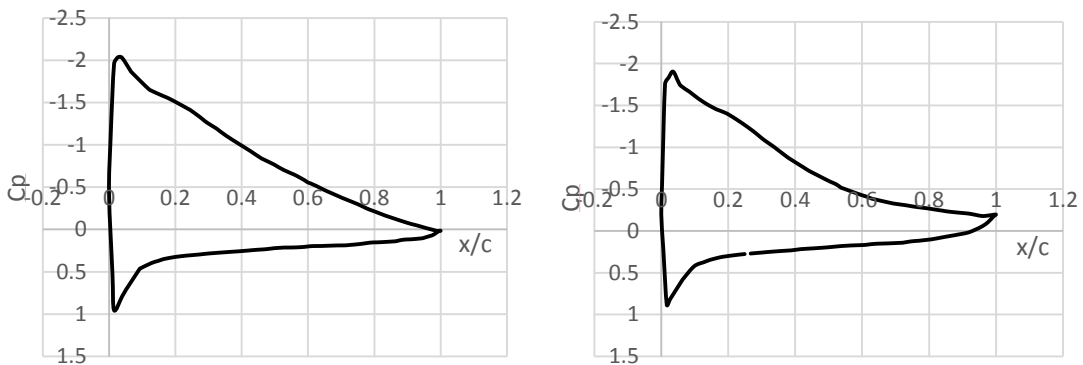
Figure 4.10 Flow visualisations for the  $k-\omega$  SST at  $R=0.8$  (a) and  $R=1.6$  (b)

From the streamline plots in Figures 4.9 and 4.10, it can be seen that as the TSR decreases, the incident AoA on the hydrofoil increases. An increase in AoA will mean higher lift but will also allow separation as can be seen in the case at TSR=2 for both turbulence models and TSR=4 for k- $\omega$  SST. These observations confirm the effect that having flow separation from the turbine blade decreases its performance.

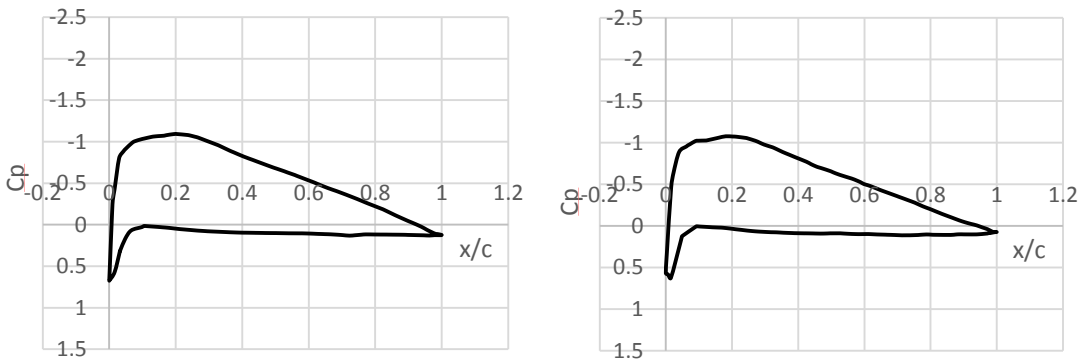
Pressure coefficient ( $C_p$ ) plots for the 75% span section of the turbine blade for TSR=2 and TSR=4 is presented in Figure 4.11 (where  $x/c$  is the position on the chord normalised by the chord length), the 75% span of the blade was chosen because this is within the area of the turbine which produces the most power. It can be seen from the  $C_p$  plot for TSR=2 for both simulations that there is a sudden drop in pressure near the leading edge of the suction side of the hydrofoil suggesting stalled flow which is also supported by the streamlines presented in Figure 4.9 and 4.10. The area inside the  $C_p$  plot represents the lift force on that section of the turbine blade, it can be seen in Figure 4.11 that the lift force in TSR=2 is less than that of TSR=4 further proving the effect of stalled flow to the lift force. Some differences between the two turbulence models is present in terms of the streamlines produced and the  $C_p$  plot as well. In terms of the streamlines, a bigger separation area can be observed for the k- $\omega$  SST which almost reached the leading edge for the streamline at  $R=0.8$ . In terms of the  $C_p$  plot, the k- $\epsilon$  RNG plot shows a higher pressure near the leading edge which suddenly dropped down whereas it started with a lower pressure and relatively gradual decrease for the k- $\omega$  SST model. The difference in the  $C_p$  value for the two models is relatively small despite this observed differences.



TSR = 2



TSR = 4



TSR = 6

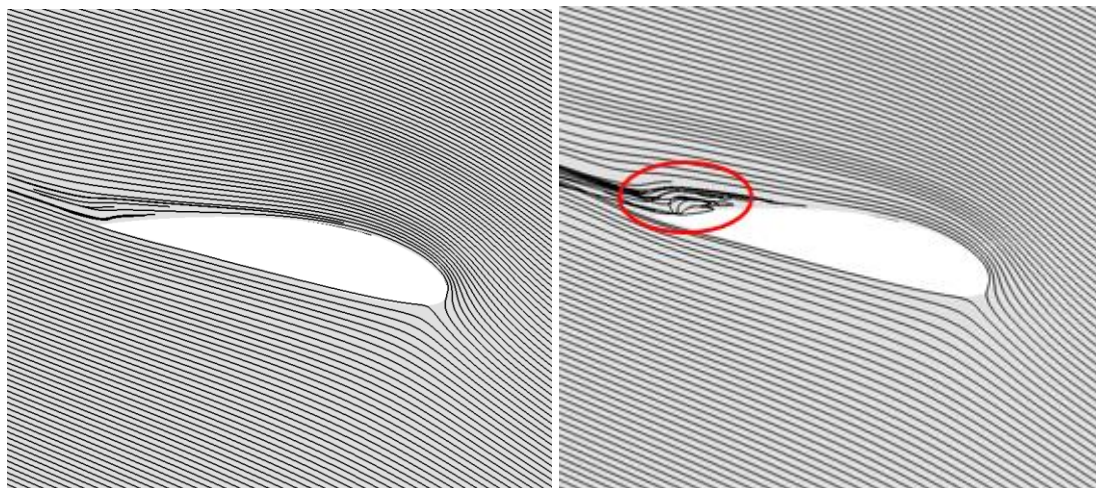
Figure 4.11 Pressure coefficient plots at 75% blade ( $R = 1.6$ ) span for TSR = 2, TSR = 4 and TSR = 6 with  $k-\epsilon$  RNG (left) and  $k-\omega$  SST (right)

Small separation was observed for the  $k-\omega$  SST streamline plots for TSR = 4 for both sections of the blade that are examined, this separation is not seen in the plots for  $k-\epsilon$  RNG.

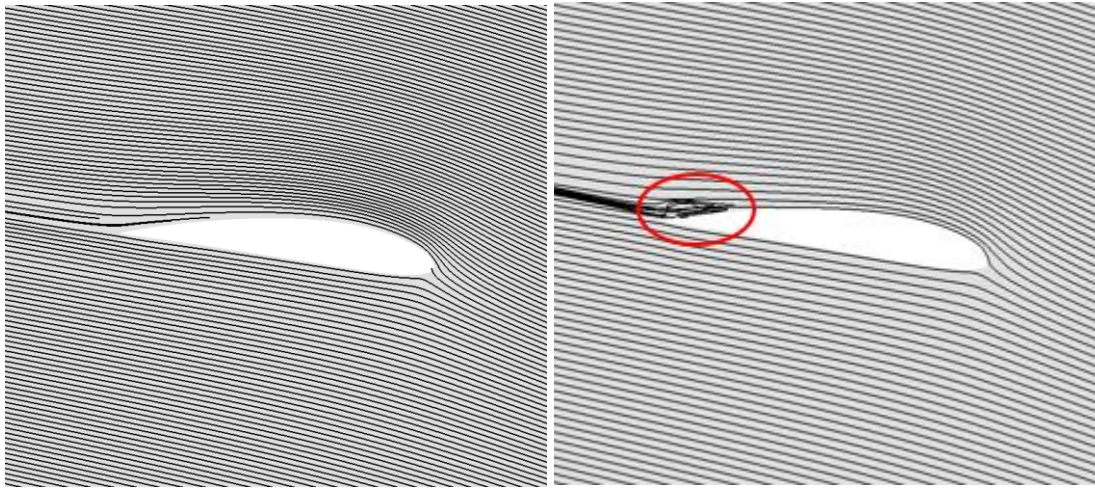
Figure 4.12 shows the difference between the two streamline plots with the separation seen for

k- $\omega$  SST. The geometric AoA computed for TSR = 4 at R=0.8 is  $26.1^\circ$  which is past beyond the separation AoA for the hydrofoil NACA 4420 which is just between  $15^\circ$  to  $17^\circ$ . This means that there should be observable separation at this operating condition which is seen in k- $\omega$  SST but not in k- $\epsilon$  RNG. Because of this observation, the author decides to use k- $\omega$  SST for the unsteady flow simulation presented in Chapters 5 and 6. Similar observation was done by Sobotta *et al.* who also chose k- $\omega$  SST after doing flow-field tests in her own turbulence model study in which k- $\omega$  SST predicted flow fields presented in reference experiments better than k- $\epsilon$  RNG (Sobotta, 2014).

Referring again to Figure 4.11, it can be seen that the area under the Cp curve for the TSR = 4 simulation is higher than that at TSR = 6, this supports the idea that lift still continue to increase even if separation happens when AoA increases. But still, the CP value at TSR = 4 is lower than that of TSR = 6, this is caused by the additional drag force caused by form drag due to separation which negatively affecting the CP as the total drag increases. At this point, the rate at which the lift increases with each increment in AoA is less than the change in drag caused by the separation, this makes the lift to drag ratio lower and hence CP decreases.



R = 0.8



R = 1.6

Figure 4.12 Isolated flow visualisations for R=0.8 at TSR=4 with  $\kappa\text{-}\epsilon$  RNG (top) and  $\kappa\text{-}\omega$  SST (bottom)

Observing the streamline plots at Figure 4.9 and 4.10, it can be seen that at TSR = 6, the incident AoA is starting to decrease to a value that is below the separation AoA for the hydrofoil sections in the turbine blade therefore a fully attached flow is observed. This point is the optimum operating condition for the Sheffield HATT and it has the best combination of lift and drag. Since the flow is fully attached, there will be no additional drag force and although the lift force is relatively lower as compared to that at TSR = 4, the existing lift to drag ratio at this point will still be higher than that of the operating conditions with higher lift. This operating condition will be used as the reference case for the succeeding unsteady simulations that will be presented in next chapters. The CP value at this point for the  $\kappa\text{-}\epsilon$  RNG simulation is at 41.8% while the  $\kappa\text{-}\omega$  SST simulation has a value of 39.46%, both of which are the maximum points for their respective plots.

Going to the right side of the turbine performance curve, region B of Figure 4.7 (highlighted by a blue circle), a continuous decrease in the CP values is observed. This is due to the lowering of the incident AoA for higher TSR's 8 and 10 which can also be observed in the flow visualisations in Figure 4.9 and 4.10. Lower AoA results to lower lift which is also

seen in the  $C_p$  plots in Figure 4.13 where the areas under the curve is smaller relative to lower TSR's. The lower surface's  $C_p$  recovery started to get closer to the upper surface distribution and even overlap for  $TSR = 10$  (highlighted by red circle). This results to the formation of negative lift which makes the total lift lower hence explaining the lower CP computed at that point coupled with the very small difference. The onset of this overlap is also observed to be earlier for  $k-\omega$  SST (highlighted by a green circle) which can mean that the AoA is also lower or more negative at that point. At this point, since the flow is fully attached and the AoA is close to  $0^\circ$ , the drag will not vary significantly and therefore the lift to drag ratio will be mostly dependent on the variation in lift. Since lift continues to decrease, the CP calculated also decreases, explaining the shape of the performance curve under region B in Figure 4.7.

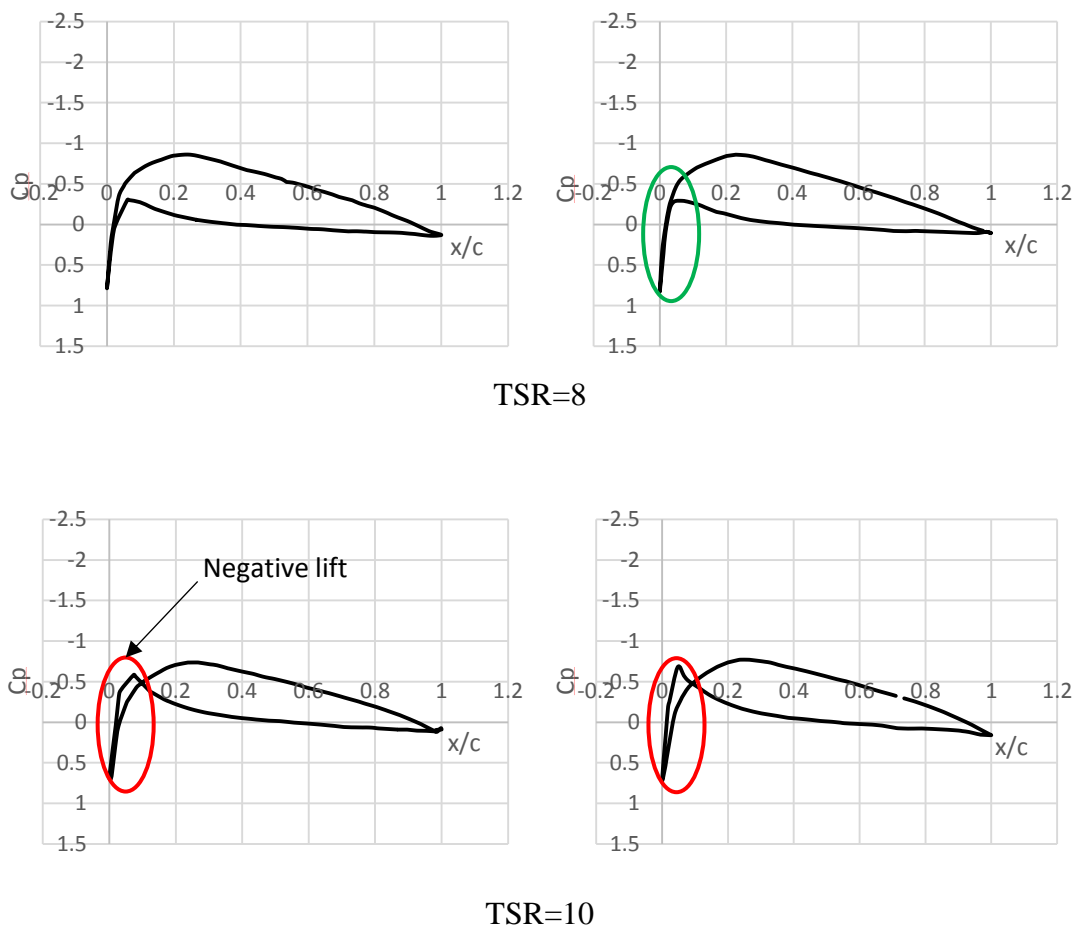


Figure 4.13 Pressure Coefficients at  $R=1.6$  at various TSR for  $k-\epsilon$  RNG (left column) and  $k-\omega$  SST (right column)

## 4.7 Summary of Chapter

This chapter discussed how the numerical model for the Sheffield HATT was created together with the numerical checks such as mesh independence study, domain size study, and turbulence model study. The final mesh to be used for succeeding studies was presented and the final turbulence model was decided to be  $k-\omega$  SST without Re corrections. The steady state simulation and methodology was also presented including analysis of the results based on the physics provided by streamline and  $C_p$  plots which was shown to be sensible and consistent. It was also shown that the CFD turbine performance curve results has good correlation and agreement with the BEM results. The maximum CP for the  $k-\omega$  SST simulation is 39.46% which happened at TSR=6 and this will be the reference case by which most the unsteady flow simulation results in the next few chapters will be compared to. The CP for the TSR=4 case is at 30.63% while it is 35.33% for TSR=8, these two cases will also be discussed with their unsteady flow counterparts in the next chapter with the aim to see the unsteady effects in cases on the left and right of the optimum case. The methodology for the unsteady flow simulation together with the results and comparisons will be discussed in the next chapter while the effects of parameter variation in the velocity inflow will be included in Chapter 6.

## Chapter 5

# Unsteady Flow Simulation of the Sheffield HATT

### 5.1 Introduction

This chapter will present the methodology developed for the unsteady flow simulations conducted for the Sheffield HATT together with the simulation results for the optimum operating condition (TSR = 6) and two off-peaks conditions (TSR = 4, 8). Analysis of the unsteady response/results is also included with emphasis on the unsteady flow effects and the comparison with the steady flow results for all three operating conditions presented.

### 5.2 Unsteady Flow Simulation

The first step for the unsteady simulation is to define the unsteady flow characteristics that will be implemented. An idealised time-varying unsteady inlet velocity will be used and it is defined to be a sine wave with mean velocity based on the steady flow velocity of 2 m/s. The amplitude of the reference case wave was set to be 25% of the mean flow ( $A = 25\%$ ) with frequency of 1 ( $f = 1$  Hz). The amplitude was chosen to provide a good range of instantaneous TSR for the hysteresis curve and to see an obvious effect in the performance curve as this is relatively high value for velocity perturbation in tidal stream flow. The concept of reduced frequency ( $k$ ) defined by Leishman (as shown in Equation 9) is the basis for the selection of the frequency used for this idealised unsteady inflow (Leishman, 2006). It is a parameter used to characterise the degree of unsteadiness in a flow and is derived when the Navier-Stokes equation is non-dimensionalised. Leishman defined that the flow is steady when  $k=0$  and flows with reduced frequency between 0 and 0.05 can be considered as quasi-steady whereas unsteady effects are assumed to be small and can be neglected. Reduced frequencies greater than 0.05 and above are defined to be unsteady and those flows having  $k=0.2$  is characterised

as highly unsteady. It must be taken into account that all the definition by Leishman is based on flows in air (helicopter blades and wind turbines) and not in water. Whelan argued that in the case of an axial velocity perturbation in tidal turbines, the effects of unsteadiness can be comparatively larger as it will be in wind turbines (Whelan, 2010). This argument is based on the fluid to structural density which is closer to 1 for rotors in water and much higher when compared to that in air although more quantification is needed for this argument as mentioned by Milne *et al.* (Milne, 2015). The main reason for the selection of the reference case idealised unsteady flow equation is for the reduced frequency to be outside the quasi-steady region and therefore be considered unsteady by Leishman definition.

$$k = \pi fc / \omega R \text{ (eq. 9)}$$

where:

f = frequency of the flow, Hz

c = chord length, m

$\omega$  = rotational velocity of the turbine, rad/s

R = radius where the foil is located

The cycle-averaged water power available in the water for the unsteady case simulation is matched to the water power for steady case discussed in chapter 4. This allows a direct comparison between the steady CP and the unsteady cycle averaged CP since they have the same available water power. To achieve the details of the unsteady flow velocity described in this section, an iterative method was conducted by the author and the final iteration was presented in Equation 10 where t (in seconds) is the time-step used for the simulation and since the frequency of the flow was set to be 1 Hz, it is not seen in the sine wave general equation.

$$u(t) = 1.940061 + 0.49 \sin(2\pi t) \text{ (eq. 10)}$$

The CFD solver used for the unsteady simulations is the same set-up described in Section 4.3 and was also simulated using the University of Sheffield’s computing service – Iceberg. The first case simulated was for the optimum operating condition (TSR=6). The moment coefficient ( $C_m$ ) per time-step was monitored and was converted to the instantaneous power coefficient (CP) by solving for the instantaneous torque provided by the turbine and multiplying it with the constant rotational velocity to acquire the power extracted by the turbine as shown in Equation 6. The simulation was continued to run until cyclic convergence was achieved at around the 12<sup>th</sup> complete rotation of the turbine which is illustrated in Figure 5.1, the red circle indicates the region where the simulation has reached periodic convergence. For this case, it took 61 hours to finish simulating 16 rotations of the Sheffield HATT. From initial observation from the CP plot over a number of rotations in Figure 1, the part inside the red circle shows asymmetry, suggesting the effect of unsteadiness for one flow cycle, this effect will be highlighted in the succeeding sections of this Chapter.

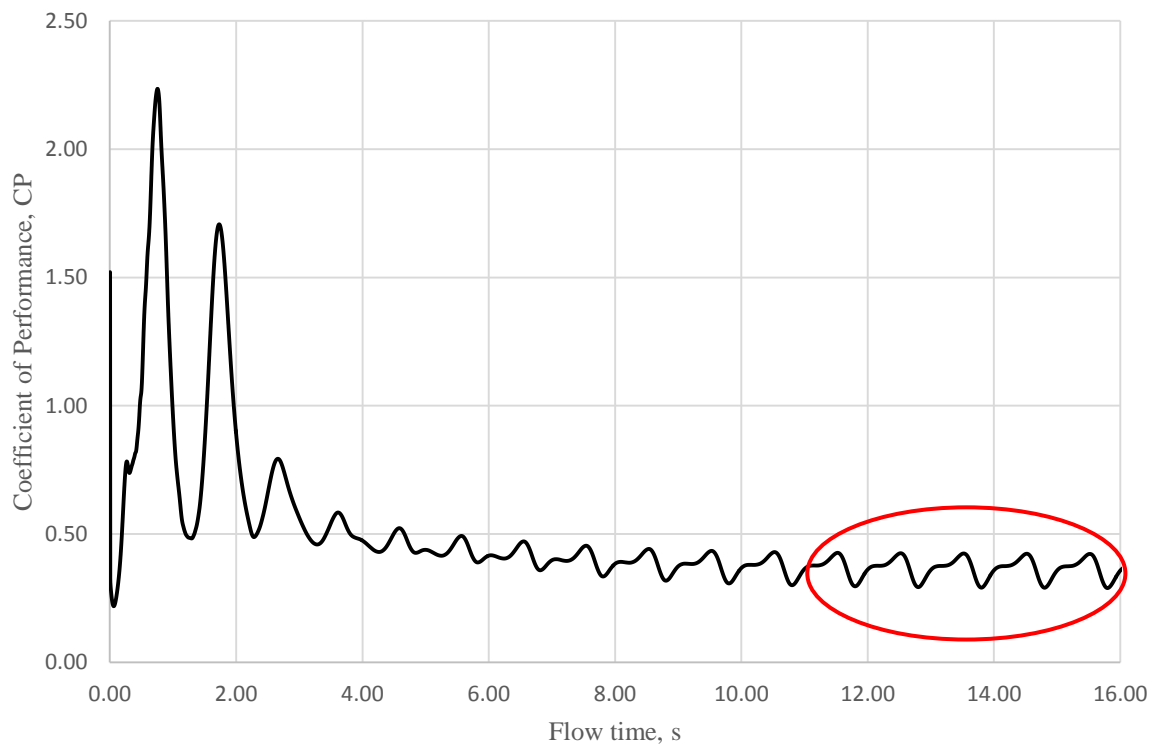


Figure 5.1 Response of the Sheffield HATT to the unsteady flow scheme implemented

The cyclic-averaged CP defined to be the cyclic-averaged power extracted by the turbine over the cyclic power available was calculated for this simulation and for the other unsteady simulations in this thesis. This is to have a comparison with the steady-state CP and quantify the effect of unsteadiness to the performance, this is also the reason why the cyclic-averaged power available was set to be equal to the steady state power available at 2 m/s. For this base case simulation, the cyclic-averaged CP was computed to be 37.50% which lower by 1.96% than that of the steady-state CP at TSR=6 which is at 39.46%. From this statement alone, it can be said that having the flow unsteady is giving a negative impact to the performance of the Sheffield HATT which also extend to the averaged power extracted since the averaged water available was maintained to be equal to the steady-state water power. To give more idea about the hydrodynamics happening for one cycle of the simulation, the instantaneous CP, instantaneous power extracted and power available were monitored and was analysed with the aid of normalised pressure plots and streamlines to be shown later in this section. The computed variation in instantaneous CP of the Sheffield HATT over one cycle of the unsteady flow is presented in Figure 5.2 and superimposed on the same graph is the instantaneous TSR which was computed from the unsteady velocity input and a constant rotational speed of the turbine. Figure 5.3, on the other hand, illustrate the unsteady velocity, instantaneous water power available and the power extracted by the turbine. All of the graphs are plotted against normalised flow time  $\tau$  which is defined as the normal flow time over the period of one cycle.

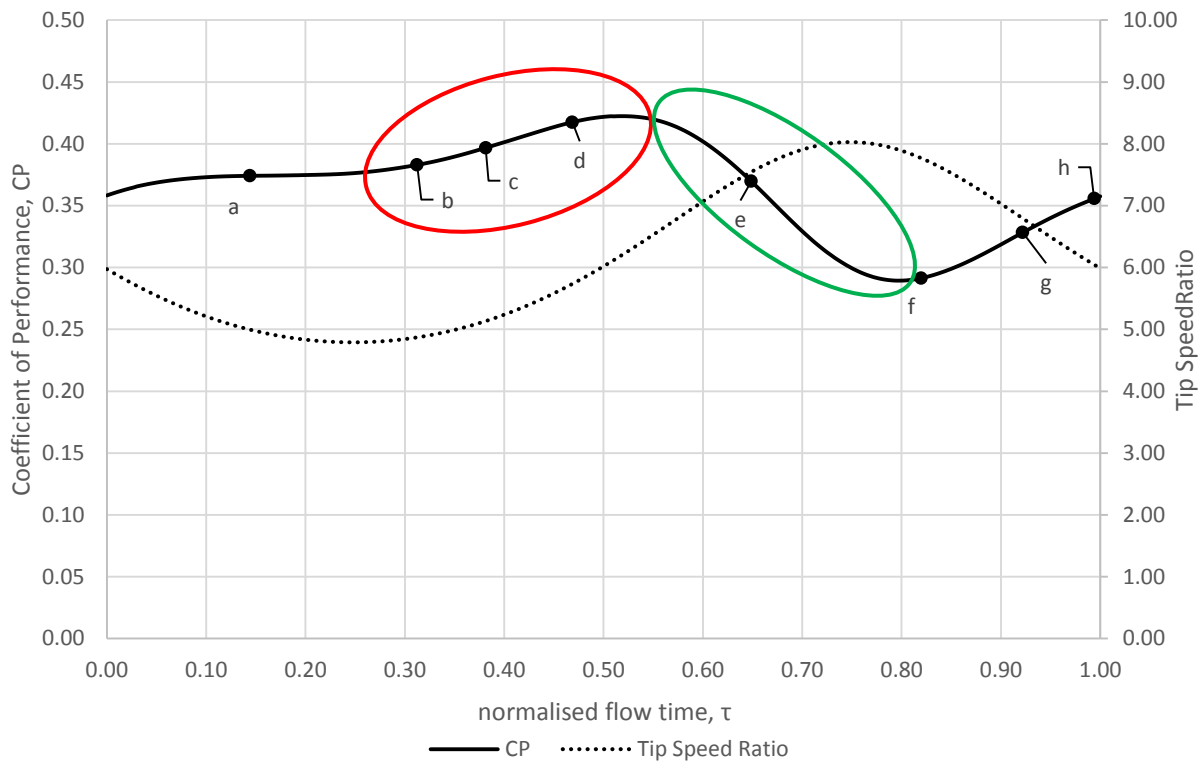


Figure 5.2 Unsteady flow response of the Sheffield HATT for one cycle with instantaneous Tip Speed Ratio (TSR)

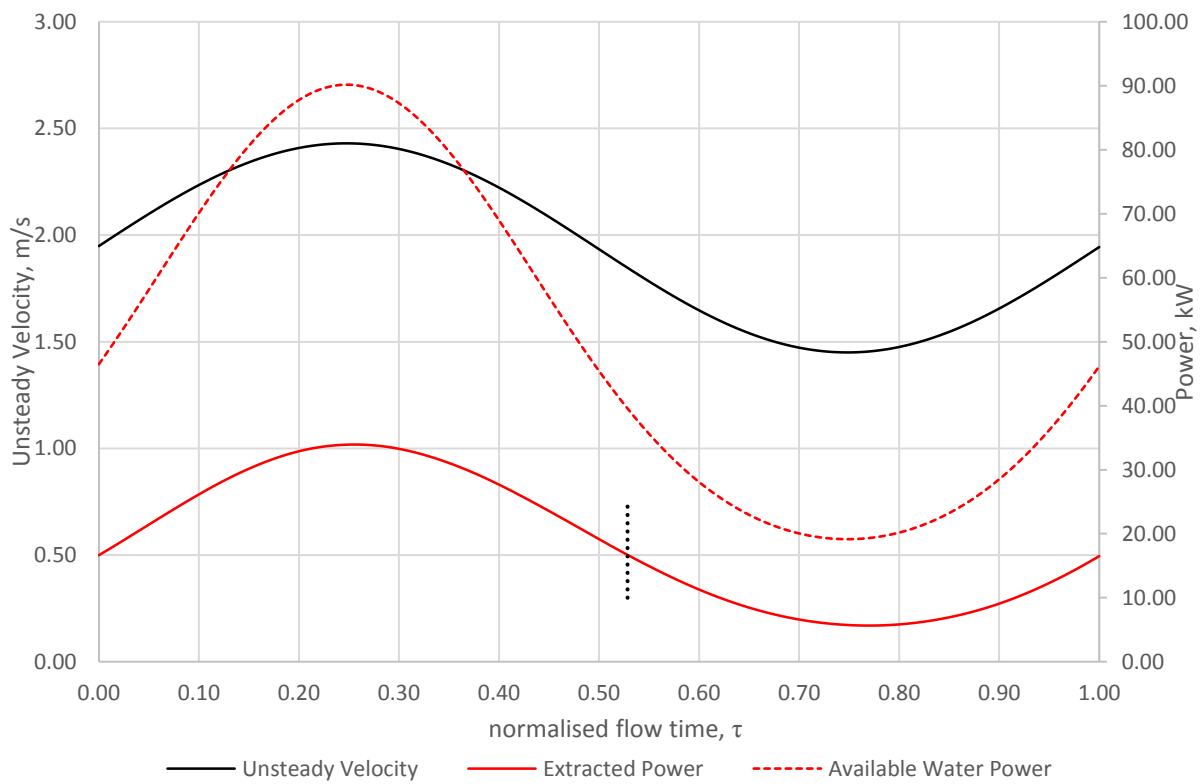


Figure 5.3 Available water power and extracted power by the turbine with unsteady velocity

It can be observed in Figure 5.3 that the instantaneous power extracted,  $P_e$ , by the turbine is not in phase with the unsteady water velocity (and so with water power available,  $P_a$ ) with a lag of 2.8% of the total cycle. The end of the lag by which the power extracted has come back to its original value is highlighted by the dotted line in Figure 5.3. The combination of the varying power potential and the power extracted by the turbine together with the lag contributes to how the unsteady performance curve in Figure 5.2 behaves. The lag develops from the start at the first half of the cycle until  $\tau = 0.528$  where the CP calculated goes back to the initial CP value. From the  $\tau = 0.25$  mark of the cycle, as the water velocity decreases, the effect of the lag to the CP is more apparent. Let us take the case for  $\tau = 0.528$ , the  $P_e$  at this point is the same as that at  $\tau = 0$  (a value of 20kW) but then it is paired to a lower  $P_a$  making the calculated CP at that point higher than the initial CP which then results to the maximum CP calculated with a value of 42.2%. This is the unsteady effect seen at the first half of the cycle which a higher  $P_e$  is paired than a lower  $P_a$  resulting to a higher CP. This is observed from  $\tau = 0.25$  until  $\tau = 0.528$  and is highlighted with a red circle in Figure 5.2.

The lag on the extracted power plot is still in effect for the latter half of the performance curve. It can be observed in Figure 5.2 that starting from  $\tau = 0.528$ , the CP calculated started to decrease, this is because  $P_e$  has also started to decline in value below the initial power. A relatively steeper line for the computed CP is observed from  $\tau = 0.528$  to 0.796 as presented in the green circle in figure 5.2, the reason being the decreasing value of  $P_e$  has an even lower denominator as  $P_a$  starts to decrease at  $\tau = 0.5$  and also the  $P_a$  plot is also steeper than that of  $P_e$ . It can also be deduced from figure 5.3 that the second half of the  $P_e$  plot is shorter than the first half, it reaches the lowest value and  $\tau = 0.764$  which is still later than the lowest available power recorded at  $\tau = 0.75$ . The minimum CP calculated is at  $\tau = 0.796$  with a value of 28.9%, this happens because at this point the already forward value of the  $P_e$  is paired with a higher  $P_a$  as the rate of increase for the extracted power is less steeper than that of the  $P_a$ . The last part of

the plots in Figures 5.2 and 5.3 shows the recovery period by which all of the plots are going back to its initial values.

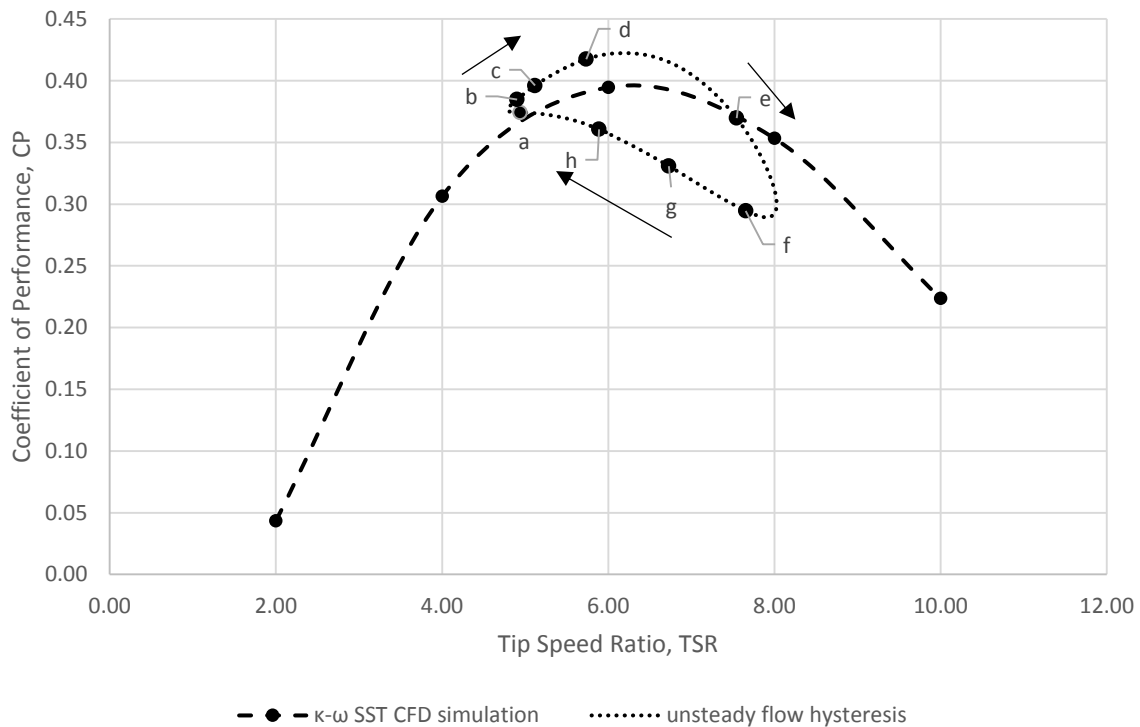


Figure 5.4 Unsteady Flow Hysteresis Curve for TSR = 6 over the steady flow performance curve for the Sheffield HATT

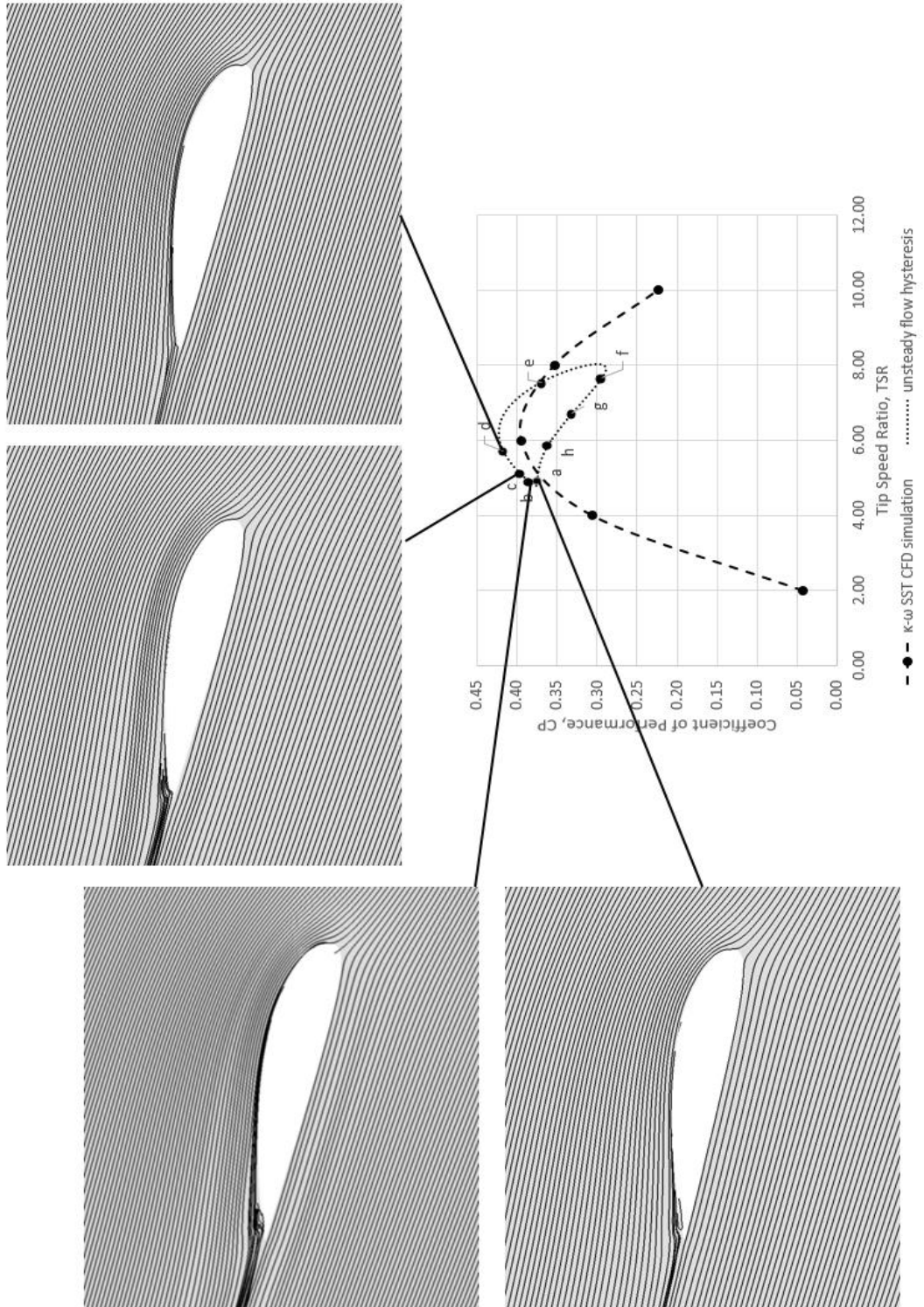
Another way of presenting the unsteady response of the Sheffield HATT is by plotting an instantaneous CP-TSR curve over the steady flow performance curve from Chapter 4 as presented in Figure 5.4. Plotting the hysteresis curve for an unsteady flow response also ensure that the simulation is fully converged as the whole curve follows one cycle which means the initial and end points of the cycle will meet each other even if the turbine will be allowed to run more rotations. Initial observation of Figure 5.4 shows that the unsteady simulation does not follow the steady flow curve and results in a hysteresis curve. The hysteresis curve has a region joined by the points **a** to **e** that shows a higher CP value than that of the steady curve with a maximum value occurring at an instantaneous TSR of 6.3 with an instantaneous CP of 42.2%. The lowest CP computed was 28.9% and is located at near-maximum TSR of 7.91 where a relatively steep decrease in CP value was also observed. This shows the availability of

some regions in the hysteresis curve that is higher than the cyclic-averaged CP and even the steady-state CP, the hydrodynamics on what is happening at each of the regions defined by the letters around the curve will be explained in details in the following section.

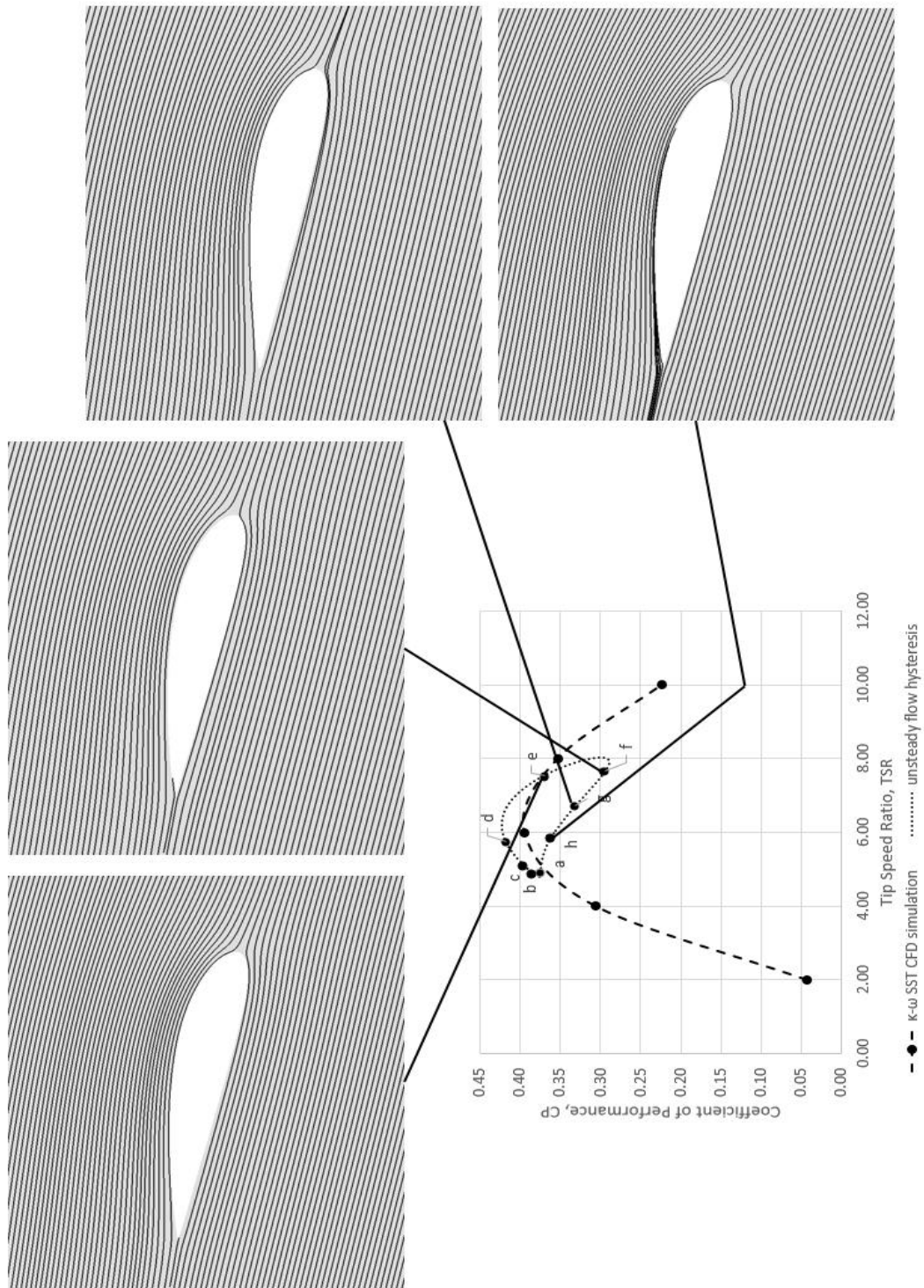
### 5.3 Results and Visualisation for TSR = 6 Simulation

In order to give an explanation for the behaviour of the unsteady flow response of the HATT, certain points around the curve were investigated and post-processed – this is to show the flow physics around the entire hysteresis curve. Each points are characterised with the corresponding instantaneous CP, TSR and/or velocity. The first data presented is the summary of the streamlines of the flow around the hydrofoil at different positions around the hysteresis curve. The velocity data was transformed into a rotational plane (*i.e.* relative velocity as seen by the rotor) so that it can be presented as the flow passing through the hydrofoil geometry of the blade. Streamlines on the aerofoil itself at the 25% and 75% span of the blade are presented in Figures 5.5.1 and 5.5.2. The first thing that can be observed from the streamline plots is the change in the incident angle of attack which is shown to increase as TSR decreases and follows the same trend with that of the steady flow simulation.

The instantaneous TSR variation for this simulation ranges from 4.8 to 8 which appears at an area in the middle of the performance curve as shown in Figure 5.4. From the streamline plots, small regions of flow separation are observed at low TSRs and this will be investigated more thoroughly in the later sections of this chapter. Two other unsteady cases are simulated and are presented in this chapter, one with a lower mean TSR of 4 and the other one at a mean TSR = 8. The unsteady TSR = 4 simulation will show more dramatic changes in the flow physics as the TSR is inclined at the region of the performance curve where big separations and stall is occurring. On the other hand, the sensitivity of the Sheffield HATT at small changes in AoA at high TSR will be investigated for the TSR = 8 unsteady simulation.

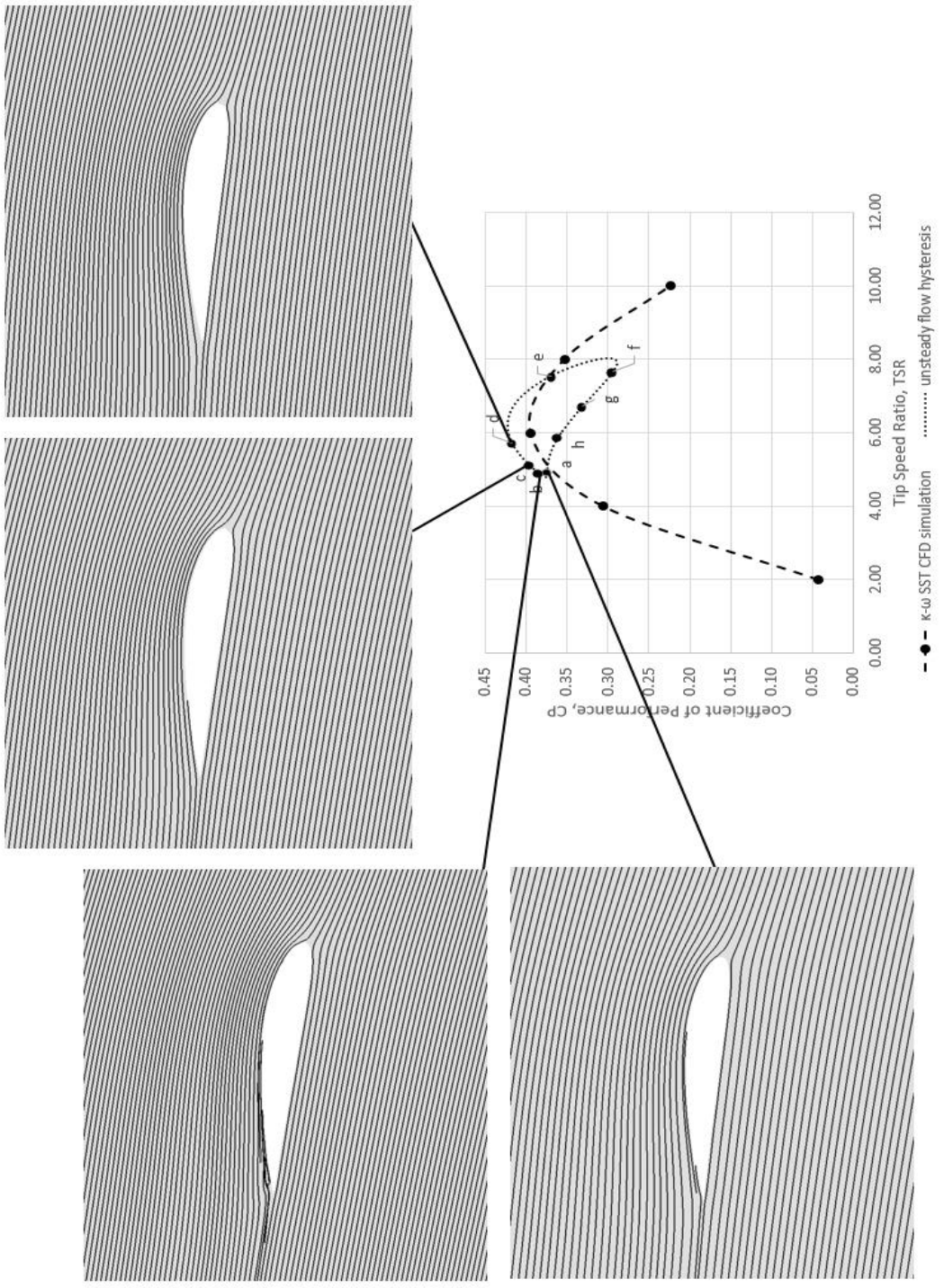


(a)

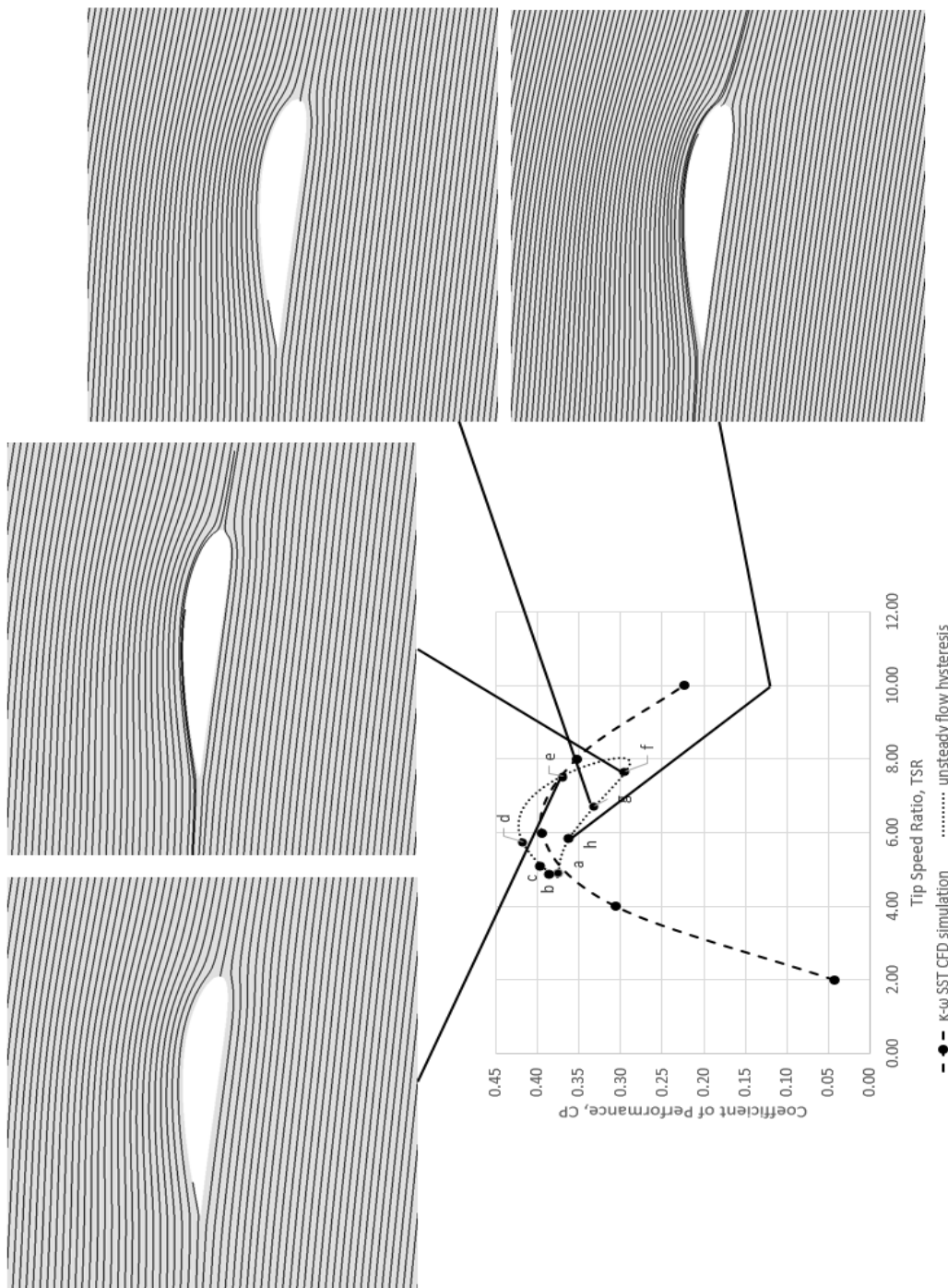


(b)

Figure 5.5.1 Streamlines for various positions in the hysteresis curve at 25% of the blade with points **a** to **d** (a) and points **e** to **h** (b) for the unsteady  $TSR = 6$  simulation



(a)



(b)

Figure 5.5.2 Streamlines for various positions in the hysteresis curve at 75% of the blade with points **a** to **d** (a) and points **e** to **h** (b) for the unsteady  $TSR = 6$  simulation

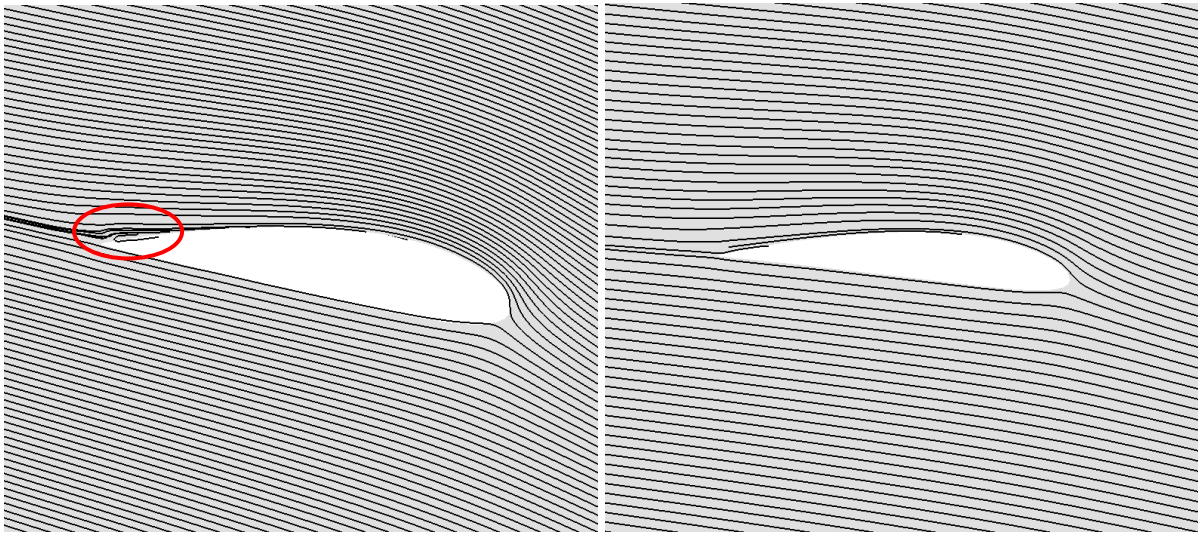
### 5.3.1 Process a to b

**a:** TSR = 4.94 (decreasing); velocity (increasing); CP = 0.374 (increasing)

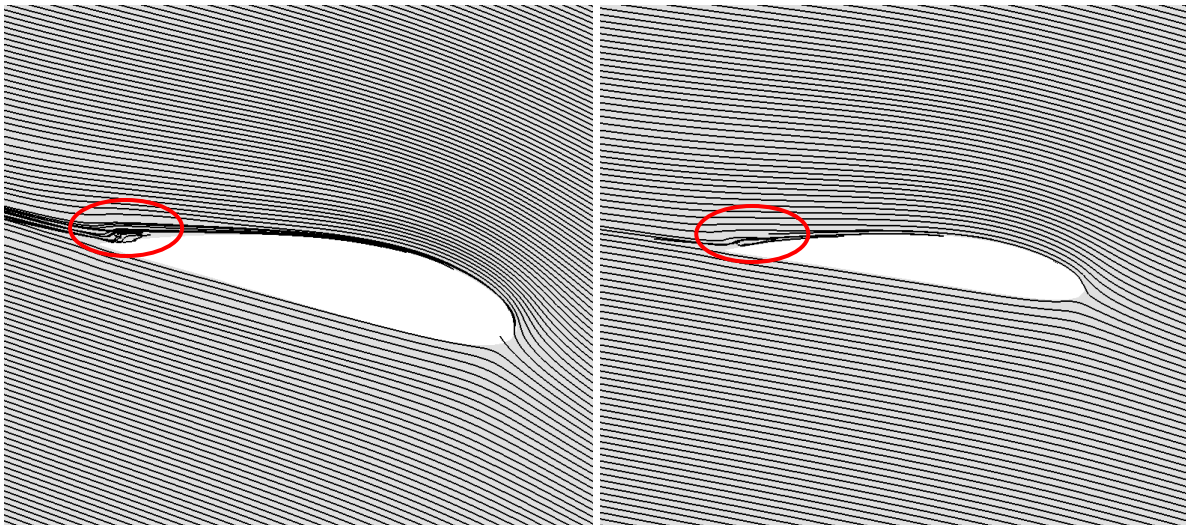
**b:** TSR = 4.82 (increasing); velocity (decreasing); CP = 0.382 (increasing)

Referring back to Figure 5.4, it can be seen that points **a** and **b** has very similar TSR's but with different CP values, this observation can also be seen for other parts of the hysteresis curve. Leishman states that circulatory effects on an aerofoil may induce the flow to have different loading at two points having the same TSR where one is approaching flow separation and the other is reattaching flow. Circulatory effects include the change on the induced velocity due to the vorticity in the shed wake and circulation in the trailing wake with the latter being associated with dynamic inflow. The observation in this study is similar to what is was observed in the unsteady flow simulation though Leishman and Milne *et al.* looks at the unsteady effect in blade loading and not the performance of the turbine (Leishmann, 2006 and Milne *et al.*, 2013).

It can be observed in Figure 5.6a that there is a small separation present near the trailing edge for the 25% blade span which is highlighted by a red circle. This means that the flow is starting to separate and this conclusion is supported by the process shown in **b** in figure 5.6b where separation has developed even at 75% blade span (also highlighted by a red circle) and where the angle of attack is lower because of the way the blade is designed with the twist being larger near the root and lower near the tip. These two points are the only parts of the hysteresis curve where separation is observed, this is again due to the fact that the variation in the instantaneous TSR is not enough to see drastic separation in the flow. Proceeding points like **c** and **d** already have attached flow therefore point **b** can be assumed to be the reattaching, this means that the flow process **a** to **b** shows similar observation to the one stated by Leishman where the turbine's response is affected by circulatory effects.



(a)



(b)

Figure 5.6 Streamlines at point **a** (a) and point **b** (b) for 25% of blade span (left) and 75% of the blade span (right) of the Sheffield HATT turbine blade

To investigate the process further, the normalised pressure for points **a** and **b** at the 75% blade span was computed and presented in Figure 5.7. The pressure was normalised using the trailing edge pressure presented in Equation 11. The addition of the atmospheric pressure in Equation 11 is to assure that all pressures will be positive and avoid sign problems in the trailing

edge but will make the difference in pressure appear larger but has the benefit of making all the plots consistent throughout.

$$P_n = \frac{P_x + P_{atm}}{P_{trailing\ edge}} \quad (eq\ 11)$$

A larger area under the pressure curve can be observed for point **b**, which means that the total lift at that time is higher than that of point **a**. Although a larger separation is observed for point **b**, which suggests larger additional drag due to form drag, the CP for point **b** is still higher than **a**. This means that the rate of increase of lift overpowered the effect of the increased drag and this has made the lift to drag ratio for point **b** to relatively higher. Going back to the steady flow simulations, at this TSR, no separation should be present based on the steady flow value of AoA, especially for the 75% span of the blade where an AoA=8.136° was calculated from the BEM simulation and does show a separation region on this profile. This suggests that the unsteady flow physics is very different to that at the steady flow.

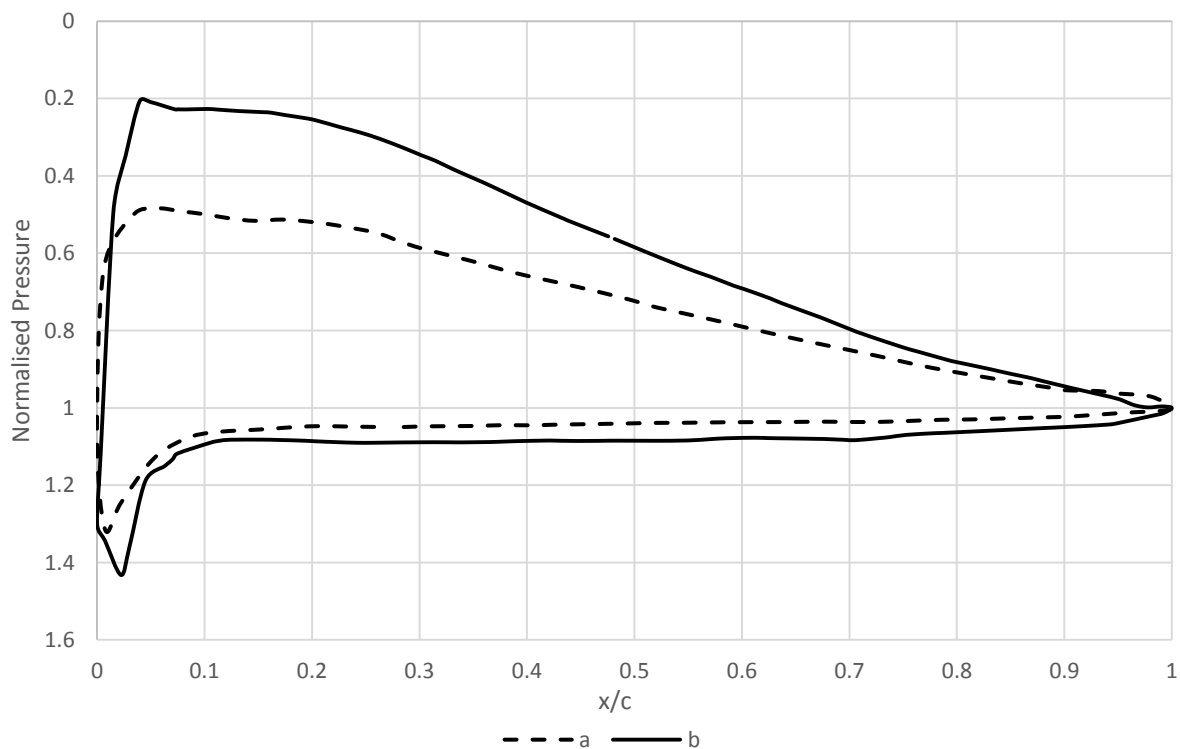


Figure 5.7 Normalised Pressure plots at 75%R for points **a** and **b**

Referring back to the cyclic unsteady response plot of the Sheffield HATT shown in figures 5.2 and 5.3, the process from point **a** to point **b** is part of the lag effect has manifested in the unsteady flow response as explained in Section 5.2. The separation on the flow that is present from points **a** and **b** will dissipate in the wake as the flow starts to reattach and the TSR starts to increase again. Lift and hence  $P_e$  should be expected to decrease at this point because the AoA is also decreasing but it is observed from the  $P_e$  plot at figure 5.2 that the power does not decrease instantaneously with the velocity change and a lag effect was observed. This can be associated with dynamic inflow whereas an induced flow happens when the flow is reattaching in the trailing edge then it will take time to reach equilibrium and the flow to be reattached. The increase in lift value can also be caused by the dissipating vortex in the trailing edge since a bigger pressure gradient will be present as the suction side pressure is becoming more negative (shown in Figure 5.7). The effect of this results into a small lag in the power extracted as presented in Figure 5.2.

### 5.3.2 Process **b**, **c**, **d** to **e**

- c:** TSR = 5.13 (increasing); velocity (decreasing); CP=0.397 (increasing)
- d:** TSR = 5.88 (increasing); velocity (decreasing); CP=0.418 (increasing)
- e:** TSR = 7.57 (increasing); velocity (decreasing); CP=0.367 (decreasing)

The effect of the lag in extracted power is still in effect in this region of the hysteresis curve, this results in a CP that is higher than the steady state curve as shown in Figure 5.4. The instantaneous TSR is continuously increasing at this point and as a result, the incident AoA on the hydrofoil sections is starting to decrease which will dictate a lower lift value. Milne and Leishman both agreed that when TSR starts to increase in value, circulatory effects will be in less effect to the turbine (Milne *et al.*, 2012). Leishman argued that unsteady effects may

manifest but only as moderate amplitude and phase variations which is what is observed in this particular process (Leishman, 2006).

Another effect of increasing TSR is that the flow around the hydrofoil sections is getting fully attached – the case of point **d** as illustrated in figure 5.8 for example. Although the lift is lower, the lift to drag ratio at this point is high which means higher performance of the turbine will be observed as the effect of form drag is negligible at fully attached flow. The decrease in AoA will continue to manifest as the TSR continued to increase as presented in Figure 5.9. The normalised pressure shown in Figure 5.10 also agree with this observation. The only difference this time is that the value of CP has started to decrease at around  $\tau = 0.528$  as described in Section 5.2. One possible explanation for this is that the rate of decrease in lift is greater than the rate of decrease in drag making the lift to drag ratio lower and the drag variation to dominate the flow. It can also be observed that for the normalised pressure plot for point **e** in Figure 5.10, the difference in pressure in the leading edge is becoming too narrow and is at the edge of overlapping. This is the effect of very low incident AoA. For high TSR's, the incident AoA will become negative and will induce a negative lift in the hydrofoil section, making the CP lower as observed in the TSR = 10 steady state pressure plots in Section 4.6.

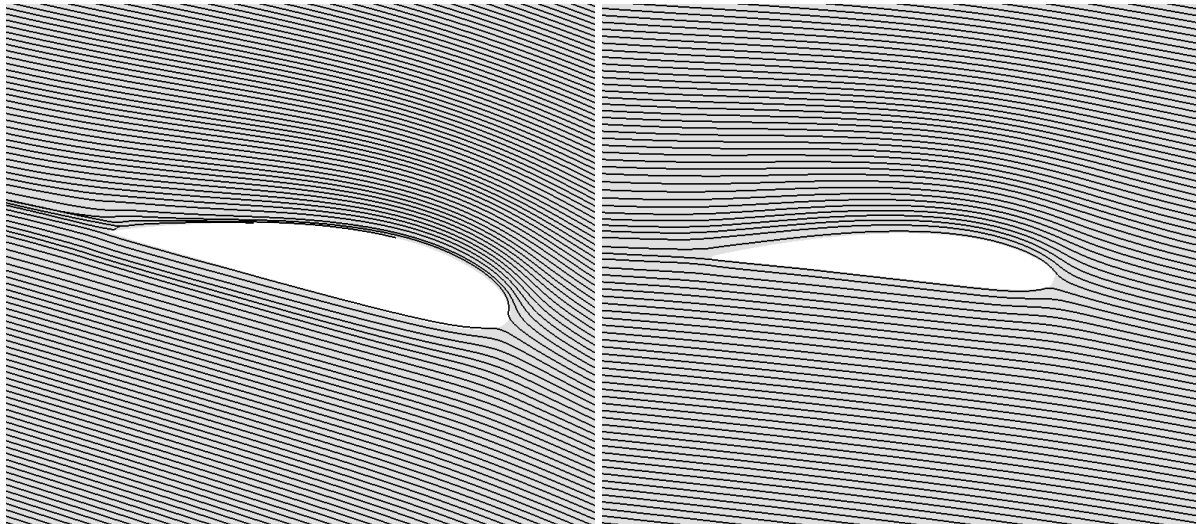


Figure 5.8 Streamlines at point **d** for 25% of blade span (left) and 75% of the blade span (right) of the Sheffield HATT turbine blade

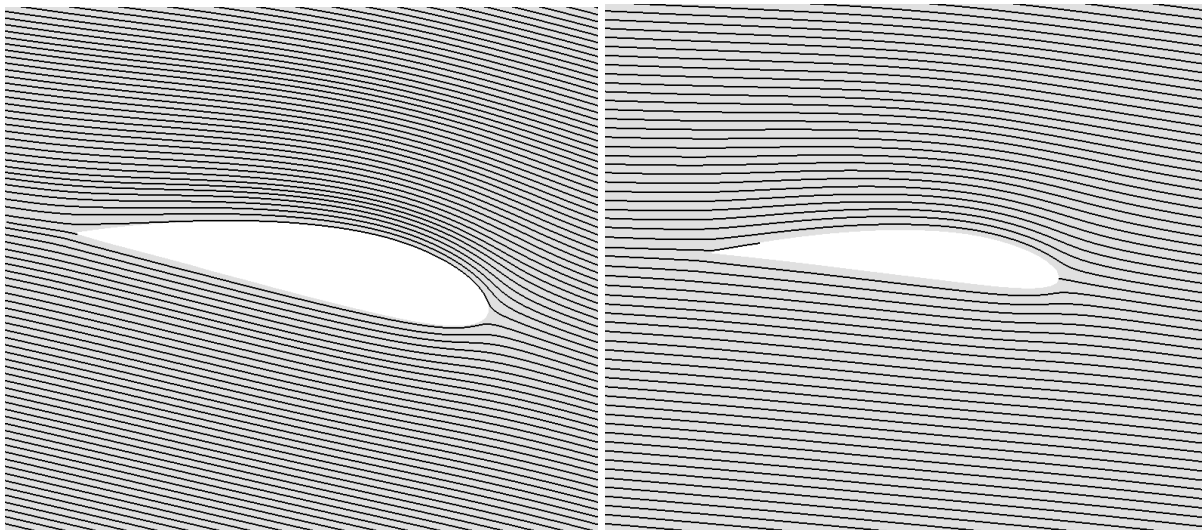


Figure 5.9 Streamlines at point **e** for 25% of blade span (left) and 75% of the blade span (right) of the Sheffield HATT turbine blade

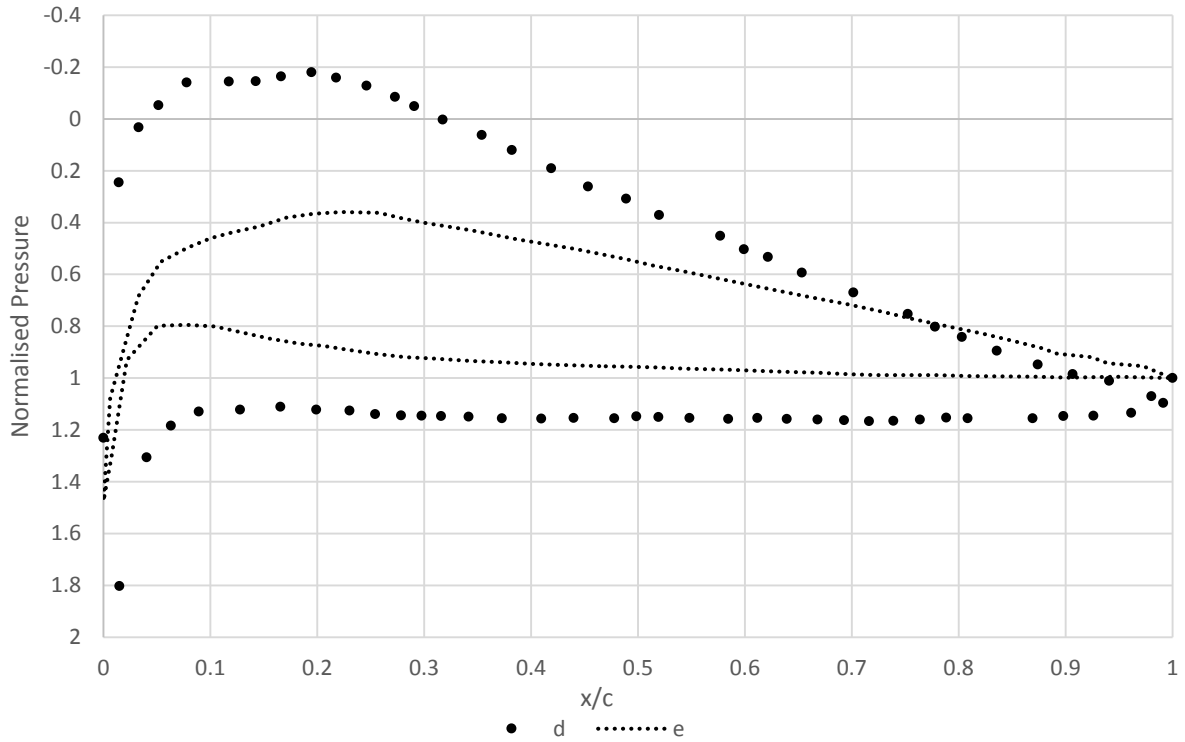


Figure 5.10 Normalised Pressure plots at 75%R for points **d** and **e**

### 5.3.3 Process e to f

**f:** TSR = 7.679 (decreasing); velocity (increasing); CP=0.294 (increasing)

Referring back to Figure 5.4, the process from **e** to **f** is the start of the unsteady response where it shows lower performance than the steady state curve. Points **e** and **f** have similar TSR but the calculated CP for those points extremely varies. Figure 5.11 shows the normalised pressure plot comparing points **e** and **f**, it can be seen that it follows the same trend observed in section 5.3.2 where the lift is decreasing as proved by the area under the pressure plots.

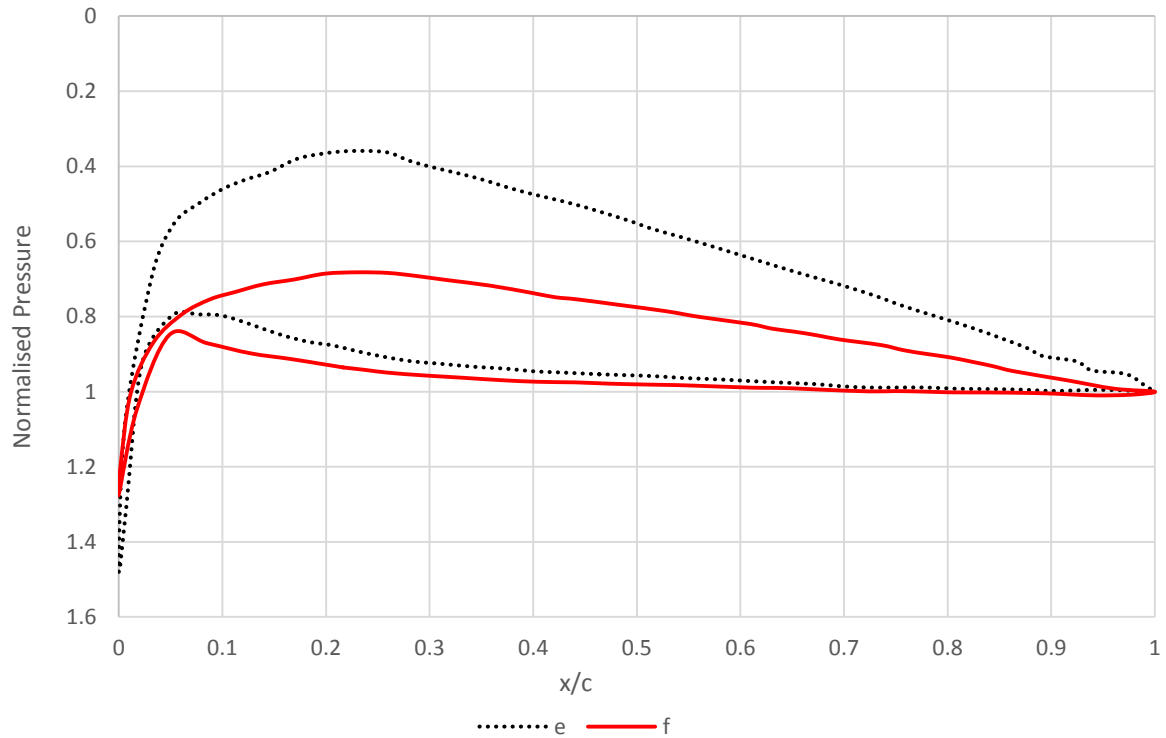


Figure 5.11 Normalised Pressure plots at 75%R for points **e** and **f**

Figure 5.12 shows the  $C_l/C_d$  plots NACA 4414 and NACA 4420. These hydrofoils are the foil sections at the 25% and 75% span of the Sheffield HATT blade. It can be observed that the maximum rate of change of  $C_l/C_d$  with AoA for the two aerofoils occurs at two locations; when the AoA is between  $-3.5^\circ$  to  $3.5^\circ$  and when it reaches between  $12^\circ$  to  $15^\circ$ . Going back to process **e** to **f** of the unsteady response, a sharp decrease in CP is observed. This is a 7.3% decrease in CP for just a difference of 0.11 in TSR (from 7.57 to 7.679). The calculated geometric incident AoA for NACA 4414 will be around  $3.5^\circ$  at TSR = 7.5 and  $2.9^\circ$  at TSR = 8. This angle corresponds to a slope of 10.27 in the NACA 4414  $C_l/C_d$  plot which means a degree change in the incident AoA will have a change of 10.27 units in the  $C_l/C_d$  value. This observation is the cause of the sensitivity of the turbine's response (in CP) at high TSR (low AoA) and also explained the large changes in CP for small changes in AoA for the process **e** to **f**.

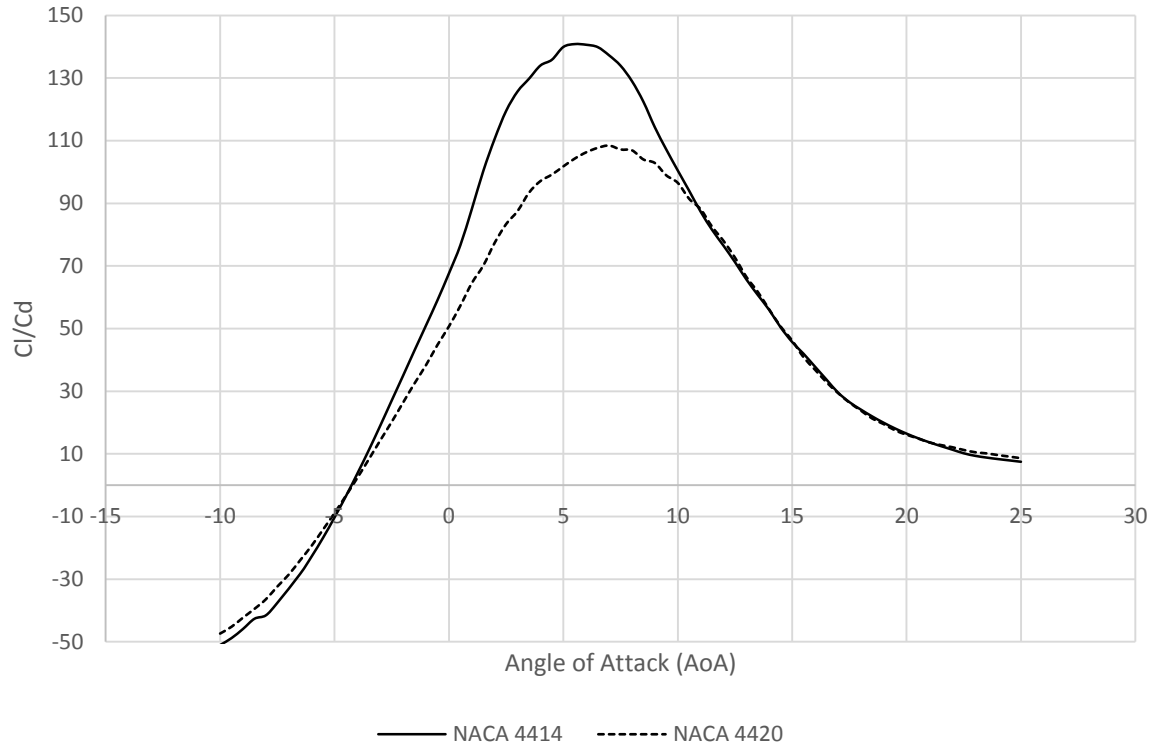


Figure 5.12 Cl/Cd plot for NACA 4414 and NACA 4420 which is the aerofoil sections at 75% and 25% of the Sheffield HATT blade respectively

### 5.3.4 Process f, g to h

**g:** TSR = 6.794 (decreasing); velocity (increasing); CP=0.328 (increasing)

**h:** TSR = 5.876 (decreasing); velocity (increasing); CP=0.361 (increasing)

This is the process by which the turbine's CP start to recover from the lowest point near point **f** as the TSR decreases and the hydrofoil gained incident AoA. The blade starts to gain higher lift again but the very low point at f does not allow complete recovery of the CP value which is lower than the steady flow performance curve. The slope of the **f-g-h** curve is steeper than that of the steady flow curve, this can mean that the rate of increase in CP for the unsteady flow is higher but again the very low CP value at point **f** makes it hard for the CP value to recover.

Another area to be noted within the hysteresis plot in Figure 5.4 is the CP values at point **d** and point **h**. The difference in TSR is very minimal but the difference in CP is the highest across the hysteresis curve for the same TSR. There is no significant difference in the streamline across the two points (as observed in Figure 5.5) but the normalised pressure showed otherwise where a higher area under the pressure curve was observed for point **d** as shown at Figure 5.13 meaning that the lift force generated was be higher for the same TSR, also supporting the lag effects as described in the earlier sections.

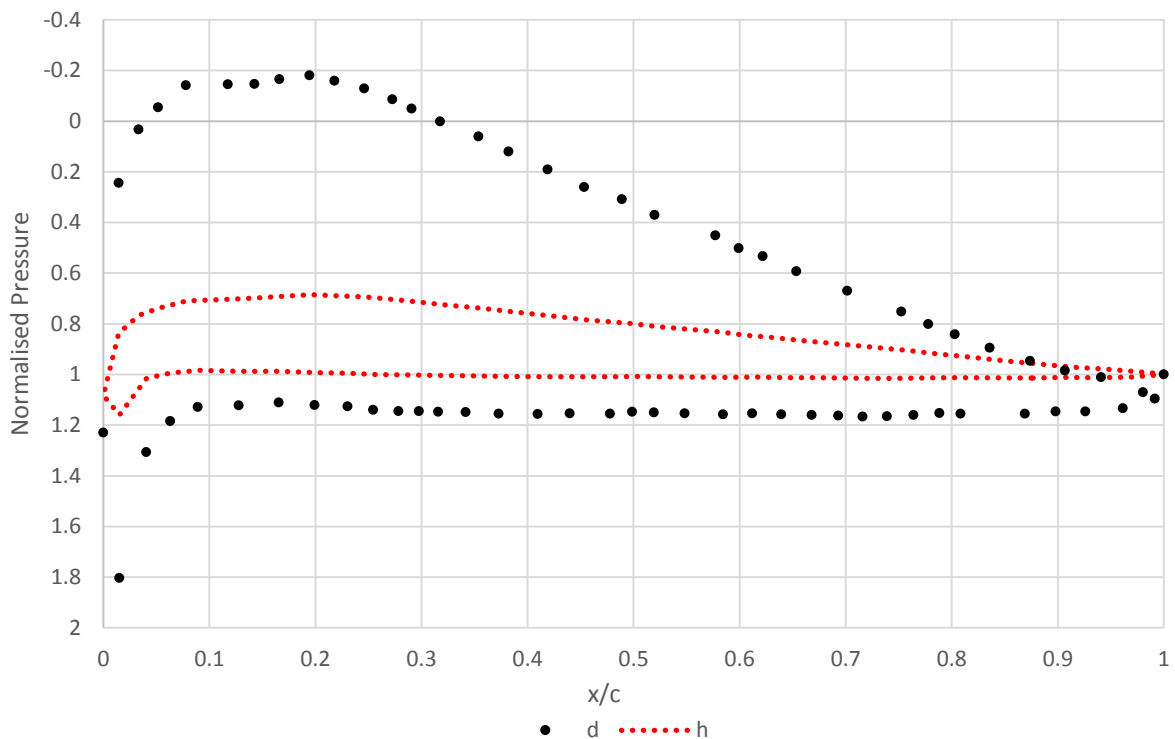


Figure 5.13 Normalised Pressure plots at 75%R for points **d** and **h**

### 5.3.5 Process **h** to **a**

This is the process by which the TSR is decreasing and where separation is starting as it was established that there is separation starts at point **a**. Comparing the process to the steady flow performance curve for the same TSR range, the CP values should be decreasing but the opposite is observed for the process **h** to **a**. The CP calculated for process **h** to **a** is still

increasing but with a rate lower than that of the **f-g-h** region until it reaches point **a** which is almost the same value as of the steady flow CP at that particular TSR. The lower rate can mean that the increase in drag, since the flow is starting to separate again, is affecting the rate of increase in CP but not enough to make the CP value decrease.

These sections above explained what is happening in each of the regions in the hysteresis curve resulting from the unsteady flow simulations but it is also better to understand what is happening at extreme cases at both ends of the turbine's turbine performance curve. In order to investigate further, unsteady simulations at TSR=4 and TSR=8 were conducted and is presented in the next sections.

#### **5.4 TSR = 4 Unsteady Flow Simulation**

One of the off-peak performance unsteady simulation that is looked at in this study is the performance simulation of the Sheffield HATT at TSR=4. This is to gain idea of what is happening at the lower TSR side of the TSR=6 hysteresis curve in the last section. Streamlines to be observed in this simulation is expected to be more dramatic as the TSR range of values is between 3.2 and 5.35 which assures flow separation because of the high AoA. The amplitude and frequency of the UDF in the TSR=6 unsteady simulation was maintained and the available water power for the steady flow simulation was also the same in accordance to the rotational velocity and the time step computed. The resulting unsteady velocity that will be implemented after an iterative process was presented in Equation 12.

$$u(t) = 1.9402 + 0.49 \sin(2\pi t) \text{ (eq. 12)}$$

The inlet velocity described above is implemented on the same mesh for the TSR = 6 simulation together with the solver used for that simulation. Cm for the simulation was monitored which was transformed further into CP and then plotted against the instantaneous

TSR to complete the hysteresis curve presented in Figure 5.14. It can be seen that the hysteresis curve for the TSR=4 simulation is thinner and longer as compared to the TSR = 6 simulation which suggests that the CP variation for this simulation will be larger. Most of the hysteresis curve is lower than the steady performance curve as well but is still following the trend of the steady-state turbine performance curve. The cycle-averaged CP for this simulation is at 22.6% which is 8% lower than the steady flow value for TSR=4 which is 30.6%. This is a bigger difference when compared to that of the base case unsteady simulation and this is mostly caused by the stall effects that will be seen in the flow streamlines over the hydrofoils at 25% and 75% blade span in Figure 5.15.

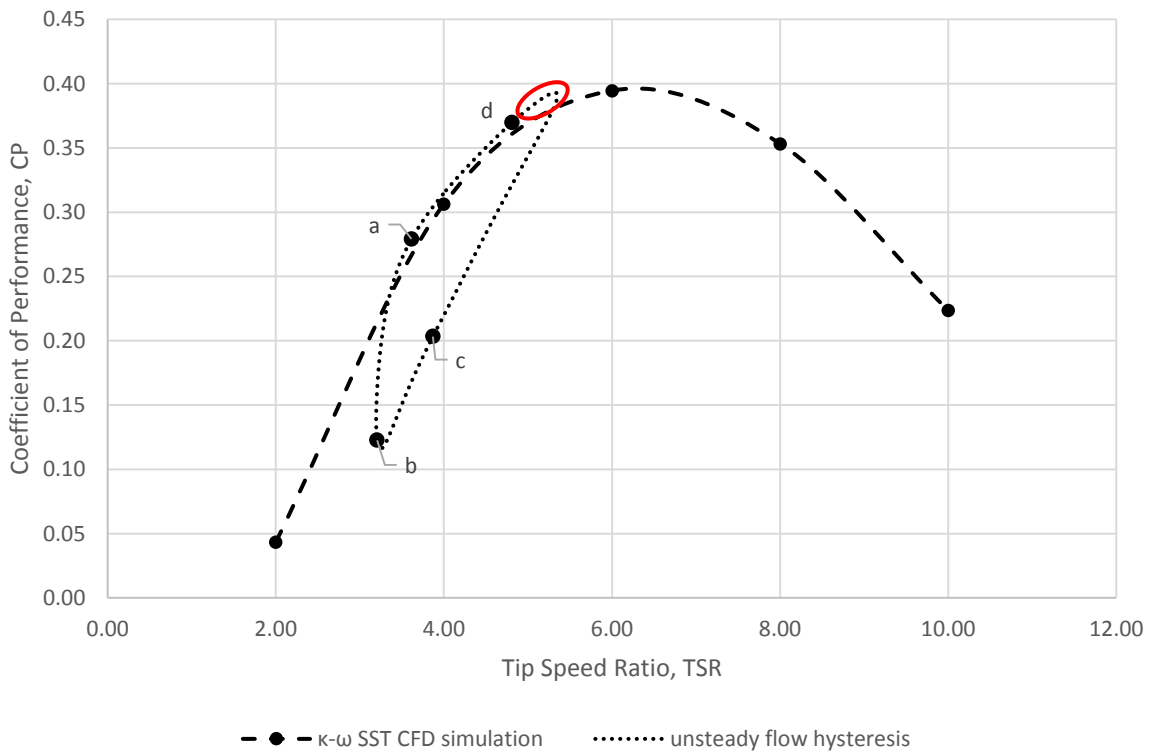
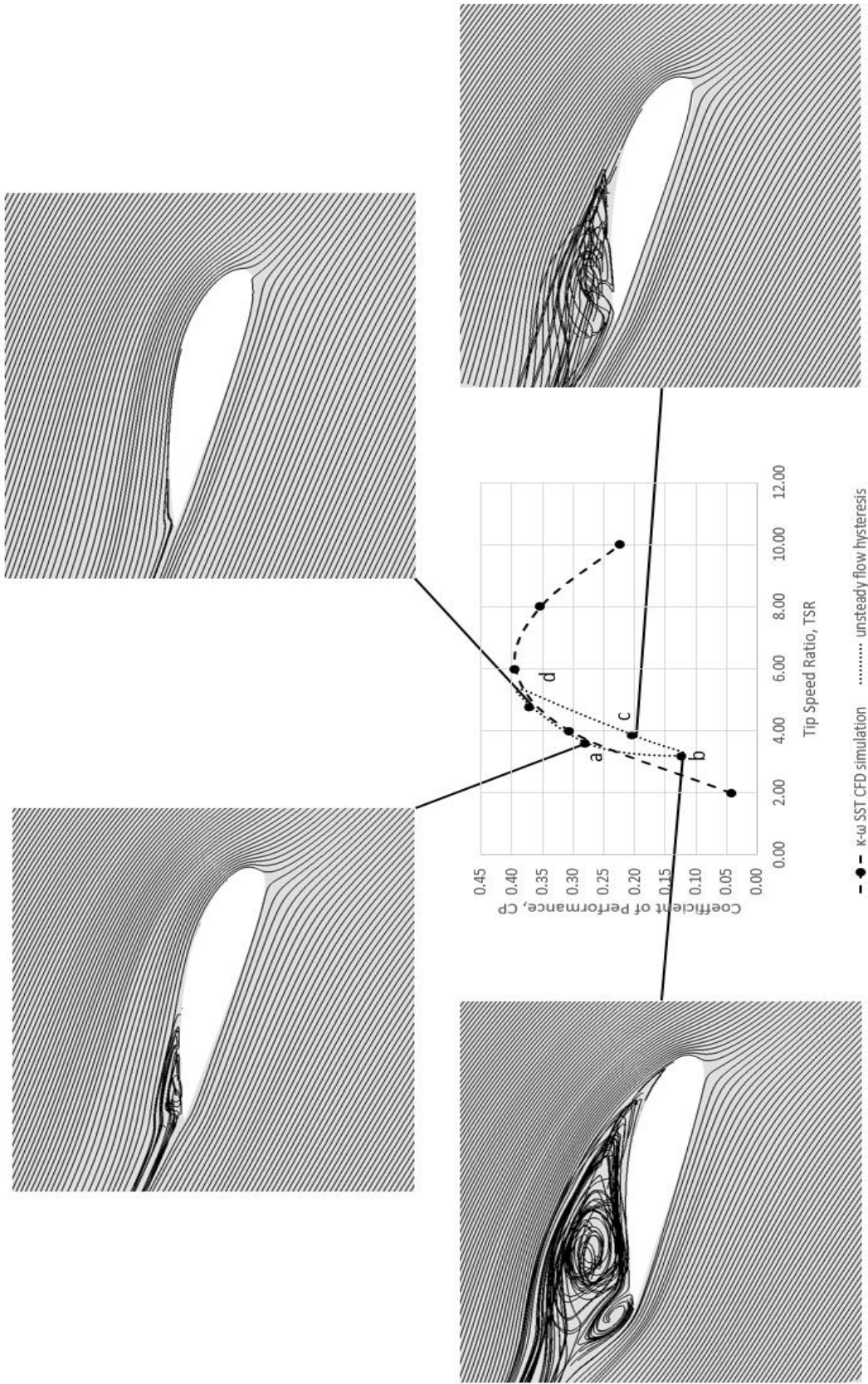
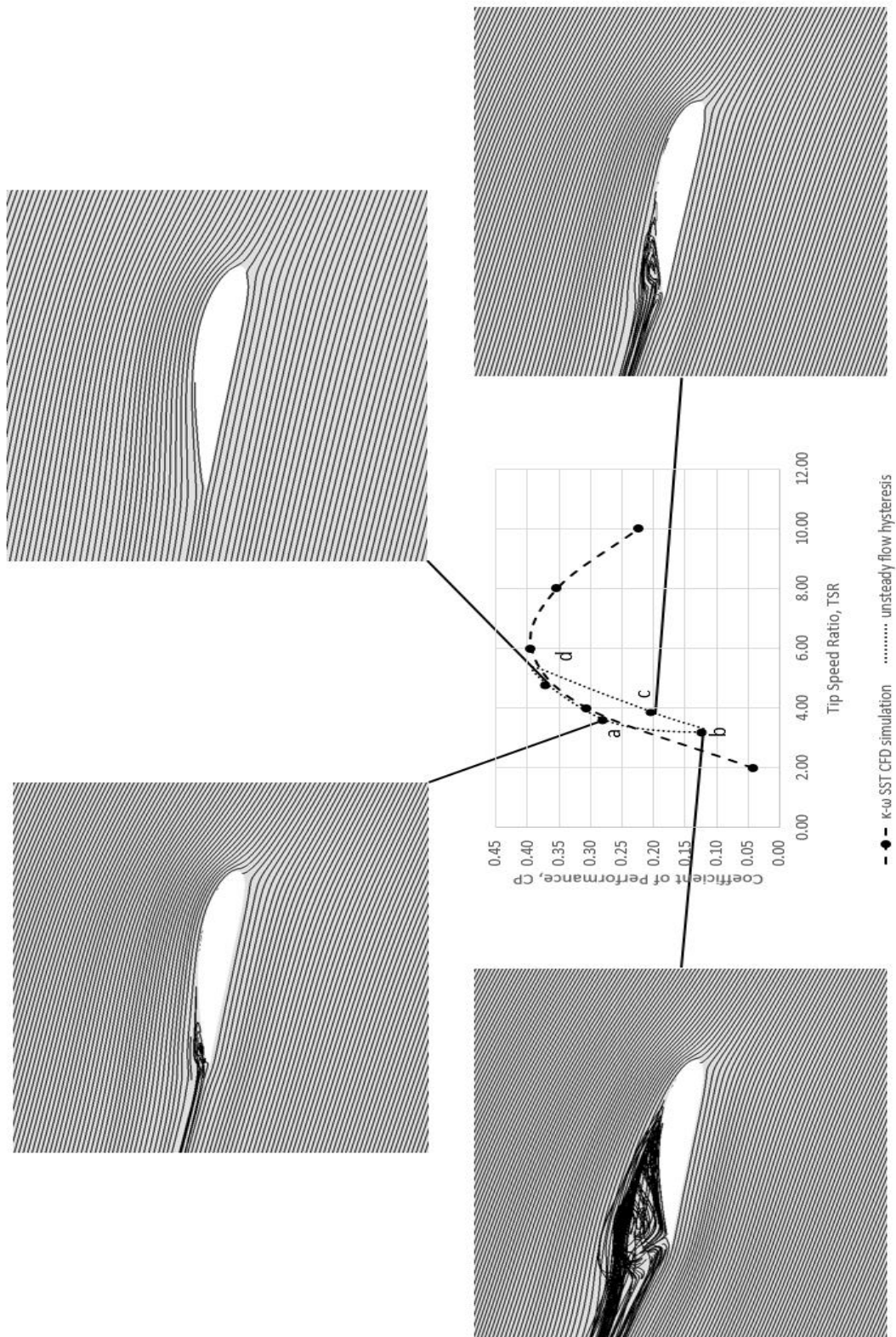


Figure 5.14 Unsteady Flow Hysteresis curve for TSR=4 over Steady flow performance curve



(a)



(b)

Figure 5.15 Velocity Streamlines for different position on the hysteresis curve at 25% (a) and 75% (b) span of the blade for unsteady TSR = 4 simulation

Initial observations of the streamlines show that this simulation shows a more dramatic flow physics around the hydrofoil sections presented at 25% and 75% blade span. Bigger separation can be seen in just the streamlines alone. It was shown in Figure 5.15 how the separation vortex was formed and developed over the hydrofoil and how the flow reattached as well. Whether the presence of the observed separation are detrimental or not to the performance will be presented in the proceeding sections. Also, as an additional visualisation of the vortices forming over the blades, they were also emphasized using the  $\lambda_2$  vortex tube determination process presented in Figure 5.16 and is explained in section 5.4.1.

#### **5.4.1 Three-Dimensional Visualisation of Vortices in the Flow Using the $\lambda_2$ criterion**

Leishman stated that circulatory effects happening in tidal turbines subjected to unsteady flow can be caused by vorticity in the shed wake at the blade and the circulation in the trail wake. (Leishman, 2006) The trail wake effect is often associated with dynamic inflow which results to a lag in the hydrodynamic response of the turbine (in attached flow) to the instantaneous changes in the inflow velocity. The interaction between dynamic inflow and shed wake effect is usually treated separately because of the difference in time scale where dynamic inflow effects has the larger time scale which is usually 1-1.5 rotor revolution which can be the reason why it is the one dominating in low frequency flows. (Milne, 2013)

Another effect that can be looked at in unsteady flow is the stall behaviour of the tidal turbine. Leishman states that dynamic stall can be associated with the dynamic induced camber effect which results to a delay in trailing edge separation. (Leishman, 2006) The formation and dissipation of a leading edge vortex along suction side of the turbine blade is also associated to unsteady flow behaviour, this results to an additional low pressure in the upper surface of the blade which affects performance and loading.

Visualisation of the vortices happening in an unsteady flow simulation is important to see if they induce an effect to the instantaneous performance of the turbine. In addition to the streamlines and pressure plots for certain hydrofoil section of the Sheffield HATT, a vortex structure visualisation was also implemented using the  $\lambda_2$  criterion. The  $\lambda_2$  criterion is an improve method of the Q-criterion method of determining vortex tubes and structures with Q being defined as the second invariant of the curl of the fluid flow. If the vorticity magnitude is greater than the magnitude of strain on a fluid element then Q is positive. If Q is positive and the pressure at that certain fluent element is lower than the ambient pressure, then a vortex structure exists. Jeong and Hussain suggested a new method to determine the presence of a vortex structure using the eigenvalue of the symmetric tensor of the variable Q. It is stated that if  $\lambda_2$  is negative, it will assure that a vortex core exists. (Proof of the method can be seen in Jeong and Hussain, 1995) Vortex structures in CFD simulation results can now be presented using iso-surfaces of  $\lambda_2$ . The four time-steps results for the unsteady simulation of the Sheffield HATT for TSR=4 was post-processed to determine the existence of vortex structures in the blade which can serve as additional information to explain the unsteady response of the tidal turbine.

Just like how the unsteady TSR=6 hysteresis curve was broken down into different sections to explain what is happening in the flow, the unsteady TSR=4 hysteresis curve was also presented in separate processes with an additional way of explaining it by way of the  $\lambda_2$  vortices as the vortices can be clearly shown for this simulation.

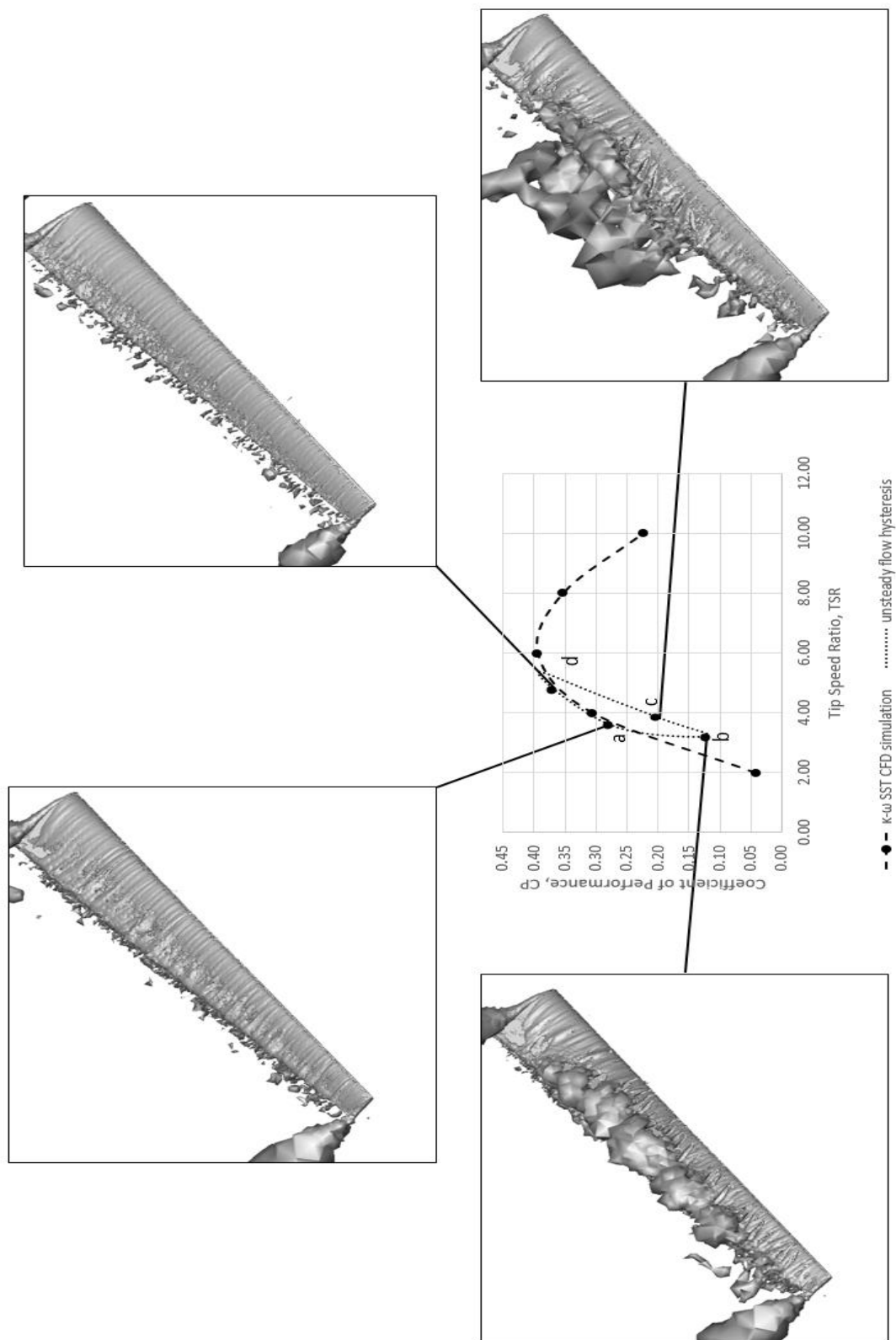


Figure 5.16  $\lambda_2$  criterion vortex tube representation at different points of the unsteady TSR = 4 simulation

#### 5.4.2 Process a to b

**a:** TSR = 3.594 (decreasing); velocity (increasing); CP=0.2767 (increasing)

**b:** TSR = 3.213 (increasing); velocity (decreasing); CP=0.1196 (decreasing)

It can be seen from process **a** to **b** that there is a steep decrease in the computed CP as the cycle goes to lower TSR value. A difference of 15.71% was calculated for just a 0.381 change in TSR. It can be seen in Figure 5.17 that at point **a**, the flow starts to separate as shown in the 25% hydrofoil section and a small separation even occur at the 75% blade span section as highlighted by a red circle. The flow continued to separate and achieve full separation and stall at point **b** as shown in Figure 5.18. A main vortex was observed in the 25% hydrofoil section for point **b** at Figure 5.18 (left) highlighted by a red circle and a secondary vortex highlighted with blue circle while relatively smaller vortex was observed for the 75% blade span hydrofoil.

For this process, it can be seen that the effect of full separation was detrimental to the performance of the turbine which is also the case for the steady flow performance curve. The normalised pressure for process **a** to **b** is presented in Figure 5.19 and it can be seen that the area under the pressure curve for the two points is not that different to each other with **b** having a slightly bigger area, this means that the lift between the points is not that different and it is the additional drag (due to form drag) caused by the separation that makes the variation in the instantaneous CP calculated. In terms of the  $\lambda_2$  criterion as presented in Figure 5.16, the vortex that started forming at point **a** has already been developed at point **b** which can be seen as bigger structures still on the suction side of the blade. This structures will be monitored and will be a main contributor in the explanation of process **b** to **c**.

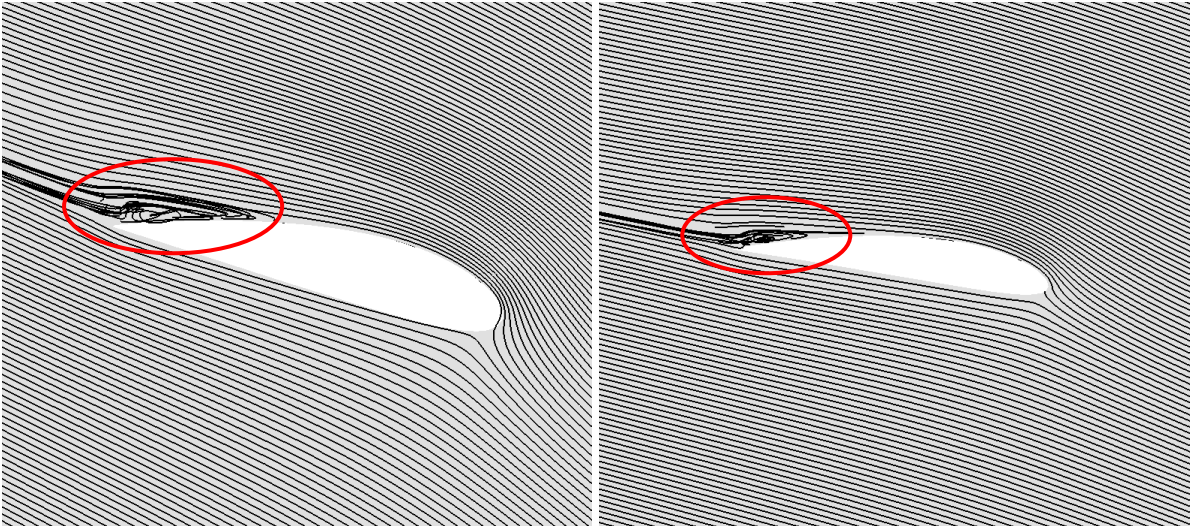


Figure 5.17 Streamlines at point **a** for 25% of blade span (left) and 75% of the blade span (right) of the Sheffield HATT turbine blade

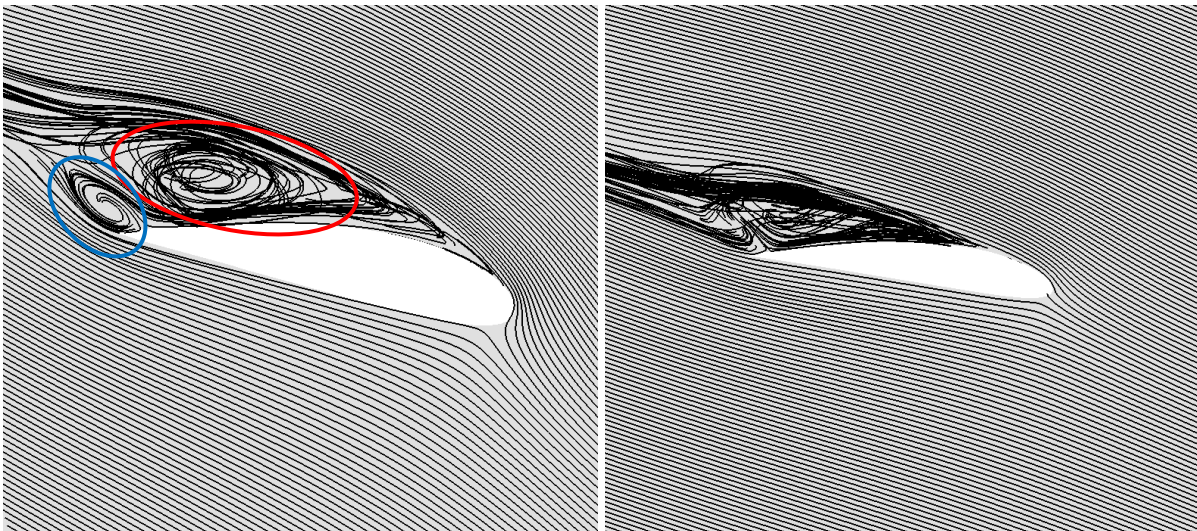


Figure 5.18 Streamlines at point **b** for 25% of blade span (left) and 75% of the blade span (right) of the Sheffield HATT turbine blade

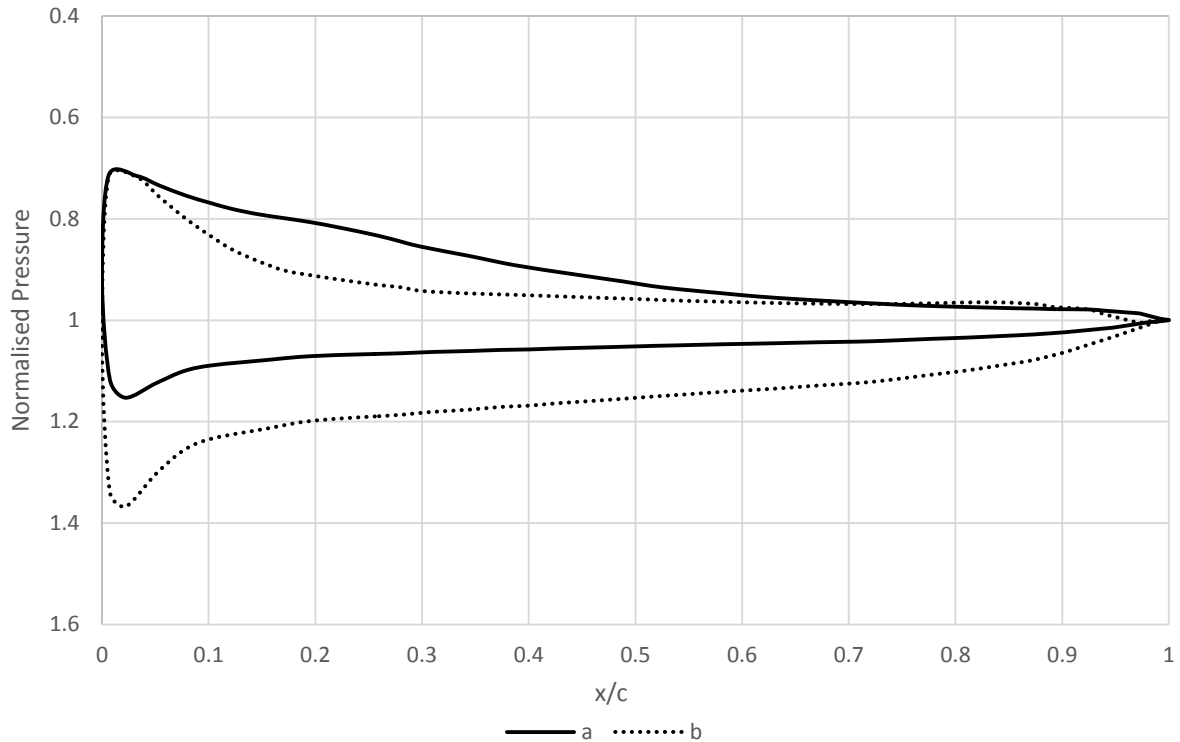


Figure 5.19 Normalised Pressure comparison at 75%R for the process **a** to **b**

### 5.4.3 Process **b** to **c**

**c:** TSR = 3.869 (increasing); velocity (decreasing); CP=0.2033 (increasing)

An increase in the CP value is observed for this process as the TSR for the turbine starts to increase and the flow around the blades to start reattaching, as can be seen in Figure 5.14. The big separation seen for point **b** is starting to dissipate and becoming smaller as shown in Figure 5.20, suggesting that the flow is reattaching. It can also be seen in Figure 5.16 that the vortices that are still in the suction part of the blade at point **b** has already been dissolved across the wake side of the blade. Normally, it is expected to have the lift force acting on the blade at this point to be decreasing because the TSR is also increasing and since the incident AoA on the blade is also decreasing but the area under the pressure curves say otherwise as presented in Figure 5.21 and suggests that there is an increase in the lift force at this point of the cycle. Starting from point **a**, an increase in lift has been observed after the vortex structures was

formed in the top of the suction side of the blade. This can be accounted to the additional negative pressure induced by the sitting vortex in the suction side making the lift higher. This is the observation Leishman has described as dynamic stall lift overshoot.

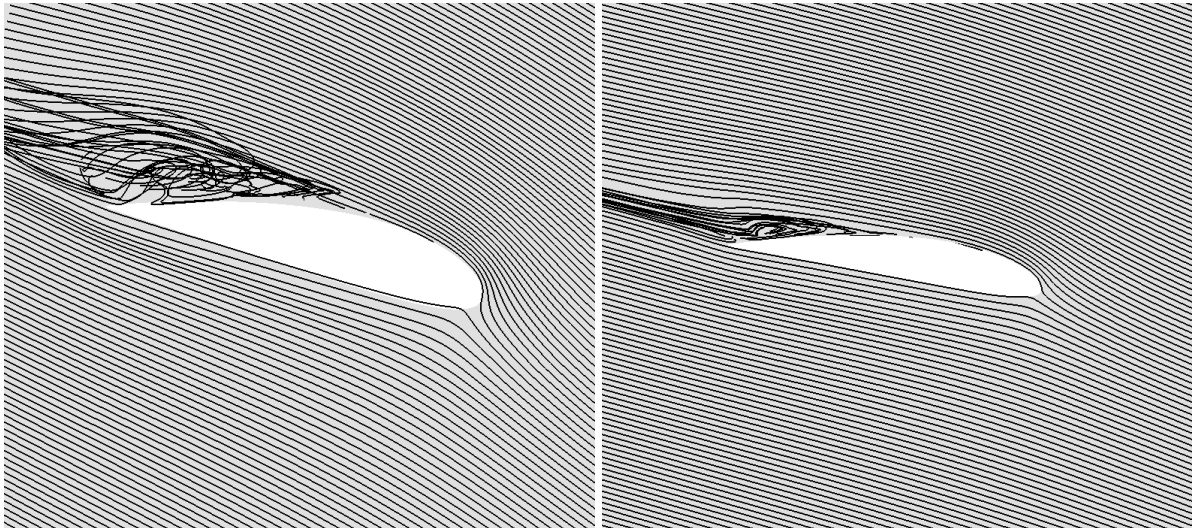


Figure 5.20 Streamlines at point **c** for 25% of blade span (left) and 75% of the blade span (right) of the Sheffield HATT turbine blade

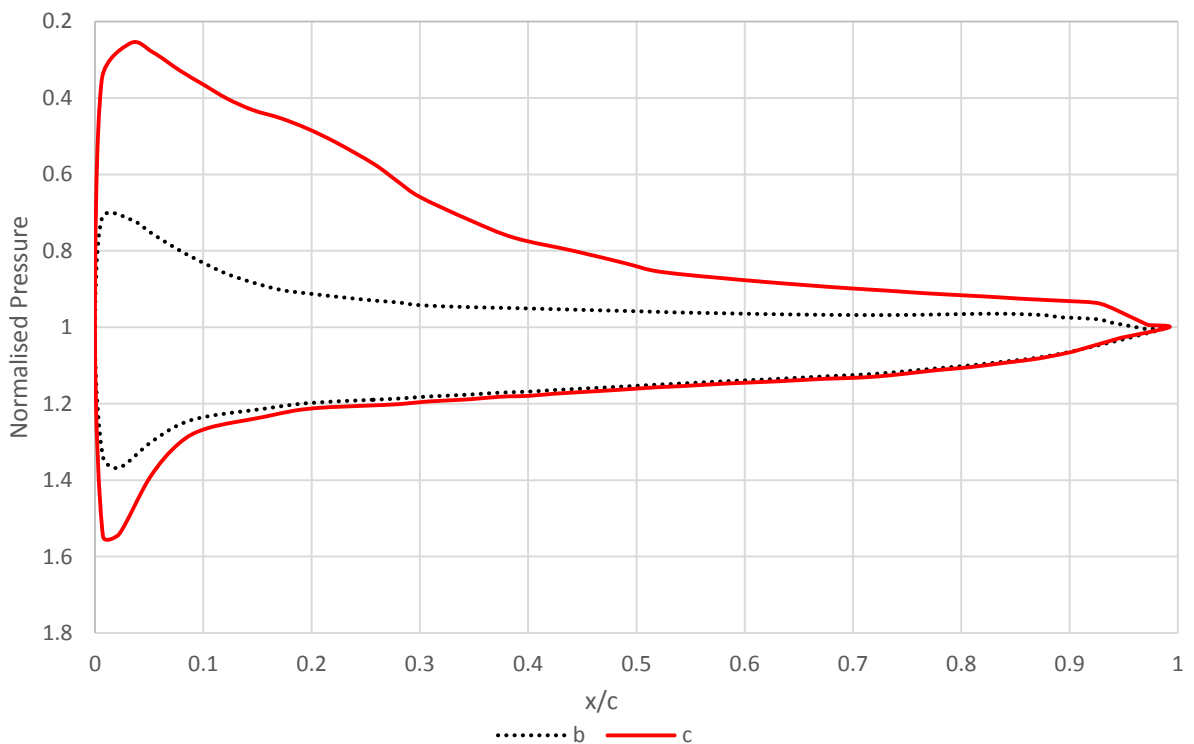


Figure 5.21 Normalised Pressure comparison at 75%R for the process **b** to **c**

Although there is a significant increase in lift, the effect in the computed CP value is not that significant because of the additional effect of form drag that is still affecting the turbine's performance. Once the sitting vortex structure on top of the suction side dissipates away completely, as can be seen happening in point **c**, the lift increase effect will not prevail but the additional drag effect will also disappear leaving.

Retuning to Figure 5.14, it can be seen that the TSR for points **a** and **c** has a difference of 0.275 with point **c** having the higher TSR. Speaking in steady-state terms, a higher TSR should mean a lower AoA and hence more attached flow but the opposite is observed as can be seen in Figures 5.17 and 5.20. The flow in point **a** is more attached, which means that there is a delay or a lag in the reattachment of the flow at the same TSR in point **c**. This could be the reason why there is a lower performance at point **c** (where the flow is reattaching) when compared to the corresponding value of CP for the same TSR when the flow is in the process of separation at point **a**. Again, this is confirming Leishman and Milne's observation of unsteadiness whereas two points in the hysteresis curve showed different values for the process of separation and reattachment.

#### **5.4.4 Process c to d**

**d:**     TSR = 4.81 (decreasing); velocity (increasing); CP=0.3697 (decreasing)

This process will complete the reattachment of the flow that will happen near the maximum CP for the simulation. When the flow process reaches point **d**, the flow is already fully attached as shown in Figure 5.22 with a very small disruption near the trailing edge for the 25% blade span hydrofoil section. The effect of the late reattachment is still observed until the flow reaches the maximum performance where the hysteresis curve went over the steady performance curve as highlighted by the red circle in Figure 5.14. CP has increased

continuously from point **c** up to the maximum point in the hysteresis curve and just started to decrease as TSR decrease again going to point **d**.

In Section 5.4.3, it was discussed that the lift can still increase as long as the vortex structure is still present sitting on the top part of the suction side but in point **d**, the vortex is finally dissolved as can be observed in Figure 5.16. There are no more structures that can be seen above the suction part of the blade. Since there will be no more additional lift from the sitting vortex structures, the lift force at point **d** should become lower as supported by the area under the pressure plots at Figure 5.23.

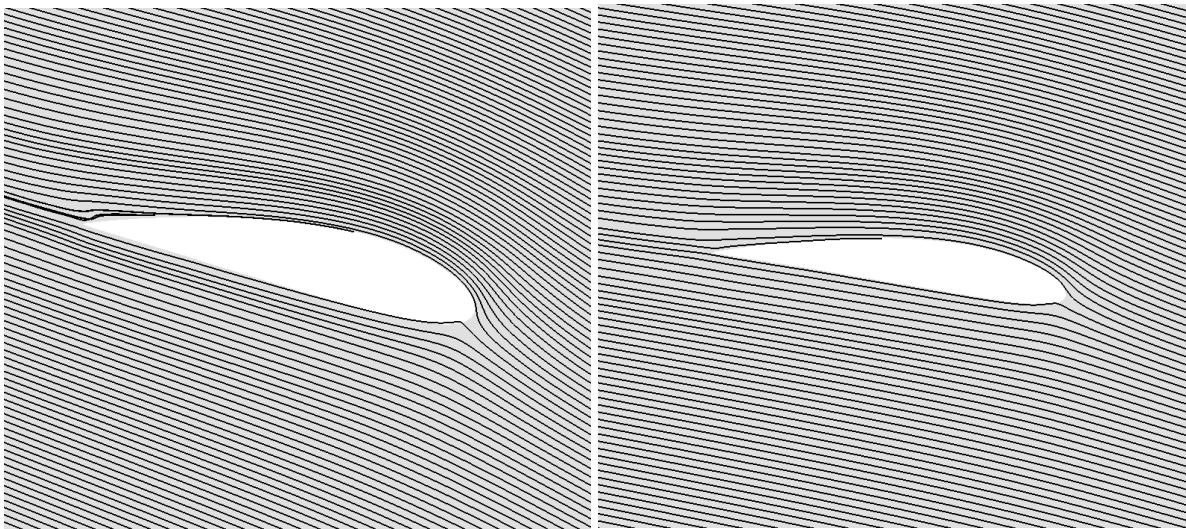


Figure 5.22 Streamlines at point **c** for 25% of blade span (left) and 75% of the blade span (right) of the Sheffield HATT turbine blade

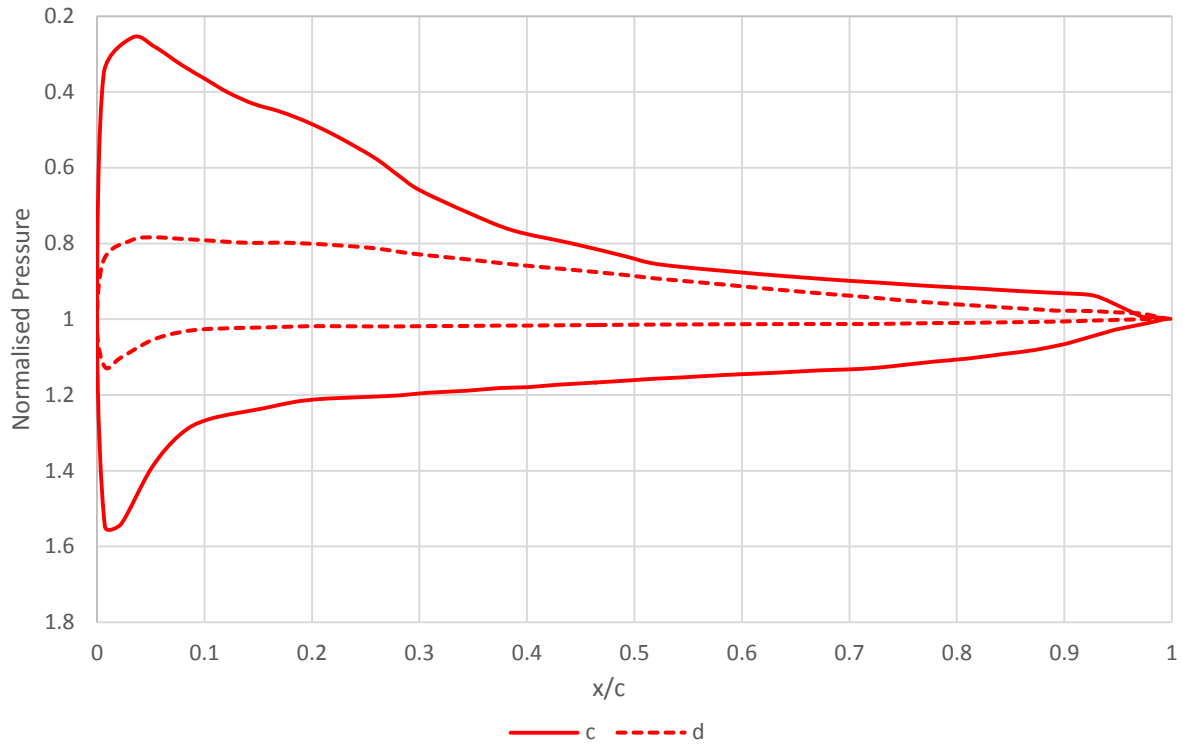


Figure 5.23 Normalised Pressure comparison at 75%R for the process **c** to **d**

#### 5.4.5 Process **d** to **a** and the conclusion for the unsteady **TSR = 4** simulation

Referring back to Figure 5.14, it can be observed that this process is very close to the steady flow performance curve. The flow around the blades is still fully attach but will start to separate as TSR starts to decrease, this will result into a decrease in CP because of the effects of separation in lift and drag in a manner that is very similar to the steady flow regime. It can be seen from Figure 5.24 that there is an increase in the lift force from **d** to **a** because of the increase in the incident AoA as TSR decreases. In terms of the vortex structures, we can see that from point **d** to **a**, there are small structures forming near the trailing edge of the blade at point **a** which proves that separation is starting.

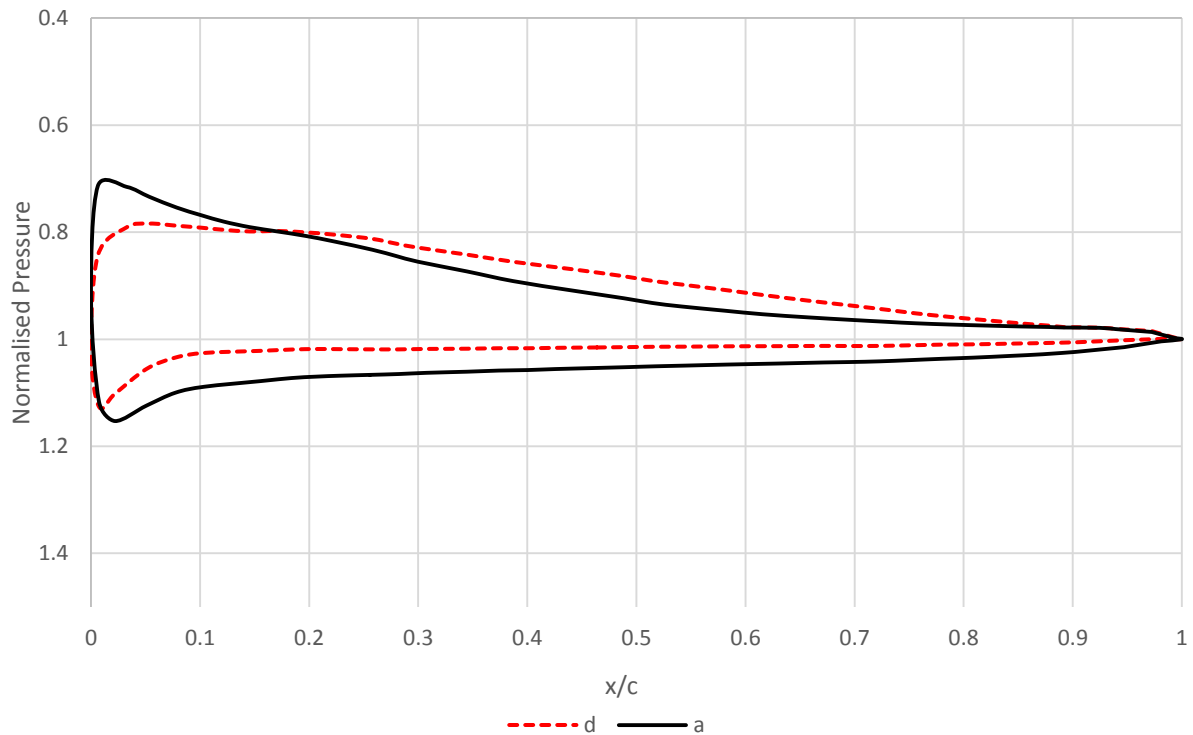


Figure 5.24 Normalised Pressure comparison at 75%R for the process **d** to **a**

In conclusion, this lower TSR unsteady simulation proved that the existence of vortex structures and separation in the flow around the blades under unsteady flow results in variation on the hydrodynamics on the blade as presented in each process in this section. Main points per process includes a negative effect in performance due to the formation of a vortex structure from the separation in the flow from point **a** to **b**, the negative effect of additional form drag due to the vortex structure at this process overpowered by the increase in lift observed. An increase in lift was observed as long as the structure remained on the suction side of the blade, lift starts to decrease when the vortex structure dissolved and the flow reattached. As the TSR increases from process **c** to **d**, the flow starts to reattach but there is a delay in the reattachment when the streamlines for similar TSR for different sides of the hysteresis curve were compared. Although lift is decreasing gradually after reattachment, the lift to drag ratio increases because the additional form drag was not present anymore. Process **d** to **a** is the start of the separation phase and the hysteresis curve behaves very close to the steady state performance curve.

## 5.5 TSR = 8 Unsteady Simulation

The Sheffield HATT model was also simulated using another offset unsteady simulation with a mean TSR of 8. The same method used for the offset TSR = 4 unsteady simulation was implemented for this simulation. The objective for this is to gain idea on the response of the Sheffield HATT for high TSR similar to what is obtained for the one in TSR=4. The unsteady incident velocity implemented for this simulation is presented in Equation 13, this is also achieved by doing an iterative method to match the water power available similar to TSR =4 and 6 simulations.

$$u(t) = 1.94 + 0.49 \sin(2\pi t) \text{ (eq. 13)}$$

The  $C_m$  for the simulation for each time-step was monitored and the resulting CP was computed and was plotted in a hysteresis plot shown in Figure 5.25. A sharper but thinner hysteresis curve was observed for this simulation, the variation of the CP values obtained was the biggest of the three cases presented in this chapter. Going from point **a** to **b** and then to **c**, it can be observed that the slope of the line tangent to the curve increases as the TSR increases. From point **b** to the lowest point of the curve alone, the CP value has a difference of 20.6%, this is higher than the difference of the highest and lowest CP calculated for the TSR = 6 unsteady case which is just 13.3%. This suggests and confirm the same observation for TSR = 6 that the turbine's unsteady performance response is very sensitive to changes for high instantaneous TSR. At point **b**, the instantaneous TSR is at 9.54, this corresponds to a steady geometric AoA of 1.5 degrees for the NACA 4414 and it has a tangent slope of 22.45 in the Cl/Cd plot presented in Figure 5.12, this slope is very close to the highest slope calculated for the that plot as well. This explains the very sensitive response in terms of the turbine's CP, since the Cl/Cd changes drastically over a small amount of change in TSR, it will also reflects on the instantaneous CP obtained for the turbine.

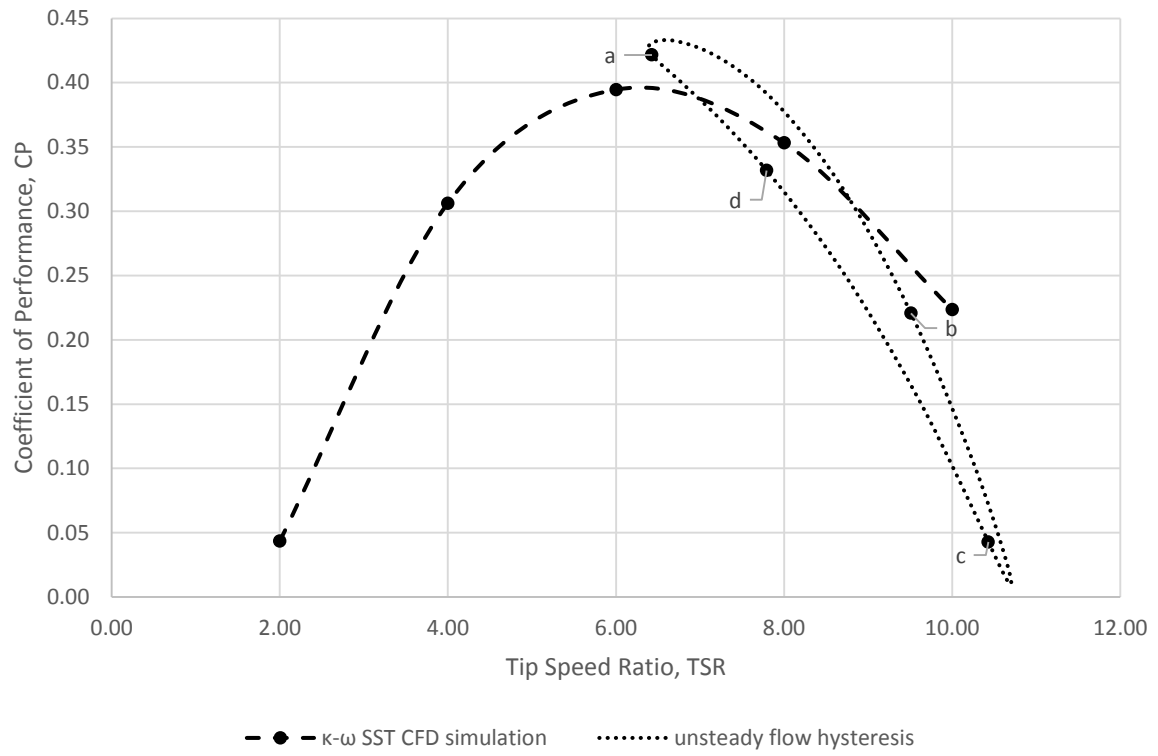
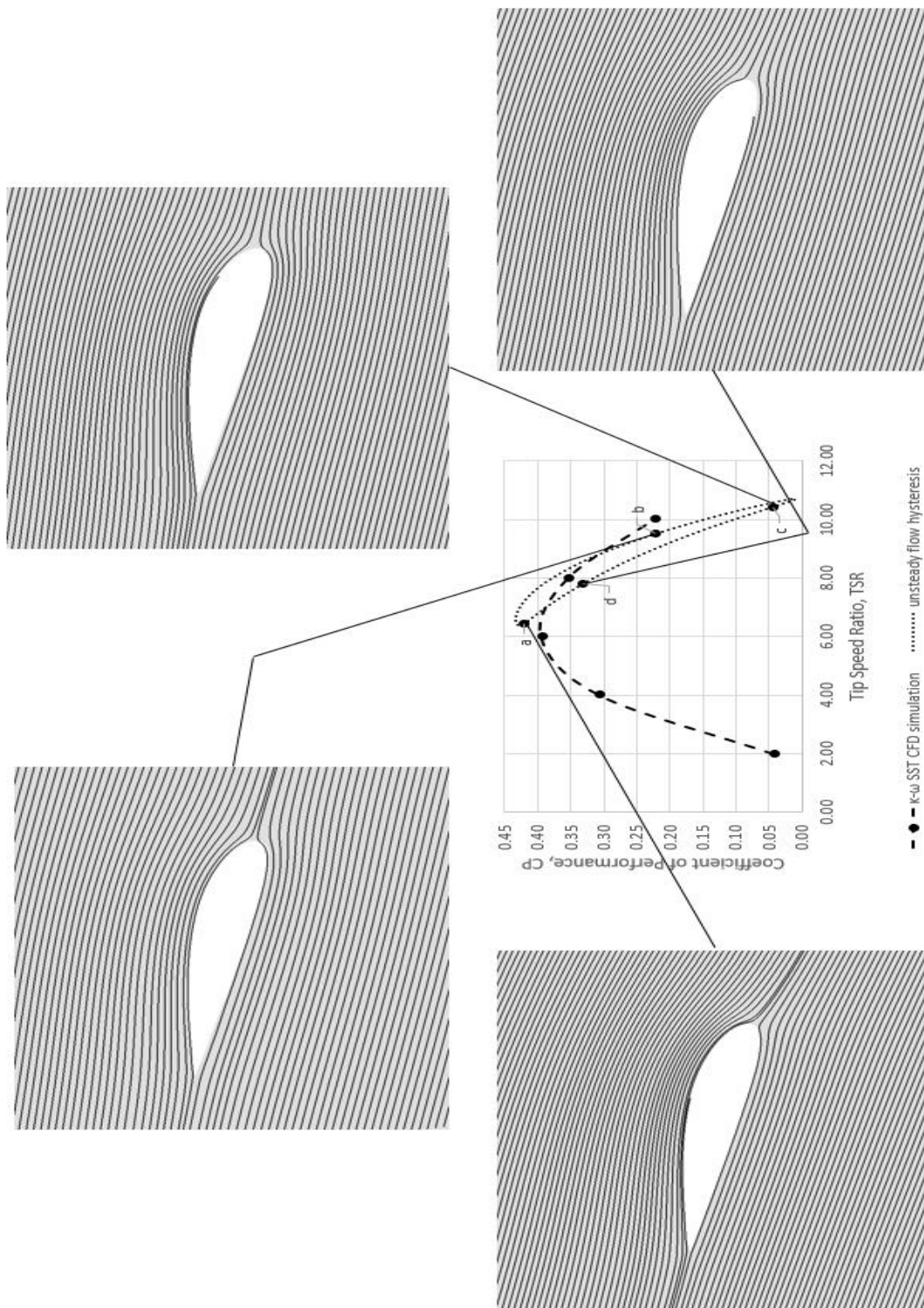
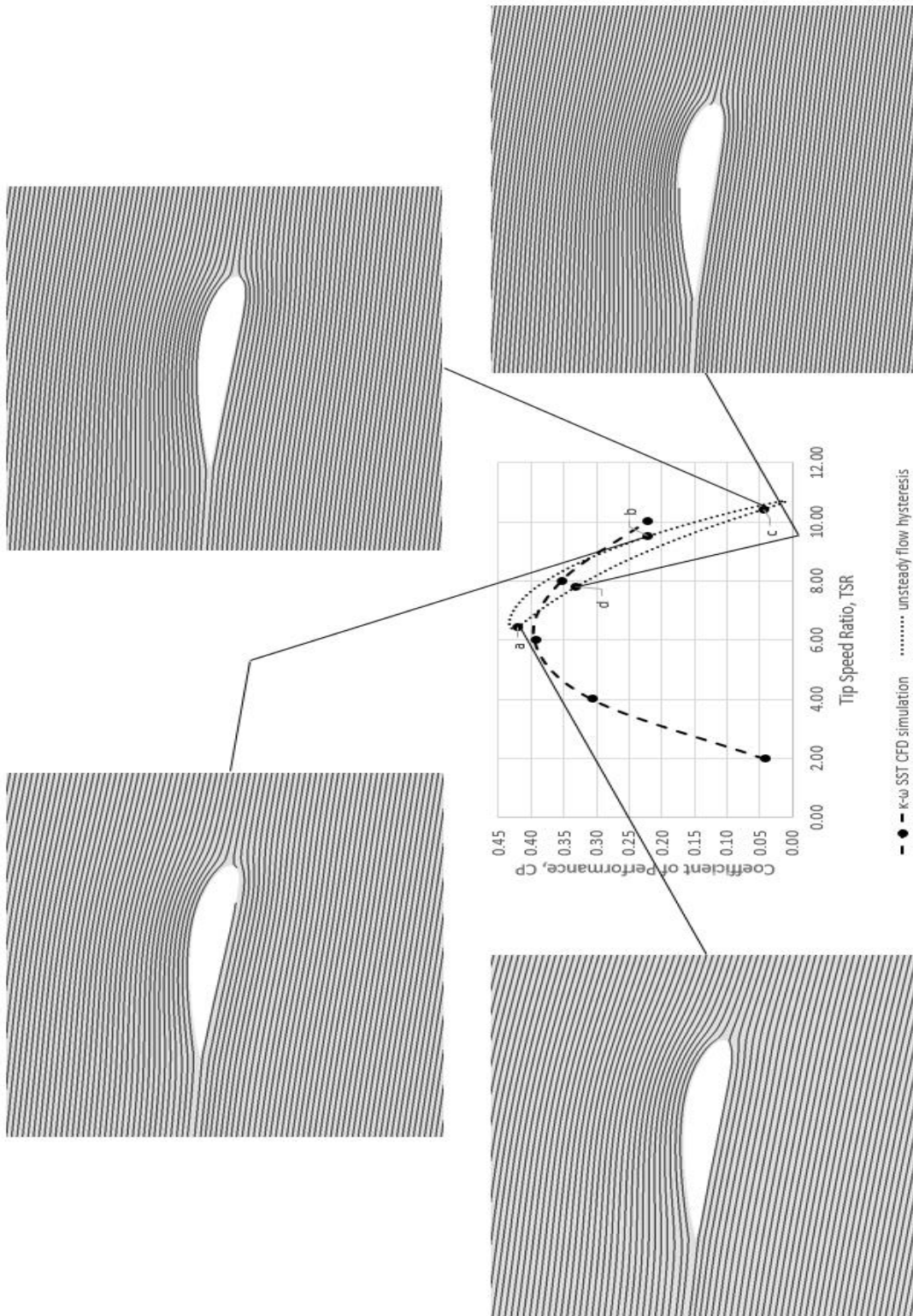


Figure 5.25 Unsteady Flow Hysteresis curve for TSR=8 over Steady flow performance curve



(a)



(b)

Figure 5.26 Velocity Streamlines for different position on the hysteresis curve at 25% (a) and 75% (b) span of the blade for unsteady TSR = 8 simulation

Presented in Figure 5.26 are the streamlines for the 25% and 75% span of the blade for certain points in the unsteady TSR=8 simulation's hysteresis curve. It can be observed that there is no separation or any disturbance within the streamlines over the blade hydrofoil sections, this means that the effects seen and presented for the TSR=4 simulation because of vortex structures will not be observed in this case as well. The changes in the incident AoA for the different data points in the hysteresis curve can also be observed visually, the decrease of the AoA as TSR increases on points **b** and **c** for the 75% span hydrofoil section can be observed just by looking at Figure 5.26. Both of which having incident AoA of negative values which will be elaborated later in this section.

The cyclic-averaged CP computed for this simulation is at 35.1% which is close to the steady state CP at TSR=8 which is at 35.33%. This is the closest unsteady simulation's CP when compared to its steady state counterpart and may be explained by having no separation at the flow at all and the decrease in the instantaneous CP is only caused by the sensitivity of the turbine to  $C_l$  changes at low AoA and the presence of negative area under the normalised pressure plots suggesting negative lift. The detailed hydrodynamics for this simulation is presented in the following sections.

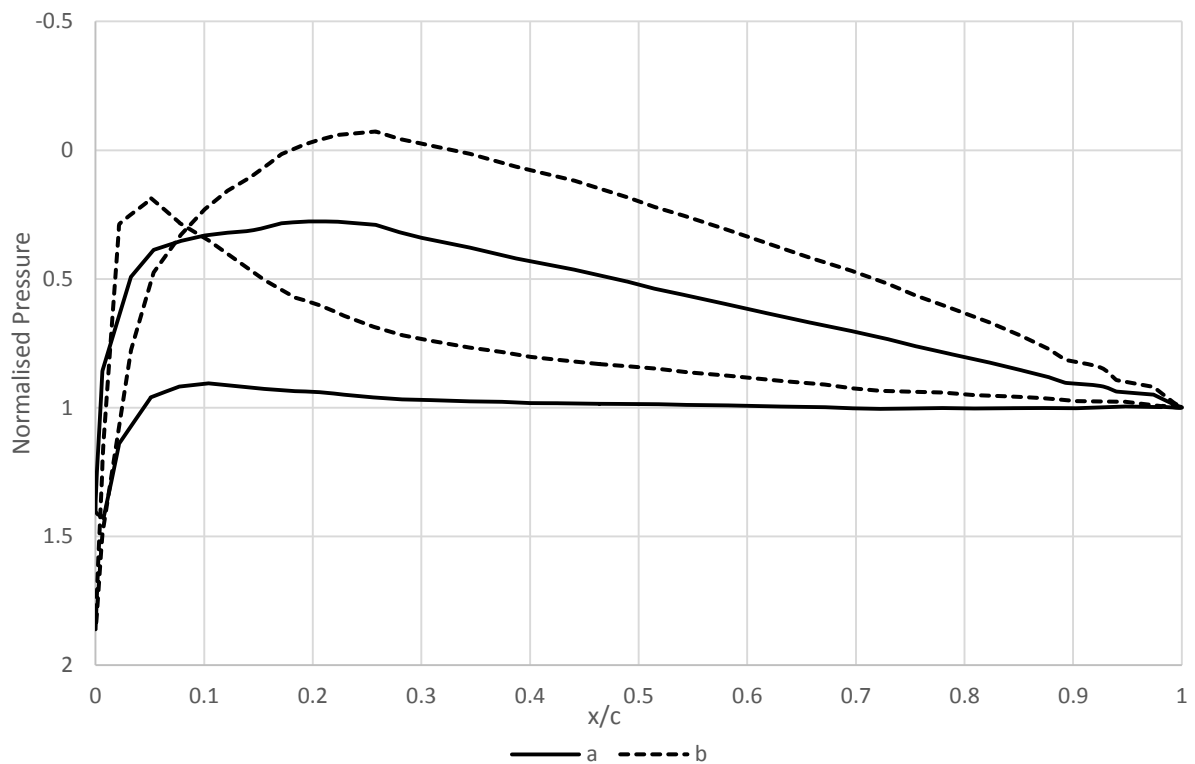
### 5.5.1 Process a to b

**a:** TSR = 6.415 (decreasing); velocity (increasing); CP=0.4226 (increasing)

**b:** TSR = 9.512 (increasing); velocity (decreasing); CP=0.2163 (decreasing)

This process showed a decrease of 20.63% in terms of the CP calculated from point **a** to point **b** which will then be attributed to the sensitivity of the  $C_l/C_d$  values at very low incident AoA. The decrease is large because the change in incident AoA for this process is also large as observed from the streamline plots in Figure 5.26. The lift value for this process also decreases as shown in Figure 5.27 where the normalised pressure around the hydrofoil sections

were plotted for both 75% and 25% span of the blade. A negative area under the pressure curves can be seen for point **b**, this indicates negative lift hence making the lift force lower. The change in drag force for the static aerofoil NACA 4414 and 4420 at this variation of AoA between  $-5^\circ$  to  $5^\circ$  will be small because the drag force has a relatively flat plot at this AoA range which can be found in Figure 5.12. This will suggest that the lift variation overpowered the change in drag making the  $C_l/C_d$  values higher.



(a)

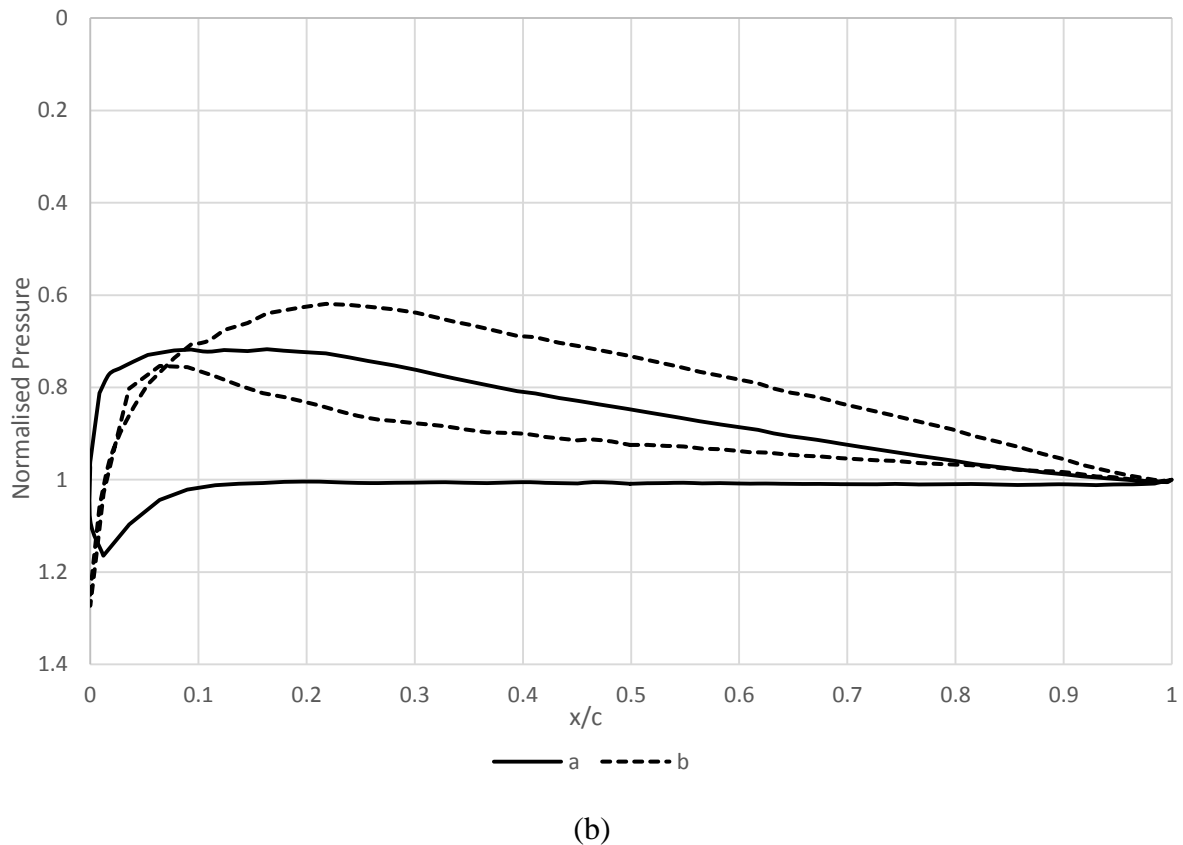


Figure 5.27 Normalised Pressure plots at 75%R (a) and 25%R (b) for process points **a** and **b**

### 5.5.2 Process b to c

**c:** TSR = 10.432 (decreasing); velocity (increasing); CP=0.0428 (increasing)

Further decrease in CP is observed in this process as the TSR still increase and reached its maximum value very close to point c. Although there is just a small difference in the incident AoA when observed visually from the streamlines, the CP drop is still a large value of 17.35%. This is still due to the fact that the incident AoA is going more negative at this point as can be observed in the pressure plots presented in Figure 5.28. A larger negative pressure area is observed for point c which reach to almost 12% of the hydrofoil section at that point, this observation together with the thinner pressure plot difference for the rest of the hydrofoil contributes to a lower lift when compared to point b which already has a low lift to begin with. This will reflect to an even lower CP value calculated as can be seen in Figure 5.25.

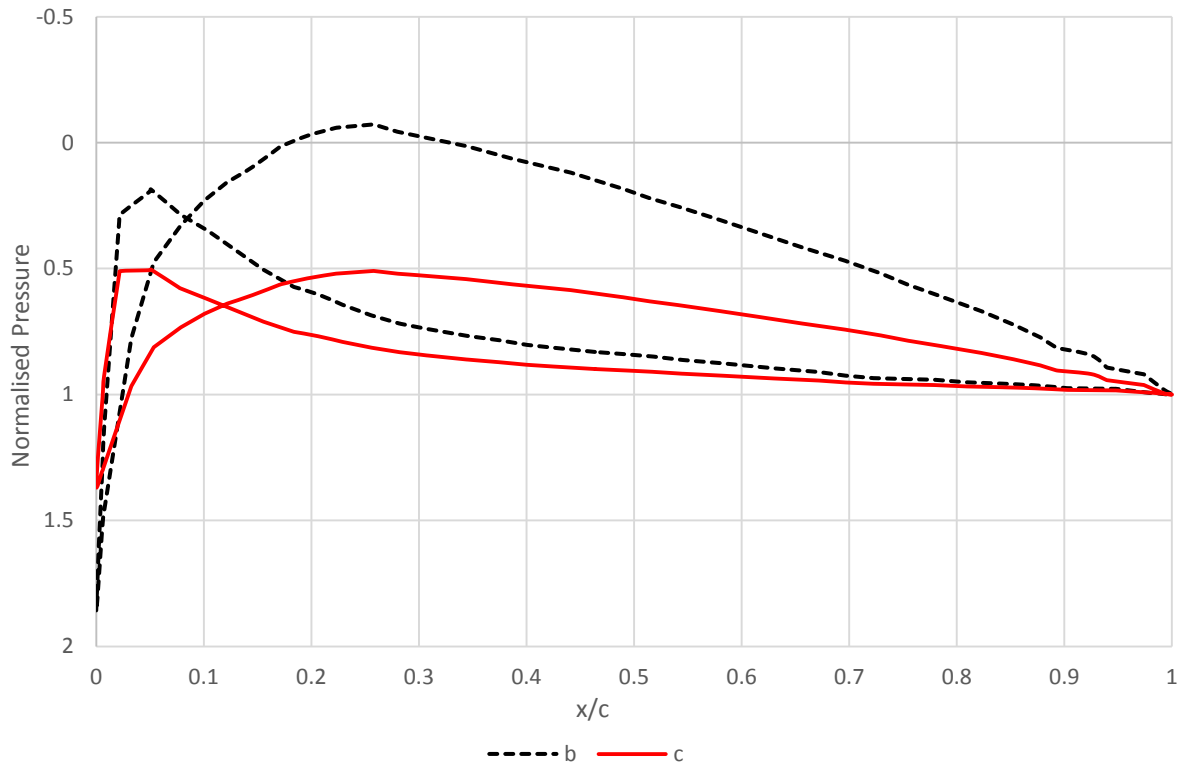


Figure 5.28 Normalised Pressure plots at 75%R for process points **b** and **c**

### 5.5.3 Processes **c** to **d** and **d** to **a**

**d:** TSR = 7.811 (decreasing); velocity (increasing); CP=0.3300 (increasing)

Process **c** to **d** shows the recovery of the CP value as the incident AoA increases due to the decrease in instantaneous TSR. Higher CP will be observed for point **c** relative to point **b** but it is lower than the same TSR value at the first half of the hysteresis curve and also lower than the steady flow performance curve. The possible reason for this is the very low value of CP when the recovery starts (point **c**) which again results to a delay in the recovery portion of the hysteresis curve. It can be seen in Figure 5.25 that the slope of the curve for this process is steeper than that of the steady state curve for the same range of TSR but because of the very low start at the minimum CP value, it took time before the curve recovered and crossed the steady state turbine performance curve again. The normalised pressure for this process is

presented in Figure 5.29, it can be seen that the negative pressure area (negative lift) has diminished for point **c** suggesting that the incident AoA is increasing as expected.

The CP recovery continued for process **d** to **a**, although a less steep curve was observed relative to that of process **c** to **d**. The hysteresis curve crosses the steady state value during this process with values even higher than that of the TSR = 6 simulation for the same TSR. The positive rate of increase here can be attributed to the favourable hydrodynamics as the flow instantaneously gets closer to the optimum TSR value, AoA is still increasing without the negative effect of drag.

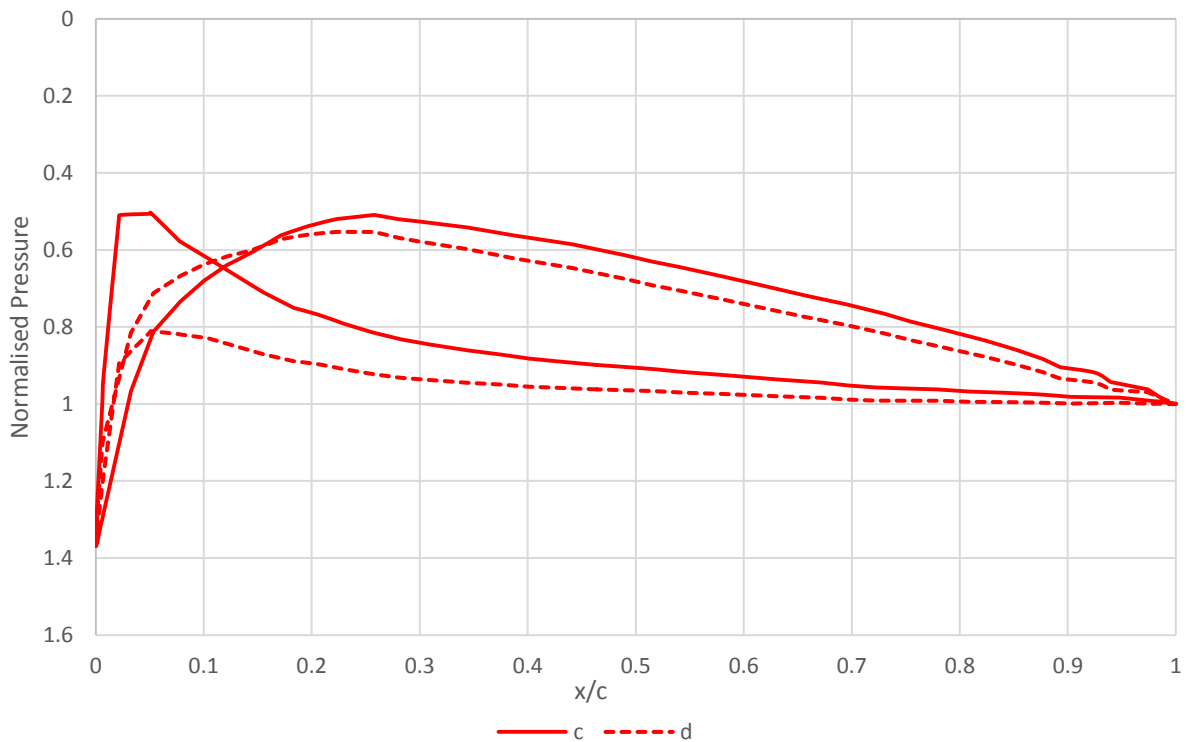


Figure 5.29 Normalised Pressure plots at 75%R for process points **c** and **d**

## 5.6 Summary of Chapter

This chapter presented and discussed the results of the unsteady simulations of the Sheffield HATT at three different operating conditions. The base case was defined to be the unsteady simulation referenced at TSR=6 which is the optimum operating condition for the turbine, this base case will be the one to be used as the reference for the amplitude and frequency comparison study in Chapter 6. The whole hysteresis curve for the base case unsteady simulation was explained in parts and each part was explained by using evidences which includes streamlines and normalised pressure around hydrofoil sections. To gain more insight into what is happening at the left-most and right-most side of the base case hysteresis curve, off-peak simulations referenced at TSR=4 and TSR=8 were also conducted. Like the base case, the hysteresis curve for both simulations explained in sections using the same set of evidences used for the base case. For the TSR = 4 simulation, separation and stall in the flow was expected so the  $\lambda_2$  vortex criterion was used to look and present vortex structures formed at different parts of the hysteresis curve and to explain how they affect the turbine's performance. The results from the TSR=8, on the other hand, proved that the turbine's performance is very sensitive for very small AoA changes which occurs at high TSR as explained using  $C_l/C_d$  plot for the hydrofoils used at 25% and 75% blade span. An image showing the three hysteresis curve for the three simulations is presented in Figure 5.30.

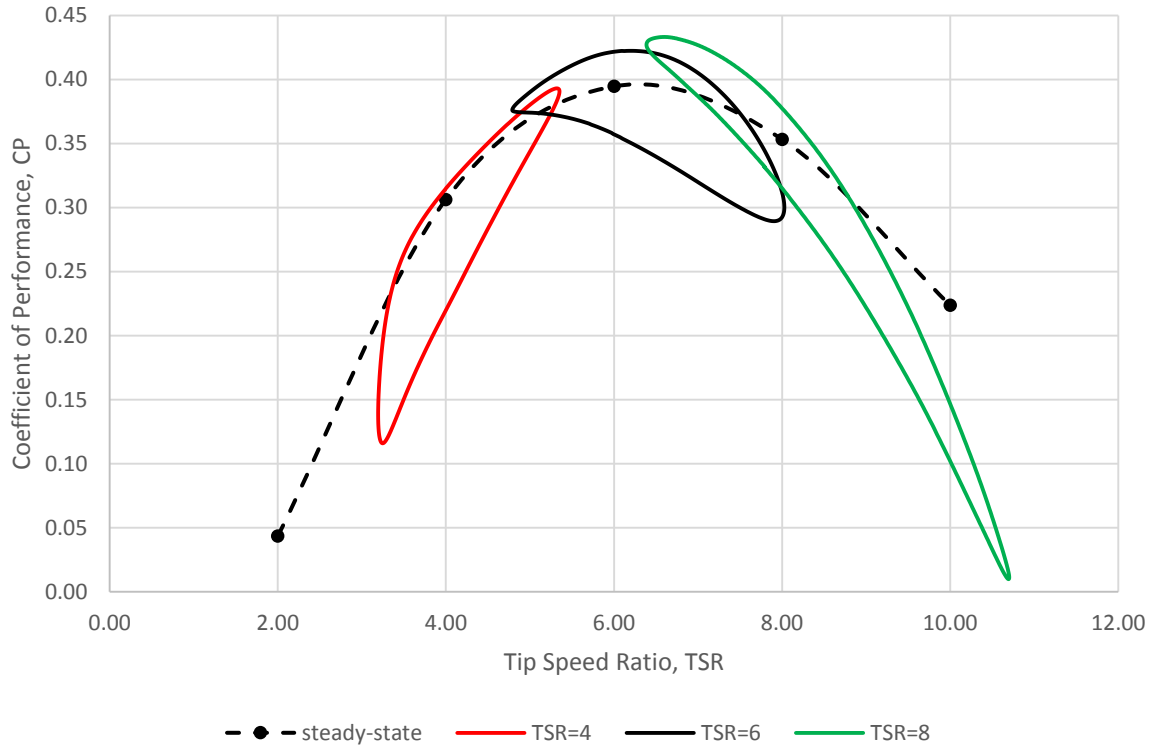


Figure 5.30 Complete unsteady simulation plot showing hysteresis curve for the three unsteady cases (TSR=4, 6, and 8)

It was also shown that the Sheffield HATT has a lower cyclic-averaged CP when compared to the steady-state CP for their corresponding mean TSR for all of the unsteady cases simulated in this chapter. Presented in Figure 5.31 are the cyclic-averaged CP for the simulations next to their steady state counterpart for comparison. It can be seen that the difference between unsteady and steady CP decreases as the TSR increases and this is attributed to the flow hydrodynamics described for each TSR in this chapter whereas big stall effects are observed for the low TSR simulation and sensitivity of the turbine at the changes in AoA for the high AoA. It can also be seen that the base case is still the optimum case for the turbine as it has the highest CP and an acceptable difference with that of the steady state simulation at the same TSR.

The next chapter will present the effect of amplitude and frequency variation on the base case velocity variation equation to the performance of the Sheffield HATT. Similar analysis using the streamlines and normalised pressure will be used to explain the hydrodynamics for each case.

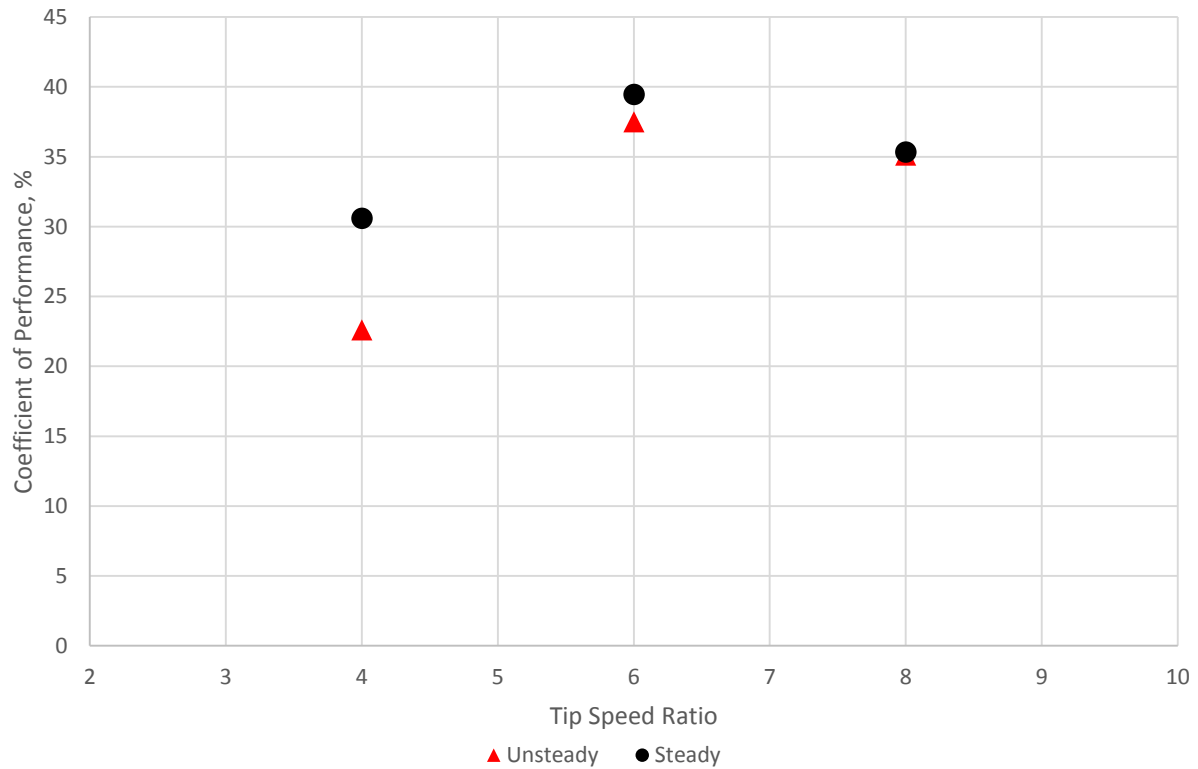


Figure 5.31 Cyclic-averaged CP for the three different unsteady simulation at their mean TSR with their steady state counterpart.

## **Chapter 6**

# **Influence of Amplitude and Frequency Variation in the Unsteady Flow to the Performance of Sheffield HATT**

### **6.1 Introduction**

The hydrodynamic performance of the Sheffield HATT in unsteady flow was explained in Chapter 5 where details for three different operating conditions were presented. In this chapter, the amplitude and frequency of the bulk flow velocity of the water flow will be varied to create new unsteady flow conditions to investigate and study the response of the turbine. Comparison between the new case results and the original set of data will be presented to explain the hydrodynamics in the flow and the turbine with the use of streamlines, pressure coefficients and other parameters such as lift and drag ratio. Two comparative studies will be presented in this chapter; the amplitude variation comparative study and the frequency variation comparative study.

### **6.2 Amplitude Variation Comparative Study**

For this study, the amplitude of the idealised unsteady velocity defined in equation 10 (see Chapter 5.2) will be altered to produce higher and lower amplitude cases as defined in Equations 14 and 15 respectively. These equations used were formulated so that the cycle-averaged power available from the varying velocity equal to the steady state case at the same TSR at a mean velocity of 2 m/s (which is  $TSR=6$  for this cases). The resulting amplitudes are 43.5% and 10% of the mean flow for the cases described. The higher amplitude of 43.5% is

chosen for an exaggeration of the velocity fluctuation in real world and to simulate extreme cases that can happen during storms and typhoons which is a more frequent event in the Philippines. The 10% amplitude is based on the real world measurement from Nova Scotia which shows an average of 10% amplitude in the paper presented by Le Roux *et al.* (Leroux *et al.* , 2016).

$$u(t) = 1.841 + 0.8 \sin(2\pi t) \text{ (eq. 14)}$$

$$u(t) = 1.99 + 0.2 \sin(2\pi t) \text{ (eq. 15)}$$

The results from the high and low amplitude simulations are presented and explained thoroughly in Sections 6.3 and 6.4 respectively. Cycle-averaged value of the coefficient of performance for both simulations are calculated and it was recorded to be 38.74% for the 10% (of the mean velocity) amplitude simulation and 34.26% for the high amplitude simulation. The main reason for this is to have a comparison with the steady state CP value at TSR = 6 which is 39.46% and the base-case unsteady simulation which have a cycle-averaged CP at 37.5% for a mean velocity amplitude of 24.5%. Comparison of these results clearly state that an increase in amplitude in the inflow velocity variation has a negative effect on the cycle-averaged CP of the Sheffield HATT. An attempt to explain hydrodynamics and flow physics causing this observation is presented in the following sections and a summary for the amplitude variation study is highlighted in Section 6.5.

### **6.3 High Amplitude Variation**

The CP values for the higher amplitude simulation is plotted against instantaneous TSR in Figure 6.1 for one cycle of the velocity, also superimposed are the steady state performance curve and the reference case hysteresis curve for steady flow to serve as the basis of comparison. It can be observed from Figure 6.1 that the 43.5% amplitude case has a larger and wider hysteresis curve, the wide range of the hysteresis curve is caused by the difference in the

range of TSR since the amplitudes of the two velocity functions used were different. The TSR values range from 4.18 – 10.61 for the 43.5% amplitude case and just from 4.79 to 8.03 for the base case. The shape of the 43.5% hysteresis loop showed the same trend when compared to the base case although higher maximum CP was observed which reached up to a value of 43.6% compared to just 42.4% for the base case.

Another visual observation from the hysteresis plot is the extremely low CP values predicted at high TSR. This observation was also seen for the TSR=8 unsteady simulation presented in Chapter 5. This effect is again attributed to the high sensitivity of the lift to drag ratio at low AoA between  $-5^\circ$  to  $5^\circ$  which is apparent at high TSR (see Figure 5.12). This will be discussed in detail in Section 6.3.3 for the process between points **c** to **d** in the hysteresis curve. There is also a loop observed within the hysteresis curve highlighted with a green circle in Figure 6.1. It can be seen from the unsteady base case hysteresis curve that it is getting sharper going to the low TSR's and this appears to continue for the higher amplitude case by which the sharp corner finally overlapped and crossed each other and formed a loop.

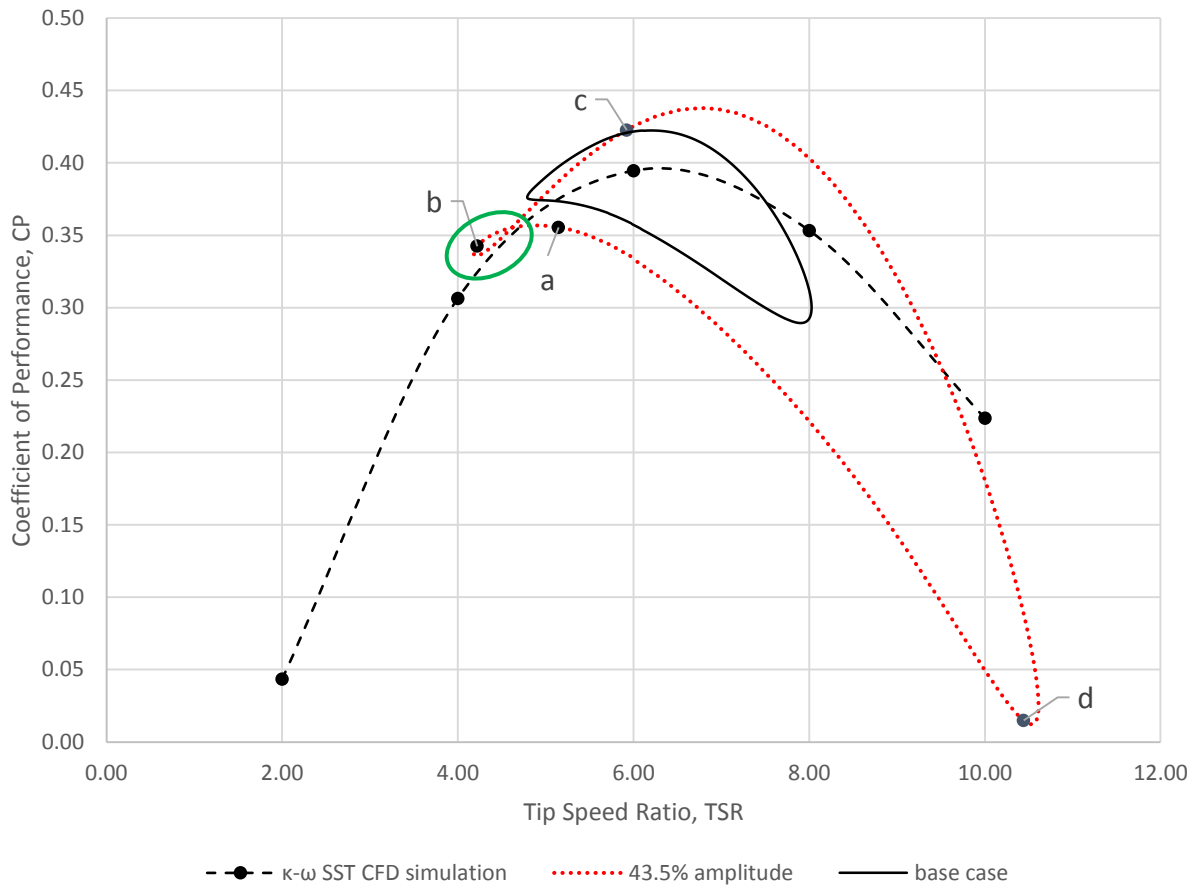


Figure 6.1 Unsteady Flow Hysteresis Curve for 43.5% amplitude over the steady flow performance curve for the Sheffield HATT and the base case hysteresis curve

The response of the Sheffield HATT to the 43.5% amplitude unsteady velocity profile was also plotted against normalised time  $\tau$  to show how the turbine behaves according to the power extracted by the turbine and the water power available to it. The response for the reference case was also superimposed as basis for comparison. It can be observed that the CP plots for the two cases show some similarity in terms of the overall trend of the graphs although a very big difference can be seen when the 43.5% amplitude plot dropped down to a very low value at the latter half of the cycle.

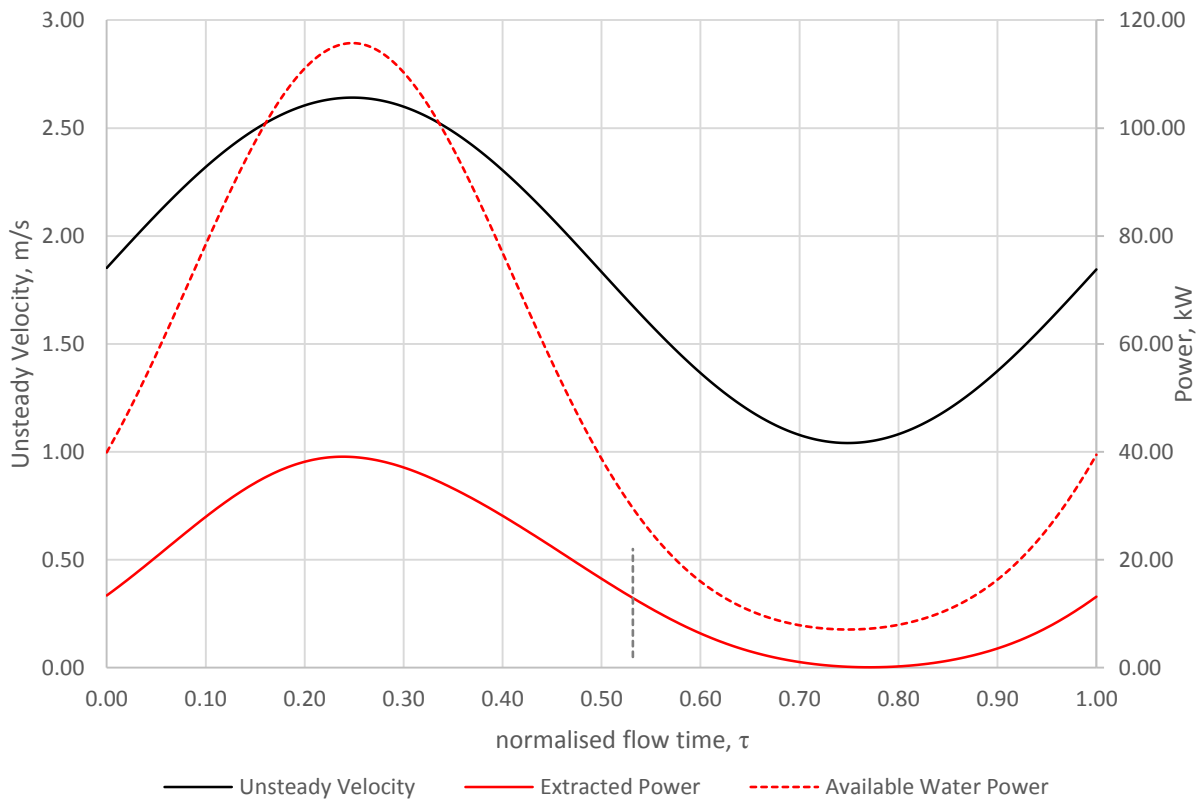
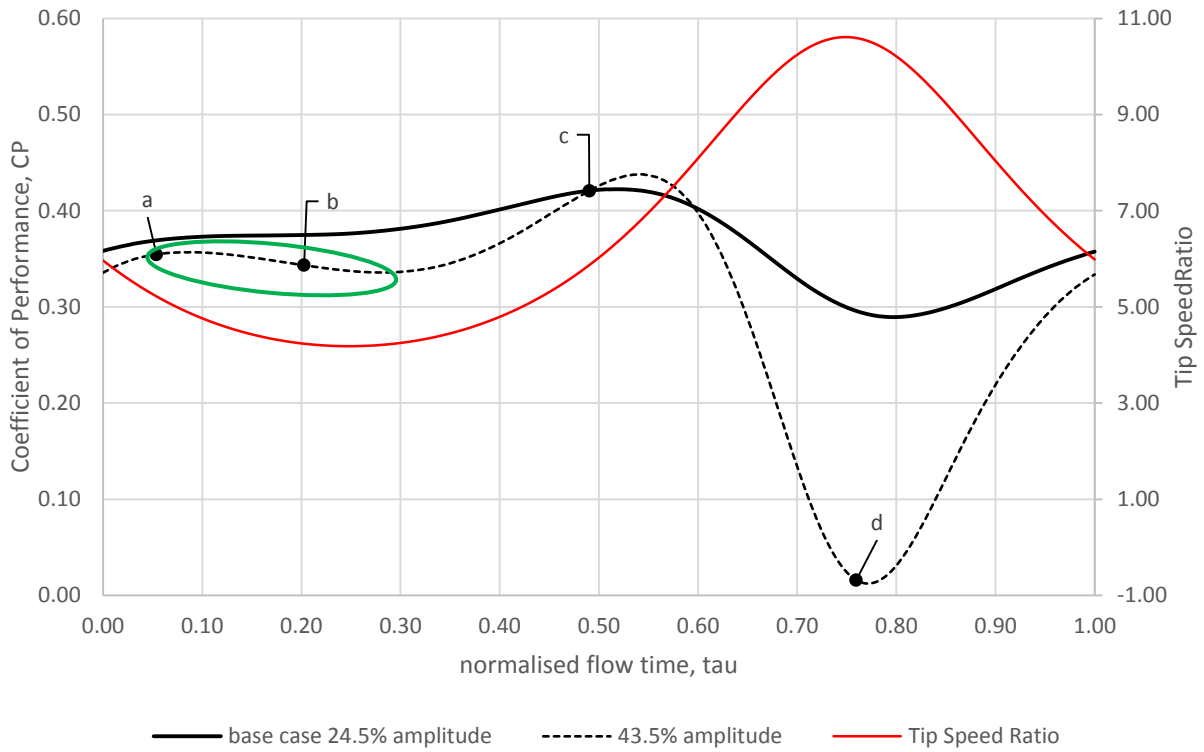
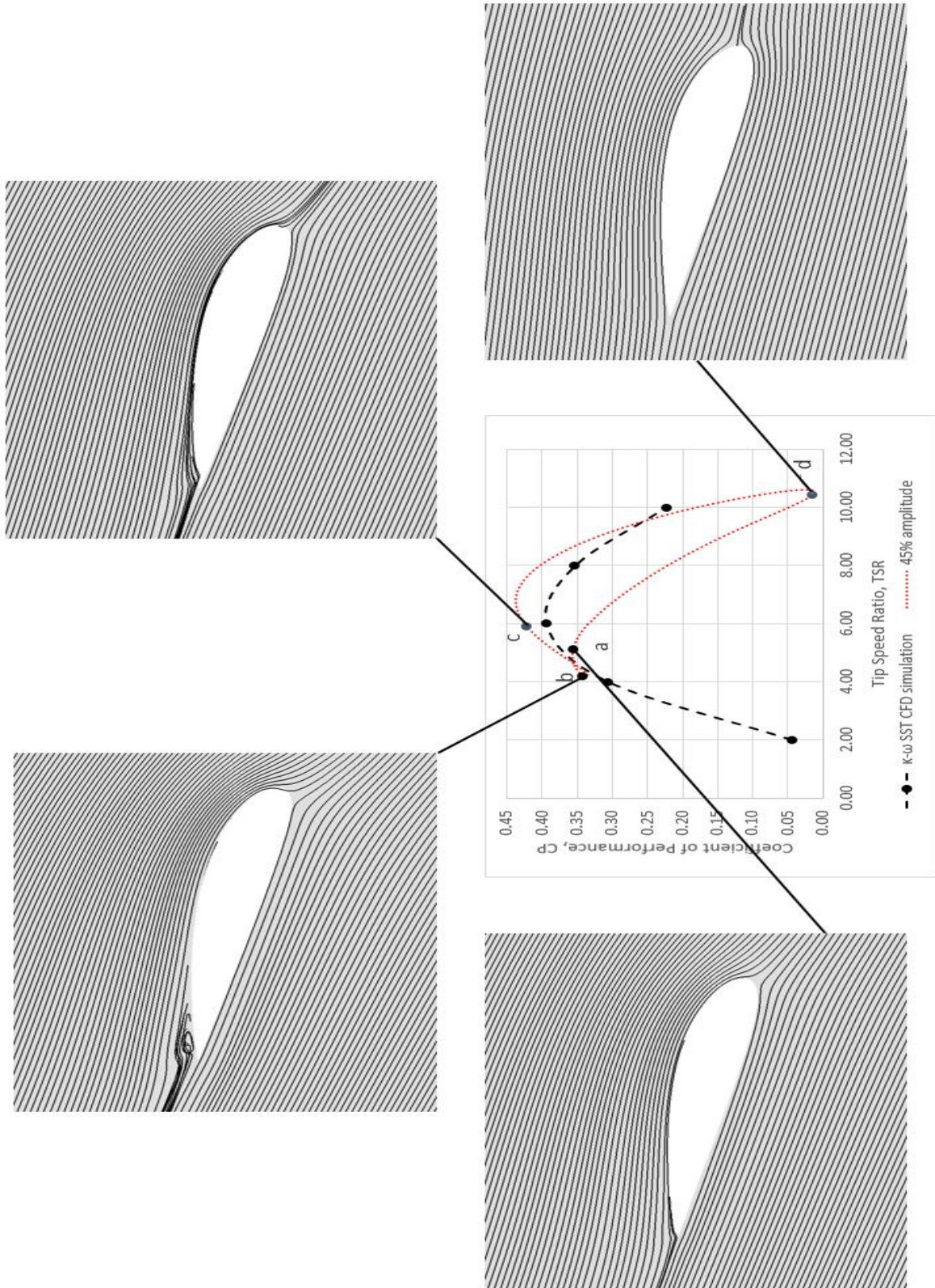


Figure 6.2 Sheffield HATT Response for the 43.5% Amplitude Simulation

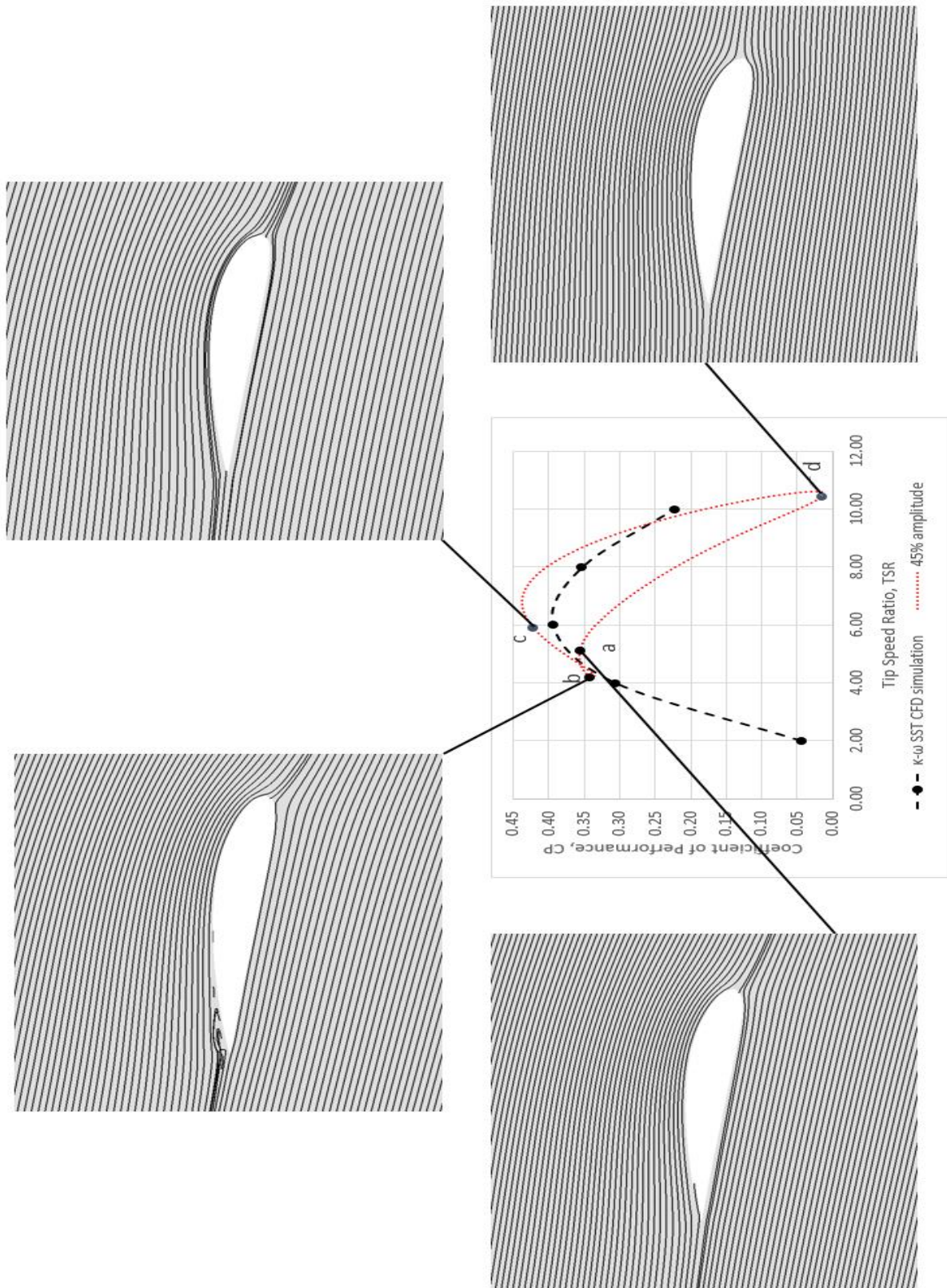
**top:** CP value plotted against normalised time superimposed with the base case CP plot and instantaneous TSR; **bottom:** Power extracted by the turbine plotted against normalised time superimposed with the water velocity profile and power available in the water

From  $\tau = 0$  to  $\tau = 0.08$ , both the power extracted ( $P_e$ ) by the turbine and the available power ( $P_a$ ) are increasing which corresponds to the increase in the instantaneous CP value as well as can be observed in Figure 6.2. Further from that point until  $\tau=0.27$ , the value of CP starts to decrease. This happens because of the higher rate of increase on the  $P_a$  plot as compared to that of  $P_e$ . This is the section by which the small loop within the hysteresis curve occurs, it is highlighted by a green circle in Figure 6.2. The instantaneous CP plot flattens for a small time until  $\tau=0.30$  but then increase again until it reaches a maximum value CP of 43.78% at  $\tau=0.54$ , the reason is that at this point,  $P_e$  starts to lag  $P_a$  with the extracted power going back to its initial value at  $\tau=0.54$ ,  $\tau=0.04$  later than that of the water power available. As a result, the instantaneous extracted power is paired to a lower  $P_a$  as both plots are decreasing at this point, making the calculated CP higher. This lag was also observed at the reference case simulation although a larger lag was observed for this simulation where the power extracted went back to its original value at  $\tau=0.54$ , which is 0.04 later than  $P_a$ . At  $\tau=0.54$  until  $\tau=0.77$ , the CP plot starts to decrease in value drastically, as shown in Figure 6.2. This happens mainly because the velocity of the water at this point has gone down to its minimum value, which is 1.041 m/s at  $\tau=0.75$ , which then results to a very low power available and even lower power extracted. The other reason is that rate of decrease of the  $P_a$  plot is much steeper than that of the  $P_e$  plot which means there is a larger denominator for the CP computation hence making the CP value lower. There is still an effect of the observed lag at this part of the cycle, that is why at  $\tau=0.77$  when the  $P_e$  plot reached its minimum point, the  $P_a$  plot has already started to recover as the water velocity increase at  $\tau=0.75$ . The CP plot starts to recover afterwards until  $\tau=1.0$  as both the  $P_e$  and  $P_a$  plots increase with rates of increase not too far from each other as seen on their respective plots.

An increase in the power extracted by the turbine was also observed for this simulation, which is due to a higher variation in the available water power. A maximum of 39.11 kW was recorded for the higher amplitude simulation which is 5.17 kW more than the base case maximum which is just at 33.94 kW, both happened just after  $\tau=0.26$ . This increase in maximum  $P_e$  accounts to a 15% increase which is still lower than the increase in maximum  $P_a$  between the two simulations which is at 28%. On the other hand, due to the large amplitude variation, a lowest available power of 0.089 kW was obtained which is lower than the minimum  $P_e$  for the base case simulation which is at 5.66 kW which happened at  $\tau = 0.77$ . The very small power extracted here reflects as a very low instantaneous CP in the CP plot as well.



(a)



(b)

Figure 6.3 Velocity Streamlines for different position on the hysteresis curve at 25% (a) and 75% (b) span of the blade for unsteady 43.5% amplitude simulation at TSR = 6

The streamline plots for various position in the hysteresis curve are presented in Figure 6.3. The same process done in Chapter 5 was used for the streamline plots showing the flow around the hydrofoils at the 25% and 75% span of the turbine blade to help explain what is happening at different processes across the hysteresis curve. Initial observation of the streamline plots in Figure 6.3 shows the variation in the incident angle of attack for each position in the hysteresis curve which follows the same trend observed for the unsteady TSR = 6 simulation presented in Chapter 5. All of the streamlines in the hysteresis curve showed fully attached flows except for one which occurs at the lowest TSR for the cycle. The following sections will discuss the different regions described in the hysteresis curve in detail.

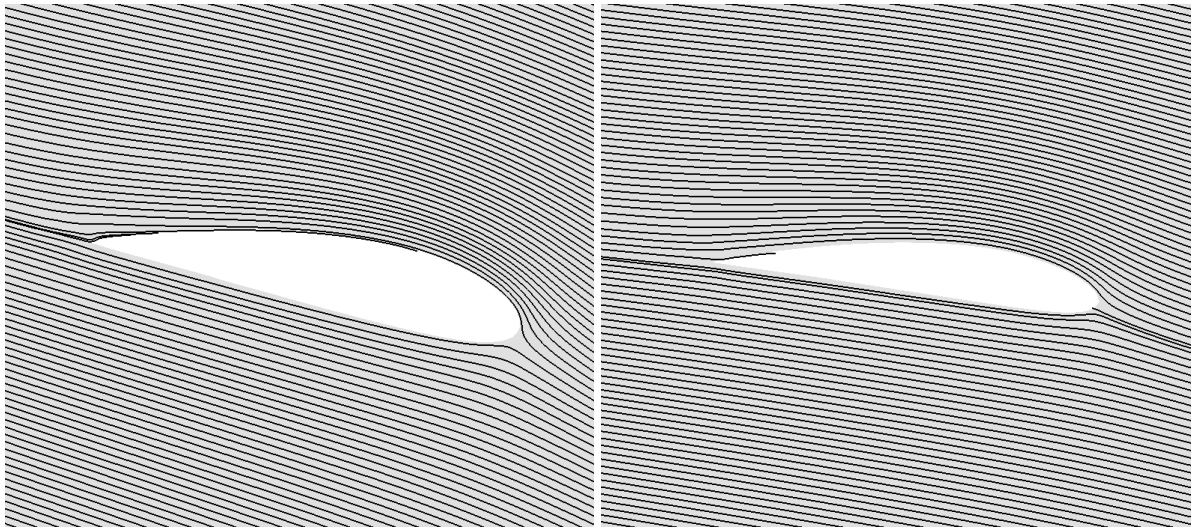
### 6.3.1 Process a to b

**a:** TSR = 5.15 (decreasing); velocity (increasing); CP = 0.355 (increasing)

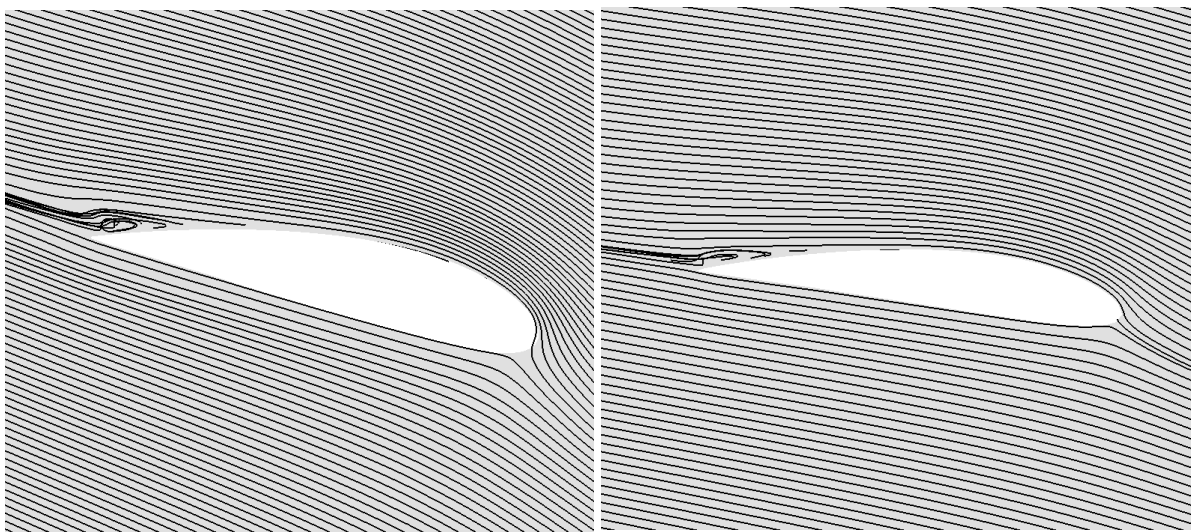
**b:** TSR = 4.22 (decreasing); velocity (increasing); CP = 0.342 (increasing)

This process shows a decrease in TSR which corresponds to a noticeable increase in the incident AoA as illustrated in Figure 6.4a and 6.4b. This increase in AoA corresponds to an increase in lift as can be seen in the difference in the normalised pressure plots in Figure 6.5. Although an increase in lift was observed, the CP value between the process still decrease which will be attributed to the separation observed at point **b** for both the 25% and 75% span of the blade as presented in Figure 6.4b. This observation was also seen in the base case unsteady simulation as the hysteresis plot goes to the lowest TSR, the only difference is that for the simulation with higher amplitude, a small loop within the hysteresis plot occurred. From point **a** to **b**, the hysteresis curve shows a rate of decrease that is less than the rate of increase from point **d** to **a**. This is due to the fact that from **d** to **a**, the lift is continuously increasing without any additional increase in drag because there is no separation present at that process. On the other hand, as the flow starts to separate from point **a**, it can be seen that the slope of

the hysteresis curve decreases because the additional drag from form drag due to separation affects the lift to drag ratio thus decreasing the CP value.



(a)



(b)

Figure 6.4 Streamlines at point a (a) and point b (b) for 25% of blade span (left) and 75% of the blade span (right) of the Sheffield HATT turbine blade for the 43.5% amplitude simulation

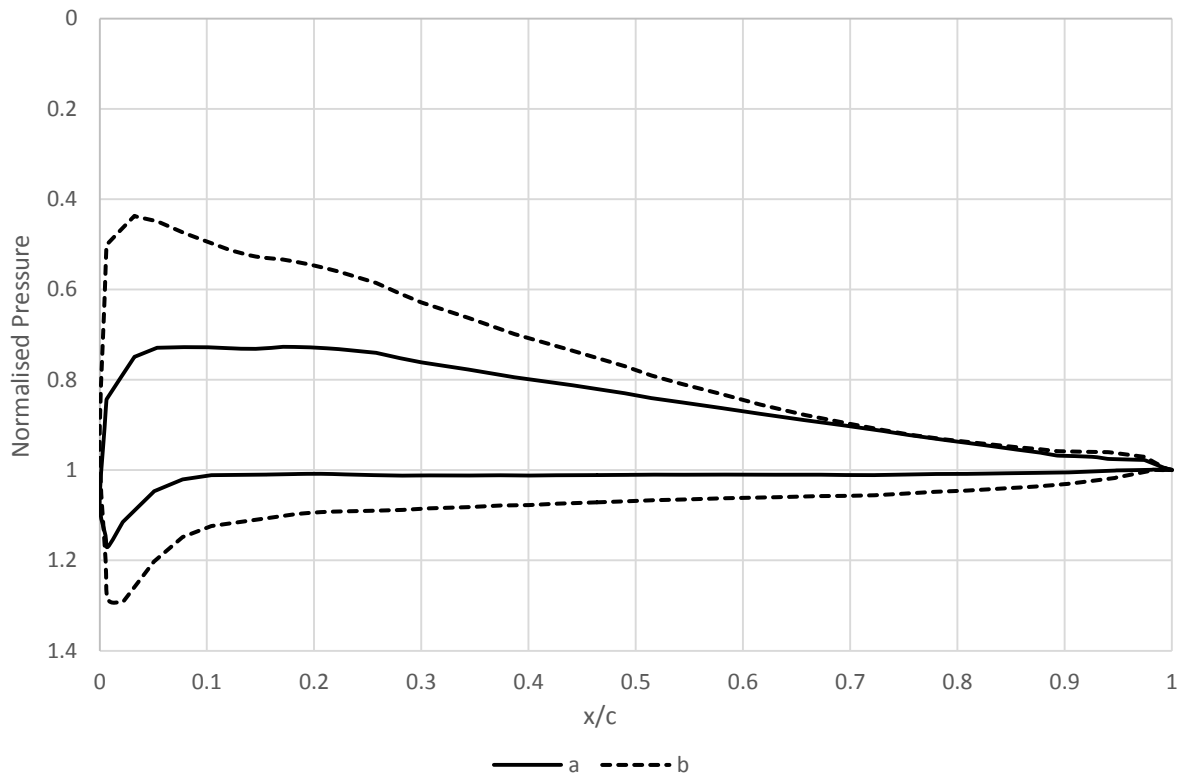


Figure 6.5 Normalised Pressure plots at 75%R for points **a** and **b** for the 43.5% amplitude simulation

### 6.3.2 Process b to c

**c:** TSR = 5.92 (increasing); velocity (decreasing); CP = 0.423 (increasing)

The hysteresis curve starts to increase again after it reached a minima near point **b**, and the slope of this increase is greater than the rate of decrease from process **a** to **b**. This is because starting from the minima at the lowest TSR, the flow around the blades starts to reattach. The flow is fully attached as it reached point **c**, streamlines for point **c** for both 25% and 75% span are shown in Figure 6.6. After the flow reattached, it is known that the drag will decrease because form drag will be out of the analysis. As the TSR increase, lift should decrease because the incident angle of attack is decreasing (as shown in Figure 6.6) but this is not observed at this point as the lift continued to increase until the flow is fully attached at point **c**. This is supported by the normalised pressure plots presented in Figure 6.7 whereas there is a big difference in the area under the pressure curve proving that lift is still increasing. The same

phenomenon was seen in the base case unsteady simulation but without the additional loop observed here in the higher amplitude simulation. Again, it was attributed to the effects of the dissolving separation in the wake making the lift overshoot as the TSR changes and a lag in the system is observed. This is the same region of the curve shown in Figure 6.2 where the lag in the power extracted was shown and presented.

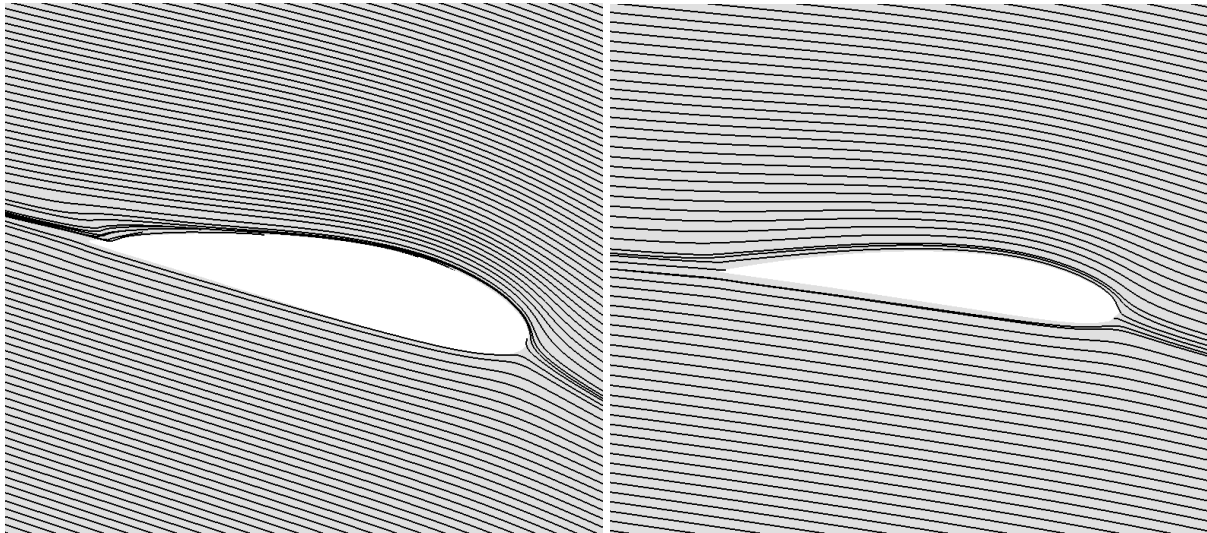


Figure 6.6 Streamlines at point c for 25% of blade span (left) and 75% of the blade span (right) of the Sheffield HATT turbine blade for the 43.5% amplitude simulation

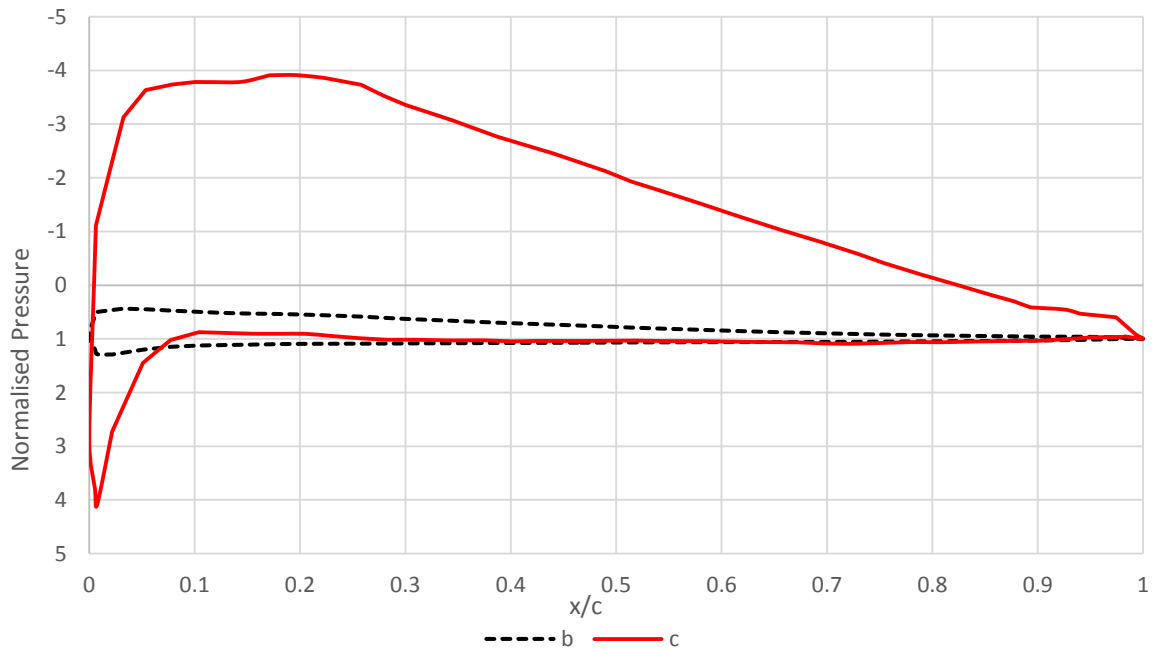


Figure 6.7 Normalised Pressure plots at 75%R for points b and c for the 43.5% amplitude simulation

### 6.3.3 Process c to d

**d:** TSR = 10.47 (decreasing); velocity (increasing); CP = 0.0136 (increasing)

After the hysteresis plot reached its maximum close to point **c**, the curve showed a drastic drop as can be seen in Figure 6.1. This is the part of the time-response plot response of the turbine in Section 6.3 by which it was explained as the combination of the effects of the lag in power extracted and the decrease in the water velocity and power available. This will be supported here by the streamlines for point **d** presented in Figure 6.8 where it can be seen that the incident angle of attack decrease drastically when compared to that at point **c**. Since it is established that the flow around the hydrofoil is fully attached at point **c**, it can be stated that the effect of drag will be minimum at this point and therefore the lift to drag ratio by which CP is dependent is more affected by the lift force in the blade. It was also supported by the difference in the area under the pressure curve as shown in Figure 6.9. It can also be seen that there is an overlap in the normalised pressure curve for point **d** (highlighted by a green circle) which means that the area under that loop is negative area making the total lift lower, this also proves that at this point, the AoA is getting more negative.

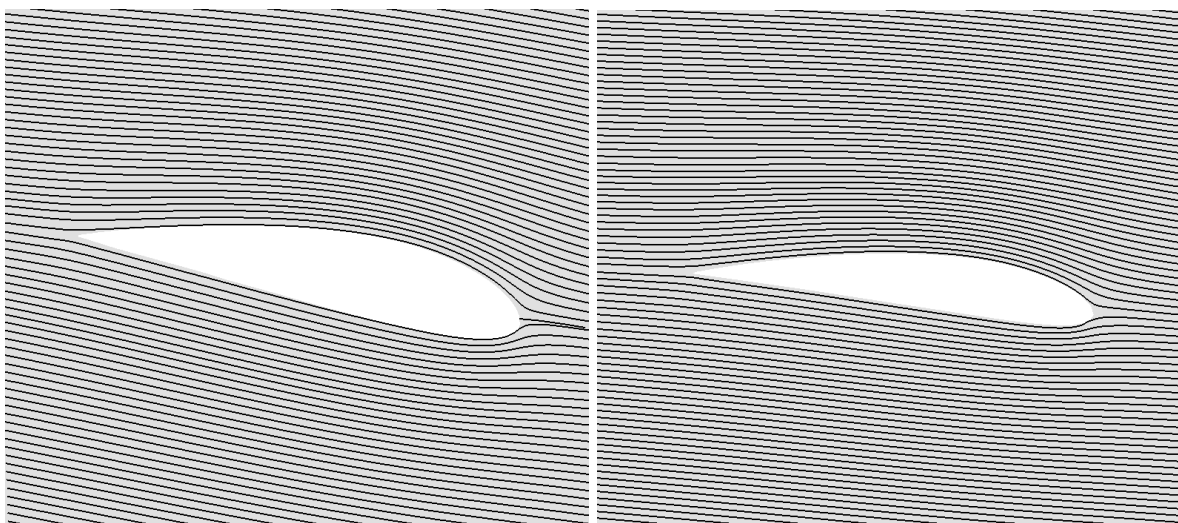


Figure 6.8 Streamlines at point **d** for 25% of blade span (left) and 75% of the blade span (right) of the Sheffield HATT turbine blade for the 43.5% amplitude simulation

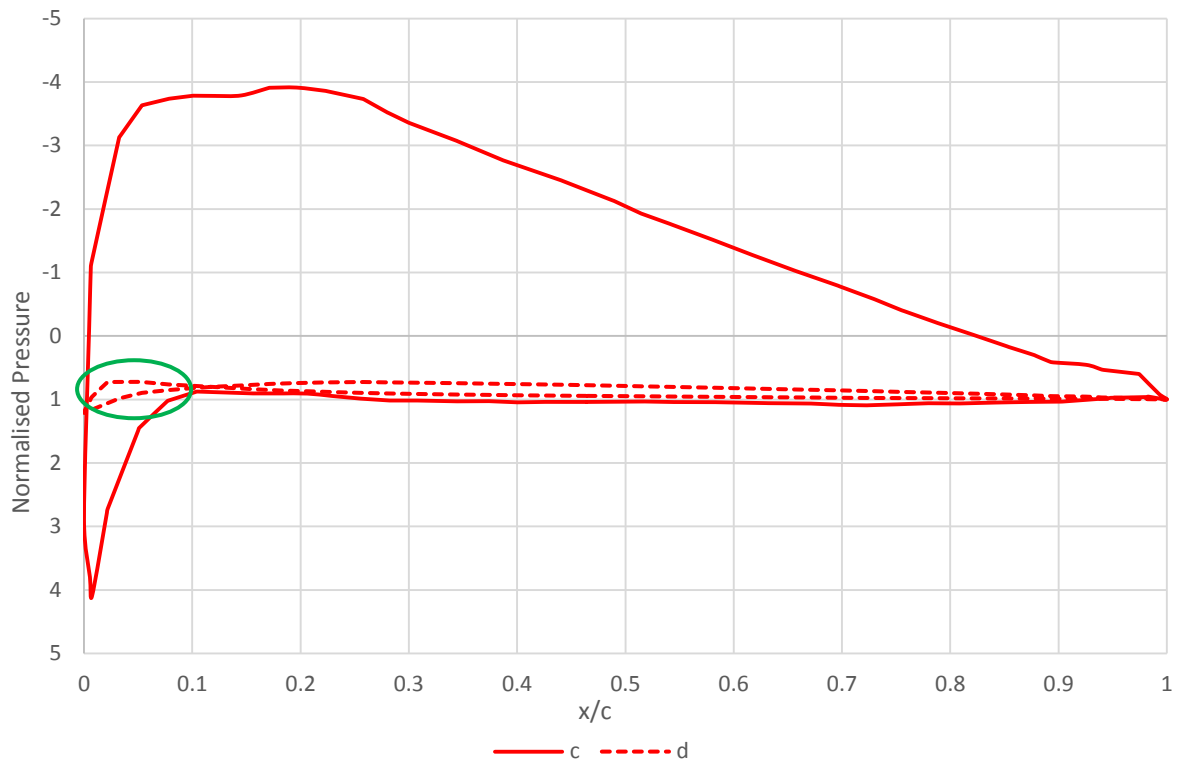


Figure 6.9 Normalised Pressure plots at 75%R for points **c** and **d** for the 43.5% amplitude simulation

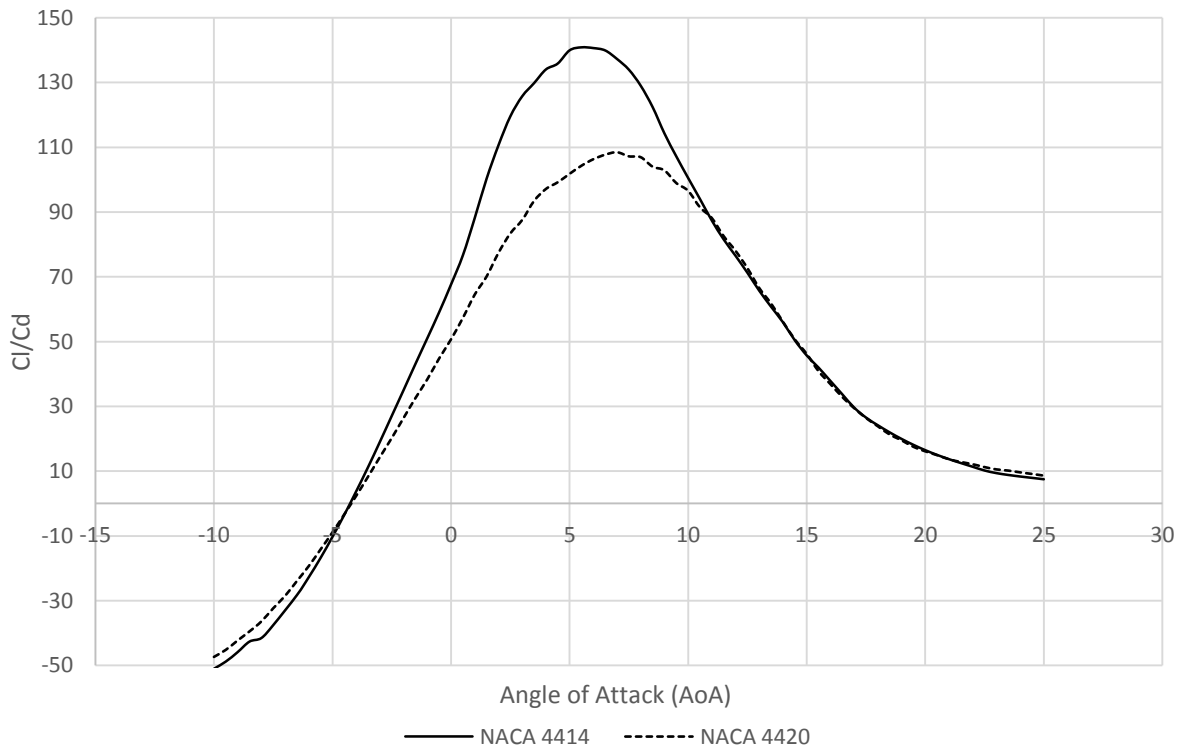


Figure 6.10.1  $C_l/C_d$  plot for NACA 4414 and NACA 4420 which is the aerofoil sections at 75% and 25% of the Sheffield HATT blade respectively

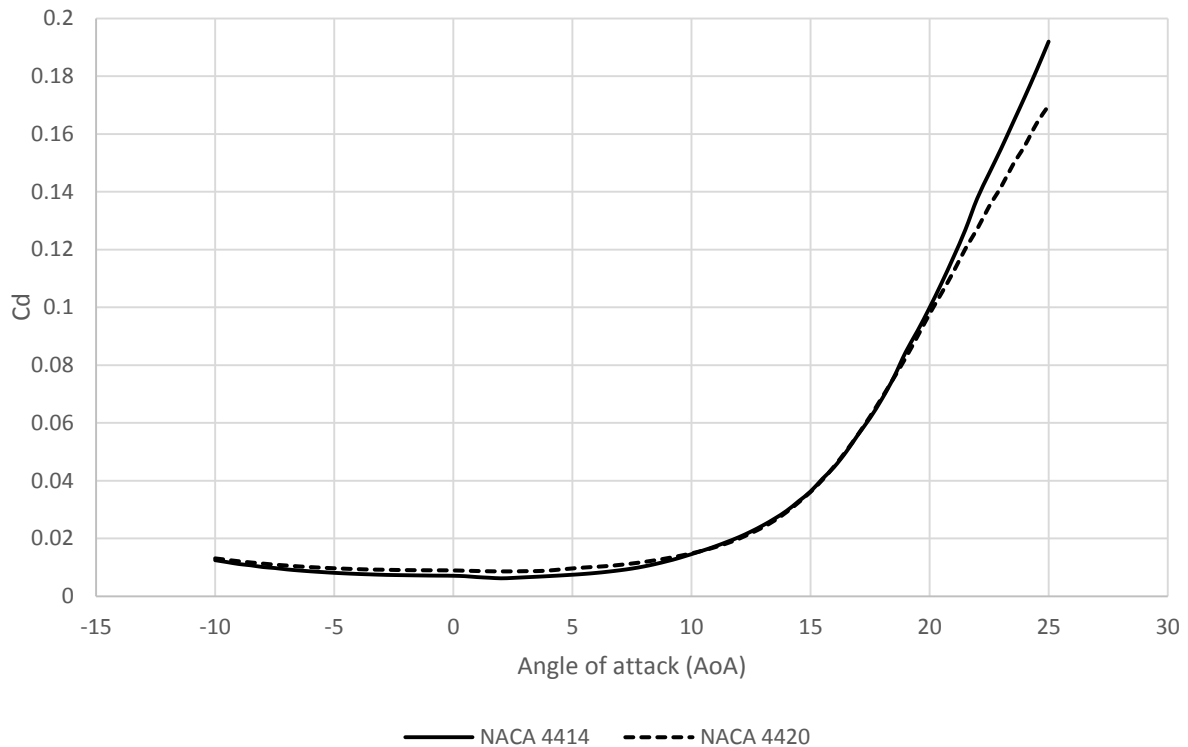


Figure 6.10.2  $C_d$  plot for NACA 4414 and NACA 4420 which is the aerofoil sections at 75% and 25% of the Sheffield HATT blade respectively

Figure 6.10.1 is a plot of the steady  $C_l/C_d$  plot for the 75% and 25% blade span cross-section hydrofoils (which is also presented in Chapter 5) and this shows that at incident AoA from  $0^\circ$  going to the negative, the  $C_l/C_d$  plot was at the steepest. This means that at high TSR, the chosen hydrofoil was very sensitive to a small change in AoA as explained in Section 5.3.3. An additional plot showing steady  $C_d$  plot for the hydrofoils shown in figure 6.10.2, this shows that at high TSR where incident AoA is close to  $0^\circ$ , the drag does not change that much and the  $C_l/C_d$  ratio is more dependent in  $C_l$  more than  $C_d$  at this region.

In Figure 6.1, it can be seen from the hysteresis curve for the 43.5% amplitude that the space on the curve between point c and d is relatively large as compared to the other processes. That is why intermediate points between points c and d named **c1** and **c2** are included in the hysteresis curve as shown in Figure 6.11. Intermediate points named **d1** and **d2** are also placed

between points **d** and **a** also shown in Figure 6.11. It was intended that points **c1** and **d2** on the hysteresis curve has the same TSR value to compare them the same way a comparison was made for Figure 5.13 discussed in Section 5.3.5 about the two values of CP for the same TSR=6. Figure 6.12 shows the normalised pressure curves for the intermediate curves **c1** and **c2** overlapped with points **c** and **d**, it can be seen that from very large area under the pressure curve for point **c**, the pressure area decreased in size for point **c1** which follows the already discussed effect of the sensitivity of the turbine response for high TSR. The area under the pressure curve for point **c2** further decreased in size as compared to the points **c** and **c1**, an overlap in the suction side and pressure side curves was also observed suggesting negative lift near the leading edge which is caused by the negative AoA at this point as it is at TSR = 10. This completes the process from points **c** and **d** showing a consistent decrease in the area under the pressure curve with intermediate points **c1** and **c2**.

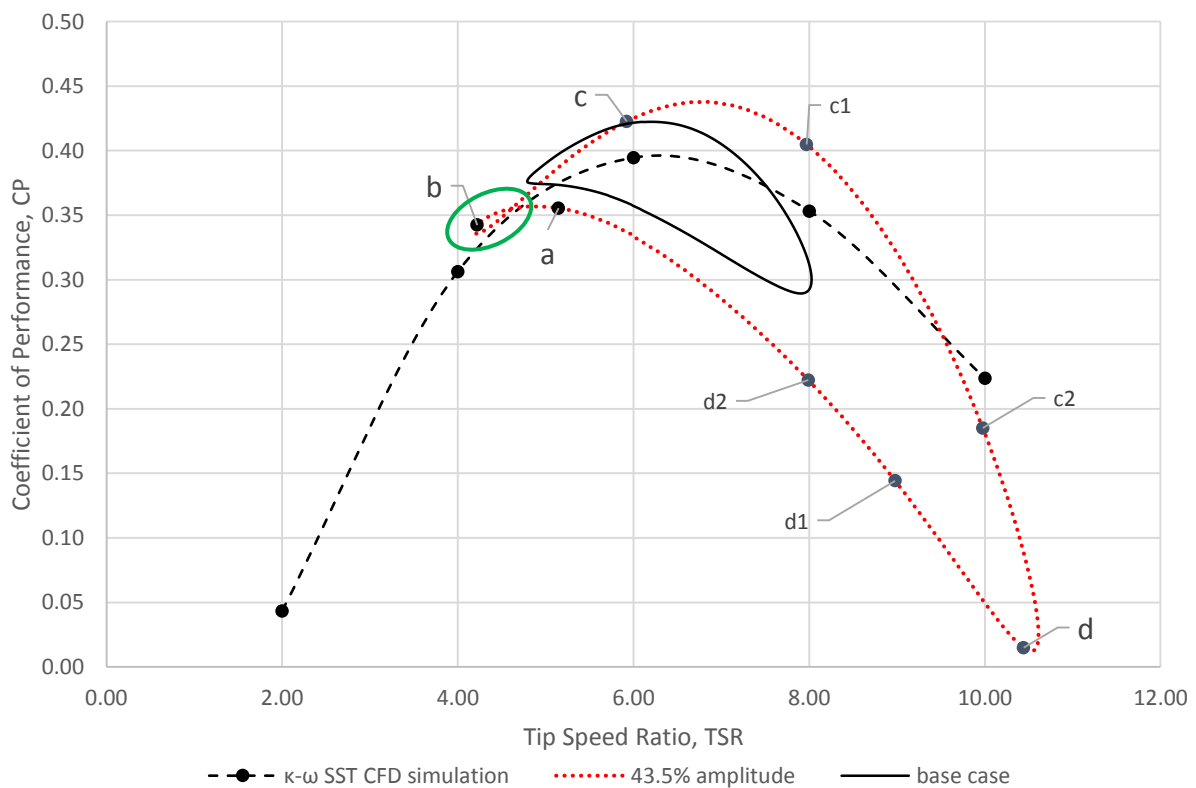


Figure 6.11 Unsteady Flow Hysteresis Curve for 43.5% amplitude over the steady flow performance curve for the Sheffield HATT and the base case hysteresis curve including points **c1**, **c2**, **d1** and **d2**

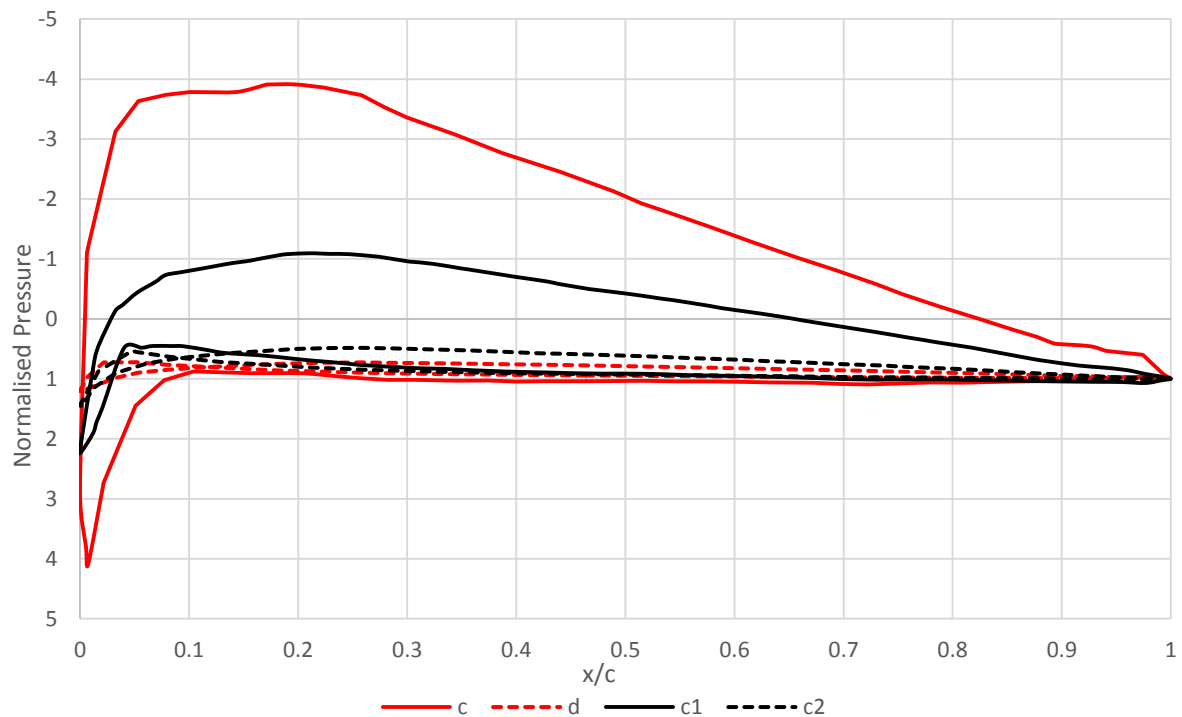


Figure 6.12 Normalised Pressure plots at 75%R for points **c** and **d** for the 43.5% amplitude simulation including the in-between points **c1** and **c2**

### 6.3.4 Process **d** to **a**

This process shows the recovery period for the turbine's response to the 43.5% amplitude unsteady simulation. From a very low CP value at point **d**, the hysteresis curve increase again but it is noticeable that the rate of increase at this process is less than the rate of decrease from the max value going to point **d** as shown in Figure 6.1 and 6.2. Lift is increasing in this process as proved by the normalised pressure plots presented in Figure 6.13 where the overlap for the pressure plot for point **d** can be seen more clearly highlighted in a green circle, this is supported by the streamlines for the points **a** and **d** in Figures 6.6 and 6.4a respectively. It should be notice in Figure 6.15 that the difference in the pressure plots area is less than that of that for the process **c** to **d**.

From the hysteresis curve in Figure 6.1, it can also be observed that the rate of increase represented by the slope of the tangent lines through the curve is gradually decreasing until in

turns flat and started to decrease starting point **a**. This is because the effect of drag is also increasing as the TSR decreases and the incident AoA increases, this effect is apparent especially with separation which happens right after point **a**.

Intermediate points between points **d** and **a**, named **d1** and **d2**, were presented and can also be seen in Figure 6.11. This was made because the gap between points **d** and **a** in the hysteresis plot in Figure 6.1 is wider when compared to other processes present in the curve. The resulting normalised pressure for the two new points is shown in Figure 6.14, it can be seen that the negative area seen from point **d** is getting smaller going to point **d1** and **d2** and the area has increased very slightly, this confirms the increase in lift in the process between **d** to **a**.

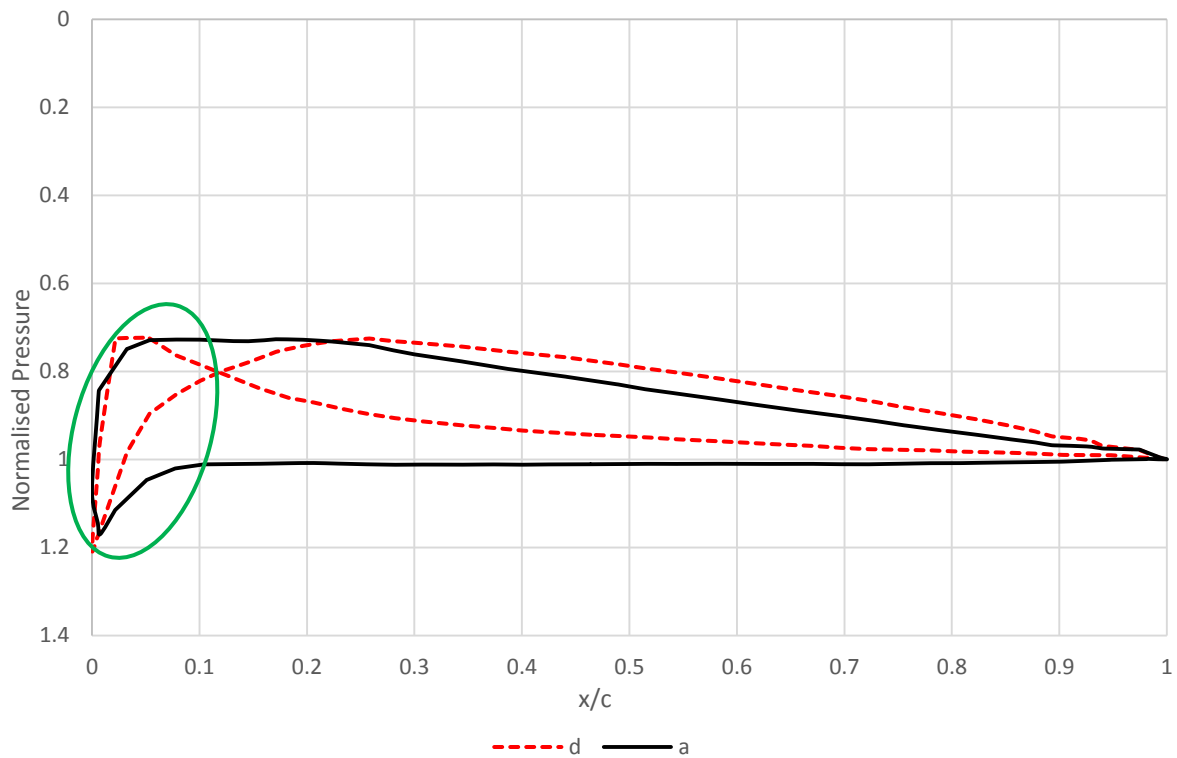


Figure 6.13 Normalised Pressure plots at 75%R for points **c** and **d** for the 43.5% amplitude simulation

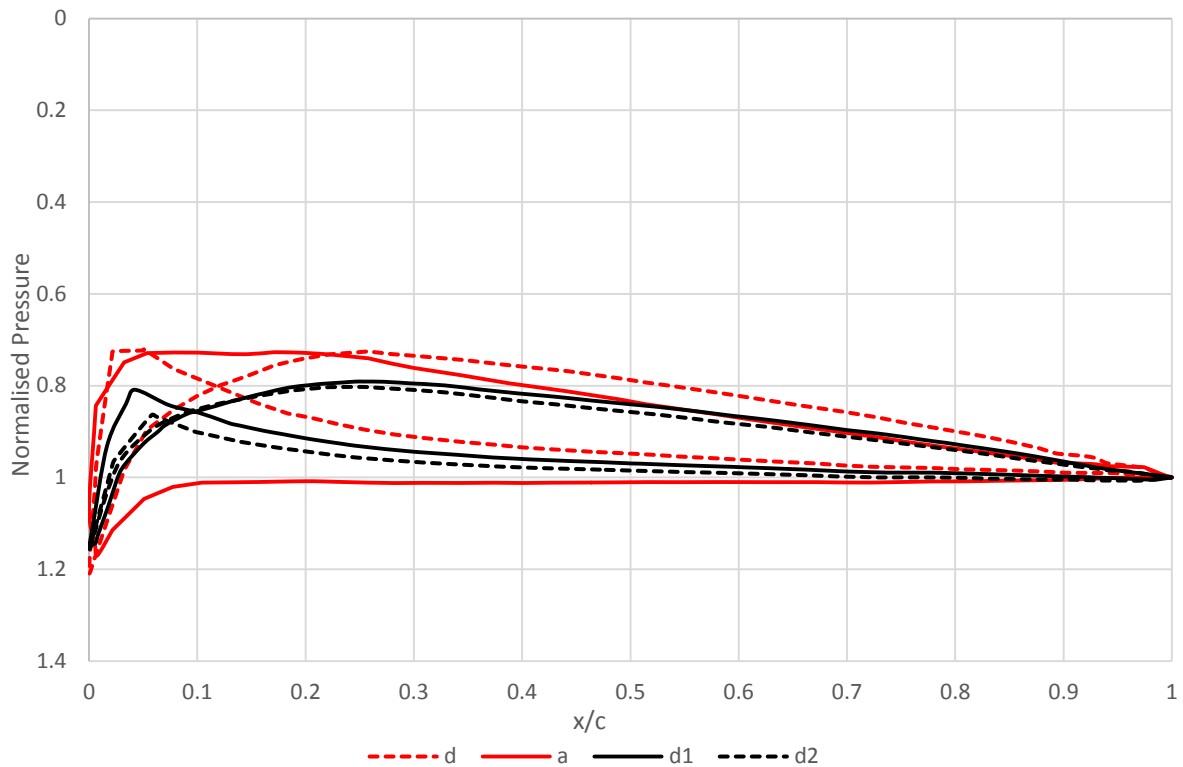


Figure 6.14 Normalised Pressure plots at 75%R for points **d** and **a** for the 43.5% amplitude simulation including the in-between points **d1** and **d2**

It was intended by the author that for points **c1** and **d2** to be points having the same TSR but on the opposite side of the hysteresis curve. Figure 6.15 shows the normalised pressure curves for the two points **c1** and **d2**, it can be seen the difference in the area under the pressure curves suggesting a higher lift for point **c1** which consistently agrees with the locations of their CP plotted as shown in Figure 6.11. It can also be observed that for point **d2**, the overlap within the suction side and the pressure side of the pressure plot is still present while it is not seen for the plot of point **c1**. It can be seen that although the suction side and pressure side has not yet overlapped, they are really close to each other also suggesting that they are going to overlap soon. This confirms the effect of the lag explained in Chapter 5 and the start of this chapter whereas there is an observed delayed for the reattachment after the separation that happened at low TSR.

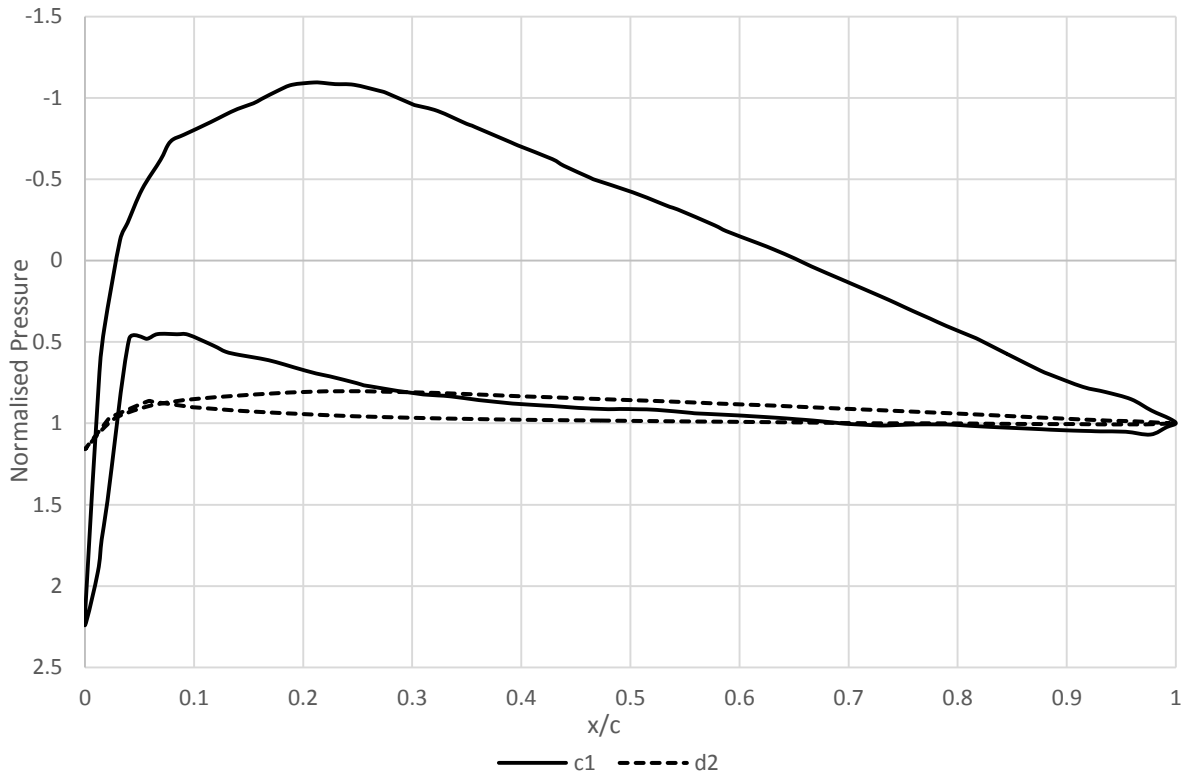


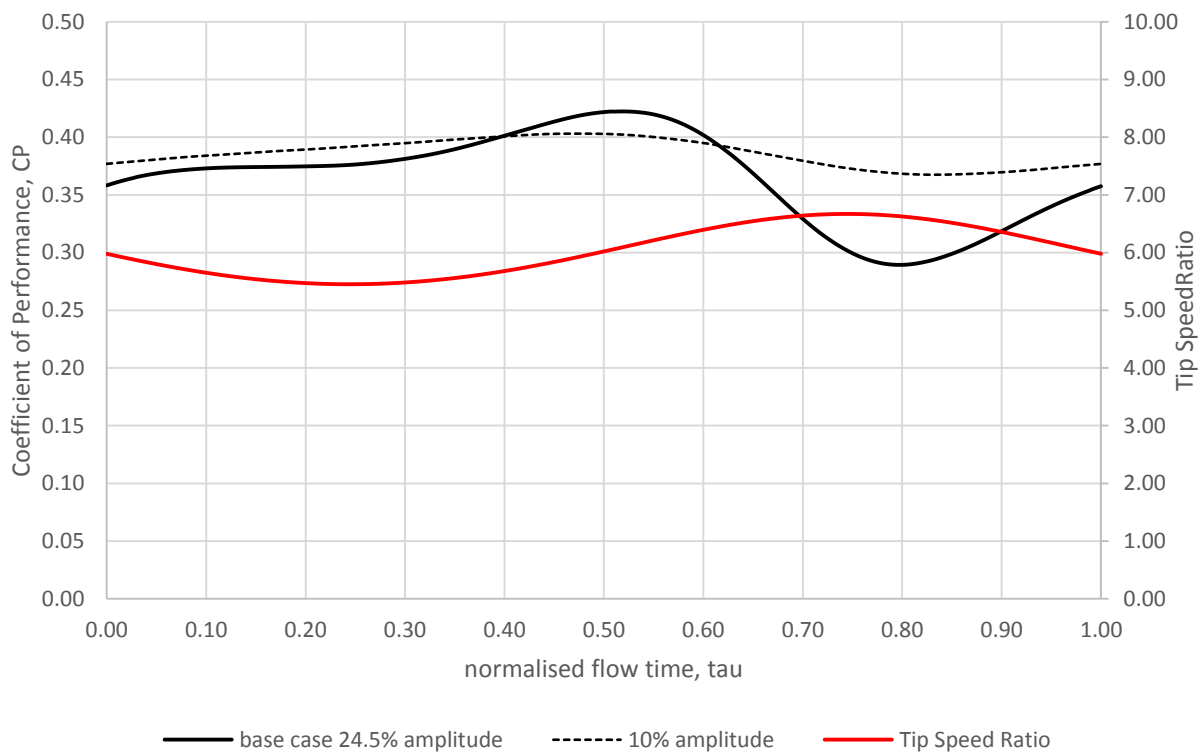
Figure 6.15 Normalised Pressure plots at 75%R for points **d** and **a** for the 43.5% amplitude simulation including the in-between points **d1** and **d2**

### 6.3.5 Summary for the 43.5% amplitude unsteady simulation

The whole 43.5% amplitude unsteady simulation shows the same trend with that of the base case with the only difference having that the hysteresis curve also increases in size which is due to the fact that the TSR range also increases with the increase in the velocity variation amplitude. Streamlines and normalised pressure data explanation shows consistency to the base case unsteady explanation. A lower cyclic-averaged CP when compared to that of the unsteady base case was also observed, which is mostly due to the very low instantaneous power extracted by the turbine for the high TSR. For the next section, the effect of decreasing the amplitude is observed and then a comparison between the three cases will be presented to look at the overall effect of velocity profile amplitude to the performance of the Sheffield HATT.

## 6.4 Low Amplitude Variation

The lower amplitude velocity profile presented in Equation 15 in Section 6.1 was used for an unsteady state simulation of the Sheffield HATT. Same conditions and solver for the base case was used with the only difference being the velocity profile, the rotation of the turbine and the time-step used. After monitoring and recording data from FLUENT, the time-response of the turbine is plotted and presented in Figure 6.16.



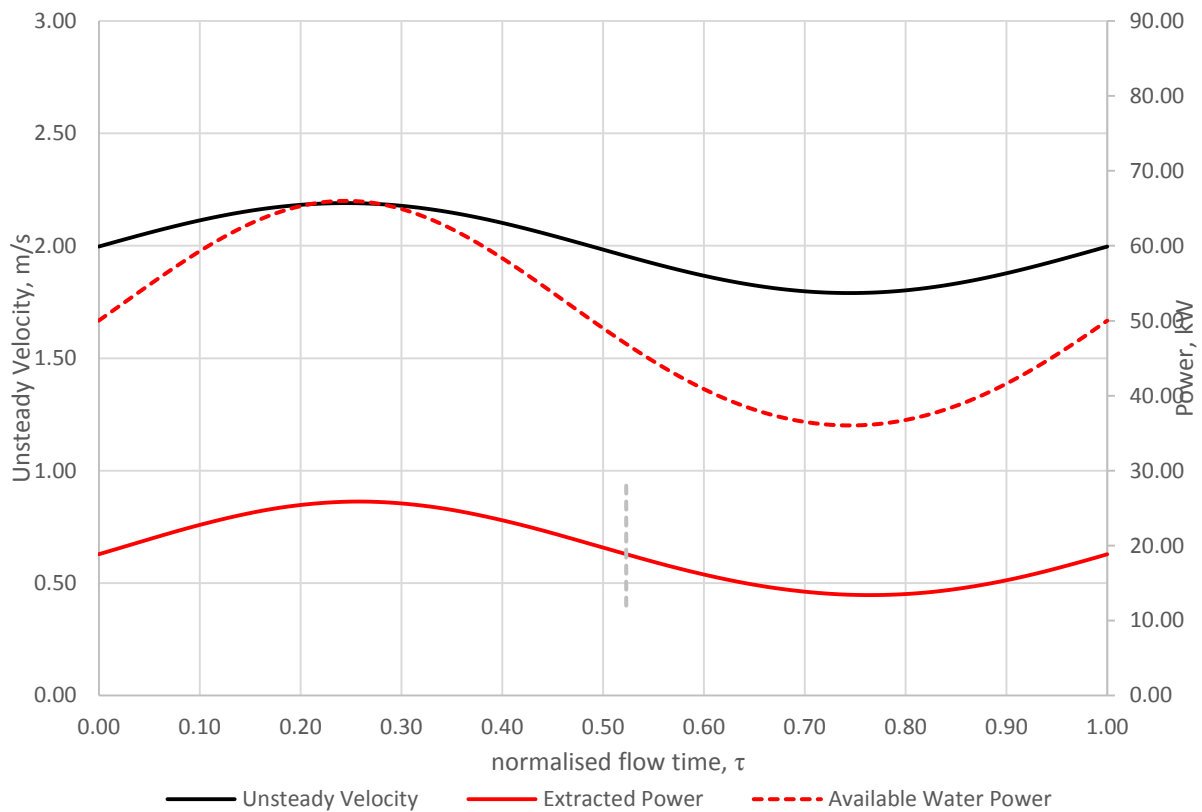


Figure 6.16 Sheffield HATT Response for the 10% Amplitude Simulation

**top:** CP value plotted against normalised time superimposed with the base case CP plot and instantaneous TSR; **bottom:** Power extracted by the turbine plotted against normalised time superimposed with the water velocity profile and power available in the water

The first observation that can be deduced from Figure 6.16 is that the variation of the CP value for the lower amplitude unsteady simulation showed smaller disparity in value when compared to that of the unsteady base case but still the trend of the plots is still similar to each other. The lag that is observed for the base case and the 43.5% amplitude simulation is still present but it becomes shorter with the power extracted returning to its original value at  $\tau=0.52$ . The effect of the sensitivity of the turbine at higher TSR is also avoided as the TSR range for this simulation is only between 5.45 and 6.67. In terms of the power extracted, a decrease was observed in terms of the maximum  $P_e$  value which was at 25.88 kW (at  $\tau=0.257$ ) compared to the 33.94 kW obtained from the base case unsteady simulation. This smaller power is again due to the smaller variation in velocity which reflects as a lower maximum instantaneous power

available. For further comparison, the response was plotted as a hysteresis curve shown in Figure 6.14. A smaller hysteresis curve was observed when compared to the unsteady base case curve. It can also be seen that the lower amplitude plot is very close to the steady flow performance curve suggesting that the effect of unsteadiness is less as the amplitude of the velocity fluctuation is decreased.

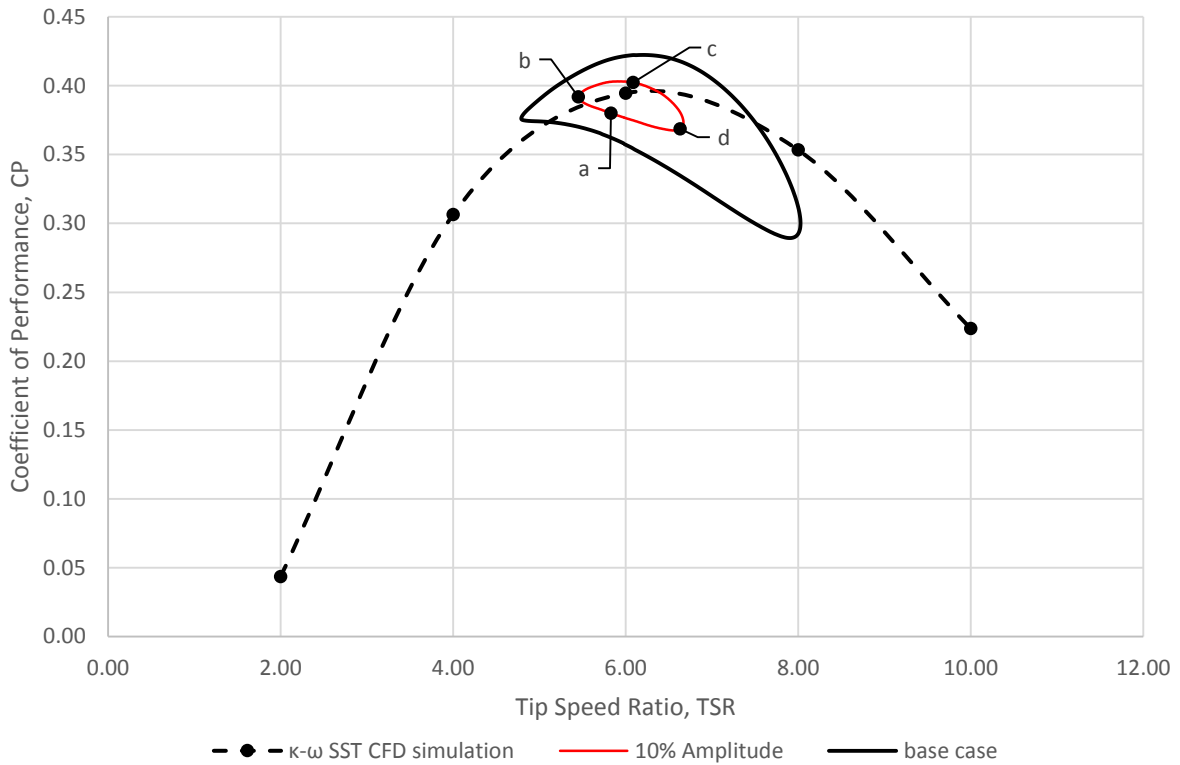


Figure 6.17 Unsteady Flow Hysteresis Curve for 43.5% amplitude over the steady flow performance curve for the Sheffield HATT and the base case hysteresis curve

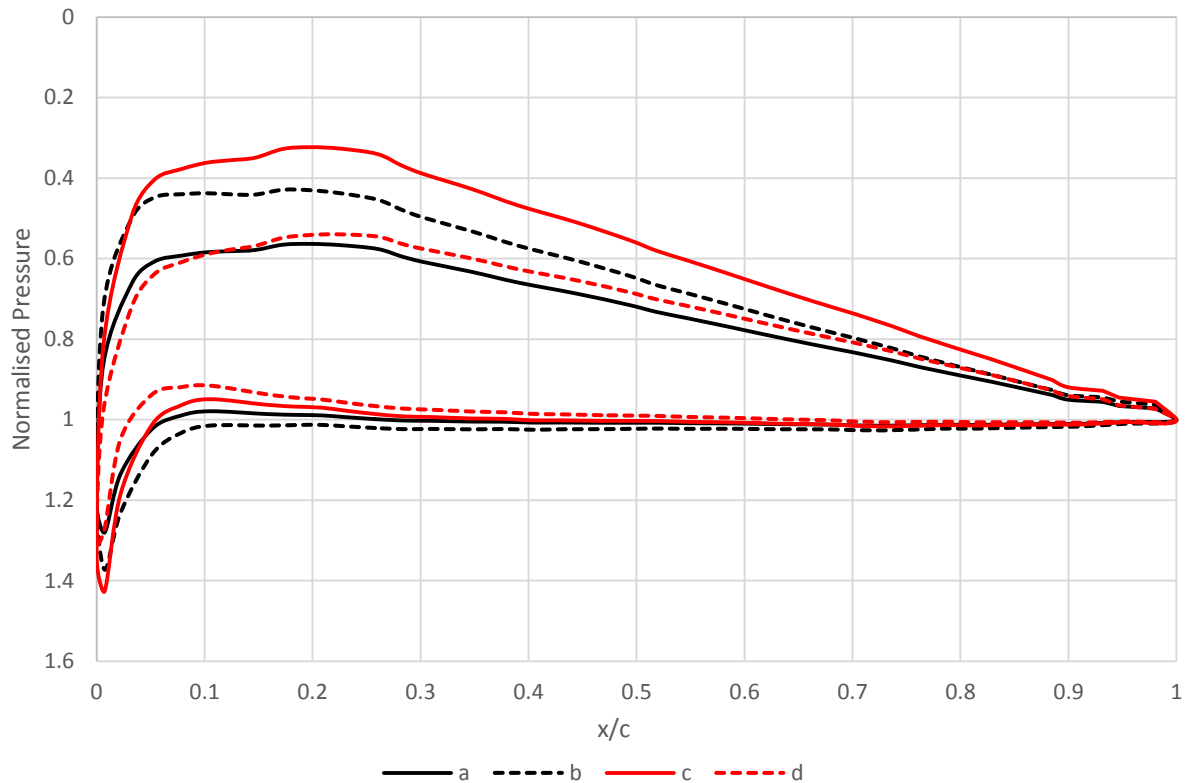


Figure 6.18 Normalised Pressure plots at 75%R for data points **a**, **b**, **c** and **d** for the 10% amplitude simulation

The normalised pressure plots for the different points in the 10% amplitude unsteady simulation is presented in Figure 6.18. Not significant changes are found within the areas under the curves although it still follows the trend showed by the unsteady base case. From **a** to **b**, as the TSR decreases, the area under the pressure curve increases signifying that lift increase during that process and since no separation was included, CP also increases. From **b**, the lift still increases despite the fact that the TSR at this point is already increasing which means that the incident AoA should be decreasing. A lag is observed at this point in terms of the power extracted by the turbine but it is shorter when compared to the base case and this causes the further increase in lift and hence CP. Once the CP curve reached its maxima near point **c**, the lift started to decrease and finally reached the minima in the hysteresis curve which is also supported by the smallest area in the pressure plots although the difference is not that

significant, this happens as the TSR increases. The streamline plots for the 10% hysteresis curve showed fully attached flow for the whole process and there is no noticeable difference in the AoA visually.

### **6.5 Effect of Amplitude Variation**

This section will present the summary of the amplitude variation study directly comparing the results from the 10% and 43.5% amplitude simulation to the base case simulation. In table 6.1, the cyclic average CP for the three cases of unsteady simulation were presented including the CP from the steady flow simulation at  $TSR = 6$ . It can be seen that as the amplitude of the velocity variation decreases, the value of the cyclic-averaged CP value was for the unsteady simulations is getting closer to the steady-state CP value. For the 10% amplitude simulation, there is only a 0.72% difference in the CP value but it reaches up to a difference of 5.2% for the highest amplitude being simulated. This suggests that increasing the amplitude for the unsteady velocity variation is detrimental to the performance of the tidal turbine being investigated in this study.

An image of the performance curve containing the three hysteresis curves from the three unsteady simulations is presented in Figure 6.19. It can be clearly seen that as amplitude increases, the hysteresis curve also became larger. The higher CP increase can be explained by larger inertial effects which results to a lag in the power extracted by the turbine. This lag also increase with the amplitude as shown in sections 6.3 and 6.4. On the other hand, the very low CP observed as TSR increases is due to the sensitivity of the turbine to a small change in AoA as explained with the  $C_l/C_d$  plots for the hydrofoil sections at the 25% and 75% span of the blade. Although higher CP values can be achieved as higher amplitude cases, the negative effect of the whole process is clearly bigger which is also reflected at the cyclic averaged values

presented in table 6.1. A good topic for future studies will be a way to utilise the higher CP areas that can be achieved due to higher amplitude velocity variation.

Table 6.1  
Cyclic-average CP value comparison for the unsteady simulation at TSR = 6

Simulation	Coefficient of Performance, %
Steady state (TSR = 6)	39.46
10% amplitude	38.74
Base case (25% amplitude)	37.50
43.5% amplitude	34.26

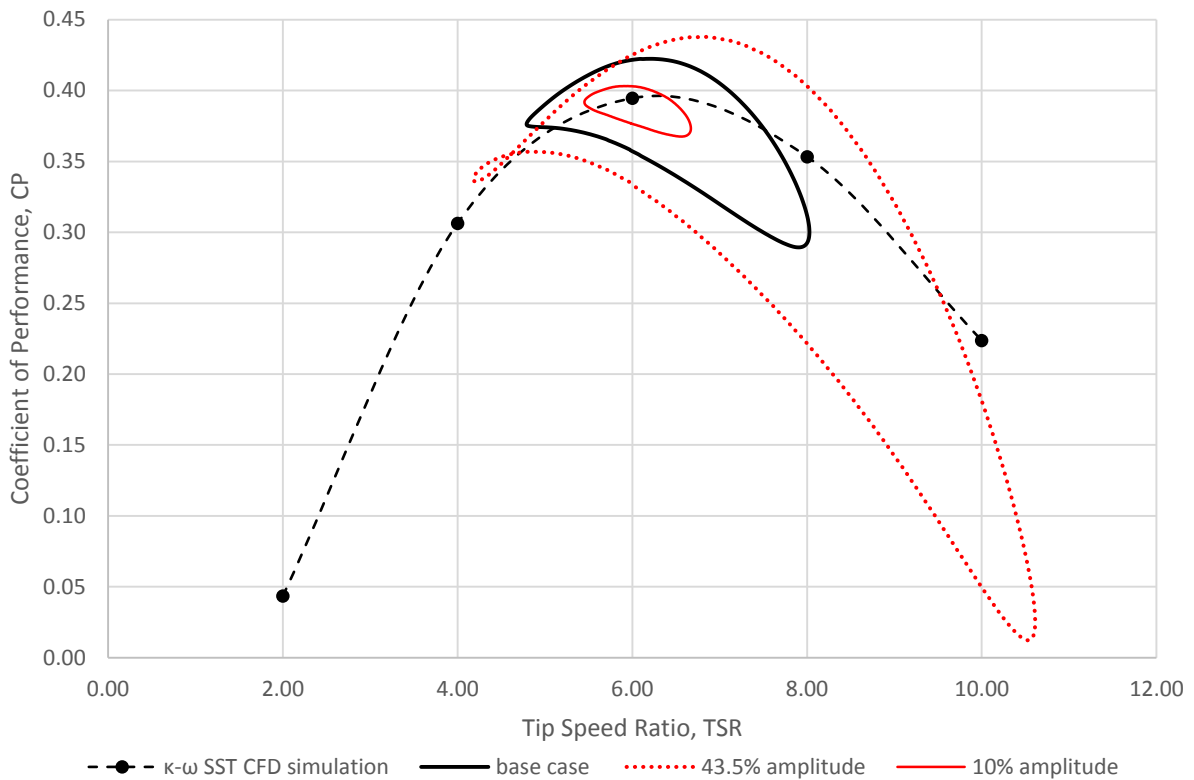


Figure 6.19 Unsteady Flow Hysteresis Curves for the amplitude variation study over the steady flow performance curve

## 6.6 Frequency Variation Comparative Study

For this section, the frequency instead of the amplitude of the idealised unsteady velocity profile will be altered. Equations 16 and 17 presents the low frequency and high frequency equations that will be used in this study. The frequency of the base case was halved and doubled respectively for the two equations defined. The cycle-averaged available power for these equations will be the same to that as the base case as the frequency is the only parameter being changed. The solver used for previous simulations is also the one used for this study. Just like previous simulations, the response of the turbine in terms of  $C_m$  was monitored and translated in CP after cyclic convergence was achieved. Some instantaneous points in the one cycle are also captured to provide additional information such as pressure curves and streamline plots.

$$u(t) = 1.940061 + 0.49 \sin(\pi t) \text{ (eq. 16)}$$

$$u(t) = 1.940061 + 0.49 \sin(4\pi t) \text{ (eq. 17)}$$

Sections 6.7 and 6.8 will present the results of the simulation in details. Just like what is presented in the amplitude variation study, the cyclic-averaged CP for both frequency simulations are also computed and recorded for comparison purposes as can be seen in Table 6.2. Two other unsteady simulations with higher frequency ( $f=3.0$  Hz and  $f=4.0$  Hz) were also presented in Table 6.2, the addition of these two data gave an idea of the cyclic-average CP trend when the frequency further increase and the flow to be more unsteady. Measurements from real tidal sites has recorded even a very high frequency for unsteady flow resulting from turbulence with  $f=4.0$  Hz being measured by Milne et al. from the Sound of Islay, UK when they tried to map the unsteadiness of the flow in that region (Milne *et al.*, 2013) It can be seen from the table of values that from the steady flow CP, a drop was observed as unsteadiness was introduced within the flow at  $f=0.5$  Hz. The averaged CP value starts to increase as the

frequency was increased to  $f=1.0$  Hz it reaches a local maxima at  $f=3.0$  Hz before dropping in value again as observed again at  $f=4.0$  Hz. Looking at the bigger picture, it can be seen that the difference in the cyclic-averaged CP for the different frequency cases is not as drastic as it was observed for the amplitude variation study. It can also be deduced that the cyclic-averaged CP fluctuation is getting smaller as the frequency increases with a very small difference as seen from the resulting CP of the  $f=3.0$  Hz and  $f=4.0$  Hz. A detailed description and explanation of this results will be presented in Section 6.9.

Table 6.2  
Cyclic-average CP value comparison for the unsteady simulation at TSR = 6 (frequency variation)

Simulation	Coefficient of Performance, %
Steady state (TSR = 6)	39.46
$f=0.5$ Hz	37.90
Base case ( $f=1$ Hz)	37.50
$f=2.0$ Hz	37.11
$f=3.0$ Hz	36.8
$f=4.0$ Hz	37.1

### 6.7 Low Frequency Simulation

The hysteresis curve for the turbine's response for the  $f=0.5$  Hz unsteady simulation is presented in Figure 6.17. It can be seen that the hysteresis curve is thinner when compared to the unsteady base case plot, the curve also appears closer to the steady flow plot. This suggests that the effect of the unsteadiness in the flow is lesser as the frequency of the velocity became smaller. This observation will be elaborated later in this section. Another noticeable observation is the presence of a small loop that emerges at the region of low TSR, which is also

seen at the 43.5% amplitude simulation. Given these observations, the cyclic-averaged CP for this low-frequency simulation is 37.9% which is slightly higher than that of the base case simulation which is at 37.5%. This can be attributed to the very small variation in the instantaneous CP as shown in Figure 6.17 which is visually seen as a thinner area when compared to that of the base case simulation. It will also be explained in detail in the following sections that the delay effect observed in previous simulations is relatively smaller for this case which makes an impact to the shape of the hysteresis curve.

For the base case simulation, the reduced frequency is calculated to have a value of 0.051 (calculated at the 75% span of the blade) which is just at the edge of the definition of unsteady flow by Leishman, however the hydrodynamics presented and the hysteresis curve for that specific simulation proved that the flow is indeed unsteady and there is some implications in the turbine's performance. The other two cases discussed in Chapter 5 which are the TSR=4 and TSR=8 simulations have their reduced frequency calculated as 0.068 and 0.034 respectively. This is still consistent with what is observed in Chapter 5 where a more drastic effect was seen for the TSR=4 unsteady simulations which has a higher reduced frequency. On the other hand, for the TSR=8 simulation, the reduced frequency is inside the value bracket for quasi-steady flow based on Leishman definitions but it can be seen from the hysteresis curve that the effect of unsteadiness is still present although this is amplified by the sensitivity of the turbine used at high TSR AoA variation.

For the low frequency simulation, the frequency in the velocity flow was set to  $f=0.5$  Hz which corresponds to a reduced frequency calculated to be 0.023, which is the lowest reduced frequency that has been used for the duration of the thesis. Having a lower  $k$  value, the effect of unsteadiness is expected to be smaller via Leishman definition which is also shown in the hysteresis curve in Figure 6.20. Saying that the flow is quasi-steady is another topic to be discuss as it clearly shows that there is an unsteady effect though smaller as compared to other

unsteady simulations. A summary of the effect of frequency will be presented at the end of this chapter.

A number of experiments that uses the reduced frequency as a parameter to describe the current flow scheme has been done in current tidal turbine literature but most of them looks at unsteadiness effects in hydrodynamic loading and not performance analysis. Whelan did experiments at low frequencies of  $k=0.02$  at high TSR and found out that the inertia effects in tidal turbine is positive which also agrees with the combined effect of dynamic inflow and added mass in turbine loading (Whelan, 2010). McNae did some experiments in the same experimental flume prior to Whelan's experiments with reduced frequencies of  $k=0.025$  and  $k=0.005$  which are both very low frequency flows and saw that there is a small phase lag on the bending moment at  $k=0.025$  but it was approximately zero for the  $k=0.005$  case but it was shown that these observations are affected by the varying rotor speed during the experiment (McNae, 2013). Milne *et al.* did a higher frequency experiments up to  $k=0.07$ . It was stated by Milne *et al.* that at high TSR simulations where boundary layers are attached, a sensitivity to the forcing frequency is recognisable. A frequency variation study was also conducted whereas the forcing frequency was varied for a constant mean TSR to see its effect on the blade out-of-plane bending moment and it was shown that the hysteresis curve response of the tidal turbine under study became thinner and closer to the steady-state values as frequency decreases (Milne *et al.*, 2015). This observation was also shown in Figure 6.20 although for performance values and not hydrodynamic loading whereas the performance of the turbine being examined is dependent on the varying velocity profile frequency.

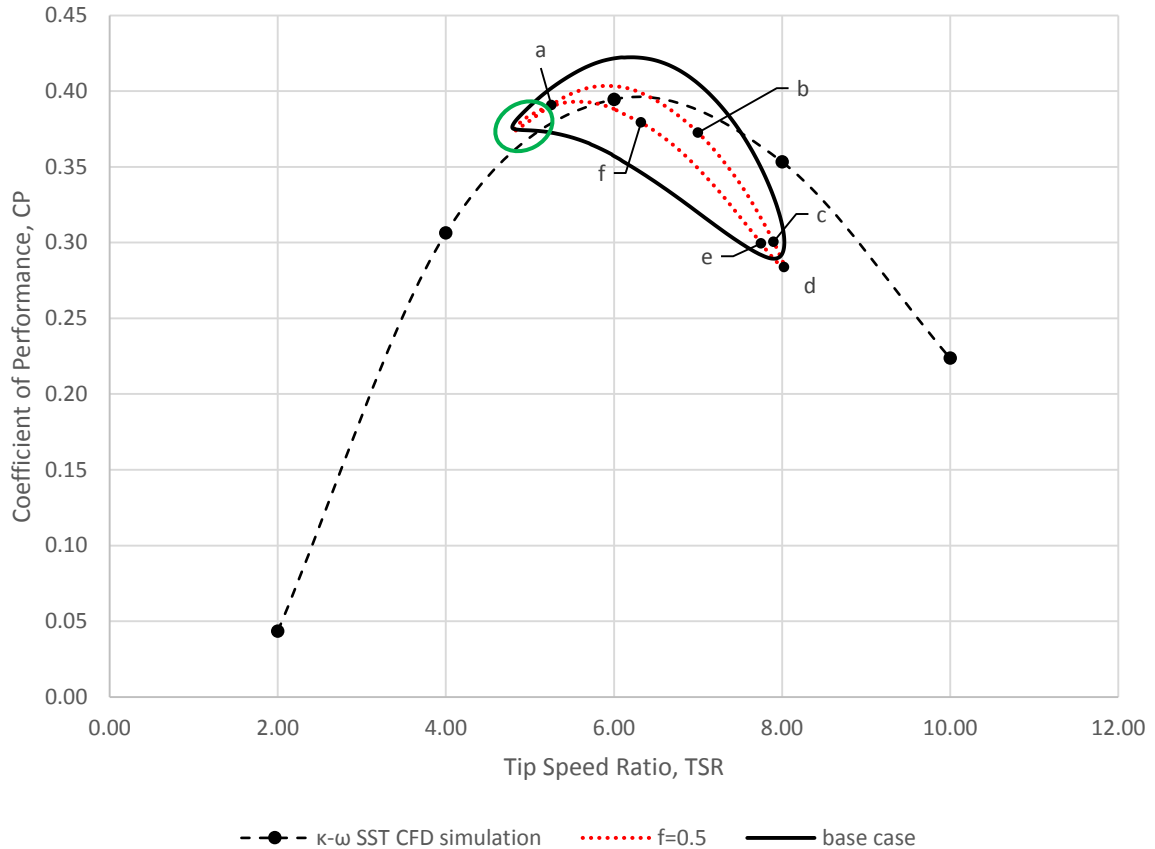


Figure 6.20 Unsteady Flow Hysteresis Curve for  $f=0.5$  Hz unsteady simulation over the steady flow performance curve for the Sheffield HATT and the base case hysteresis curve ( $f=1.0$  Hz,  $A=25\%$ )

The cyclic response of the turbine is presented in Figure 6.21 superimposed with the base case response to serve as basis for comparison. Also plotted is the power extracted and power available for this simulation. The lag that was observed for the other simulations in this chapter was still observed but it is very small as compared to the other cases. The power extracted went back to its initial value at  $\tau=0.506$  as highlighted by the dotted vertical line in Figure 6.21. This is another proof that shows the unsteadiness effect to the performance became lesser. The effect of the sensitivity of the turbine to small changes to the AoA at high TSR is still observed as the hysteresis curve still contains the sharp decrease at high TSR although it is less abrupt as compared to the base case simulation's rate of decrease over the same range of TSR. A better comparison of the extracted power is present for the frequency variation study

as the instantaneous power available plot will be the same since the amplitude of the velocity variation was maintained constant. For  $f=0.5$  Hz simulation, the maximum  $P_e$  reached a value of 33.65kW which is very close to the 33.94 kW obtained at the base case simulation. The difference is the time where it occurred which is at  $\tau=0.25$  which is earlier when compared to the base case which occurred at  $\tau=0.26$ , this is important because this means that the maximum  $P_e$  was paired with the peak available power which occurs at  $\tau=0.25$  whereas for the base case the maximum  $P_e$  value was paired with a lower  $P_a$  as the  $P_a$  curve was already dropping at  $\tau=0.26$ , resulting to a higher CP which is reflected in the difference shown in Figure 6.20.

The small loop within the hysteresis curve in Figure 6.20 is seen as a small complete cycle in the normalised flow time plot in Figure 6.21 where it is highlighted by a green circle. Unlike the one observed at the high amplitude simulation where the loop inside the hysteresis curve was explained to be caused of the delay/lag on the extracted power of the turbine to the available power in the water. The same explanation will not be applicable for the low frequency simulation as there is a very small lag in the extracted power. Streamlines for the data points for the hysteresis curve in Figure 6.20 is presented in Figure 6.22. For the whole duration of the cycle, it can be seen that the flow around the hydrofoil sections at 25% and 75% span of the blade is fully attached and there is no separation observed even for lower TSR. This is different from the one observed even for the base case simulation whereas small separation near the trailing edge is observed for low TSR and high AoA. The only notable changes in terms of the streamlines is the incident AoA which still follows the same trend as per the previous simulations.

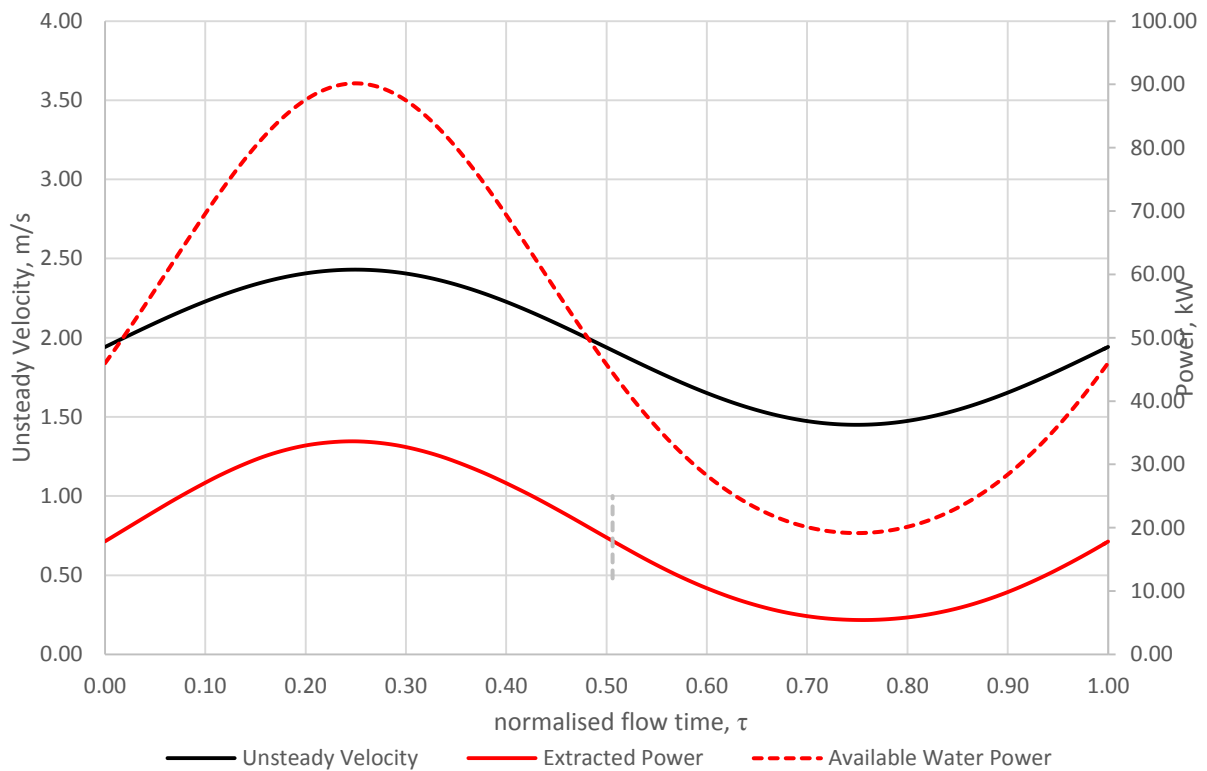
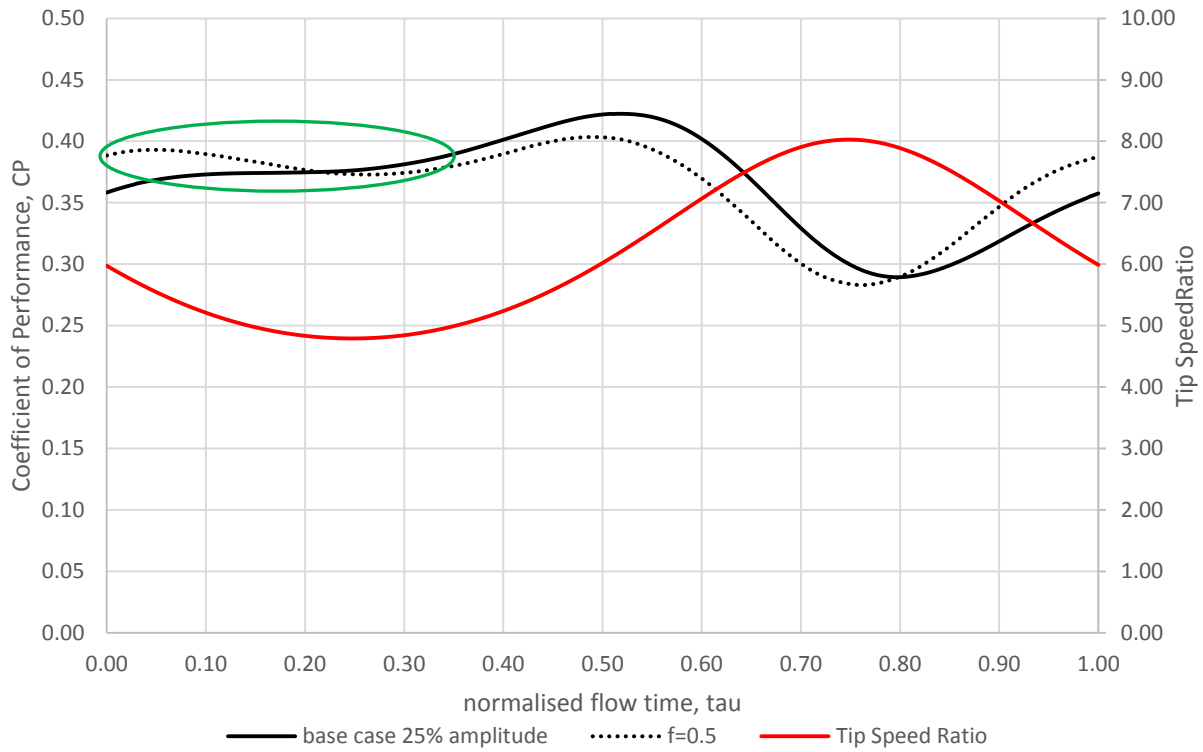
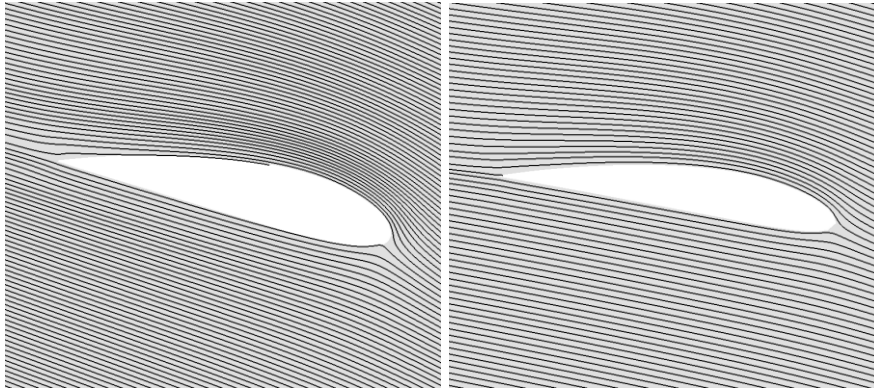
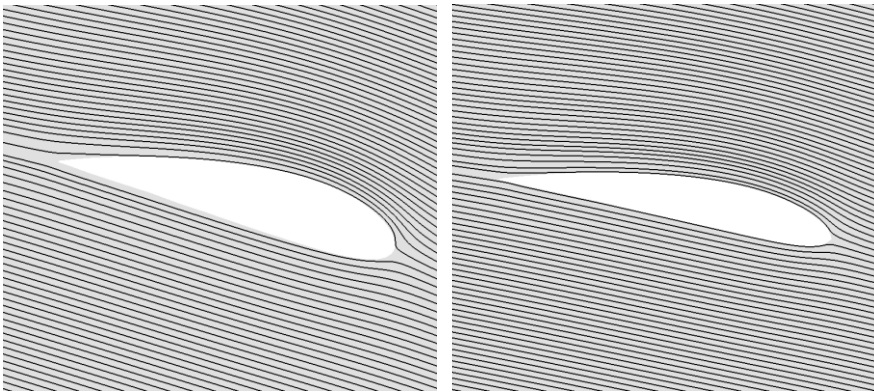


Figure 6.21 Sheffield HATT Response for the  $f=0.5$  Hz unsteady Simulation

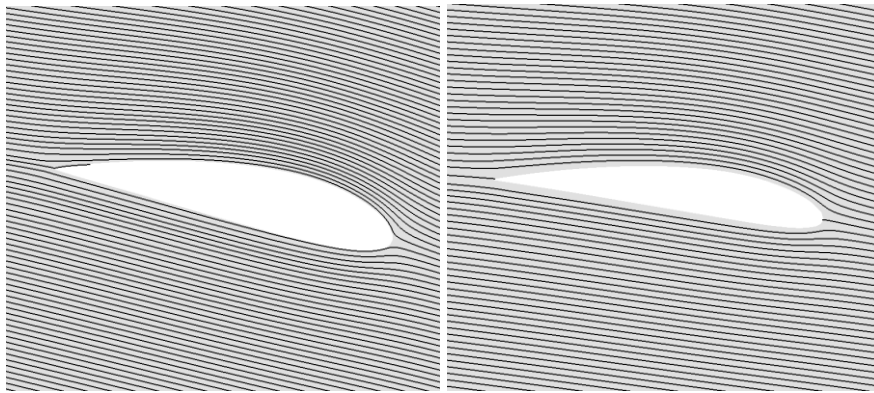
**top:** CP value plotted against normalised time superimposed with the base case CP plot and instantaneous TSR; **bottom:** Power extracted by the turbine plotted against normalised time superimposed with the water velocity profile and power available in the water



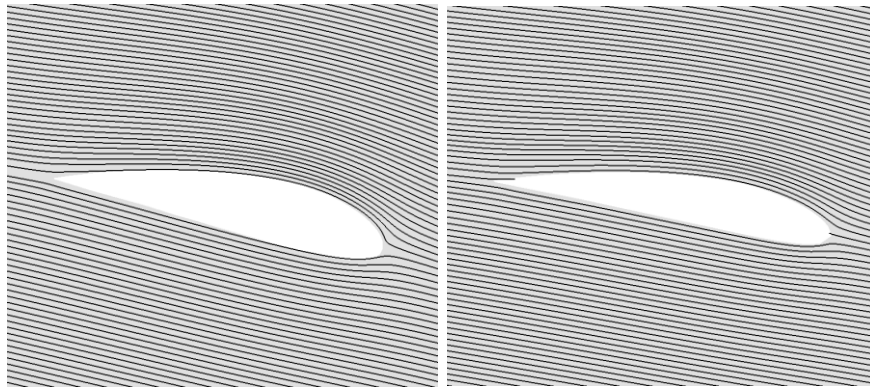
(a)



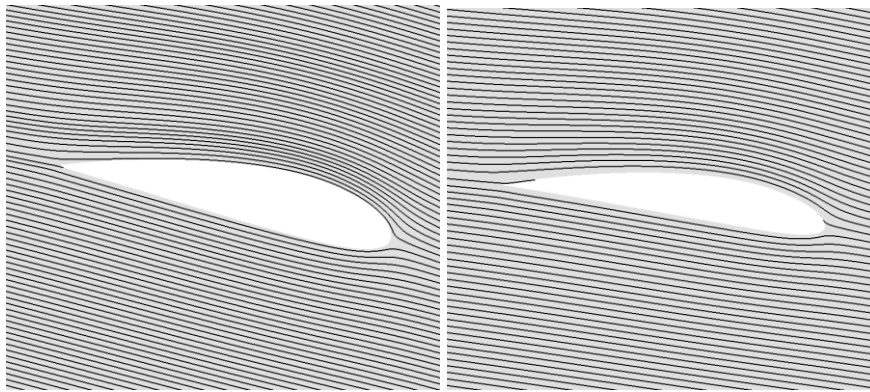
(b)



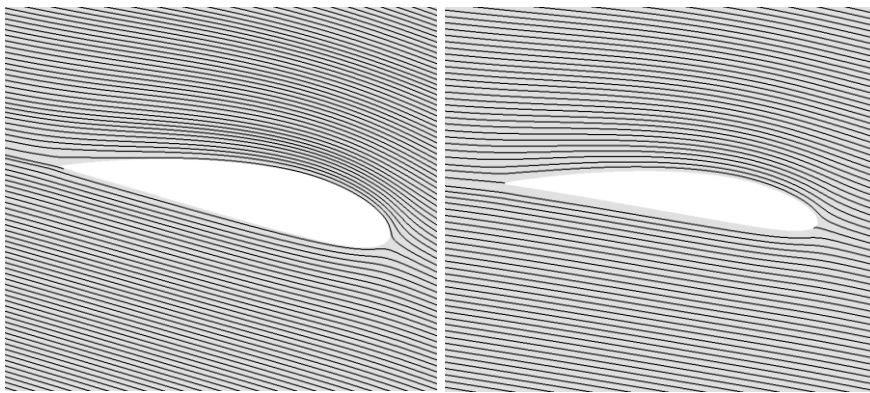
(c)



(d)



(e)



(f)

Figure 6.22 Streamlines at various part of the hysteresis curve for the  $f=0.5$  simulation with correspondence

## 6.8 High Frequency Simulation

Like the other simulations present in the thesis, the instantaneous CP values for the high frequency simulation were plotted against the instantaneous TSR to form the hysteresis curve as shown in Figure 6.23. The resulting curve is superimposed with the steady state turbine performance curve for the turbine and the unsteady base-case simulation for comparison purposes. It can be seen from the plot that the hysteresis curve for the  $f=2$  Hz simulation has a shape that is not similar to any of the previous hysteresis curve observed in the thesis. The hysteresis plot shows a more circular curve with bulging especially at the high TSR's as oppose to the sharp curve as observed from both the unsteady base case curve and the low frequency simulation. The curve traced by the points **d-e-f-a** shows a very small variation in CP values at high TSR which is also very different from the other hysteresis curve plotted beforehand where the lower part of the curve still follows the trend of the steady state performance curve. These differences can be attributed to the high reduced frequency for this simulation at  $k=0.1025$  which makes the flow more unsteady as per Leishman definition.

In the case of the amplitude variation study, it was shown that having a higher amplitude for the inlet velocity variation results to a lower cyclic-averaged CP for the simulation but for the case of the high frequency simulation, the cyclic-averaged is computed to be 37.11% which is 0.39% lower than that of the unsteady base case. From the hysteresis curve alone, the higher cyclic-averaged CP can be attributed to the area of the curve that is higher than the steady-state performance curve. It can be seen from Figure 6.23 that the curve traced by the points **a-b-c-d** is higher than that of the steady turbine performance curve with the area b-c-d higher than that of the unsteady base case simulation. The curve reached an instantaneous CP of 44.71% at TSR=6 and reaches a maximum value of 46.32% at TSR=6.8. From there, the CP starts to decrease slowly until it reaches point c where the slope of the curve started to get steeper as still can be attributed to the sensitivity of the blade to small AoA variations at high TSR.

Although a steep decrease was observed at that point, the curve did not reach a very low value because of the high starting value when the CP dropped. Another point that can be part of the reason for the high cyclic-averaged curve is the region **e-f-a** of the curve, as noted earlier, shows very small variation in the instantaneous CP.

The instantaneous CP plot over normalised time for the  $f=2$  Hz simulation is presented in Figure 6.24 (top) while the Power extracted plot superimposed with the power available plot is in the bottom plot of the same figure. It can be observed from the extracted power plot that there is again a delay that has been observed since the unsteady base case and the one for the  $f=2$  Hz simulation shows the largest lag so far in the thesis. For this case, the extracted power goes back to its initial value at  $\tau=0.57$  which is 0.07 further than that of the available power and water velocity.

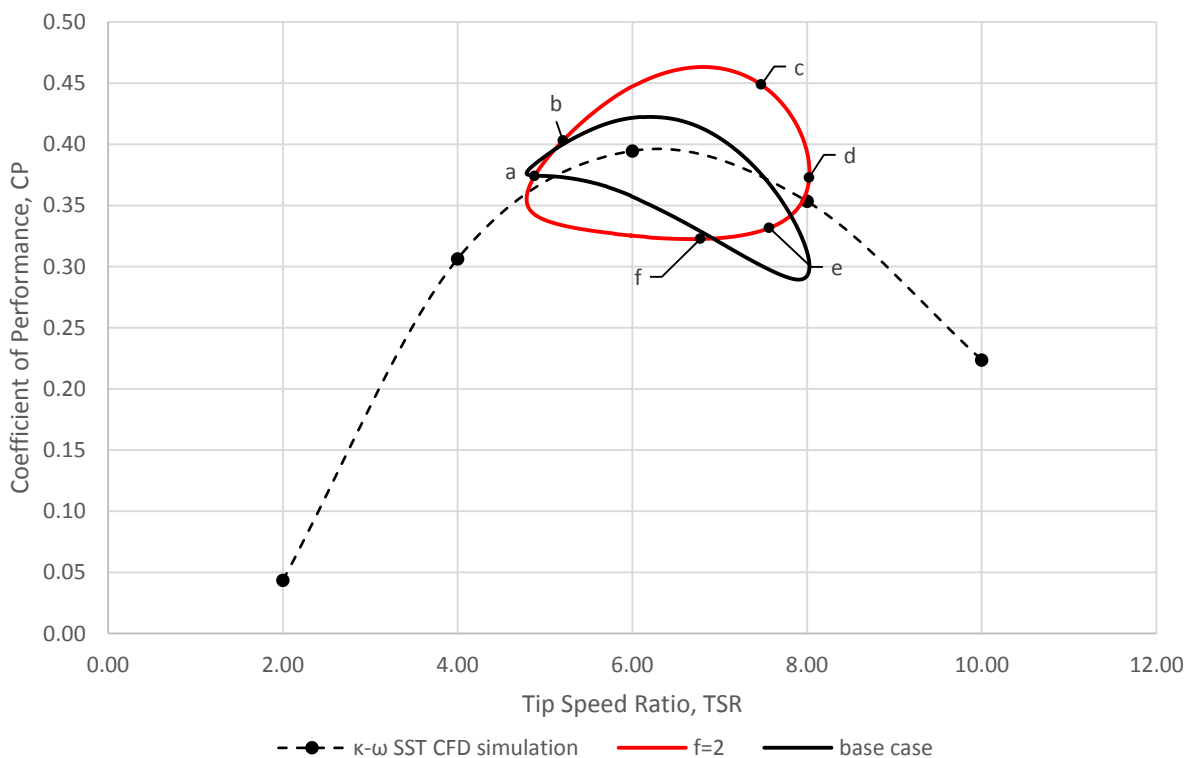


Figure 6.23 Unsteady Flow Hysteresis Curve for  $f=2$  Hz unsteady simulation over the steady flow performance curve for the Sheffield HATT and the base case hysteresis curve ( $f=1.0$  Hz,  $A=0.25$ )

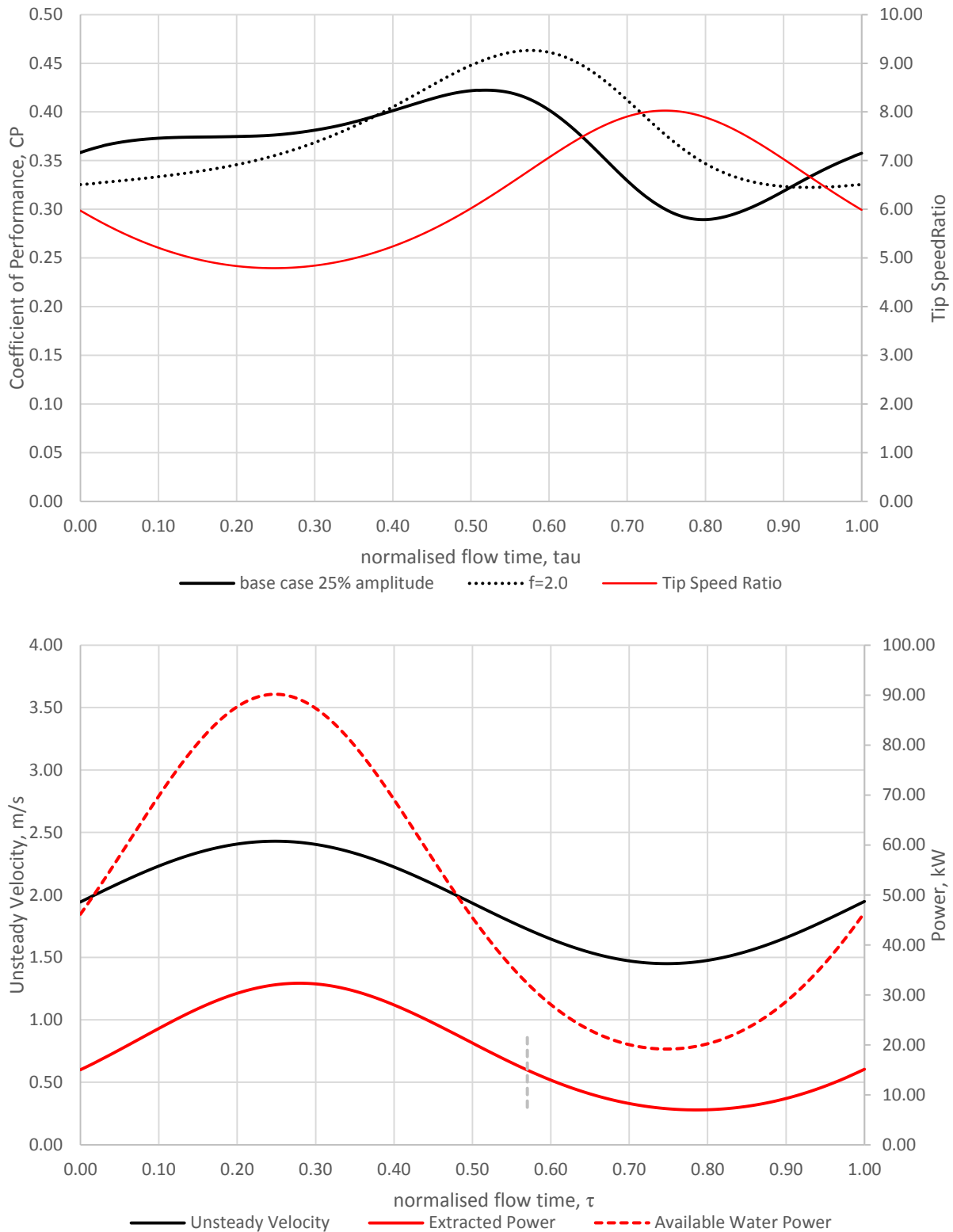


Figure 6.24 Sheffield HATT Response for the f=2 Hz unsteady Simulation

**top:** CP value plotted against normalised time superimposed with the base case CP plot and instantaneous TSR; **bottom:** Power extracted by the turbine plotted against normalised time superimposed with the water velocity profile and power available in the water

This lag results to an even more delay in the CP plot, where the maximum instantaneous CP occurred at  $\tau=0.575$  which is very close to where the extracted power goes back to its initial value. A continuous increase in the CP curve is observed from  $\tau=0$  to  $\tau=0.575$ . The first half from  $\tau=0$  to 0.25 is increasing as both the power extracted and power available are increasing, the power available starts to drop at  $\tau=0.25$  but the power extracted continued to increase until  $\tau=0.28$  causing a continued increase as it paired down with a lower denominator. By the time the plot for the power extracted starts to drop in value, the power available is already at a lower value, hence CP still increase. At  $\tau=0.50$ ,  $P_a$  has returned back to its initial value but  $P_e$  is still decreasing and not returned to its initial value having a pair of a higher  $P_e$  and lower  $P_a$  resulting again to a still increasing CP plot. This continuous increase in CP is another reason for the high cyclic-average CP value. The increase in CP stops at  $\tau=0.57$  as the rate of decrease in  $P_a$  became greater than  $P_e$  which results to a higher denominator hence lower CP. A maximum  $P_e$  of 32.33 kW at  $\tau=0.28$  was obtained for this simulation, this value is lower than both of the base case simulation and that of the  $f=0.5$  Hz simulation but again because of the delay by which this maximum  $P_e$  happened, a higher CP was still obtained for this simulation reflecting on the hysteresis curve in Figure 6.23.

It can be also be observed from the instantaneous CP plot vs normalised flow time that the minimum point for the curve is not observable at all. The minimum value happened at  $\tau=0.934$  with a value of 32.3% which is in fact very close to the initial value of the instantaneous CP at 32.5%. From  $\tau=0.57$  to 0.80, a sudden drop in the instantaneous CP can be observed from the plot because both  $P_e$  and  $P_a$  is decreasing at this range while  $P_a$  starts to increase again at  $\tau=0.75$  which makes the CP even lower. Afterwards, the CP decrease continued because the rate of increase for the  $P_a$  plot is higher than that of the  $P_e$  plot but the decrease is at a very slow pace as  $P_a$  and  $P_e$  are both increasing at this point as reflected in the instantaneous CP plot.

## 6.9 Additional Higher Frequency Simulations

To further understand the effect of unsteadiness in the turbine's performance specifically at high frequency, two even higher frequency velocity variation at  $f=3.0$  Hz and  $f=4.0$  Hz were used as inflow equations for the Sheffield HATT simulation. Figure 6.25 shows the plot of the cyclic-averaged CP vs frequency that is presented earlier in Section 6.6. It can be seen that although there are differences in the cyclic-averaged CP's at various frequencies, all of them are still below the steady-state value at the same TSR. This still supports the idea presented in Chapter 5 that unsteadiness in the flow produced a negative effect on performance. But this is not the most interesting observation from the data presented in Figure 6.25, it can be seen that as the frequency increases, the rate of drop on the CP value decreases and has a very small variation specially at the  $f=3.0$  Hz and  $f=4.0$  Hz simulations. This can be attributed to the turbine cannot cope up with how fast the velocity changes and is being saturated with turbulence flow.

Going back to Section 6.1 to 6.4, it was shown that as the amplitude of the velocity variation in the idealised inflow increased, the cyclic-averaged CP of the turbine decreased. This is affected by a number of factors which includes the increased variation in TSR range with increased amplitude resulting to a difference on flow characteristics especially at low TSR where separation and dynamic inflow effects are inferred to have occurred. The sensitivity of the turbine at high TSR small AoA changes was also highlighted to be very detrimental for the high amplitude analysis. These factors results to a linear summary of the amplitude effect study. Since the TSR range is constant for the frequency variation study, the effect of sensitivity of the turbine at low and high TSR were eliminated and only the response of the system to frequency changes were observed as presented in Figure 6.26 which shows drastic changes in the hysteresis curves as the frequency was altered.

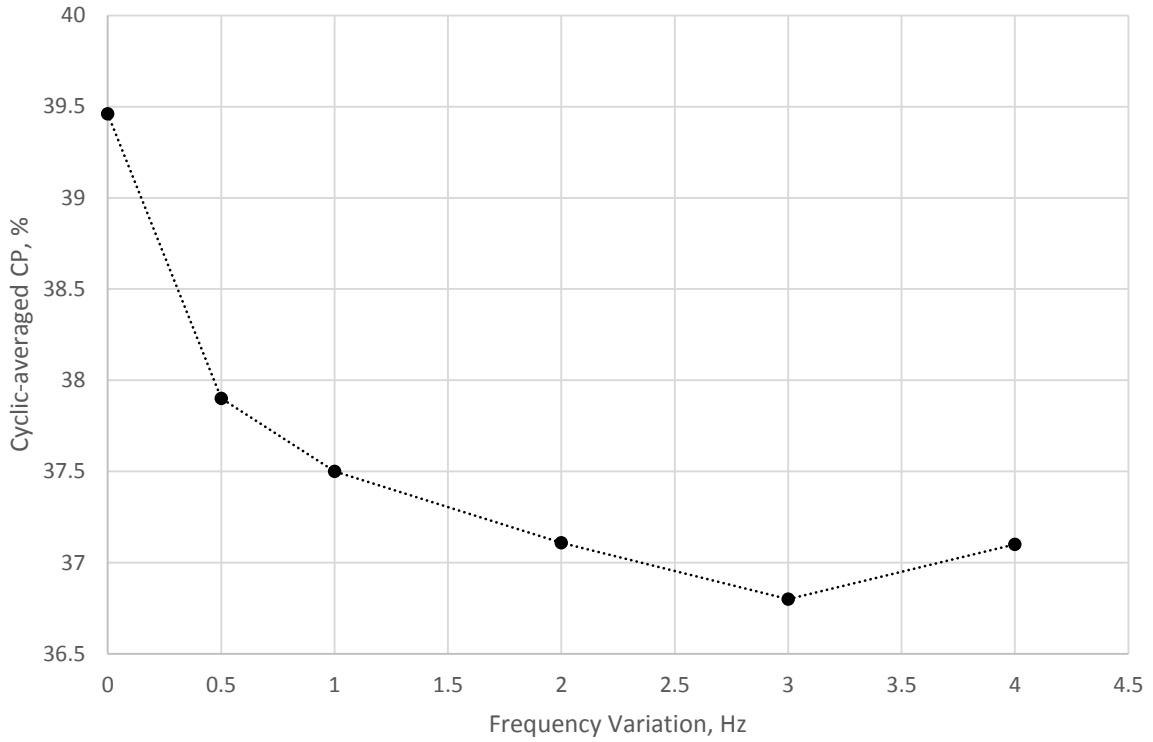


Figure 6.25 Cyclic-averaged CP plotted against the frequencies used in the unsteady simulations with the steady-state CP plotted at  $f=0$ .

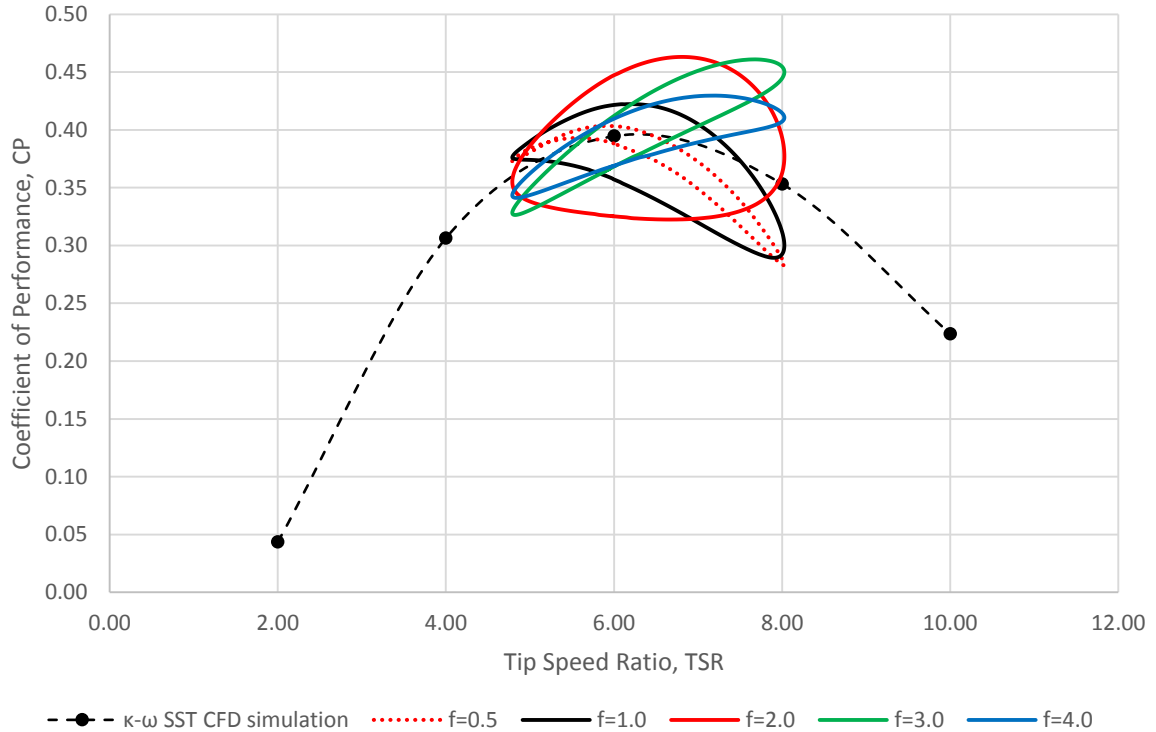


Figure 6.26 Unsteady Flow Hysteresis Curve for all unsteady simulation under the frequency variation study over the steady flow performance curve for the Sheffield HATT

The  $f=0.5$  Hz simulation shows a very thin hysteresis curve as described in detail in section 6.7, the high cyclic-averaged CP for this simulation is because most of the curve is actually just under the steady curve especially for high TSR and also the fact that the curve is the closest to the steady turbine performance curve. A wider hysteresis curve was observed for  $f=1.0$  Hz where the effect of the delay in the extracted power was already in effect. Going to  $f=2.0$  Hz, a sudden difference in the shape of the hysteresis curve has observed, as mentioned already in section 6.8, a larger delay effect in the extracted power is present in this simulation resulting to an increase in the instantaneous CP as the TSR increases from its lowest point at the left of the curve. The drop caused by the high TSR sensitivity of the turbine was still observed but it is not enough to bring the CP at a low enough value as seen in other simulations, this is also the reason why the curve has a very flat bottom part.

The  $f=3.0$  Hz simulation shows another different looking curve when compared to the other previous simulations but shows a similarity with the shape of the unsteady  $TSR=4$  simulation hysteresis curve shown in Figure 5.14. At this point, another definition of the reduced frequency will be presented which can be useful in explaining why the shape of the hysteresis curve changes with the increase of frequency. The frequency ratio,  $\bar{k}$  can also be defined as the ratio of the frequency of the flow and the turbine's rotational frequency as shown in Equation 18, having a  $\bar{k}=1$  means that the complete cyclic variation in the unsteady velocity is equal to the rotational velocity of the turbine. In Figure 6.27, a scatter plot of the  $\bar{k}$  value for all of the simulation in this thesis is presented. Using the hysteresis plot in Figure 6.26 and the  $\bar{k}$  values at Figure 6.27, it can be observed that simulations with values of  $\bar{k}$  less than or close to 1 have the same shape/trend, they only differs on their thickness and/or location in the steady-state turbine performance curve (for the case of the unsteady  $TSR=4$  and 8 simulations) and that shape follows the steady state performance curve as well. For the unsteady  $TSR=4$  simulation, the value of  $\bar{k}$  is 1.619 and this is the first simulation with a different shape of

hysteresis curve. It was shown and detailed in Chapter 5 that the shape is mostly affected by the separation present, vortices formed, and the occurrence of stall at low TSR, which can be argued as effect of the unsteadiness of the flow which is higher at that case than that at the unsteady TSR=6 simulation.

$$\bar{k} = \frac{2\pi f}{\omega} \text{ (eq. 18)}$$

Highlighted by a green ellipse in Figure 6.27 are those simulation that has  $\bar{k}$  values that is far from the unit value represented by a dashed line. Those cases are the ones with hysteresis curves not following the steady-state turbine performance curve and completely deviating from the other cases in terms of the shape and trend. This supports the idea that it is the frequency of the velocity inflow which mostly define the unsteadiness of the flow and its effect with the performance. Referring back to the amplitude variation study, it can be said in a broader perspective, that the effect of amplitude in the cyclic-average CP is rather linear as compared to how complicated it has become when the frequency is the variable being manipulated. Increasing the amplitude of the flow variation increases the TSR range and in effect, as shown in Chapter 5, increases the size of the hysteresis curve. Although drastic changes were observed, all the hysteresis plots are still in the same shape and trend and still with very close similarity with the steady-state performance curve which is not observed when frequency is the one being altered.

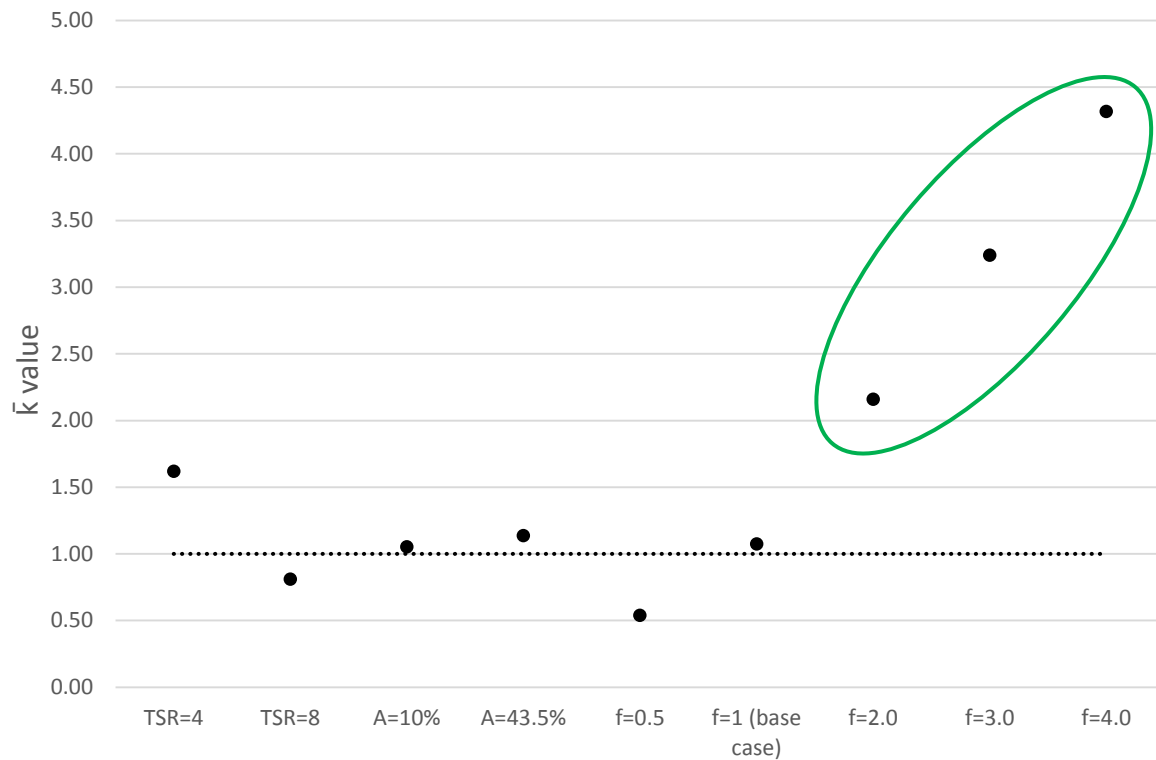


Figure 6.27  $\bar{k}$  values for all of the present cases discussed in detail in the thesis

Continuing with the description for the higher frequency simulations, the cyclic CP plot and extracted power plot for both  $f=3.0$  Hz and  $4.0$  Hz simulations are presented in Figures 6.28 and 6.29 respectively. It can be seen that for the  $f=3.0$  Hz simulation, the extracted power goes back to its initial value at  $\tau = 0.530$  which suggest that the delay effect is lower than that observed for the  $f=2$  Hz simulation. This results to an extracted power plot that is almost in phase with the available turbine performance curve. This corresponds to a CP plot and hysteresis plot that shows very different shape than every CP plot observed before as the maximum point of the instantaneous curve shifted to the right and happened at  $\tau = 0.66$  which is also a point of high TSR which is at  $TSR=7.64$ . This effect can be due to the fact that the turbine needed time to react with how fast the incoming velocity is varying but cannot cope up because of the large difference in frequencies as the  $\bar{k}$  value for this case is already greater than 3. Going back to the hysteresis plot for the  $f=3.0$  Hz simulation in Figure 6.26, it can be seen

that the increase in instantaneous CP at high TSR also results to a curve without the sudden drop that is observed in other cases. A decrease in CP was observed as TSR decreases which is also not observed for the base case simulation and other simulation with  $\bar{k}$  values less than or close to 1. Again, this is caused by the turbine cannot catch up with the very fast variation in the incoming velocity. All of the characteristics of the unsteady  $f=3.0$  Hz simulation are also observed in the one with  $f=4.0$  Hz with just a slight difference in the occurrence of the cycle maximum value which happened at  $\tau = 0.6$ . The power extracted curve also has its initial value returned at  $\tau = 0.535$  which is later than that of the  $f=3.0$  Hz simulation but its effect shows an earlier maximum resulting to a lower hysteresis curve when observed in Figure 6.26.

The fully detailed hydrodynamics behind this results regarding the higher frequency simulations is not presented in this thesis and will be a good topic for future study. A similar study was made by Danao when he investigated the effect of frequency variation in unsteady flow but in VAWT. It was found that there is not much difference in CP between the base unsteady case and the ones with lower and higher frequency (Danao, 2012). The possible cause for this difference in result may be because of the large difference in Re and also because of the reduced frequency of the unsteady simulations where in a VAWT, the turbine will undergo a number of rotation already before one cycle of wind ends which is not the case for HATT as the rotation of the tidal turbine is a lot slower than wind turbines. Nevertheless, the general trend, whereas the difference in CP for the frequency variation study is relatively smaller than that of the amplitude variation study, is both observed for this thesis and the results of Danao, The effect of the frequency variation in HAWT is currently under study by a colleague of the author under the same research group.

In conclusion, these higher frequency simulations proved that the effect of the velocity variation frequency to the performance of the tidal turbine under study is complicated in a way that there is no simple trend or linearity within the observations unlike what was observed in

the study of amplitude variation. It was also shown in this section how the  $\bar{k}$  value can be used for characterising the unsteadiness effects of frequency whereas simulations with  $\bar{k}$  values of less than or close to one, showed similar hysteresis curve characteristics with each other and  $\bar{k}$  value greater than 1 showed very different hysteresis plot as shown in Figure 6.26 where they presented hysteresis curves not following the trend of the steady turbine performance curve anymore. Also, with these final simulations, it can also be concluded that all of the unsteady flow simulations done for the Sheffield HATT in this thesis has a cyclic-averaged CP less than the steady state value suggesting that the general effect of flow unsteadiness to the HATT performance is detrimental.

## 6.10 Summary of Chapter

This chapter looks at the effects of the variation in amplitude and frequency of the incoming flow velocity equation to the performance of the Sheffield HATT. It was shown from all of the simulations in this chapter (and the thesis in general) that if the incoming flow to the Sheffield HATT is unsteady, the cyclic-average CP is lower than the steady state CP which suggests that unsteadiness in the flow is detrimental to the turbine's performance. Table 6.3 and 6.4 show the summary of the cyclic-average CP's that are calculated for all the unsteady simulations present in this chapter. It can be seen that all of the values are less than the steady state CP at TSR=6 which is at 39.46%. Variations in amplitude and frequency of the base case inflow velocity variation has been done to show their effects in the cyclic-averaged CP and the hydrodynamics differ from the steady and the base unsteady case to some extent.

The effect of the amplitude variation is linear whereas as the amplitude of the incoming flow increases, the cyclic-average CP decreases which is due to an increase size of the hysteresis curve as response to the larger range in the instantaneous TSR as shown in the 43.5% amplitude simulation in Section 6.3. The cyclic-averaged CP for the high amplitude simulation

became lower due to the very low values of instantaneous CP at high TSR. Although the cyclic-average is low, the high amplitude simulation also has the very high CP recorded which reached up to 43.78% at one point which is due to the delay effect in the turbine's extracted power which can be attributed to inertial effects specially dynamic inflow as shown in the previous sections in this chapter.

On the other hand, the frequency variation study shows a very complicated effect on the shape of the hysteresis curve and the cyclic-averaged CP. The frequency simulations with  $\bar{k}$  values less than 1 shows the same shape and trend with all the other unsteady simulations before the frequency study. Starting from  $f=2.0$  Hz simulation, where the  $\bar{k}$  value starts to be greater than 1, a drastic change in the shape of the hysteresis curve was observed, as shown in Section 6.8 and reflects a lower cyclic-averaged CP. The decrease continued for  $f=3.0$  Hz but with a very close CP values. Still, the general trend observed is that the variation of the cyclic-averaged CP for the frequency study is relatively smaller than that of the amplitude study as presented earlier in this Chapter.

Table 6.3  
Cyclic-average CP value comparison for all unsteady simulations under the amplitude variation studies

Amplitude	CP, %
10%	38.74
24.5%	37.50
43.5%	34.26

Table 6.4  
Cyclic-average CP value comparison for all unsteady simulations under the frequency variation studies

Frequency, Hz	CP, %
f=0.5	37.90
f=1.0	37.50
f=2.0	37.11
f=3.0	36.80
f=4.0	37.10

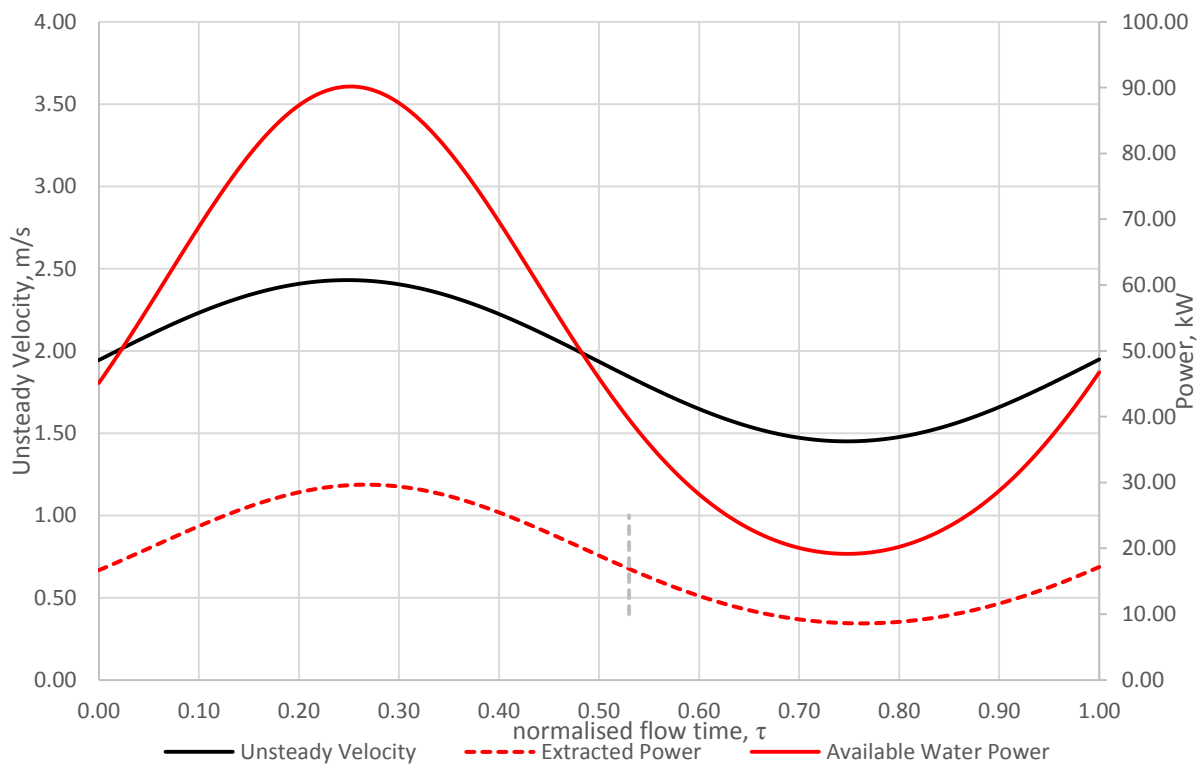
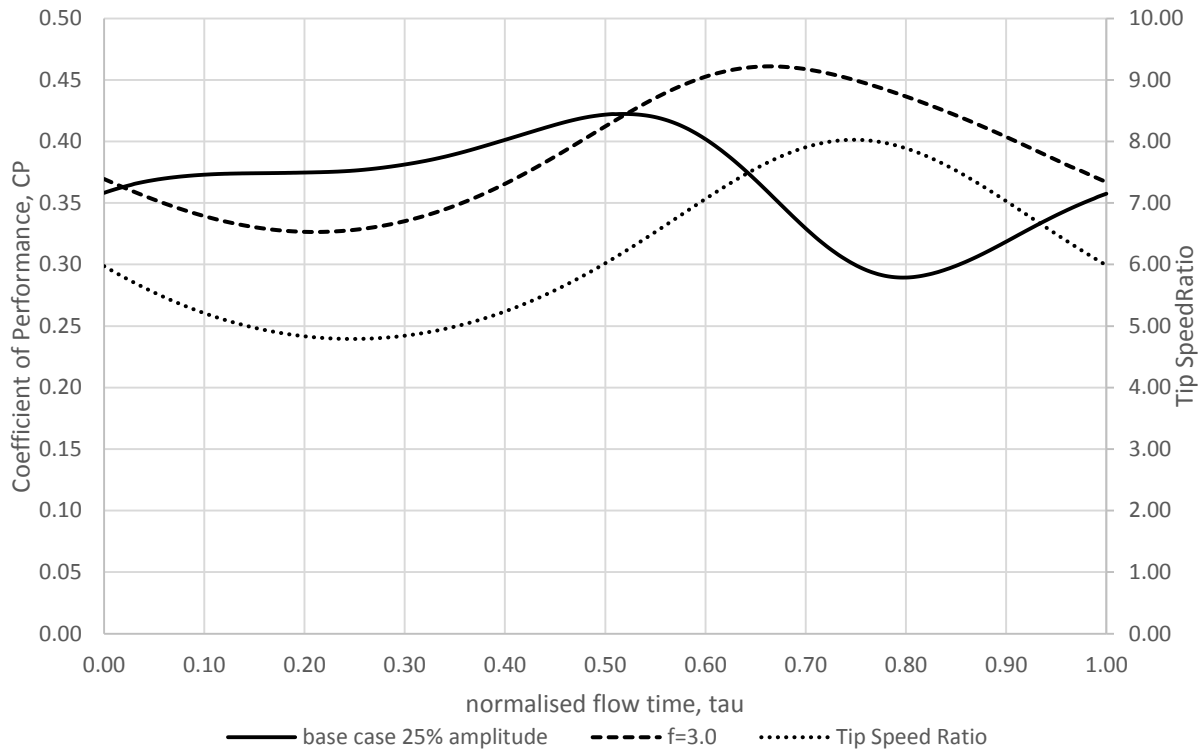


Figure 6.28 Sheffield HATT Response for the  $f=3.0$  unsteady Simulation

**top:** CP value plotted against normalised time superimposed with the base case CP plot and instantaneous TSR; **bottom:** Power extracted by the turbine plotted against normalised time superimposed with the water velocity profile and power available in the water

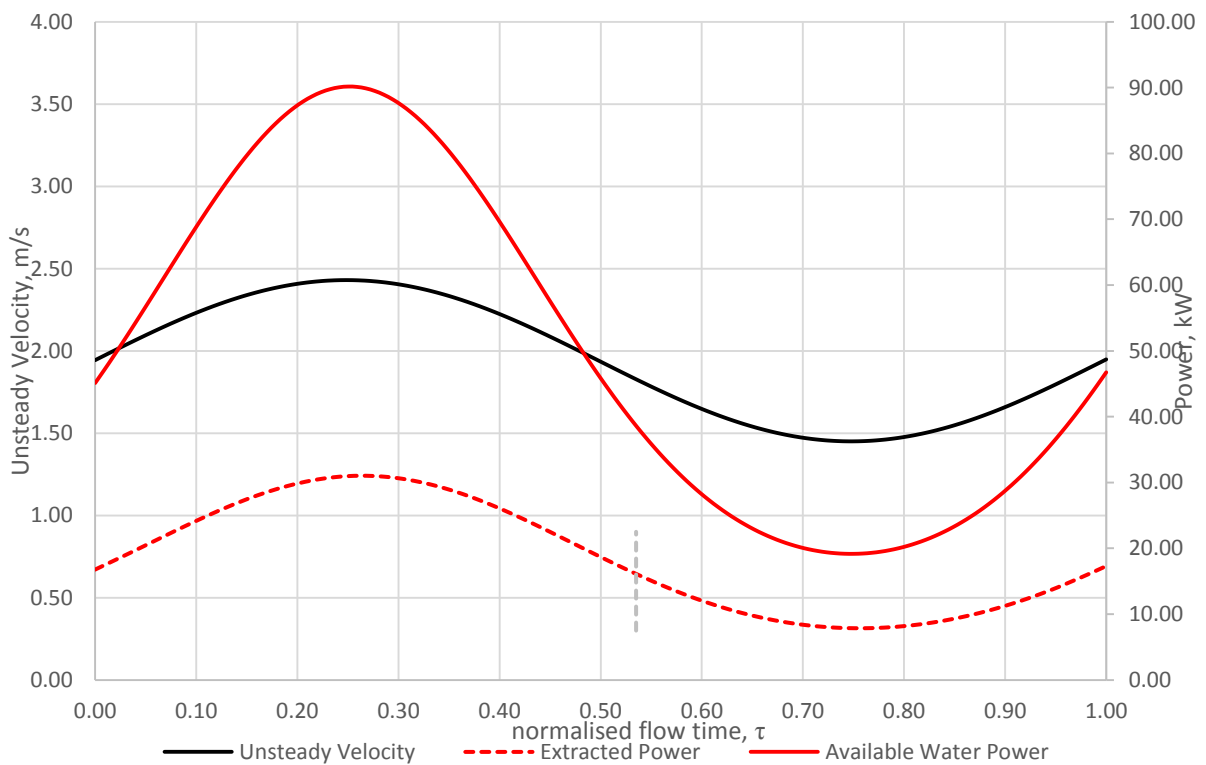
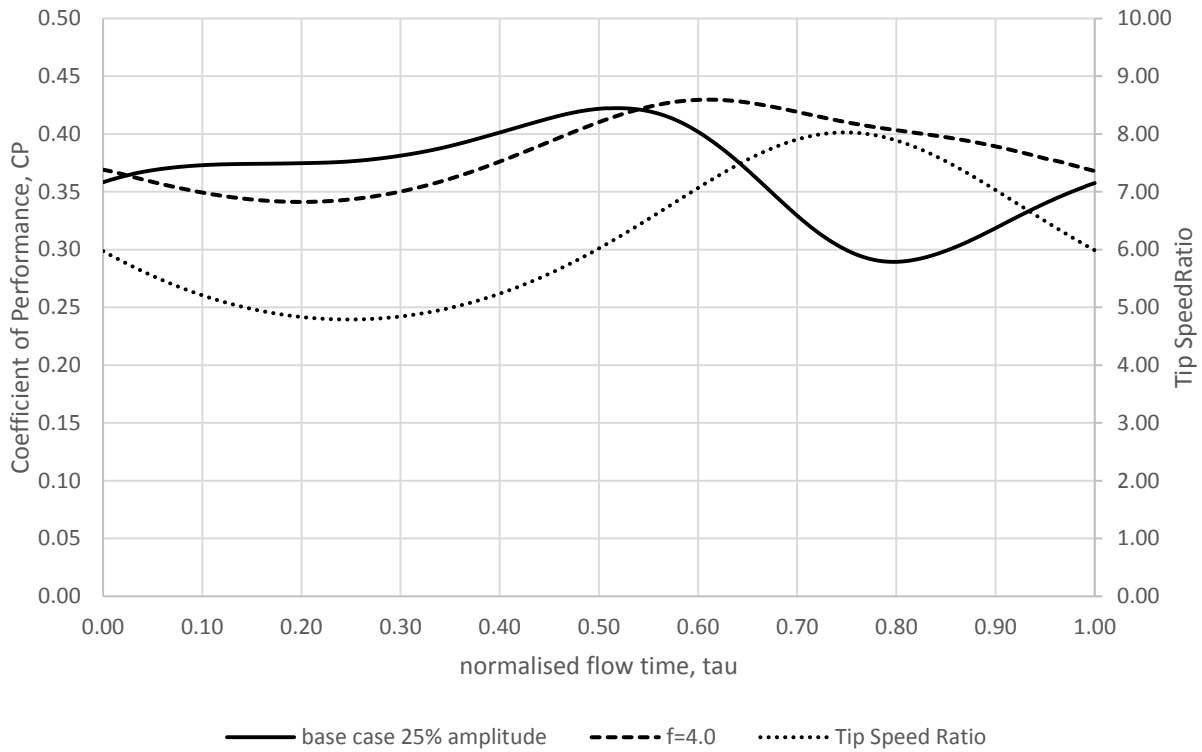


Figure 6.29 Sheffield HATT Response for the  $f=4.0$  unsteady Simulation

**top:** CP value plotted against normalised time superimposed with the base case CP plot and instantaneous TSR; **bottom:** Power extracted by the turbine plotted against normalised time superimposed with the water velocity profile and power available in the water

## Chapter 7

# Conclusions and Recommendations

### 7.1 Conclusions

The effect of flow unsteadiness to the performance and hydrodynamics of a newly-designed horizontal-axis tidal turbine was investigated in this thesis. This topic is explored due to the lack of current data available in the literature regarding unsteady flow in tidal turbine. An idealised unsteady flow regime was used to simplify the problem and allow a deeper understanding of the flow physics involved. Other researchers have used more complicated inflow boundary conditions but in the view of the author, this impedes the understanding of the flows. The Sheffield HATT, the tidal turbine used in this thesis, was designed to have a flatter performance curve over a large TSR range near its optimum TSR condition when compared to other tidal turbine at the same size. This is to have a better performance in unsteady flow whereas the TSR is instantaneously changing. A structural study using the Sheffield HATT blade was also conducted to determine if the design can be applied in real life construction.

A CFD model of the turbine was used to simulate the performance of the turbine in steady flow. RANS based simulations were conducted to complete the performance curve of the Sheffield HATT. The resulting curve was compared to the BEM simulation results in the design phase of the turbine and good agreement was obtained. The hydrodynamics of the turbine subjected in steady flow at different TSR was also presented.

Unsteady flow simulations of the Sheffield HATT CFD model were conducted by using an idealised velocity variation equation. The unsteady simulation at the optimum performance which is at  $TSR=6$  was denoted to be the base case, two other simulations (one at lower TSR and one at higher TSR) were conducted at  $TSR=4$  and  $TSR=8$  to provide comparison in terms

of the unsteady effects at different TSR's. The equation for the velocity variation used for the base case unsteady simulation was varied in terms of amplitude and frequency. The cyclic-averaged CP for each simulation and the unsteady effects in the flow hydrodynamics was compared against each other. The main findings and results of this study will be summarised and presented into the following list that can be mapped with the Objectives list presented in Chapter 1.

- The design for the Sheffield HATT is presented in Chapter 3 including the BEM simulation for the turbine's performance curve and the structural analysis for the turbine blade. The CP-TSR curve for the turbine shows a flat curve for a good range of TSR value near the optimum TSR for the turbine. The structural analysis proved that the blade design has a good structural response with low stress level and deformation for a mean tidal stream velocity of 2 m/s and an extreme case with mean tidal stream velocity of 5 m/s.
- The steady-state performance of the Sheffield HATT is presented in Chapter 4 together with the CFD methodology for the whole thesis. This is considered to be the reference cases for the comparison with the unsteady flow simulations in Chapter 5. The first unsteady case is considered to be the base unsteady case and was simulated at a mean TSR of 6 with a 25% amplitude for a flow frequency of 1 Hz which combined to  $k=0.051$ . The cyclic-averaged CP for this case is 37.5% which is lower than that of the steady-case CP at the same TSR which is at 39.46%. It was also shown that the instantaneous CP curve over TSR for this unsteady case shows a hysteresis curve that does not follow the steady-state performance curve. This is caused by the delay that was observed for the extracted power plot of the turbine showing that the first part of the cycle is not the same as the second half and thus resulting to an asymmetrical CP response. The physics of what's happening in the turbine that was explained using the

flow streamlines and pressure plots at the 75% hydrofoil span is also presented in Chapter 5.

For the unsteady TSR=4 simulation, a cyclic-averaged CP of 22.6% was obtained which is again lower than the steady-state counterpart which has a CP of 30.6%. More pronounced separation was observed for this simulation thus allowing the effect of vortices forming on the blade to be presented using the  $\lambda_2$ -criterion. The unsteady TSR=8 simulation shows the same results by which the cyclic-averaged CP obtained to be 35.1% is still lower than that of the steady case CP which is at 35.33%. This confirmed that for the three unsteady cases presented, all of the cyclic-averaged CP is lower than their steady-state counterpart and a lag/delay in the turbine's response is present causing the hysteresis curve that does not follow the steady-state performance curve. A trend regarding the cyclic-averaged CP was also observed in which it was shown that as the mean TSR increases, the cyclic-averaged CP gets closer to the corresponding steady state CP.

- The effects of variations in amplitude and frequency in the unsteady velocity equation (base case equation) to the performance of the Sheffield HATT are also explored in this thesis. For the amplitude variation study it was shown that the effect of amplitude on performance is linear by which a decrease cyclic-averaged CP was observed as the amplitude of the unsteady equation was increased. A cyclic-averaged CP of 38.74% was observed for the 10% amplitude simulation while 34.26% was recorded for the high amplitude simulation with  $A=43.5\%$ .

In terms of the frequency variation study, the low amplitude unsteady simulation at  $f=0.5$  Hz shows a higher cyclic-averaged CP at 37.9% which is 0.4% higher than that of the base case simulation at  $f=1$ Hz. A thinner and smaller hysteresis curve was observed for this case showing a very small variation on the instantaneous CP thus

resulting to a higher cyclic-averaged CP. As the frequency was increased to  $f=2.0$  Hz,  $f=3.0$  Hz and  $f=4.0$  Hz, the cyclic-averaged CPs obtained were 37.11%, 36.8% and 37.1% respectively. This shows a decrease in the cyclic-averaged CP as the frequency increases although the variation is smaller when compared to the amplitude variation study especially in the high frequency cases.

Overall, it was shown that for all of the unsteady cases presented in the thesis, the cyclic-averaged CP of the Sheffield HATT is lower than the steady state reference case suggesting that the presence of unsteadiness in the velocity inflow is detrimental to the turbine's performance. It was also presented in this section that all of the objectives presented in the opening chapter have been met although the thesis still has some limitations which will be detailed in the next sections.

## **7.2 Implications of the Results**

The main contribution of this research to the current body of knowledge is the idea that an idealised unsteady flow, that is less chaotic and less complicated than the actual tidal stream flow, has a detrimental effect to the performance of the HATT design used in the study. It was shown in the thesis that all of the cases simulated using any of the unsteady flow equation has a cyclic-averaged CP less than that of the steady state CP. Despite this observation, there are regions of the instantaneous CP plot that shows higher than that of the steady-state curve which will be a good area for future studies to look upon. This gives an idea for turbine designers that the unsteady flow effect should be included in the design phase of HATT's not only in terms of the unsteady loadings that is currently being established in the literature but also in terms of the performance of the turbines being designed.

### **7.3 Recommendations for future work.**

This research shows a good addition to the body of knowledge in terms of imparting the idea about the effects of unsteadiness to HATT's performance but there are some limitations present in the thesis that will hinder it as a direct application of knowledge in the real world. The first one is the limitations of the unsteady flow equation used in the thesis, the equation is a periodic function which will provide unsteadiness but is not an exact model of the real tidal stream flow. Another limitation is the formulation of the numerical model which is based on a tunnel instead of having a free surface on the top part domain, it was made this way because of the possibility of wind tunnel or water flume testing by the duration of the research but the author does not have the facilities available in time. The following are the recommendations by the author to be considered for future research:

- Adjustments on the 3D CFD model where a free surface will be used as the boundary conditions on the top part of the domain and have a comparison with the results of this study in terms of the steady and unsteady simulation. Also, a good addition will be a complete bathymetry of a potential tidal site to be part of the CFD simulation. This will give an idea on the effects of the contours present under water to the hydrodynamics around the turbine. This is actually a plan for future research as the turbine design was planned to be brought to the Philippines and use the bathymetric data from a local source in the CFD model.
- Another recommendation is the addition a real velocity fluctuation data to be used in the unsteady flow simulation. This is also part of a future project as tidal stream velocity mapping is currently on-going in the Philippines. Results from this recommended study will show the comparison on the results when compared to that of the results found on this thesis. This can also be expanded by having a Fluid-Structure Interaction (FSI) analysis of the Sheffield HATT under real unsteady flow. This model is the closest to

real life operation and will give data on both the turbine's unsteady performance and blade loading.

- A complete set of experiments regarding unsteady flow (even for the idealised one) is another good addition to this study. This will serve as a more concrete validation for the results that has been presented in the thesis. Experiments using a moving carriage in steady water flow has been done to model the velocity variation but the case by which the turbine is steadily mounted while the water flow velocity is varying will be better as it is the one imitating the real flow closer. Velocity variation can be done with the use flaps under water which is similar to the set-up used by Danao in his unsteady experiments in the wind tunnel for VAWT.
- A fluid-structure interaction (FSI) simulation of the Sheffield HATT in both steady and unsteady flow is one of the planned direction for this research, it will combine the ANSYS Mechanical and ANSYS Fluent simulation and solve them simultaneously to account to the deformations on the blade due to the loads and its effects to the performance of the turbine. Having the FSI simulation work for unsteady flow will be a very difficult feat but with the current developments on the simulation software nowadays, this modelling, which is closest to the real life situation will be possible.

## References

- Afgan, I., McNaughton, J., Rolfo S., Apsley, D., Stallard, T., & Stansby, P. (2013). Turbulent flow and loading on a tidal stream turbine by LES and RANS. *International Journal of Heat and Fluid Flow*, 96-108.
- Anderson, Jr., J. D. (2001). *Fundamentals of Aerodynamics*. McGraw Hill.
- ANSYS. Ansys Composite Materials Database. *Ansys Composite PrepPost Module*.
- Aqua Marine Power. (2017, January). Retrieved from Aqua Marine Power: <http://www.aquamarinepower.com/>
- Atlantis Resource Ltd. (2017, January). *Meygen*. Retrieved from Meygen: <https://atlantisresourcesltd.com/projects/meygen/>
- Bahaj, A., & Myers, L. (2001). Cavitation prediction in operating marine current turbine. *Proceedings of Renewable Energy in Maritime Island Climates* (pp. 222-229). The Solar Energy Society.
- Bahaj, A., Batten, W., & McCann, J. (2007). Experimental verifications of numerical predictions for the hydrodynamic performance of horizontal axis marine current turbines. *Renewable energy*, 2479-2490.
- Bahaj, A., Molland, A., Chaplin, J., & Batten, W. (2007). Power of thrust measurements of marine current turbines under various hydrodynamic flow conditions in a cavitation tunnel and towing tank. *Renewable Energy*, 407-426.
- Barber, R., & Motley, M. (2016). Cavitating Response of Passively Controlled Tidal Turbines. *Journals of Fluids and Structure*.
- Batten, W., Bahaj, A., Molland, A., & Chaplin, J. (2006). Hydrodynamics of marine current turbines. *Renewable Energy*, 249-256.
- Batten, W., Bahaj, A., Molland, A., & Chaplin, J. (2007). Experimentally Validated Numerical Method for the Hydrodynamic Design of Horizontal Axis Tidal Turbines. *Ocean Engineering*, 1013-1020.
- Batten, W., Blunden, L., & Bahaj, A. (2006). CFD simulation of a small farm of horizontal axis marine current turbines. *Proceedings of world renewable energy congress (WREC) VIII*, (pp. 19-25). Florence.
- Blue Energy. (2017, January). *Vertical Axis Hydro Turbine*. Retrieved from Blue Energy: <http://www.blueenergy.com/vertical-axis-turbine/vaht/>
- Bryden, I. G., Couch, S. J., Owen, A., & Melville, G. (2007). Tidal Current Resource Assessment . *Power and Energy*, 125-135.
- Budynas, R., Nisbett, J., & Shigley, J. (2015). *Shigley's Mechanical Engineering Design*. New York, NY: McGraw-Hill Education.
- Burton, T. (2001). *Wind Energy Handbook*. Chichester: Wiley.

- Carbon Trust. (2005). United Kingdom Wave and Tidal Energy Study. *Variability of UK Marine Resources*.
- Chamorro, L., Hill, C., Morton, S., & Ellis, C. (2013). On the interaction between a turbulent open channel flow and an axial-flow turbine. *Journal of Fluid Mechanics*, 658-670.
- Chen, C. C., Choi, Y. D., & Yoon, H. Y. (2013). Blade Design and Performance Analysis of a Horizontal Axis Tidal Current Turbine for low water level channel. *IOP Conf. Ser. Mater. Sci. eng.*
- Chen, L. (2015). A review of survivability and remedial actions of tidal current turbines. *Renewable and Sustainable Energy*, 891-900.
- Churchfield, M., Li, Y., & Moriarty, P. (2013). A large-eddy simulation study of wake propagation and power production in an array of tidal-current turbines. *Philosophical transaction of the Royal Society A., Mathematical, Physical and Engineering Sciences*.
- CO2CRC. (2017, January). *CO2CRC Building a low emission future*. Retrieved from CO2CRC: <http://www.co2crc.com.au/>
- Danao, L. M. (2012). *The Influence on Unsteady Wind on the Performance and Aerodynamics of Vertical Axis Wind Turbines*. Sheffield: University of Sheffield.
- Dick, E. (2015). *Fundamentals of Turbomachines, Fluid Mechanics and Its Applications*. Springer Science Business Media Dordrecht.
- Douglas, C. A. (2007). Life Cycle Assessment of the Seagen Marine current turbine. *Journal of Engineering for Maritime Environment IMechE*, 1-12.
- EMEC. (2017, January). *Alstom (Formerly TGL)*. Retrieved from EMEC: <http://www.emec.org.uk/about-us/our-tidal-clients/alstom/>
- Faudot, C., & Dahlhaug, O. (2012). Prediction of Wave Loads on Tidal Turbine Blades. *Energy*, 116-133.
- Froude, W. (1878). On the Elementary Relation between Pitch, Slip and Propulsive Efficiency. *Transaction of the Institute of Naval Architects*, 22-33.
- Galloway, P. (2013). Performance Quantification of Tidal Turbines Subjected to Dynamic Loading. *PhD Thesis*. University of Southampton.
- Gant, S., & Stallard, T. (2008). Modelling a tidal turbine in unsteady flow. *Proceedings from Offshore and Polar Engineering Conference*. Vancouver.
- Geize, V., Szydlowski, J., & Costes, M. (2004). Numerical and Physical Analysis of the Turbulent Viscous Flow Around a NACA 0015 Profile at Stall. *European Congress on Computational Methods in Applied Sciences and Engineering*.
- Glauert, H. (1935). Airplane Propellers. In W. Durrand, *Aerodynamic Theory* (pp. 169-269). Springer.
- Gorlov, A. M. (2001). *Tidal Energy*. Northeastern University Academic Press.

- Gov.uk. (2016, March). *Renewable sources of energy*. Retrieved from [https://www.gov.uk/government/uploads/system/uploads/attachment\\_data/file/547977/Chapter\\_6\\_web.pdf](https://www.gov.uk/government/uploads/system/uploads/attachment_data/file/547977/Chapter_6_web.pdf)
- Hardisty, J. (2009). *The Analysis of Tidal Stream Power*. Wiley-Blackwell.
- Hau, E. (2006). *Wind Turbines: Fundamentals, technologies, application, economics*. Springer.
- Hellio, C., Yebra, D., Apolinario, M., & Coutinho, R. (2009). Understanding the biofouling of offshore and deep-sea structures. In *Advances in marine antifouling coatings and technologies* (p. 132). Cambridge: Woodhead Publishing.
- Kang, S., Borazjani, I., Colby, J., & Sotiropoulos, F. (2012). Numerical simulation of 3D flow past a real-life marine hydrokinetic turbine. *Advances in Water Resources*, 33-43.
- King, J., & Tryfonas, T. (2009). Tidal Stream Power Technology - State of the Art. *IEEE*.
- Ladson, C. I. (1988). *Effects on independent variation of Mach and Reynolds numbers on the low-speed aerodynamic characteristics of the NACA 0012 Airfoil section*. NASA technical memorandum 4074.
- Lee, T., & Gerontakos, P. (2004). Investigation of flow over oscillating airfoil. *Journal of Fluid Mechanics*, 313-341.
- Leishman, J. G. (2006). *Principle of Helicopter Aerodynamics*. Cambridge University Press.
- Leroux, T., Osbourne, N., McMillan, J., Groulx, D., & Hay, A. (2016). Numerical Modelling of a Tidal Turbine Behaviour under Realistic Unsteady Tidal Flow. *3rd Asian Wave and Tidal Conference*. Marina Bay Sands, Singapore.
- Liu, P., & Veitch, B. (2012). Design and optimization for strength and integrity of tidal turbines rotor blades. *Energy*, 393-404.
- Lunar Energy. (2017, January). *Lunar Energy Harnessing Tidal Power*. Retrieved from Lunar Energy: <http://www.lunarenergy.co.uk/>
- Luznik, L., Flack, K. A., Lust, E., & Taylor, K. (2013). The Effect of Surface Waves on the performance characteristics of a model tidal turbine. *Renewable Energy*, 108-114.
- MacLeod, A., Barnes, S., Rados, K., & Bryden, I. (2002). Wake effects in tidal current turbine farms. *Proceedings from International Conference of Marine Renewable Energy*. Newcastle.
- Malki, R., Williams, A., Croft, T., & Masters, I. (2013). A coupled blade element momentum - Computational fluid dynamics model for evaluation of tidal stream turbine performance. *Applied mathematical Modelling*, 3006-3020.
- Marine Current Turbines. (2017, January). *Seagen Technology*. Retrieved from Marine Current Turbines: <http://www.marineturbines.com/Seagen-Technology>

- Mason-Jones, A., O'Doherty, D., Morris, C., & O'Doherty, T. (2013). Influence of a velocity profile & support structure on tidal stream turbine performance. *Renewable energy*, 23-30.
- Massey, B. S. (1979). *Mechanics of Fluid* (4th ed.). Van Nostrand Reinhold Company Ltd.
- Masters, I., Chapman, J., Orne, J., & Willis, M. (2010). A robust blade element momentum theory model for tidal stream turbines including tip and hub loss corrections. *Journal of Marine Engineering Technology*, 25-35.
- McNae, D. (2014). Unsteady hydrodynamics of Tidal Stream Turbines. *PhD Thesis*. Imperial College London.
- Menter, F. R. (1994). Two-equation eddy-viscosity turbulence models for engineering applications. *AIAA* , 1598-1605.
- Met Office. (2017, January). *Met Office*. Retrieved from <http://www.metoffice.gov.uk/climate-guide/climate-change>
- Milne, I. A., Sharma, R. N., Flay, R. J., & Bickerton, S. (2013). Characteristics of the turbulence in the flow at a tidal stream power site. *Philosophical Transactions of the Royal Society A*.
- Milne, I., Day, A., Sharma, R., & Flay, R. (2016). The characterisation of the hydrodynamic loads on tidal turbines due to turbulence. *Renewable and Sustainable Energy*.
- Milne, I., Day, A., Sharma, R., & Flay, R. (2012). Blade loads on tidal turbines in planar oscillatory flow. *Ocean Engineering*, 163-174.
- Minesto. (2017, January). *The future of renewable energy*. Retrieved from Minesto: <http://minesto.com/our-technology>
- Miniaci, D. (2012). investigating the Influence of the Added Mass Effect to Marine Hydrokinetic Horizontal-Axis Tidal Turbines Using a General Dynamic Wake Wind Turbine Code. *Marine Technology Society Journal*.
- Montomerie, B., & Forskningsinstitut, T. (2004). *Methods for Root Effects, Tip Effects and Extending the Angle of Attack Range to +- 180°, with Application to Aerodynamics for Blades on Wind Turbines and Propellers*. Swedish Defence Research Agency.
- Morris, C. (2015). Influence of Solidity on the Performance, Swirl, Characteristics, Wake Recovery and Blade Deflection of a Horizontal Axis Tidal Turbine. *PhD Thesis*. Cardiff University.
- Mycek P, et al. (2013). Numerical and experimental study of the interaction between two marine current turbines, *International Journal of Marine Energy*, pp 70-83.
- Myers, L. (2005). Operational parameters of horizontal axis marine current turbines. *PhD Thesis*. University of Southampton.
- Neftel, A., Friedli, H., Moore, E., Lotscher, H., Oeschger, H., Siegenthaler, U., & Stauffer, B. (1994). Historical carbon dioxide record from the Siple Station ice core. In D. K. T.A. Boden, *Trends'93: A Compendium of Data on Global Change* (pp. 11-14). Oak Ridge.

- Nicholls-lee, R. F., & Turnock, S. R. (2007). Enhancing Performance of a Horizontal Axis Tidal Turbine Using Adaptive Blades. *Ocean*.
- O'Doherty, T., Mason-Jones, A., O'Doherty, D., Evans, P., Wooldridge, C., & Fryett, I. (2010). Considerations of a horizontal axis tidal turbine sited off the Welsh coast. *8th European Wave and Tidal Conference*.
- Openhydro. (2017, January). *Openhydro*. Retrieved from Openhydro: <http://www.openhydro.com/>
- Osborne, N. A. (2015, August). 3D modelling of a tidal turbine – a numerical investigation of wake phenomena. *Masters of Applied Science*. Halifax: Dalhousie University.
- Ostawari, C., & Naik, D. (1985). *Post-Stall Wind Tunnel Data for Naca 44xx Series Airfoil Sections*. Golden, Colorado: Technical Report No. SERI/STR-217-2559, Solar Energy Research Institute.
- PhysicalGeography. (2010, April). *PhysicalGeography*. Retrieved from PhysicalGeography: <http://www.physicalgeography.net/fundamentals/7y.html>
- Pinkerton, R. M. (1938). *The Variation with Reynolds Number of Pressure Distribution over an Airfoil Section*. Cranfield, UK: Technical Report No. 613, NASA.
- Reynolds, O. (1883). An investigation into the circumstances which determine whether the motion of water shall be direct or sinuous and the law of resistance in parallel channels. *Philosophical Transaction of the Royal Society*, 935-982.
- Snel, H., & Schepers, J. G. (1993). Investigation and Modelling of Dynamic Inflow Effects. *ECWEC*. Travemunde.
- Sobotta, D. (2014). The aerodynamics and performance of small scale wind turbine starting. *PhD Thesis*. University of Sheffield.
- The earth project. (2017, January). *All You Need to Know about Tidal Power*. Retrieved from The earth project: <http://theearthproject.com/know-tidal-power/>
- TidalEnergyToday. (2017, January). *Estimate of global potential tidal resources*. Retrieved from TidalEnergyToday: <http://tidalenergytoday.com/2015/02/17/estimate-of-global-potential-tidal-resources/>
- Viterna, L., & Corrigan, R. (1982). *Fixed Pitch Rotor Performance of Large Horizontal Axis Wind Turbines*. Cleveland, Ohio: NASA Lewis Research Center.
- Vogel, C., Wilden, R., & Houlsby, G. (2014). The Power Potential of a Tidal Turbine Array with Turbine Power Capping. *2nd Asian Wave and Tidal Energy Conference*.
- Walker, S. (2014, November). Hydrodynamic interactions of a tidal stream turbine and support structure. *PhD Thesis*. University of Sheffield.
- Wang, D., Atlar, M., & Sampson, R. (2007). An experimental investigation on cavitation, noise, and slipstream characteristics of ocean stream turbines. *Part A: Journal of Power and Energy*, 219-231.

- Wendler, J., Marten, D., Pechlivanoglou, G., Nayeri, C., & Paschereit, C. (2013). QBlade: An Open Source Tool for Design and Simulation of Horizontal and Vertical Axis Wind Turbines. *International Journal of Emerging Technology and Advanced Engineering*, 264-269.
- Whelan, J. I. (2010). A fluid dynamic study of free-surface proximity and inertia effects of tidal turbines. *PhD Thesis*. imperial College of Science, Technology and Medicine.
- Whelan, J., Graham, J., & Piero, J. (2009). Inertia Effects on Horizontal Axis Tidal Turbines. *Proceedings of the 8th European Wave and Tidal Conference*.
- Wood, R., Bahaj, A., Turnock, S., Wang, L., & Evans, M. (2010). Tribological design constraints of marine renewable energy systems. *Philosophical Transactions of the Royal Society A*.
- Yebra, M., Rasmussen, S., Weinell, C., & Pedersen, L. (2010). Marine Fouling and Corrosion Protection for Off-Shore Ocean Energy Setups. *3rd International Conference on Ocean Engineering*, (pp. 1-6).
- Young, Y., Motley, M., & Young, R. (2010). Three-Dimensional Numerical Modelling of the Transient Fluid-Structural Interaction Response of Tidal Turbines. *Journal of Offshore Mechanics and Arctic Engineering*.